Study of fluorescent nano-emulsions : formulation, optimization and study of the encapsulation of model molecules

Xinyue Wang

UNIVERSITÉ DE STRASBOURG

ÉCOLE DOCTORALE DES SCIENCES CHIMIQUES

CNRS 7199 Conception et Application de Molécules Bioactives

THÈSE

présentée par :

WANG Xinyue

soutenue le : **18 septembre 2020**

pour obtenir le grade de

Docteur de l'université de Strasbourg

Discipline/ Spécialité : Science pharmaceutiques

Étude de nano-émulsions fluorescentes, formulation, optimisation et étude de l'encapsulation de molécules modèles

THÈSE dirigée par :

M. ANTON Nicolas	Maître de conférences, Université de Strasbourg

RAPPORTEURS :

Mme. NOUVEL Cécile	Professeur, Université de Lorraine / ENSIC
Mme. CHAMBIN Odile	Professeur, Université de Bourgogne

AUTRES MEMBRES DU JURY :

M. BEDUNEAU Arnaud	Maître de conférences, Université de Franche-Comté
M. COLLOT Mayeul	Chargé de recherches CNRS, Université de Strasbourg
M. VANDAMME Thierry	Professeur, Université de Strasbourg

Acknowledgements

Looking back through the three years spent here, I feel so lucky that I can be a student here, in Faculty of Pharmacy, University of Strasbourg, and I always believe that the good luck I got comes from the generosity of my benefactors.

Foremost, I would like to express my sincere gratitude to my supervisor Dr. Nicolas Anton. I still remember the day when I received his invitation from e-mail, as a Christmas gift, with his words: *We can have a try!* It is the encouragement that gives me the opportunity to pursue my PhD overseas, and it is the encouragement that supports me during the last years. I would like to thanks for his inspiration to let me express my ideas; thanks for his patience, to correct my paper over and over again; thanks for his trust, to let me do whatever I am interested; and thanks for his knowledge, to lead me in the way to scientific exploration. Without his guidance and persistent help, this thesis could not become a reality.

Beside my supervisor, I would like to express my deep gratitude to Dr. Mayeul Collot. Most of my synthesis and fluorescence work is supervised by him. Thanks for his patience to teach me everything from the very beginning, and thanks for his motivation, enthusiasm, open-mind and creative ideas, letting me realize that a scientist's life can be that 'colorful'.

And also, I would like to thank dear Prof. Thierry Vandamme. It is a great honor to be a member of his research group. Thanks for providing me everything for my research work and the opportunities to express myself in international conferences. From him, I've learned not just the attitude towards science, but also the way to be a good person.

My sincere thanks also go to Dr. Andrey Klymchenko for precise discussions and advices on the fluorescence projects, to Dr. Pichandi Ashokkumar for two-photon experiment, to Dr. Halina Anton for cellular experiment, to Dr. Delphine Garnier for her assistance in NMR analyses, to Dr. Tkhe Kyong Fam and to Mme. Sophie Bou. It was a pleasure to work with them and learn from them.

My appreciation extends to jury members, Prof. Cécile Nouvel, Prof. Odile Chambin and Dr. Arnaud Beduneau, thanks for their precious time to evaluate this work.

I would also thank all my colleagues. Thank Dr. Minjie Zhao for academic discussions and daily care. I appreciate the friendly atmosphere, useful suggestions and joyful discussions from Group Biogalenique. Thanks to Asad, Bilal, Salman, Aidar, Riccardo, Abdelaziz, Germain, Usama,

Sidy, Mady and Alphonse, for every tea time and football match, I'll never forget the happy time spent with you.

Besides, I want to acknowledge China Scholarship Council to provide me the funding to study here.

My special thanks would like to go to my boyfriend, for taking care of me, encouraging me and providing useful chemical suggestions.

Many thanks to my friends here in Illkirch for sharing delicious food, for keeping me accompany and for good memories about hiking and cycling. Thanks to my best friends Xiaoyou, Qingnan and Lunxiang in China, no matter how far away we are from each other, their concerns and encouragements are always by my side.

Last but not the least, I would like to express my sincere thanks and loves to my parents, whatever decision I made, they are always supporting me.

Xinyue Wang

University of Strasbourg

August 2020

Table of Contents

List of Abbreviations

ACQ	Aggregation-caused quenching	AF4	Asymmetric flow field flow fractionation
AFM	Atomic force microscope	AIE	Aggregation-induced emission
API	Active pharmaceutical ingredient	APTES	(3-aminopropyl) triethoxysilane
AUC	Plasma concentration-time curve	BBB	Blood brain barrier
	Analytical ultracentrifugation		
BCS	Biopharmaceutical classification systems	BODIPY	Boron-dipyrromethene
CMC	Critical micelle concentration	Cryo-TEM	Cryogenic transmission electron microscopy
DBS	Dioxaborine barbituryl styryl	DBI	Dioxaborine barbituryl indolyl vinyl
DDPD	N,N-dicyclohexyl-1,7-dibromo-3,4,9,10-perylenetetracarboxylic diimide	DLS	Dynamic light scattering
DMF	Dimethylformamide	DOSY	Diffusion ordered NMR spectroscopy
DOX	Doxorubicin	DSC	Differential scanning calorimetry
DSPC	Distearoylphosphatidylcholine	EDX	Energy dispersive X-ray spectroscopy
EELS	Electron energy-loss spectroscopy	ELS	Electrophoresis light scattering
EME	Emulsified microemulsion	EPR	Enhanced peemeability and retention
ESEM	Environmental scanning electron microscope	EUNCL	European Nanomedicine Characterization Laboratory
FCS	Fluorescence correlation spectroscopy	FRET	Förster resonance energy transfer
fSPT	Fluorescence single particle tracking	HATU	Hexafluorophosphate azabenzotriazole tetramethyl uranium
HD	Dihydroxyxanthene hemicyanines (Huda dye)	HNPs	Hybrid nanoparticles
HPH	High-pressure homogenization	HPS	Hexaphenylsilole
LBN	Lipid-based nanoparticle	LCT	Long chain triglycerides
LDH	Lactate dehydrogenase	MALS	Multi angle light scattering
MCF-7/ ADR	A multidrug-resistant breast cancer model		
		MCT	Medium chain triglycerides
MDR	Multidrug resistance	MRI	Magnetic resonance imaging
MTT	3-(4,5-dimethylthiazol-2-yl)-2,5-diphenyltetrazolium bromide	NE	Nano-emulsion

NCI-NCL	National Cancer Institute Nanotechnology Characterization Laboratory	NEP	Nanoparticle enabled medicinal product
NMR	Nuclear magnetic resonance	NR	Nile red
NSAID	Nonsteroidal anti-inflammatory drug	NTA	Nanoparticle tracking analysis
OSA	Octadecyl succinic anhydride	o/O/W	Oil-in-oil-in-water
O/W	Oil-in-water	o/W/O	Oil-in-water-in-oil
PCS	Photon correlation spectroscopy	PD	Pharmacodynamics
PDI	Polydispersity index	PEG	Polyethylene glycol
PFG-NMR	Pulsed field gradient NMR	PGPR	Polyglycerol polyricinoleate
PIT	Phase inversion temperature	PMAO	Poly(maleic anhydrade-alt-1-octadecene)
PK	Pharmacokinetics	PSD	Particle size distribution
RES	Reticuloendothelial system	RO	Red raspberry oil
SANS	Small-angle neutron scattering	SAXS	Small-angle X-ray scattering
SD	Solid dispersions	SDS	Sodium dodecyl sulfate
SEDDS	Self-emulsifying drug delivery system	SEM	Scanning electron microscopy
SLN	Solid lipid nanoparticles	SLS	Static light scattering
SNEDDS	Self-nano-emulsifying drug delivery system	SOR	Surfactant to oil ratio
SOWR	Surfactant + oil to water ratio	Span	Sorbitan esters
SPION	Superparamagnetic iron oxide nanoparticle	SPT	Single particle tracking
TEA	Triethylamine	TEER	Transepithelial electrical resistance
TEM	Transmission electron microscopy	TEOS	Tetraethylorthosilicate
THF	Tetrahydrofuran	THP	Tetrahydropyrimidine
TPB	Tetraphenylborate	TPGS	Tocopheryl polyethylene glycol succinate
TRPS	Tunable Resistive Pulse Sensing	Tween	Polysorbate
VEA	Vitamin E acetate	W/O	Water-in-oil
w/O/W	Water-in-oil-in-water	W198	Bromotetrandrine, a P-gp inhibitor

Résumé en Français

1. Introduction

Les nano-émulsions sont définies par une dispersion colloïdale de gouttelettes d'huile dans une phase continue aqueuse, stabilisées par des molécules amphiphiles. Leur diamètre hydrodynamique est compris entre 20 et 300 nm [1]. Les nano-émulsions sont généralement utilisées pour la délivrance de molécules lipophiles, et sont considérées comme un système de délivrance de médicaments à fort potentiel du fait de leur remarquable stabilité, de leur biocompatibilité, biodisponibilité, et la simplicité de leur préparation [2,3].

Les nano-émulsions peuvent être fabriquées par différentes méthodes, classifiées en deux catégories : *(i)* les méthodes haute-énergie et *(ii)* les méthodes basse-énergie. Parmi ces deux méthodes la méthode basse énergie est la plus intéressante en termes de rendement énergétique, de capacité d'encapsulation, et également du fait qu'il est aisé de réaliser à la transposition industrielle du procédé. Parmi les méthode *basse-énergie*, l'émulsification spontanée un exemple très intéressant de méthode de formulation, et fût une des méthodes les plus étudiées dans ce domaine, au cours des dernières années [4-7].

L'émulsification spontanée tire bénéfice des propriétés physico-chimiques des surfactants non-ioniques pour créer une très fine division de la phase huileuse, à l'échelle nanométrique. Le principal phénomène qui est utilisé dans l'émulsification spontanée, est le fait que les surfactants non-ioniques ont leur solubilité qui varie avec la température, ce qui a pour conséquence de leur conférer une solubilisation soit dans l'eau, soit dans l'huile. La simplicité de ce procédé le rend tout particulièrement intéressant pour des applications dans le domaine pharmaceutique et dans la formulation de molécules lipidiques.

De nombreuses applications notamment en imagerie médicale et cellulaire nécessitent l'encapsulation de sondes fluorescentes pour le suivi *in vitro* ou *in vivo* de la localisation des nano-gouttelettes. Ainsi, cela permettra de suivre le devenir et le comportement de ses cargos notamment lors de la mise en place de stratégies de ciblage. Un second aspect lié à ce premier, est la stabilité de l'encapsulation de ses sondes fluorescentes et notamment la compréhension et le contrôle des mécanismes de libération lorsque les gouttelettes sont en présence d'un milieu accepteur capable de solubiliser les molécules hydrophile et lipophile.

Mon travail de thèse porte sur de l'étude de la formulation de nano-émulsions, l'études de l'encapsulation de sondes fluorescentes, de la stabilité de l'encapsulation et des mécanismes qui entrent en jeu dans leur libération, ainsi que sur l'optimisation de leurs propriétés de brillance et d'imagerie.

2. Résultats et discussions

Le travail de thèse est composé de plusieurs parties, La **première partie** de ce travail de thèse a porté sur l'étude de l'optimisation de la fluorescence des nano-émulsions. Nous avons étudié l'impact de la nature de la sonde fluorescente encapsulée, et de la nature de l'huile (viscosité, polarité), sur propriété de brillance des gouttelettes. Une application fût le développement de gouttelettes ultrabrillantes que l'on peut suivre *in vitro* individuellement. Pour ce faire, une série de nouvelles sondes fluorescentes à base de Dioxaborin Barbituryl Styryl (DBS). Ces nouveaux fluorophores DBS présentent des pics d'absorptions et d'émissions très étroits, et une excellente photo-stabilité. Nous avons déterminé que la viscosité de l'huile est un facteur important pour augmenter la brillance.

Dans ce travail, et j'ai pu comparer plusieurs fluorophores DBS ont été comparés ainsi que différentes conditions expérimentales, faisant varier les milieux de solubilisation (huile et solvant), et en jouant sur une multitude de conditions expérimentales de formulations. Nous avons pu améliorer notre compréhension des propriétés des gouttelettes fluorescentes. Comme application, nous avons effectué un suivi des gouttelettes individuelles au sein d'une cellule, dans différentes conditions et nous avons montré qu'il est possible de détecter des variations de vitesses des particules *in cellulo*, en fonction de leurs propriétés physico-chimiques (Fig. 1).

Ce travail a été publié dans *ACS Applied Materials and Interfaces* (IF = 8.46) Wang *et al.* 2019, 11, 14 (https://doi.org/10.1021/acsami.8b22297).

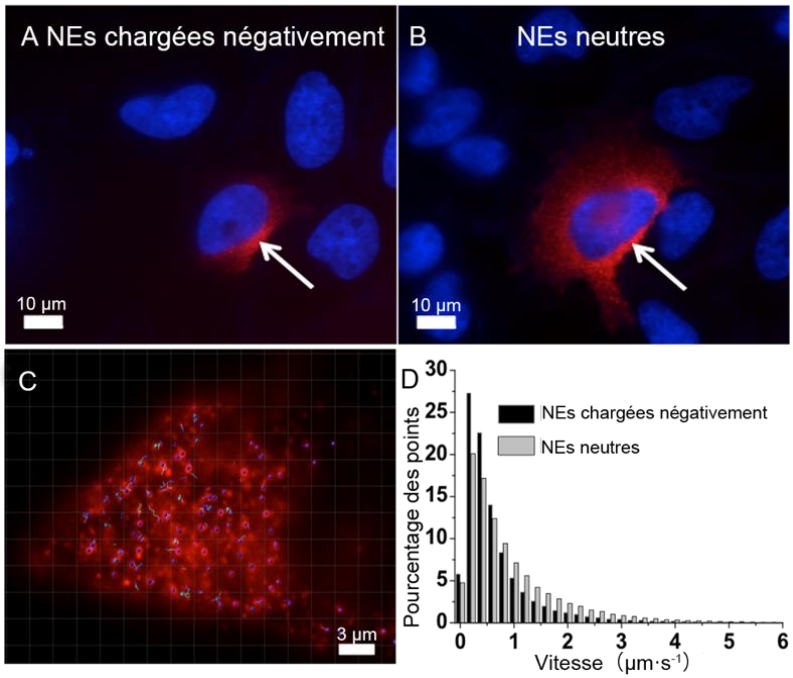

Figure 1 : Micro-injection de nano-émulsions encapsulant du DBS-C_8 loaded, dans des cellules Hela. (A) Nano-émulsions dont la surface est chargée négativement, (B) nano-émulsions neutres, (C) et (D) suivi individuel des gouttelettes et profils des vitesses dans ces deux conditions.

La **seconde partie** de ma thèse de doctoratporte sur un aspect également important de l'encapsulation d' un actif dans les nano-émulsions : l'étude de l'encapsulation, de la stabilité de l'encapsulation et des mécanismes de libération des molécules lipidiques encapsulées. Pour ce faire, c'est un dérivé lipidique de la sonde fluorescente Nile rouge (NR668), qui fût solubilisée dans le cœur huileux des gouttelettes de la nano-émulsion. La concentration choisie, importante, implique un effet optique appelé inhibition auto-induite, due à l'agrégation des sondes fluorescentes. De ce fait, une libération de la sonde aura pour incidence de la diluer et donc d'augmenter la fluorescence. Nous avons suivi ce phénomène avec le calcul du *rendement quantique*. En mettant en contact des gouttelettes *chargées* de sondes fluorescentes, avec des gouttelettes *vides* nous avons pu mettre en évidence le mécanisme de libération des principes actifs lipophiles, ainsi que les paramètres de formulations et les paramètres thermodynamiques qui ont un impact sur ce mécanisme de libération. Cette étude originale a montré que la libération d'un principe actif lipophile suit le principe de mûrissement compositionnel, et qui est très dépendant de la nature du milieu accepteur ainsi que des paramètres thermodynamiques environnementaux.

Nous avons ainsi montré que la libération de molécules lipidiques encapsulées dans les gouttes passe par une solubilisation partielle dans la phase continue aqueuse (Fig. 2 (A) et (B)) et les mécanismes sont dépendants des facteurs qui vont influencer cette solubilisation. Le modèle qui décrit cette libération est celui du mûrissement compositionnel, conduisant à un équilibre thermodynamique au bout de 5h, équilibre qui peut considérablement varier en fonction des conditions expérimentales, comme la composition du milieu accepteur, le rapport donneur / accepteur, la température, ou encore la concentration en fluorophores dans le compartiment donneur.

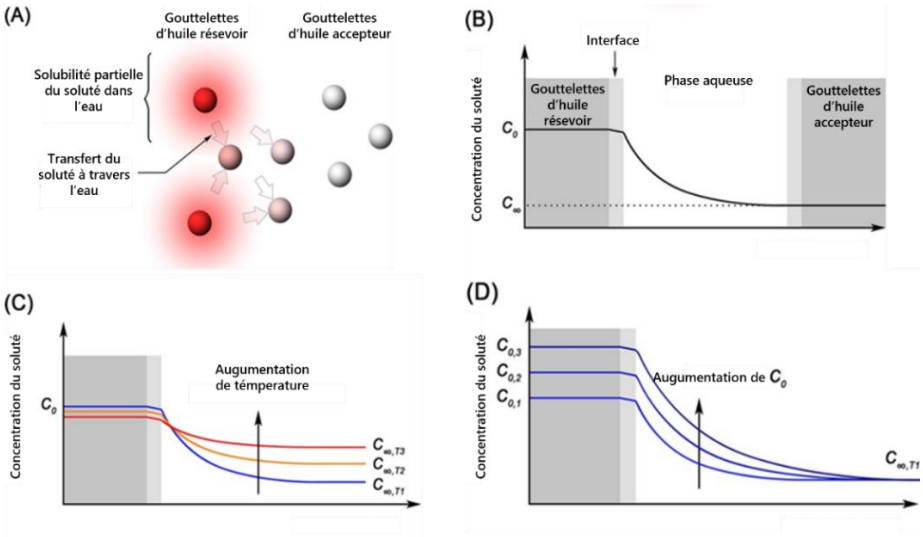

Figure 2 : (A) et (B) Représentation schématique du transfert des fluorophores, du compartiment réservoir vers le compartiment donneur ; (B) impact de la température et (C) de la concentration dans le donneur, sur la solubilité dans la phase continue.

La libération des molécules encapsulées passe par leur solubilisation dans la phase aqueuse. Cette dernière est en équilibre avec le milieu accepteur. Nous avons montré que le relargage est plus important lorsque l'on augmente le nombre d'accepteurs, la température (Fig. 2(C)), ou la concentration des gouttelettes « donneurs » (Fig. 2 (D)).

Ces résultats ont été publié dans *Journal of Colloid Interface and Science* (IF = 6.36) (https://doi.org/10.1016/j.jcis.2020.06.028)

la troisième partie porte sur l'étude de l'émulsification spontanée, le rôle du surfactant dans le procédé de formulation et l'impact de sa structure chimique sur le résultat de l'émulsification, la taille des gouttes, et la polydispersité de la suspension. Le but de cette étude a été de synthétiser différents types de nouveaux surfactants biocompatibles, variant très légèrement la longueur de la chaîne hydrophile et/ou de la chaîne lipophile, ainsi que leur charge et le nombre des chaînes. Nous avons ensuite évalué l'incidence de ces modifications structurelles sur le processus d'émulsification, et mis en évidence quels sont les facteurs les plus importants dans l'optimisation de cette méthode. Nous avons construit de nouvelles molécules tensioactives. Mon travail a consisté en la synthèse et la purification de ses différentes molécules, ainsi que la réalisation d'essais d'émulsification, en utilisant comme phase huileuse la vitamine E acétate connue pour sa compatibilité avec la méthode d'émulsification spontanée.

Cette étude a révélé les structures qui permettent d'améliorer le procédé d'émulsification, notamment la structure A qui se différencie nettement des autres structures et permet de produire des gouttes très fines et une suspension monodisperse. Il apparaît que le procédé d'émulsification est largement dépendant des affinités des molécules tensioactives pour la phase aqueuse et la phase huileuse, en plus de la fraction volumique de phase dispersée, de la concentration en surfactants, et de la température.

Le **dernier chapitre de** ce travail de thèse présente une série de travaux connexes sur les nano-émulsions fluorescentes auxquels j'ai participé. Un exemple est celui du développement de nouvelles méthodologies pour caractériser les gouttelettes lipidiques, notamment basées sur l'électrophorèse, permettant la caractérisation fine des propriétés de particules comme la composition de la surface, sans nécessairement employer des purifications sur colonne ou par dialyse qui sont des méthodes, dans certaines mesures, délicates à mettre en œuvre.

3. Conclusion générale

Le travail de thèse a principalement porté sur l'étude (i) de nano–émulsions encapsulant des molécules fluorescentes, (ii) l'optimisation des formulations, (iii) des propriétés physico-chimiques et d'imagerie, et (iv) l'application à la compréhension de ses systèmes dispersés et des propriétés de libération. Ce travail m'a beaucoup apporté tant sur le plan expérimental que sur le plan de la théorie des systèmes dispersés et de la caractérisation de la fluorescence. Les études menées au cours de cette thèse m'ont appris à concevoir, mener et gérer des projets de recherches multidisciplinaires.

4. Références

1. Anton N, Vandamme TF. The universality of low-energy nano-emulsification. *International Journal of Pharmceutics*. 2009;377(1-2):142-147.
2. Li X, Anton N, Vandamme TF. Nano-emulsions: Overview and applications. Nanopharmaceutics: the potential application of nanomaterials: *World Scientific*; 2013. p. 21-48.
3. Jafari SM, McClements DJ. Nanoemulsions: Formulation, applications, and characterization: *Academic Press*; 2018.
4. Rehman AU, Collot M, Klymchenko AS, Akram S, Mustafa B, Vandamme TF, et al. Spontaneous nano-emulsification with tailor-made amphiphilic polymers and related monomers. *European Journal of Pharmaceutical Sciences*. 2019;1(1):27-36.
5. Wang X, Anton N, Ashokkumar P, Anton H, Fam TK, Vandamme TF, et al. Optimizing the fluorescence properties of nanoemulsions for single particle tracking in live cells. *ACS Applied Materials and Interfaces*. 2019;11(14):13079-13090.
6. Attia MF, Dieng SM, Collot M, Klymchenko AS, Bouillot C, Serra CA, et al. Functionalizing nanoemulsions with carboxylates: Impact on the biodistribution and pharmacokinetics in mice. *Macromolecular Bioscience*. 2017;17(7): 1600471.
7. Bou S, Wang X, Anton N, Bouchaala R, Klymchenko AS, Collot M. Lipid-core/polymer-shell hybrid nanoparticles: Synthesis and characterization by fluorescence labeling and electrophoresis. *Soft Matter*. 2020; 16(17): 4173-4181.

Introduction to Thesis

In the last decade, the development and application of nanotechnology and/or nanomaterials in medicine field have derived nanomedicine. Since most of nanomaterials are within a scale of biological molecules and structures, nanomaterials are considered with many advantages in diagnosis and treatment of varieties of diseases. They have the ability to improve the solubility, biocompatibility and pharmacokinetic properties of certain active pharmaceutical ingredients (APIs). Functionalities can also be added by interfacing them with biological molecules or structures thus improving therapeutic index by targeting delivery.

There are a lot of nanomaterials that used for drug or constant agent delivery, including organic nanoparticles (micelles, carbon-based materials, liposomes, etc.), inorganic nanoparticles (quantum dots, magnetic nanoparticles, etc.) and hybrid nanoparticles. Among various advanced systems, nano-emulsions play an important role. Nano-emulsion is defined as an isotropic dispersed system of two immiscible liquids, with a droplet size ranging from 20 to 200 nm. The nanoscale size provides emulsion droplets with high surface area and good physicochemical stability, which makes it an ideal carrier for efficient delivery. Comparing with other delivery systems, the oily core of nano-emulsions ensures a relatively low toxicity and an improved loading capacity of poorly dissolved drugs. Thus, nano-emulsions are becoming promising carriers not only in research field but also in industry.

The development of nano-emulsion systems has been through three stages. The history of injectable emulsion can go back to 17th century, since when the conventional emulsions were clinically used as energy sources for hospitalized patients by providing essential fatty acids and vitamins. On the second stage, the utilization of nano-emulsions for delivering lipophilic therapeutic agents, intravenously, has been continuously growing due to its biocompatible nature, and with some formulations came into market through various administration routes. To date, recent interests of nano-emulsions are focused on advanced and functionalized delivery. For example, the multi-layer emulsions show the potential of controlled release while the employment of polymers provides the possibilities for chemical modification and further targeted delivery.

Although there are some nano-emulsion products available on the market, the scale-up of nano-emulsion products from laboratory to industry is not as fast as we expected. Still, there are lots of problems waiting to be solved. One refers to the preparation methods. The conventional high-energy methods suffer from the problems of low energy efficiency, hard to reach nanoscale size and expensive equipment. While the low-energy methods, which are extensively investigated in these years, realize the emulsification just by simple stirring. Although the low-energy emulsification somehow has innovated the emulsion field, those

methods are quite limited in the type of components and preparation conditions. Therefore, expanding the components range for low-energy emulsification is of crucial importance for nano-emulsion systems.

The second concern is about how nano-emulsions behave after administration. As most of the nanocarriers, nano-emulsions can be delivered by passive targeting, active targeting or other means. However, there are still some incomprehensible physicochemical mechanisms, for example, how the APIs release from emulsion droplets, how the droplets interact with biological molecules and how those carriers behave by different routes of administration in different sites are still remaining unclarified. It is true that some markers (like fluorescent probes) can be used for tracking the delivery systems, but most of them suffer from the unreliability because of the leakage or the instability of the probe-loaded systems.

Moreover, the new demands for nano-emulsion systems, like specific targeting, are in need of advanced functionalized nano-emulsion systems. The application of polymers in nano-emulsion formulations not only enhances the stability of formulations, but also can provides more possibilities for further functionalization. With the advances of the products, the characterization and evaluation methods are required to keep up with the trends.

This PhD thesis centers around nano-emulsion delivery systems. The aims of this research are 1) to study spontaneous emulsification process, from the viewpoint of surfactant design; 2) to design new fluorophores which are suitable for nano-emulsion systems; 3) with the help of fluorescent probes, to further investigate in the release mechanisms 4) and to visualize the interactions between nano-emulsion droplets and cells in a nanoscale.

The thesis is composed of 5 chapters. The first chapter will give a literature overview about nano-emulsion delivery systems. The first section (Chapter 1.1) presents a general background about nano-emulsions, including basic concept, specific advantages, different preparation methods and state-of-the-art applications. The second section (Chapter 1.2) is focused on the characterization and evaluation methods of nano-emulsion systems, which not only describes regular characterization methods but also introduces some up-to-date spectra or fluorescence-based methods.

In the first study (Chapter 2), we will aim at designing an ultra-bright nano-emulsion system for *in cellulo* single particle tracking, by taking advantage of fluorescence, we are supposed to have some ideas about how nano-emulsion droplets behave and interact in cells. Firstly, we

introduce a series of fluorophores with new dioxaborine backbone and bulky cyclohexyl moieties, which are designed not only for an enhancement of brightness and photostability, but also to show a great potential to be encapsulated in nano-emulsion systems. Next, varieties of oils are selected for their ability to be compatible for spontaneous emulsification, and the average size of emulsion droplets can be adjusted by controlling the surfactant/oil ratio (SOR%). Beside the characterization of size distribution, photochemical properties and cytotoxicity, nano-emulsions are also characterized by Fluorescence Correlation Spectroscopy (FCS) to check whether there is a leakage of free dye from emulsion droplets. The results demonstrated the high quantum yield, exciting brightness, excellent photostability and non-leakage of the fluorescent nano-emulsions. On the other hand, we introduce a polymer, poly(maleic anhydrade-alt-1-octadecene) (PMAO), which can hydrolyze on oil/water interface and make the emulsion droplets negatively charged. With the ultrabright nano-emulsion system, we intended to visualize the different behavior of neutral and negatively charged droplets by micro-injection in Hela cells.

In the second study (Chapter 3), we will focus on the stability of nano-emulsion systems. We present a simple fluorescence-based method to investigate the release mechanisms from nano-emulsions. By encapsulating a lipophilic Nile red derivative (NR668), which was shown with a 681-fold fluorescence enhancement in oily core of nano-emulsions than in bulk water, the mass transfer of dye molecules from encapsulated nano-droplets to blank nano-droplets is investigated by a self-quenching strategy. Specifically, fluorescence efficiency of model dye at high concentrations can be inhibited due to the aggregation-caused quenching (ACQ) phenomenon, in presence of acceptors like blank nano-emulsions, dye molecules will release, thus causing an improvement of optical properties. Here, in this study, quantum yield (an optical parameter indicating the efficiency of photon emitting by dye molecules) of the global system is measured and calculated as an indicator of the release process. Besides, due to the solvatochronism property of NR668, the maximum emission wavelength of fluorescent nano-emulsions also shifted along the transfer in solubilizing media, which acts as an additional indicator of the release process. From the study, we showed the release following the compositional ripening instead of Ostwald ripening since the size remained constant all along the process. By investigating four factors impacting on the release mechanisms, precisely, the existence of micelles, donor-acceptor ratio, temperature and the dye concentration, we also discuss the mechanism behind.

The third study (Chapter 4) aims at the spontaneous emulsification process. In order to find a simple but useful tool to investigate spontaneous emulsification, we will design three new amphiphilic molecules. The synthesis and purification methods are supposed to be simple. The

aim of the study was to find the critical characteristics of surfactants for the spontaneous emulsification, to find the universal factors impacting the performance, and also, to provide a promising tool for further mechanism investigation.

In the last section (Chapter 5), we will introduce some other participated projects related to fluorescent nano-emulsions/nanoparticles. The first participated project refers to lipid-core/polymer-shell hybrid nanoparticles, which is also the developing trend of advanced functionalized nano-emulsions. In this section (Chapter 5.1), we present a new strategy to investigate the integrity of lipid nanoparticles. By labeling the oily core with a green BODIPY dye and the polymer shell with covalent attached red Rhodamine dye, the composition and stability of the new hybrid nanoparticles can be analyzed by electrophoresis. We suppose it can be applied as a valuable tool to comply regular characterization. The second participated project introduces a pro-dye for evaluating the cargo release by nano-emulsions. In this study (Chapter 5.2), we chemically acetylate a fluorescent Huda dye into a non-fluorescent pro-dye, and encapsulate it into nano-emulsions. The idea is to transfer the pro-dye into its active form once delivered in the cells. On one hand, this can be a new strategy to monitor the integrity of nano-emulsion systems when interacting with cells, on the other hand, we would lead to the development of efficient prodrugs based on similar modifications and deliver strategy. The third participated project presents a w/O/W double emulsion system, in this study (Chapter 5.3), we introduce a nano-scaled multi-layer emulsion system, where the structure will be confirmed by a fluorescence-based characterization method to comply the microscopy. We expect the investigation can further encourage a development of nano-scaled multiple emulsion.

Chapter 1 Literature Review

1 General background about nano-emulsions

Abstract: In this review, we introduce basic concept and development of nano-emulsions, from definition, composition to advantages over other kinds of nanocarriers in pharmaceutical field. We will be focused on varieties of preparation methods for nano-emulsions, including conventional high-energy methods, advanced low-energy methods and particular methods for multiple emulsions. Owing to the specific physicochemical properties, the diverse fabrication methods, and the possibility for advanced functionalization, during the last few decades, nano-emulsions have been through a development from basic nutrition supply to advanced drug delivery systems by various administration routes including oral, parenteral, ocular, topical, and transdermal delivery, consequently, with many commercially available products came into market.

Key words: concept, advantages, preparation methods, applications, development.

2 Characterization and evaluation of nano-emulsions

Abstract: Over the last decade, nano-emulsions have gained a considerable interest in biomedical research area; however, still limited laboratory fulfilments have achieved industrial production or clinical application. One of the reasons behind, like most of the nanomedicines, is the lack of reliable characterization and evaluation methods that can present the unique properties of individual product, while they are playing important roles with more and more advanced and functionalized delivery systems occurring. Therefore, in this review, firstly, we aim at drawing an overview of regular characterization and evaluation methods for nano-emulsion systems, from size distribution to *in vitro* and *in vivo* evaluation. Besides, we also focus on varieties of new methods (*e.g.*, spectra-based and fluorescence-based methods) with higher resolution, specific characterization and better reliability in complex environment.

Key words: characterization, evaluation, nano-emulsions, spectra, fluorescence

Chapter 2

Nano-emulsions for single particle tracking in live cells

1 Introduction

Fluorescent probes are wildly used in biomedical field for pathological research and disease diagnosis, especially combined with advanced nanoparticles as trackers for monitoring the *in vivo* absorption, biodistribution, metabolism and elimination of these drug delivery systems. Nano-emulsion, as one of these advanced drug delivery systems, with the advantages of high encapsulation efficiency and low toxicity, has the ability to be an ideal carrier for fluorescent probes.

However, there are still many challenges for fluorescence-based *in vivo* tracking, one of the biggest problems comes with the integrity of the system. Once leakage occurs with the dye-loaded system, the signal comes from the free dye can impose significant interference with the identification of integral nano-emulsions. Therefore, the encapsulated fluorophores should fulfill some requirements.

Firstly, we need to design a structure with a high brightness, precisely, a high molar extinction co-efficiency (ε) and a high quantum yield (QY), the former ensuring enough photons being absorbed while the latter determining an efficiency to produce photons. Besides, it is necessary to avoid the quenching caused by aggregation and photobleaching. In addition, the leakage can be persisted by improving the lipophilicity of the probe and the viscosity of the oily core. Last but not the least, the sharper of the spectra, the more sensible of the probe.

With all those strategies in mind, in this chapter, we introduce DBS dyes, a new family of lipophilic and neutral styryl fluorophores that are composed of a barbituryl dioxaborine acceptor moiety and different aniline donor groups. These new synthesized fluorophores display high molar extinction coefficients with relatively low quantum yields in solvents and impressive fluorescence enhancement when dissolved in viscous oils. These features together with high loading capability and low aggregation induced quenching encouraged us to formulate ultrabright nano-emulsions with an average size <50 nm. Thanks to their brightness, dye-loaded nano-emulsions performed well both on two-photon excitation imaging and individual tracking in living cells. We also showed that negatively charged nano-emulsions displayed lower moving velocity compared to neutral nano-emulsions when micro-injected in Hela cells. We believe that this system will contribute in extending the knowledge on lipid nanoparticles and their interactions with biological environment.

This part of study has been published on *ACS Journal of Applied Materials and Interface*, and the article is enclosed as below.

ACS APPLIED MATERIALS & INTERFACES

Research Article

Cite This: ACS Appl. Mater. Interfaces 2019, 11, 13079−13090

www.acsami.org

Optimizing the Fluorescence Properties of Nanoemulsions for Single Particle Tracking in Live Cells

Xinyue Wang,[†] Nicolas Anton,*[,†] Pichandi Ashokkumar,[‡] Halina Anton,[‡] Tkhe Kyong Fam,[‡] Thierry Vandamme,[†] Andrey S. Klymchenko,*[,‡] and Mayeul Collot*[,‡]

[†]Université de Strasbourg, CNRS, CAMB UMR 7199, F-67000 Strasbourg, France

[‡]Laboratory of Biophotonic and Pathologies, CNRS UMR 7021, Université de Strasbourg, Faculté de Pharmacie, 74, Route du Rhin, 67401 Illkirch, France

Supporting Information

ABSTRACT: Nanoemulsions (NEs) are biocompatible lipid nanoparticles composed of an oily core stabilized by a surfactant shell. It is acknowledged that the surface decoration with poly(ethylene glycol), through the use of nonionic surfactants, confers high stealth in biological medium with reduced nonspecific interactions. Tracking individual NE by fluorescence microscopy techniques would lead to a better understanding of their behavior in cells and thus require the development of bright single particles with enhanced photostability. However, the understanding of the relationship between the physicochemical properties and chemical composition of the NEs, on the one hand, and its fluorescence properties of encapsulated dyes, on the other hand, remains limited. Herein, we synthesized three new dioxaborine barbituryl styryl (DBS) dyes that displayed high molar extinction coefficients (up to 120 000 M^{-1} cm^{-1}) with relatively low quantum yields in solvents and impressive fluorescence enhancement when dissolved in viscous oils (up to 0.98). The reported screening of nine different oils allowed disclosing a range of efficient "oil/dye" couples and understanding the main parameters that lead to the brightest NEs. We determine vitamin E acetate/DBS-C_8 as the representative most efficient couple, combining high dye loading capabilities and low aggregation-induced quenching, leading to <50 nm ultrabright NEs (with brightness as high as 30×10^6 M^{-1} cm^{-1}) with negligible dye leakage in biological media. Beyond a comprehensive optical and physicochemical characterization of fluorescent NEs, cellular two-photon excitation imaging was performed with polymer-coated cell penetrating NEs. Thanks to their impressive brightness and photostability, NEs displaying different charge surfaces were microinjected in HeLa cells and were individually tracked in the cytosol to study their relative velocity.

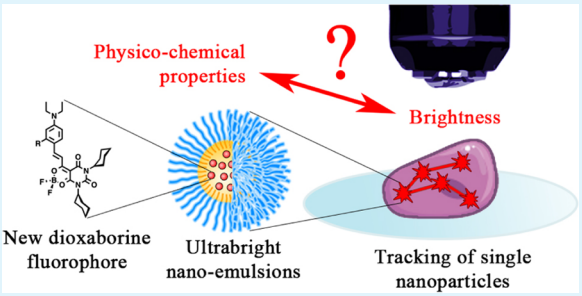

KEYWORDS: *lipid nanoparticles, nanoemulsions, dioxaborine, two-photon imaging, single particle tracking*

INTRODUCTION

A great variety of nanocarriers of drugs and contrast agents has been developed to date in nanomedicine,[1−4] notably those based on mesoporous silica[5,6] semiconductors,[7] gold or iron oxide[8] as well as organic materials, such as dendrimers,[9,10] polymers,[11−15] and lipids (including liposomes[16] and solid lipid naoparticles[17]). Although the current organic nanocarriers are dominated by the well-established polymer and lipid nanoparticles, nanoemulsions (NEs) that are composed of an oily core stabilized by surfactants are rapidly emerging in the last 10 years.[18−20] They are promising vehicles for a functional cargo owing to their low toxicity, high encapsulation efficiency, simple fabrication methods, and finally (and not least), very high stability compared to microscale emulsions. Interestingly, the use of a highly PEGylated surfactant (e.g., Kolliphor ELP, that decorate the droplets with an M_w 1500 poly(ethylene glycol) (PEG) chain) leads to a drastic reduction of their nonspecific interaction with cells[21−23] as well as increases the circulation time in blood before complete clearance.[24,25] In addition, intrinsically related to their formulation process, the NE size and surface properties can be very finely tuned and adapted to given specifications. It follows therefrom that encapsulating lipophilic fluorescent probes in such oily NEs gives rise to fluorescent NEs that are valuable tools in bioimaging—compatible with various accessible fluorescence imaging techniques.[26−28] This study aims at understanding, the relationship existing between the nature of oil, the chemical structure of the fluorescent probe, and the physicochemical properties of the NEs (see the graphical abstract). Regarding the oil, the main required property is its ability to form stable NEs. However, several other parameters like hydrophobicity, polarity, and viscosity could greatly influence not only the physicochemical properties of the NEs themselves but also the photophysical properties of the encapsulated fluorophore, thus

Received: December 21, 2018
Accepted: March 7, 2019
Published: March 7, 2019

DOI: 10.1021/acsami.8b22297
ACS Appl. Mater. Interfaces 2019, 11, 13079−13090

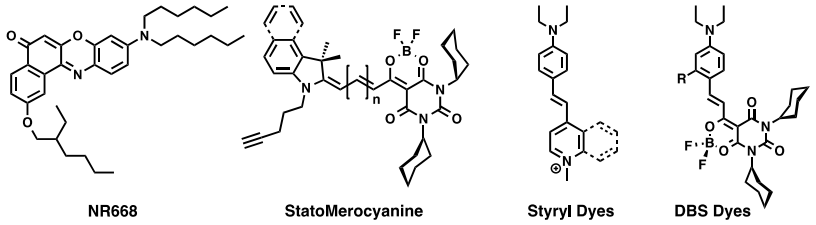

Figure 1. Structure of the different fluorophores discussed in this work.

leading to important changes in the fluorescence properties of the NEs.

The encapsulated fluorophores have to fulfill several requirements: (1) they should be well solubilized in oil to reach high dye loading; (2) they should be sterically bulky enough to prevent aggregation-caused quenching (ACQ)[29] that would limit the quantum yield of the NEs and therefore their brightness; (3) these dyes should be hydrophobic enough not to escape from the NEs;[21] and (4) they should be photostable enough to allow tracking of the NEs over the time. As fluorophores, cationic carbocyanines bearing long hydrocarbon chains were used for this purpose.[27,30] Our group improved this approach by combining these cyanines with bulky hydrophobic tetraphenyl borate counterions that led to brighter NEs due to two synergic effects:[26] (i) enhancing hydrophobicity and thus allowing higher dye loading percentage and (ii) preventing ACQ by the bulkiness of the counter ion.[31] The obtained NEs were successfully used for tracking single NEs in the zebrafish embryo[26] and for monitoring their integrity in the bloodstream and tumor in the living mice.[28] Although this approach led to bright NEs, the use of borate counterions can lead to cytotoxic effects,[32] which can be detrimental for the cellular or in vivo studies. Noncharged fluorophores can circumvent this issue, as they can be sufficiently hydrophobic to be dissolved in oil without any other additive. Nile red (NR) is a noncharged solvatochromic dye that is commonly used to stain the cellular lipid droplets[33] and to fluorescently label NEs. However, it was shown that, due to insufficient lipophilicity, Nile red undergoes rapid leakage in biological media.[21] To prevent the dye leakage, a hydrophobic version of NR, NR668 (Figure 1), bearing three alkyl chains was developed and successfully loaded in NEs providing bright particles.[21] Even though NR668 constitutes a valuable tool for making fluorescent NEs,[25,34] there is still a room for improvement as it has a limited brightness with a molar extinction coefficient of 45 000 M^{-1} cm^{-1}. Also, NR derivatives can suffer from limited photostability and their broad absorption and emission spectra are detrimental in multicolor bioimaging when combined with additional fluorophores or fluorescent proteins.[35] In addition, a systematic study on the effect of oil and the nature of the fluorophore on the fluorescence characteristics of dye-loaded nanoemulsions is still missing. To circumvent these limitations, we got interested in dioxaborine fluorophores as they were shown to be efficient to develop bright fluorescent nanomaterials.[36−38] We recently introduced a new family of fluorophores called StatoMerocyanines composed of an indolenine moiety and a bulky barbiturate stabilized by a dioxaborine complex (Figure 1). These fluorogenic dyes display ultrabright fluorescence in oil and were used as lipid droplet markers in cellular and tissue imaging.[35] Although StatoMerocyanines are bright in oil, the one compatible with common 488 nm laser excitation, namely SMCy3, was limited by modest quantum yield (0.25). To obtain a fluorophore absorbing in this range and with enhanced fluorescence properties, we conserved the barbituryl dioxaborine moiety and replaced the indolenine part by aniline donors to give rise to hemicyanine-like fluorophores (also called styryl dyes, Figure 1) that we named dioxaborine barbituryl styryl (DBS) dyes. These new dyes displayed interesting properties for NE loading and were compared to NR668. This study led to ultrabright NEs with improved photophysical properties that were highly suitable for tracking individual NEs in cells.

MATERIALS AND METHODS

Materials. Labrafac WL 1349 (medium chain triglycerides, MCT) was obtained from Gattefossé (Saint-Priest, France), vitamin E acetate (VEA) was purchased from Tokyo Chemical Industry (Tokyo, Japan). All the other oils used for spectra study are of chemical grade, except for colza oil, which is of food grade. The surfactant, Kolliphor ELP, was from BASF (Ludwigshafen, Germany). Poly(maleic anhydride-*alt*-*a*-octadecene) (PMAO) was purchased from Sigma-Aldrich (St. Louis). NR668 is a homemade modified Nile Red fluorophore.[21] Phosphate buffered saline (PBS) was from Eurobio (Courtaboeuf, France) and fetal bovine serum (FBS) from Lonza.

Synthesis. All starting materials for synthesis were purchased from Alfa Aesar, Sigma-Aldrich or TCI Europe and used as received unless stated otherwise. NMR spectra were recorded on a Bruker Avance III 400 MHz spectrometer. Mass spectra were recorded using an Agilent Q-TOF 6520 mass spectrometer. Synthesis of all new compounds is described in the Supporting Information (SI).

Spectroscopy. The water used for spectroscopy was Milli-Q water (Millipore), all the solvents were of spectro-grade. Absorption and emission spectra were recorded on a Cary 400H HP Scan ultraviolet−visible spectrophotometer (Varian) and a FluoroMax-4 spectrofluorometer (Horiba Jobin Yvon) equipped with a thermostated cell compartment, respectively. For the standard recording of fluorescence spectra, the emission was collected 10 nm after the excitation wavelength. All the spectra were corrected from the wavelength-dependent response of the detector. Quantum yields were determined by comparison with Rhodamine 6G in water[39] as the reference using the following equation

$$QY = QY_R \times \frac{I \times OD_R \times n^2}{I_R \times OD \times {n_R}^2}$$

where QY is the quantum yield, I is the integrated fluorescence intensity, n is the refractive index, and OD is the optical density at the excitation wavelength. R represents the reference.

Solubility of DBS Dyes in Oils. An excess amount of dye was weighted, first, dissolved in acetone to obtain a stock solution, and then was added to an appropriate amount of oil quickly. Next, the oil solution was heated to 60 °C and vortexed to a homogeneous solution. After that, acetone was evaporated to get a saturated oil solution and then centrifuged. Finally, the upper oil solution was taken and diluted in dioxane by 50 times for the absorption test. DBS-H, DBS-OH, and DBS-C_8 were tested in Labrafac, castor oil, and VEA, respectively. The solubility percentage was calculated as follows

DOI: 10.1021/acsami.8b22297
ACS Appl. Mater. Interfaces 2019, 11, 13079−13090

$$S\ (\%) = \frac{\mathrm{OD} \times 50 \times 1\mathrm{mL} \times \mathrm{MW}}{\varepsilon_{\mathrm{dioxane}} \times m} \times 100$$

where OD is the measured optical density, 50 is the dilution factor, 1 mL is the final volume after dilution used for the absorption test, MW is the molar weight of the dye, $\varepsilon_{\mathrm{dioxane}}$ is the molar extinction coefficient of the dye in dioxane, and m is the weight of saturated dye−oil solution.

Two-Photon Excitation (TPE) Measurements and TPE Imaging. Two-photon absorption cross-section measurements were performed using Rhodamine 6G in methanol as a calibration standard according to the method of Webb et al.[40] Two-photon excitation was provided by an InSight DS+ laser (Spectra-Physics) with a pulse duration of 120 fs. The laser was focused with an achromatic lens (f = 2 cm) in a cuvette containing the dye (DBS-H: 16 μM, DBS-OH: 28 μM, DBS-C_8: 18 μM and NR668: 10 μM) in dioxane and the spectra were recorded with a fibered spectrometer (Avantes) by collecting the fluorescence emission at 90° with a 20× Olympus objective. Two-photon fluorescence microscopy imaging was performed using a home-built two-photon laser scanning set-up based on an Olympus IX70 inverted microscope with an Olympus 60× 1.2NA water immersion objective.[41] Two-photon excitation was provided by an InSight DS+ laser (Spectra-Physics, 80 MHz, 120 fs) with an excitation power around 5 mW (930 nm for DBS-C_8, 910 nm for NR668, and 750 nm for Hoechst), and photons were detected with avalanche photodiodes (APDs SPCM-AQR-14-FC, PerkinElmer) connected to a counter/timer peripheral component interconnect board (PCI6602, National Instrument). Imaging was carried out using two fast galvo mirrors in the descanned fluorescence collection mode. Images corresponding to the blue (Hoechst) and green (DBS-C_8 and NR668 dye) channels were recorded simultaneously using a dichroic mirror (Beam splitter 495 nm DCXR) and two APDs. Typical acquisition time was 50 s. Since the excitation of Hoechst stain at 910 and 930 nm in our experimental conditions did not yield a good quality image, we used 750 nm excitation for Hoechst and independent images were taken for blue and green channels and then processed with ImageJ.

X-ray Crystallography. Single crystals of DBS-C_8 were obtained by a solvent exchange method using DCM as the solvent and cyclohexane as the antisolvent.[42] X-ray diffraction data collection was carried out on a Bruker APEX II DUO Kappa-CCD diffractometer equipped with an Oxford Cryosystem liquid N2 device, using Mo Kα radiation (λ = 0.71073 Å). The crystal-detector distance was 38 mm. The cell parameters were determined (APEX2 software)[43] from reflections taken from three sets of 12 frames, each at 10 s exposure. The structure was solved by direct methods using the program SHELXS-2013.[44] The refinement and all further calculations were carried out using SHELXL-2013.[45] The H atoms were included in calculated positions and treated as riding atoms using SHELXL default parameters. The non-H atoms were refined anisotropically, using weighted full-matrix least-squares on F^2. A semi-empirical absorption correction was applied using SADABS in APEX2;[43] transmission factors: $T_{\mathrm{min}}/T_{\mathrm{max}}$ = 0.6697/0.7456.

Cytotoxicity Assay. Cytotoxicity assay of the DBS dyes and NR668 was quantified by the (3-(4,5-dimethylthiazol-2-yl)-2,5-diphenyltetrazolium bromide) (MTT assay). A total of 1 × 10^4 HeLa (ATCC CCL-2) cells per well were seeded in a 96-well plate for 24 h prior to the cytotoxicity assay in Dulbecco's modified Eagle medium (Gibco Life technologies, DMEM) complemented with 10% fetal bovine serum, gentamicin (100 μg mL^{-1}), L-glutamine (2 mM), nonessential amino acids (1 mM), and MEM vitamin solution (1%) and were incubated in a 5% CO_2 incubator at 37 °C. After medium removal, an amount of 100 μL DMEM containing 5, 1, or 0.2 μM of DBS dye (DBS-H, DBS-OH, DBS-C_8) or NR668 was added to the cells and incubated for 24 h at 37 °C (5% CO_2). As a control, for each 96-well plate, the cells were incubated with DMEM containing the same percentage of dioxane (0.5% v/v) as the solution with the tested dyes or with Triton X-100 0.1% as a positive control of cytotoxicity. After 24 h of a dye incubation, the medium was replaced by 100 μL of a mixture containing DMEM + MTT solution (diluted in PBS beforehand) and the cells were incubated for 4 h at 37 °C. Then, 75 μL of the mixture was replaced by 50 μL of dimethyl sulfoxide (DMSO) (100%) and gently shaken for 15 min at room temperature to dissolve the insoluble purple formazan reduced in the living cells. The absorbance at 540 nm was measured (absorbances of the dyes at 540 nm were taken into account). Each concentration of dye was tested in sextuplicate in three independent assays. For each concentration, we calculated the percentage of cell viability in reference to the control DMEM + 0.5% dioxane.

Formulation and Characterization of Nanoemulsions. Nanoemulsions (NEs) were formulated with a spontaneous emulsification method, as described previously.[34] First, the dye was dissolved in a proper amount of acetone and then added to the oil (80 °C) quickly. After the system was mixed homogeneously, acetone was evaporated at 80 °C for several hours and then at room temperature overnight. Next, the surfactant was added and the mixture was homogenized at 80 °C. With the addition of Milli-Q water (or PBS for the cell experiments), NEs were formed under vortex. Different surfactant/oil ratios (SOR)[41] were selected for different oils. To promote the penetration of NEs into cells, PMAO was used as an interface-active polymer, which is dissolved in the oil before all the steps.[34] After formulation, the size and ξ-potential of all the NEs were tested by dynamic light scattering (DLS) with the instrument Zetasizer (Malvern, U.K.). For the size measurement, all the emulsions were diluted by 100 times and measured at a temperature of 25 °C. Both the size distribution and polydispersity index (PDI) were recorded. For the ξ-potential measurement, emulsions with PMAO and without PMAO using PBS were tested after 1 h to ensure the sufficient hydrolysis of PMAO at the interface, with a dilution factor of 1000.

Photostability Test. NEs with 1% dye loading were chosen for the photostability test. All the NEs were diluted to keep the dye concentration at 1 μM in the final solutions. To make sure that all the NEs were excited at the same ε (40 000 M^{-1} cm^{-1}), 520 nm was chosen as the excitation wavelength for NR668 NEs, whereas 490 nm was chosen for DBS-H/DBS-OH/DBS-C_8 NEs. The emission signal was monitored at 600 nm for all fluorophores. The measurement was conducted for 1 h. A relative fluorescence intensity (%) was normalized to the maximum intensity at the starting point.

Fluorescence Correlation Spectroscopy (FCS). FCS measurements were performed on a home-built confocal set-up based on a Nikon inverted microscope with a Nikon 60× 1.2NA water immersion objective.[47] Excitation was provided by a cw laser diode (532 nm, Oxxius) and photons were detected through a bandpass 580/84 nm filter (Semrock) with a fibered avalanche photodiode (APD SPCM-AQR-14-FC, PerkinElmer) connected to an online hardware correlator (ALV7000-USB, ALV GmbH, Germany). The typical acquisition time was 5 min (10 × 30 s) with an excitation power of 0.5 mW at the sample level. The data were analyzed using PyCorrFit software.[48] 100 times diluted NEs for the size measurement were used for the FCS study. Before measurement, another 100-fold dilution was performed for all the samples, respectively, in PBS and 10% FBS + 90% PBS solutions. Different dye-loaded NEs (0.2, 1.0, and 2.5% loading in oil) of two dyes (DBS-C_8 and NR668) were used for comparison. Fifty nanomolar solution of 6-carboxytetramethylrhodamine (TMR) in water was used as a reference. 200 μL of each sample was placed in a 96-well plate. The measurement was performed for 10 s and 15 times for each NE sample.

Cellular Imaging. HeLa cells (ATCC CCL-2) were grown in Dulbecco's modified Eagle medium without phenol red (DMEM, Gibco−Invitrogen) supplemented with 10% fetal bovine serum (FBS, Lonza), 1% L-glutamine (Sigma-Aldrich), and 0.1% antibiotic solution (gentamicin, Sigma-Aldrich) at 37 °C in humidified atmosphere containing 5% CO_2. The cells were seeded onto a 35 mm glass-bottomed imaging dish (ibidi) at a density of 5 × 10^4 cells per well 24 h before the microscopy measurement. For imaging, the culture medium was removed and the attached cells were washed with Opti-MEM (Gibco−Invitrogen). Next, the cells were incubated in Opti-MEM with Hoechst (5 μg mL^{-1}) to stain the nuclei, the living cells were washed twice with Opti-MEM and visualized in Opti-MEM. The

DOI: 10.1021/acsami.8b22297
ACS Appl. Mater. Interfaces 2019, 11, 13079−13090

solutions of NEs were placed in a Femtotip II (Eppendorf) at a dye concentration of 3 μM and were microinjected using a Femtojet 4i device (Eppendorf), parameters: P_i = 90 hPa; T_i = 0.3 s; P_c = 10 hPa. Right after microinjection, the video of the cell was acquired with an integration time of 50 ms for 30 s (600 frames) and then multicolor pictures were taken followed by a second movie (5 min post-injection). The images were acquired with a Nikon Ti-E inverted epifluorescence microscope, equipped with CFI Plan Apo × 60 oil (NA = 1.4) objective, and a Hamamatsu Orca Flash 4 sCMOS camera. The acquisition settings were: Hoechst (ex. 395 nm, em. 475 ± 50 nm) and DBS-loaded NEs (ex. 470 nm, em. 531 ± 40 nm). The images were recorded using NIS elements and then processed with Icy software. For TPE imaging, the cells were incubated with NEs in Opti-MEM for 2 h at 37 °C then with Hoechst (5 μg mL^{-1}) for 15 min to stain the nuclei and images were taken from a home-built two-photon laser scanning microscope (vide supra).

Tracking of Individual NEs. The movies were acquired at 20 Hz for the total duration of 30 s. The tracking analysis was performed using Imaris 9.2.1 software (Bitplane Inc.). Individual fluorescent foci were identified in each frame and the fluorescent spots in different frames were joined to form trajectories if the centroid positions of the spots were within 500 nm between subsequent frames. Trajectories that lasted 10 frames or longer were kept for subsequent analysis. To calculate the velocity of each spot, the displacement between the subsequent frames was divided by the acquisition time (50 ms). For each type of NEs, 3 cells were analyzed with roughly 1000 trajectories and (2−4) × 10^4 displacements detected in each cell. The mean fluorescence intensity of the single NEs in the time-lapse images was measured using ImageJ software. Five images, corresponding to t_1 = 0 s, t_2 = 1.5 s, t_3 = 3 s, t_4 = 4.5 s, and t_5 = 6 s were analyzed. The time interval of 1.5 s between the analyzes was chosen to ensure the turnover of the NEs. The images were thresholded to isolate the fluorescent spots corresponding to NEs from the fluorescent background. Then, a particle analysis function was used to identify their borders. Their coordinates were saved in ROI manager and applied to the initial image to measure the mean fluorescence intensity of the spots. Finally, all the values were pooled and plotted as a frequency distribution plot (histogram).

RESULTS AND DISCUSSION

Synthesis. DBS fluorophores resulted from the condensation of barbiturate dioxaborine **2** on three different 4-(diethylamino)benzaldehydes bearing various substituents at the meta position (Figure 1A). The obtained DBS fluorophores are thus composed of an aniline donor moiety and an acceptor barbiturate moiety linked through a double bond. The dioxaborine complex prevents the rotation of the acceptor and thus enhances the planarity of the π system leading to potentially bright fluorophores. Moreover, we showed recently that boron bridge renders a push−pull dioxaborine (DXB-Red) highly photostable in nonpolar media.[49] The two cyclohexyl moieties were chosen for their hydrophobicity and bulkiness that can help in preventing the formation of nonemissive H-aggregates by π-stacking.[50,51,52] Compared to DBS-H, an oxygen atom was introduced in DBS-OH to reinforce the electron density of the donor. This oxygen served to add an octyl hydrocarbon chain (DBS-C_8) to enhance the lipophilicity. The three DBS fluorophores were characterized by ^{1}H, ^{13}C, and ^{19}F NMR as well as high-resolution mass spectroscopy (see the SI). Additionally, the X-ray diffraction of a single crystal provided the crystallographic structure of DBS-C_8 that confirmed the co-planarity of the aniline and the barbituryl rings as well as the bulkiness brought by the two cyclohexyl moieties (Figure 2B).

Spectroscopic Studies of DBS. The photophysical properties of DBS were first studied in various organic solvents

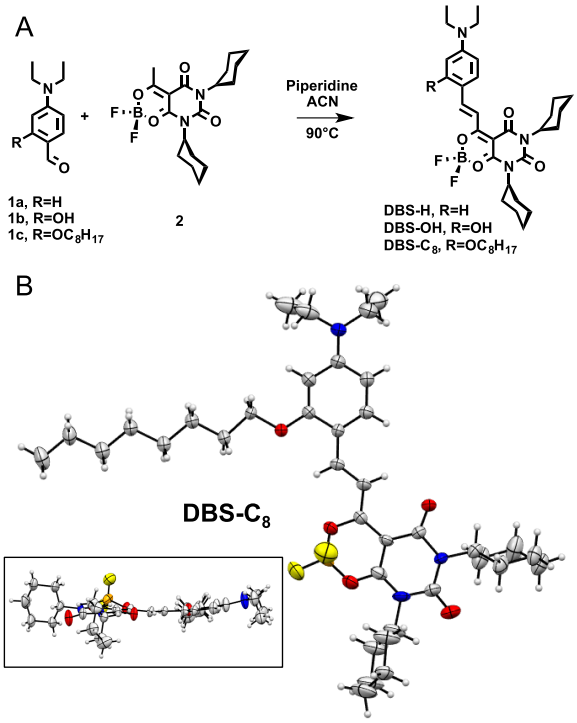

Figure 2. Synthesis of the DBS fluorophores (A) and ORTEP representation of DBS-C_8 obtained from X-ray diffraction (B), inset is the top view. For clarity, heteroatoms were colored: boron (orange), nitrogen (blue), oxygen (red), and fluorine (yellow).

with increasing polarity from cyclohexane to DMSO (all spectrum and values are available in Figure S1 and Table S1). In nonpolar solvents, they are efficiently excitable at 488 nm, emit in the green-yellow range of the visible spectrum, and possess a quite similar absorption and emission maximum wavelengths with a slight red shift in emission when an additional oxygen atom on the aniline moiety was added (DBS-OH). DBS fluorophores showed a positive solvatochromism both in absorption and emission, where bathochromic shifts occurred upon increase of solvent polarity (Figure 3 and Table 1). DBS-H displayed the highest solvatochromism with 40 and 71 nm in absorption and emission, respectively. Nevertheless, when the maximum emission wavelengths of DBS dyes were plotted against the solvent polarity parameter $E_T(30)$, no linear correlation has been found (data not shown) indicating that other parameters such as the viscosity might influence their spectral properties. In comparison with styryl dyes,[53,54] DBS dyes display shorter Stokes shifts ranging from 13 to 50 nm combined to sharper absorption and emission spectra (see full width at half maximum (FWHM) values in Tables 1 and S1). Additionally, they possess high molar extinction coefficients ranging from 94 000 to 125 800 M^{-1} cm^{-1} in DMSO. Regarding the brightness, although DBS-H and DBS-C_8 displayed good quantum yields in toluene (0.62 and 0.50, respectively), quantum yield values in other solvents were generally modest to low (Tables 1 and S1).

We then assessed the spectral properties of DBS in nine different oils with various compositions and polarities and compared to NR668 (all spectrum and values are available in Figure S2 and Table S2). The results showed that maximum absorption wavelengths were all close to those obtained in EtOAc but with shorter emission wavelengths. Herein, we

DOI: 10.1021/acsami.8b22297
ACS Appl. Mater. Interfaces 2019, 11, 13079−13090

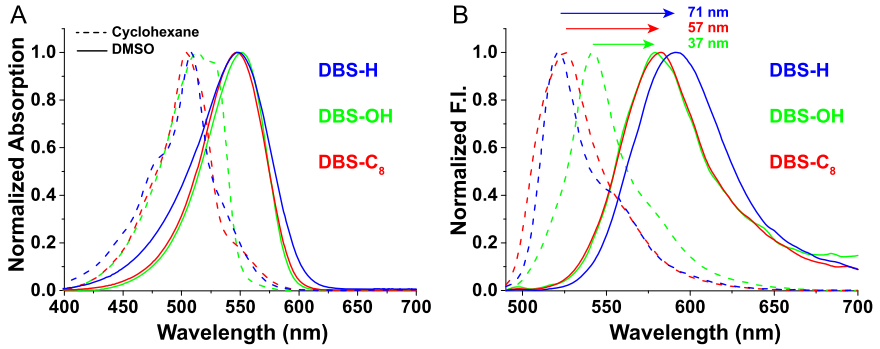

Figure 3. Normalized absorption (A) and emission (B) spectra of DBS (1 μM) in cyclohexane and DMSO. Excitation wavelength was 480 nm.

Table 1. Photophysical Properties of DBS Dyes in Cyclohexane and DMSO

dye	solvent	λ_{Abs} (nm)	ε (M^{-1} cm^{-1})	FWHM Abs (nm)	λ_{em} (nm)	FWHM em (nm)	Stokes shift (nm)	ϕ[b] (QY)	brightness[c] (M^{-1} cm^{-1})
DBS-H	cyclohexane	508	78 000	50	521	32	13	0.13	10 100
	DMSO	548	98 400	74	592	66	44	0.04	3900
DBS-OH	cyclohexane[a]	513	67 200	58	542	37	29	0.20	13 400
	DMSO	551	94 000	60	579	59	28	0.03	2800
DBS-C8	cyclohexane	504	97 500	47	525	43	21	0.12	11 700
	DMSO	547	125 800	62	582	59	35	0.03	3800

[a]Absorption spectra displayed a second peak at 526 nm. [b]Quantum yields were measured using Rhodamine 6G in water (ϕ = 0.95) as a reference. [c]Brightness is $\phi \times \varepsilon$.

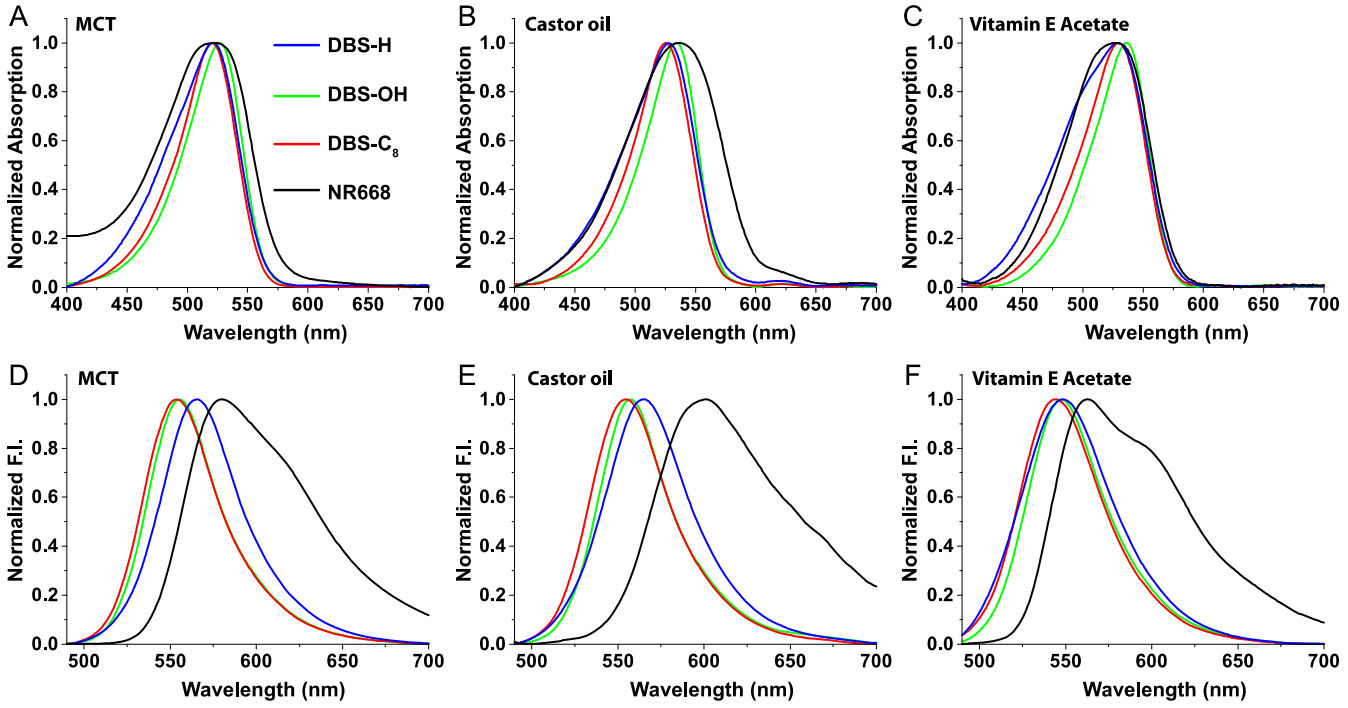

Figure 4. Normalized absorption (A–C) and emission (D–F) spectra of DBS dyes and NR668 in MCT (A, D), castor oil (B, E) and VEA (C, F). Concentration was 1 μM. Excitation wavelength was 480 nm.

chose to focus on the photophysical properties of DBS dyes obtained in medium chain triglycerides (MCT, Labrafac WL 1349) as a representative and FDA approved oil, widely used in the formulation of parenteral emulsions,[23] and well represented in the low-energy nanoemulsification processes. Other types of oils, such as outstandingly viscous castor oil and vitamin E acetate (VEA) also showed a very high brightness (see Table S2). When compared to NR668, DBS dyes displayed similar absorption maxima (~530 nm) and blue-shifted emission (Figure 4A–C). Importantly, absorption and emission bands of DBS dyes were significantly sharper in comparison to NR668 (Figure 4D–F). In addition, DBS dyes displayed equivalently high quantum yields but with ~2-fold larger molar extinction coefficients than NR668 (Table 2). Even though the molar extinction coefficients were slightly decreased in oils when compared to organic solvents, the

DOI: 10.1021/acsami.8b22297
ACS Appl. Mater. Interfaces 2019, 11, 13079–13090

Table 2. Photophysical Properties of DBS Dyes in Selected Oils

dye	oil	λ_{Abs} (nm)	ε (M^{-1} cm^{-1})	FWHM Abs (nm)	λ_{em} (nm)	FWHM em (nm)	Stokes shift (nm)	ϕ[a] (QY)	brightness[b] (M^{-1} cm^{-1})
DBS-H	MCT	521	76 300	68	566	54	45	0.42	32 000
	castor oil	528	76 700	69	557	59	29	0.80	61 400
	VEA	527	59 100	81	548	63	21	0.62	36 600
DBS-OH	MCT	527	87 200	55	555	49	28	0.38	33 100
	castor oil	534	98 400	54	559	49	25	0.87	85 600
	VEA	534	68 900	55	548	53	14	0.95	65 400
DBS-C8	MCT	520	102 300	56	554	51	34	0.48	49 100
	castor oil	525	99 900	55	554	52	29	0.96	96 900
	VEA	527	80 200	60	544	56	17	0.86	69 000
NR668	MCT	525	40 100	87	593	84	58	0.98	39 300
	castor oil	537	41 800	94	602	98	65	0.10	4200
	VEA	525	41 400	79	563	85	38	0.86	35 600

[a]Quantum yields were measured using Rhodamine 6G in water (ϕ = 0.95) as a reference. [b]Brightness is $\phi \times \varepsilon$.

quantum yields were much higher, thus leading to a significant increase of brightness when dissolved in oils (Table 2).

Similarly to the StatoMerocyanines,[35] DBS form soluble aggregates in water that are nonemissive (data not shown). Therefore, DBS are fluorogenic dyes that undergo an impressive fluorescence enhancement from water to oil.

MCT, castor oil, and VEA were detected as interesting candidates for the formulation of fluorescent NE, owing to the outstanding fluorescence properties of DBS when solubilized in these oils. To verify whether high QY values of DBS dyes in oils are related to their high viscosity, we studied the dependence of QY on dynamic viscosity η of the organic phase (solvent or oils). The results are reported in Figure S3, showing a linear correlation between the value of QY and $\log(\eta)$. The viscosity is known to enhance the quantum yield of dyes by restricting intramolecular rotational relaxation, which is commonly observed for the so-called molecular rotors.[55,56] This phenomenon is also known as "motion-induced change in emission".[57] Our data showed that DBS fluorophores exhibit a molecular rotor behavior, which is in line with the previously reported push−pull dioxaborine DXB-red dye.[49] Interestingly, although the three DBS dyes showed very similar behavior (with similar fit slopes of 0.90, 0.97, and 0.92 for DBS-H, DBS-OH, and DBS-C_8, respectively), NR668 did not disclose any trend, likely due to its highly solvatochromic nature, thus being more sensitive to the polarity than to the viscosity. Altogether, the photophysical features of DBS dyes, and this new sight on possibilities for optimizing their optical properties in these oils, constitute a promising system for the design of novel ultrabright NEs.

Nanoemulsions. Considering the high performance of DBS dyes in oils, this system was selected for the formulation of fluorescent NEs. The simple methodology followed was a spontaneous nanoemulsification method designed with nonionic PEGylated surfactant as a water/oil interface stabilizer.[24,25,46,58] The three oils mentioned above, related to the most efficient fluorescence properties of DBS, were formulated into NEs: (i) MCT: medium chain triglycerides (triglycerides composed of capric and caprylic acid), (ii) castor oil (composed of long chain C_{18} triglycerides), (iii) VEA (also known as tocopherol acetate), an acetylated phenol bearing a long branched aliphatic chain. As expected with spontaneous nanoemulsification,[46] the increase in the relative amount of a nonionic surfactant decreased the NEs' mean size and polydispersity indexes (PDI) (assessed by dynamic light scattering, DLS, data Figure S4). However, significant differences in the function of the oil used were noteworthy: although the castor oil systematically led to larger particles, MCT and VEA gave rise to a similar size range, gradually decreasing from 185 to 22 nm as the ratio of the surfactant (the surfactant to oil weight ratio, SOR) was increased (Figure S4A). Interestingly, compared to MCT and castor oil, VEA NEs presented a significantly lower PDI independent of the surfactant/oil ratio (Figure S4B). This means that the emulsification protocol was much more efficient with this oil−surfactant couple.

In the second step, we determined the limit of solubility of the dyes in the oils, since it determines the maximum loading capacity of the NE droplets, thus conditioning their maximum brightness. The results showed a quite important variability between the different conditions (Table S3), as the solubility varies from 0.3 to 7.6 wt %. DBS-OH and DBS-H present relatively constant values whatever the nature of oil, around 2.7 and 4 wt %, respectively. This difference could be attributed to the difference of hydrophobicity between the DBS dyes. Indeed, the presence of the hydroxyl group in DBS-OH decreases its hydrophobicity and therefore decreases the solubility in oils compared to DBS-H. By contrast, the solubility of DBS-C_8 showed a high variability: although it was poorly soluble in relatively polar MCT (maximum solubility 0.3 wt %), it was well solubilized in castor oil (2.9 wt %) and even better in VEA (7.6 wt %). It follows therefrom that VEA oil provided the most interesting results, regarding (i) high quantum yields when solubilizing DBS dyes, (ii) high dye loading capability, (iii) smaller NEs with smaller PDI values. For these reasons, VEA was chosen to design DBS-loaded fluorescent NEs, study and optimize the suspensions, and evaluate their imaging properties in cellular imaging.

DBS-Loaded Fluorescent NE. The brightness of a nanoparticle (B) is defined by eq 1, where n is the number of loaded dye, ε is the molar extinction coefficient value of the loaded dye, and ϕ the quantum yield of the nanoparticle.[14]

$$B = n \times \varepsilon \times \phi \quad (1)$$

A simple way to increase the brightness of NEs would be to increase the number of fluorophores loaded in the oily core. Unfortunately, this approach is limited by the aggregation-caused quenching (ACQ) provoked by the close proximity of the fluorophores.[14] This phenomenon leads to an important decrease of the NEs' quantum yield. To study the fluorescence

DOI: 10.1021/acsami.8b22297
ACS Appl. Mater. Interfaces 2019, 11, 13079−13090

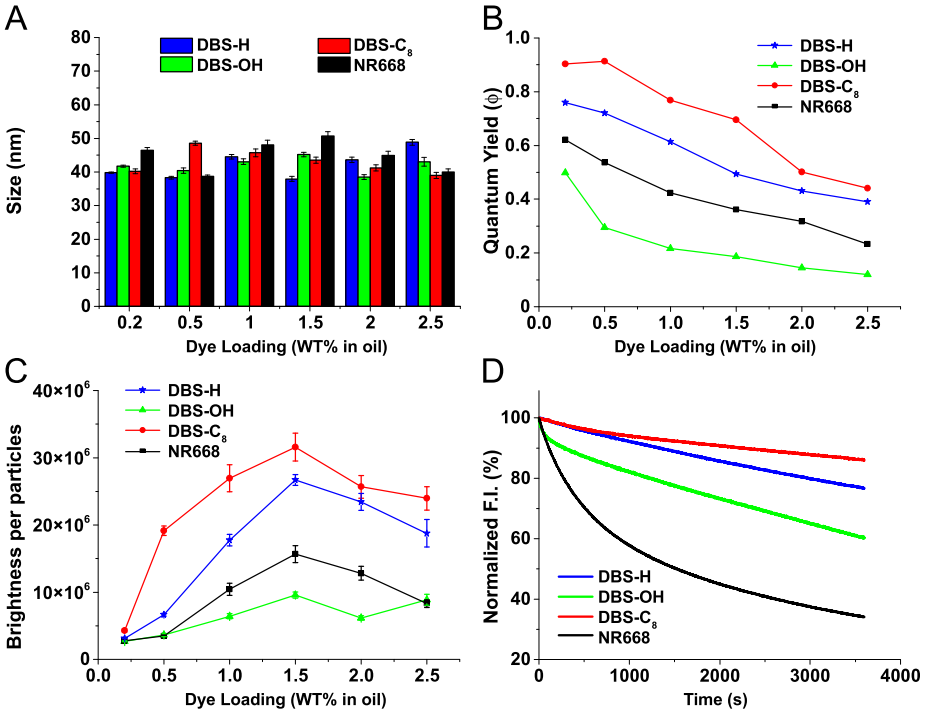

Figure 5. Characterization of dye-loaded VEA NEs. (A) Size of the NEs by DLS (diluted 100 times from formulation solution). (B) Quantum yields of NEs with increasing loading of dyes. (C) Brightness (M^{-1} cm^{-1}) of single NEs calculated from eq 1 and according to the measured size. (D) Photostability of 1% dye-loaded NEs under continuous illumination (λ_{ex} were set to excite the fluorophores at the same ε value), fluorescence was monitored at 600 nm. NEs were formulated in water. QY were obtained using Rhodamine 6G as a reference (ϕ = 0.95 in water).

properties and brightness of NEs and to compare the efficiency of DBS dyes and NR668 in providing bright NEs, we fixed the formulation parameters SOR = 50 wt %, i.e., the droplet size of around 50 nm (see Figure S4A), and then formulated different NEs, at different dye loadings (ranging from 0.2 to 2.5 wt % in oil). The sizes of the DBS-loaded and NR668-loaded NEs were very close (41.9 ± 3.3 and 44.5 ± 4.6 nm, respectively) with very good PDI values <0.09 (Figure 5A), showing that the emulsification process is robust and not affected by a slight modification of the oil composition. To assess the stability of the formed NEs over time, their sizes were measured after 10 days. The results, reported in Table S4, suggested good stabilities of NEs, with the exception of highly loaded DBS-H NEs, showing slight signs of size and PDI increase. To assess the ACQ phenomenon in this system, the quantum yields of the NEs were measured. The results showed that, globally, the quantum yields were quite different in function of the dyes (Figure 5B): DBS-OH appeared as less effective with a quantum yield starting at 0.50 which then underwent a fast drop upon increase of the dye loading. Compared to DBS-OH, DBS-H displayed much higher quantum yield values with a slower decrease upon dye loading. The best candidate was DBS-C_8 displaying high quantum yields at low loading (up to 0.91) and a quite high value of 0.44 at loading as high as 2.5%, which corresponds to a concentration of 37 mM in oil. As a result, it seemed that the C_8 side arm (of DBS-C_8), in addition to enhancing the brightness of DBS in oils (Table 2), helps to prevent ACQ, probably by inducing steric hindrance or a favorable spatial orientation.

Although NR668 provided descent QY values at high concentrations (Figure 5B), the formed NEs were less bright (Figure 5C) as the molar extinction coefficient ε of NR668 was about half of that of DBS dyes. Indeed, when the brightness per nanodroplet (calculated from the measured size and the values of QY and ε) was plotted vs dye loading, NEs loaded with DBS-H and especially DBS-C_8 appeared much brighter than those loaded with NR668 (Figure 5C). According to Figure 5C, it appeared as a general trend that loadings superior to 1.5 wt % did not provide brighter NEs as the brightness systematically decreased at higher loading.

In bioimaging, the photostability is of major importance, especially for the tracking of a fluorescent object over time. For this purpose, NEs containing 1% of dyes were continuously irradiated and their fluorescence intensity was monitored over 1 h (Figure 5D). Taken as a reference, NR668 showed a relatively weak photostability as 65% of its fluorescence intensity was lost over 1 h. On the other hand, DBS dyes globally displayed a much better photostability but some notable difference between each other. Once again, the best results were obtained with DBS-C_8 that presented an impressive photostability, losing only 15% of its fluorescence intensity after 1 h photoirradiation (Figure 5D).

Given that DBS-C_8 displayed the highest brightness in NEs, the higher solubility in VEA, and the best photostability, it was chosen for the next studies. In preparation of biological studies, the next experiment was designed to evaluate the potential early leakage of the dye from the NEs to the biological media. Biomolecules, cells, tissues, contain many lipophilic domains (e.g., membranes or proteins) that can act as acceptors for the lipophilic dyes. Although DBS dyes were shown to have reduced brightness in nonviscous environments, in bioimaging experiments, such a dye leakage phenomenon can lead to decreasing of NE brightness itself and thus enhancing the background noise.[21,59]

To estimate the dye leakage, fluorescence correlation spectroscopy (FCS) measurements were conducted in PBS

DOI: 10.1021/acsami.8b22297
ACS Appl. Mater. Interfaces 2019, 11, 13079−13090

alone and in the presence of 10% (v/v) fetal bovine serum (FBS) (Table 3). Serum is an appropriate model of the biological dye acceptor as it contains a high variety of amphiphilic biomolecules, especially lipoproteins. We thus compared NR668 and DBS-C_8-loaded NEs with increasing dye loading. First, the results confirmed the sizes obtained by DLS analysis and that DBS-C_8-loaded NEs were much brighter than the NR668 ones. Regarding the dye leakage, NR668, as well as DBS-C_8-loaded NEs, showed limited leakage as the size and the concentration of fluorescent objects remained similar in the presence of 10% serum even at high dye loading percentage (Table 3). At this stage of our work, cytotoxicity studies (MTT assay) were performed with the DBS dyes and NR668. The results showed no significant cytotoxicity up to 5 μM except for DBS-H that showed some sign of toxicity at 5 μM (Figure S5).

Table 3. Assessment of the Dye Leakage by Fluorescence Correlation Spectroscopy (FCS)[a]

dye	(dye) (%)	solvent	τ (ms)	d (nm)	relative brightness	(droplets) (nM)
DBS-C_8	0.2	PBS	1.45	57.3	105	1.21
DBS-C_8	1.0	PBS	1.74	68.7	442	1.12
DBS-C_8	2.5	PBS	1.32	52.3	306	1.04
DBS-C_8	0.2	10% FBS	1.42	52.9	120	1.55
DBS-C_8	1.0	10% FBS	1.51	56.0	481	1.26
DBS-C_8	2.5	10% FBS	1.42	52.8	334	2.21
NR668	0.2	PBS	1.34	42.2	43.4	1.47
NR668	1.0	PBS	1.34	42.3	85.5	1.90
NR668	2.5	PBS	1.14	35.9	42.7	2.61
NR668	0.2	10% FBS	1.43	45.2	40.4	1.98
NR668	1.0	10% FBS	1.49	46.9	95.7	1.97
NR668	2.5	10% FBS	1.27	40.1	34.1	4.92

[a] τ (ms)—correlation time; d (nm)—hydrodynamic diameter; brightness—brightness per particle with respect to reference (TMR); [droplets] (nM)—concentration of nanodroplets. All measurements were done using TMR as a reference.

Two-Photon Imaging. Two-photon excitation (TPE) imaging possesses many advantages in bioimaging including limited photobleaching, lower phototoxicity, and reduced cell auto-fluorescence.[60−62] For these reasons, we investigated the two-photon absorption characteristics of DBS dyes. First, their TPE cross-section spectra in dioxane were measured (Figures 6A and S6) along with their quadratic intensity dependence (Figure S7). DBS dyes displayed similar spectra with two major excitation peaks at 980 nm and at 930 nm with absorption cross-section values between 430−734 GM and 76−130 GM, respectively. As a comparison, NR668 has a weaker absorption (maximum at 980 nm, 140 GM) and displayed an additional peak at 810 nm (Figure S8A). To prove that these properties are conserved in NEs, TPE imaging was performed in live HeLa cells. Following our recently developed protocol,[34] we formulated 1% DBS-C_8-loaded NEs presenting negative charges (carboxylate groups) at the interface of nanodroplets to stimulate their internalization in the cells. After incubation with the NEs, the cells were imaged by TPE microscopy. Multicolor images with a high signal-to-noise ratio were obtained showing that NEs were internalized by endocytosis (Figure 6B), which is in line with our previous studies.[34] As a control the same experiment was conducted with NR668, giving similar results (Figure S8B). These results demonstrated the compatibility of these new NEs with TPE imaging, thus extending the choice in their imaging modality.

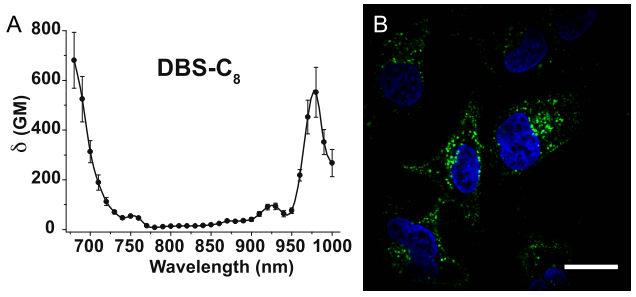

Figure 6. (A) Two-photon excitation cross-section spectra of DBS-C_8 in dioxane (18 μM). (B) Two-photon excitation imaging of HeLa cells incubated for 2 h in the presence of NEs containing 1% PMAO and loaded with 1% DBS-C_8 (λ_{ex} = 930 nm). Concentration of dye was set at 1 μM. Nucleus was stained with Hoechst. Scale bar is 10 μm.

Altogether, these results prove that NEs arising from the combined use of DBS-C_8 dye with VEA oil lead to small and exceptionally bright lipid nanoparticles without nonspecific interactions or leakage of the dye. Compared to our reference dye NR668, DBS-C_8 presents important improvements namely: (1) sharper excitation and emission peaks, (2) enhanced photostability, (3) enhanced brightness, and (4) higher two-photon absorption cross-section. All these features are important properties for bioimaging, especially for the tracking of individual NEs.

Tracking of Single NEs in Cells. Aware of the advantageous features of our system, we undertook the tracking of single NEs in cells. Herein, the influence of the NEs' charge surface on their diffusion in the cytosol was studied as a model parameter to evidence the potential of this new bioimaging tool. Neutral NEs loaded with 1% DBS-C_8 (SOR = 50%) were prepared, as well as exactly the same formulation with the negatively charged surface, using our described protocol.[34] After checking that both NEs had similar size (41 nm) and different ζ-potentials (Table S5), they were microinjected into HeLa cells at the same dye concentration (3 μM) and were imaged at various times after injection. To check that the same amount of NEs was microinjected in both cases, the mean fluorescence of injected cells were measured and showed similar values of 647 ± 89 and 690 ± 110 (a.u.) for neutral and charged NEs, respectively (quintuplicate experiment).

The analysis of recorded images evidenced clear differences in the distribution and mobility of the two types of NEs in the cytoplasm (Figure 7A−F). At 15 s post-injection, the neutral NEs were distributed all over the cytoplasm with a gradient of intensity from the injection point (Figure 7E), whereas negatively charged NEs were mainly localized nearby the injection point (Figure 7B). Maximum intensity projection of movies acquired 5 min post-injection confirmed that neutral NEs reached the entire volume of the cytoplasm, whereas the negatively charged NEs remained confined to a restricted volume around the injection point probably due to nonspecific interactions with biomolecules, membranes, or organelles.

In the second step, this global observation was confirmed by individual tracking of NEs. Due to their intense brightness, high-quality movies were obtained, where individual NEs could be clearly distinguished with a high signal-to-noise ratio and minimal photobleaching (movie available in the SI). For both

DOI: 10.1021/acsami.8b22297
ACS Appl. Mater. Interfaces 2019, 11, 13079−13090

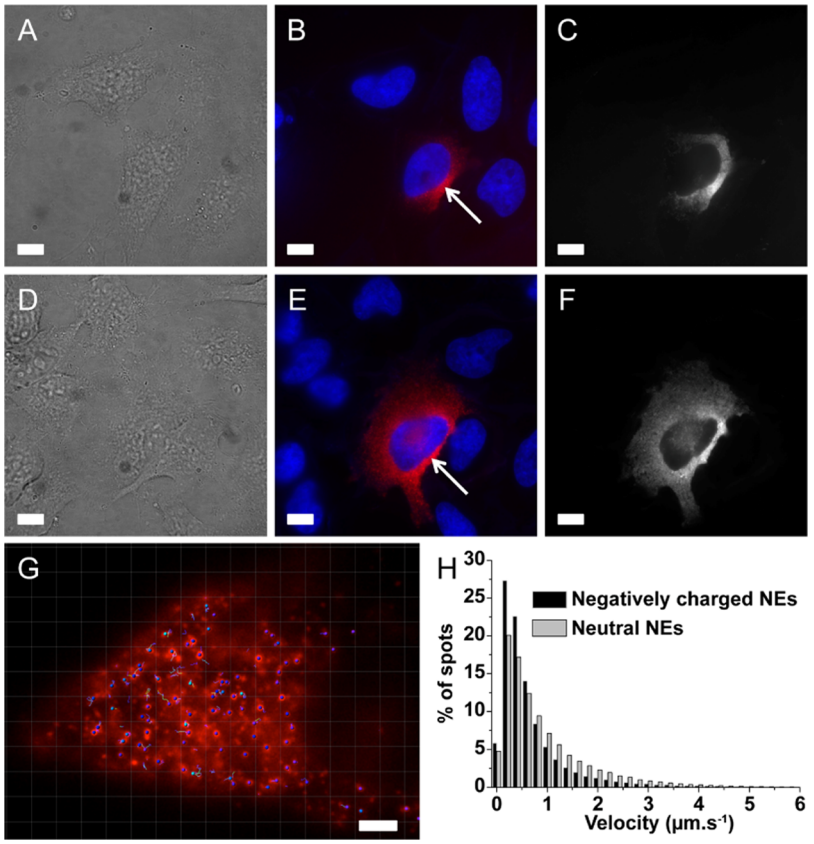

Figure 7. Microinjection of NEs (41 nm) in HeLa cells and their individual tracking. Images of HeLa cells microinjected with negatively charged NEs (A–C) and neutral NEs (D–F). (A, D) Transmission light microscopy 5 min after injection. (B, E) Epifluorescence imaging 15 s post-injection; the NEs are in red and the nuclei are in blue (Hoechst 5 μg mL^{-1}); white arrows indicate the injection point. (C, F) NEs' maximum intensity projection of a 30 s time laps (50 ms acquisition time, a total of 600 images), 5 min post-injection. Scale bar is 10 μm. (G) Example of a HeLa cell microinjected with neutral NEs where single NEs have been spotted (blue spots) and their trajectory tracked using Imaris 9.2.1 (Bitplane Inc) software, scale bar is 3 μm. (H) Histogram of NEs' velocity in the cytosol obtained by individual NEs' tracking from movies right after injection (30 s, 50 ms acquisition time).

NEs, individual particles were tracked and their trajectory and velocity in the cytoplasm have been determined (Figures 7G and S9). Although PEGylated NEs were already shown to be prevented from aggregation in complex media,[24,25] the distribution of their mean fluorescence intensity was first plotted to prove that NEs did not aggregate in the cytosol of the cells (Figure S10). The results presented in a histogram (Figure 7H) showed first that the majority of the NEs moves with a relatively low velocity, lower than 1 μm s^{-1}. Then, it is noteworthy that neutral NEs display higher velocities compared to the negatively charged ones. Indeed, above 0.8 μm s^{-1}, the proportion of neutral NEs is systematically higher than the negatively charged ones and below this value, this tendency reverses. Among all velocities measured for the displacements of negatively charged NE, only 30% were higher than 0.8 μm s^{-1}, whereas this fraction represents 46% for the neutral ones. These results showed that the charges at the NE interface influence their mobility in the cytoplasm. Presumably, in comparison to neutral NEs, negatively charged NEs are more likely to be involved in nonspecific interactions with biomolecules such as free proteins or those anchored in organelles, thus slowing down their progression.

CONCLUSIONS

In this work, we introduced DBS dyes, a new family of lipophilic and neutral styryl fluorophores that are composed of a barbituryl dioxaborine acceptor moiety and different aniline donor groups. In addition to their fluorescence enhancement from solvents to viscous oils, these dyes display improved properties compared to the previously used fluorophore NR668 including enhanced brightness and photostability, higher two-photon absorption, and sharper peaks. With the prospection of using these new fluorescent and lipophilic molecules in the formulation of NEs, we proposed in this study to screen the main physicochemical parameters and establish a relationship between the fluorescence properties and physicochemical properties of the NEs. After evaluating their photophysical properties in various oils, we found that NEs composed of vitamin E acetate as the lipid core loaded with DBS bearing an octyl chain (DBS-C_8) led to small NEs (~40 nm) with a low polydispersity index. Additionally, they displayed the highest brightness and photostability with no leakage of the dye out of the particle. These NEs were used in TPE imaging and in microinjection experiments in HeLa cells. Thanks to their superior fluorescence properties, we obtained movies that allowed the tracking of individual NEs. We were able to demonstrate significant differences in the NEs' velocity when spreading in the cytosol dependent on their interface charges. The combination of their interesting photophysical properties and their two-photon absorption might make DBS dyes suitable for tracking individual NEs in tissues or in vivo experiments. We believe that this system will contribute to

DOI: 10.1021/acsami.8b22297
ACS Appl. Mater. Interfaces 2019, 11, 13079–13090

extending the knowledge on lipid nanodroplets and nanoparticles and their interactions with biological environments.

■ ASSOCIATED CONTENT

Supporting Information

The Supporting Information is available free of charge on the ACS Publications website at DOI: 10.1021/acsami.8b22297.

Synthesis protocol, NMR and mass characterization of the compounds, tables with photophysical properties in various media, emission spectra, stability tests, solubility of DBS in oils, characterization of emulsions as well as cytotoxicity assays and two-photon absorbance (PDF)
Microinjection of DBS-C_8 loaded NEs (AVI)
Crystallographic data (CIF)

■ AUTHOR INFORMATION

Corresponding Authors

*E-mail: nanton@unistra.fr (N.A.).
*E-mail: andrey.klymchenko@unistra.fr (A.S.K.).
*E-mail: mayeul.collot@unistra.fr (M.C.).

ORCID

Nicolas Anton: 0000-0002-7047-9657
Halina Anton: 0000-0003-1304-8671
Andrey S. Klymchenko: 0000-0002-2423-830X
Mayeul Collot: 0000-0002-8673-1730

Author Contributions

This manuscript was written through contributions of all authors. M.C. synthesized and characterized the DBS dyes. X.W. performed the emulsions and all the spectroscopic experiments and measurements. H.A. tracked the single particles. P.A. measured the two-photon absorption and performed the TPE imaging. M.C. performed the microinjection and imaging. T.K.F. assessed the cytotoxicity. N.A., A.S.K., and M.C. supervised the work and wrote the manuscript. T.V. contributed to materials and analysis tools. All authors have given approval to the final version of the manuscript.

Funding

This work was supported by ERC Consolidator grant BrightSens 648528 and ANR BrightRiboProbes (ANR-16-CE11-0010). X.W. was funded by the China Scholarship Council Ph.D. fellowship (CSC No. 201706240033).

Notes

The authors declare no competing financial interest.

■ ACKNOWLEDGMENTS

We acknowledge Dr Delphine Garnier from the Service de Chimie Analytique (SCA) for her assistance in the LC-MS and RMN analyses and Dr Lydia for the crystallographic data.

■ REFERENCES

(1) Pelaz, B.; Alexiou, C.; Alvarez-Puebla, R. A.; Alves, F.; Andrews, A. M.; Ashraf, S.; Balogh, L. P.; Ballerini, L.; Bestetti, A.; Brendel, C.; Bosi, S.; Carril, M.; Chan, W. C. W.; Chen, C.; Chen, X.; Chen, X.; Cheng, Z.; Cui, D.; Du, J.; Dullin, C.; Escudero, A.; Feliu, N.; Gao, M.; George, M.; Gogotsi, Y.; Grünweller, A.; Gu, Z.; Halas, N. J.; Hampp, N.; Hartmann, R. K.; Hersam, M. C.; Hunziker, P.; Jian, J.; Jiang, X.; Jungebluth, P.; Kadhiresan, P.; Kataoka, K.; Khademhosseini, A.; Kopeček, J.; Kotov, N. A.; Krug, H. F.; Lee, D. S.; Lehr, C.-M.; Leong, K. W.; Liang, X.-J.; Ling Lim, M.; Liz-Marzán, L. M.; Ma, X.; Macchiarini, P.; Meng, H.; Möhwald, H.; Mulvaney, P.; Nel, A. E.; Nie, S.; Nordlander, P.; Okano, T.; Oliveira, J.; Park, T. H.; Penner, R. M.; Prato, M.; Puntes, V.; Rotello, V. M.; Samarakoon, A.; Schaak, R. E.; Shen, Y.; Sjöqvist, S.; Skirtach, A. G.; Soliman, M. G.; Stevens, M. M.; Sung, H.-W.; Tang, B. Z.; Tietze, R.; Udugama, B. N.; VanEpps, J. S.; Weil, T.; Weiss, P. S.; Willner, I.; Wu, Y.; Yang, L.; Yue, Z.; Zhang, Q.; Zhang, Q.; Zhang, X.-E.; Zhao, Y.; Zhou, X.; Parak, W. J. Diverse Applications of Nanomedicine. *ACS Nano* **2017**, *11*, 2313−2381.

(2) Liong, M.; Lu, J.; Kovochich, M.; Xia, T.; Ruehm, S. G.; Nel, A. E.; Tamanoi, F.; Zink, J. I. Multifunctional Inorganic Nanoparticles for Imaging, Targeting, and Drug Delivery. *ACS Nano* **2008**, *2*, 889−896.

(3) Peng, H.-S.; Chiu, D. T. Soft Fluorescent Nanomaterials for Biological and Biomedical Imaging. *Chem. Soc. Rev.* **2015**, *44*, 4699−4722.

(4) Kunjachan, S.; Ehling, J.; Storm, G.; Kiessling, F.; Lammers, T. Noninvasive Imaging of Nanomedicines and Nanotheranostics: Principles, Progress, and Prospects. *Chem. Rev.* **2015**, *115*, 10907−10937.

(5) Li, Z.; Barnes, J. C.; Bosoy, A.; Stoddart, J. F.; Zink, J. I. Mesoporous Silica Nanoparticles in Biomedical Applications. *Chem. Soc. Rev.* **2012**, *41*, 2590−2605.

(6) Tang, F.; Li, L.; Chen, D. Mesoporous Silica Nanoparticles: Synthesis, Biocompatibility and Drug Delivery. *Adv. Mater.* **2012**, *24*, 1504−1534.

(7) Zhou, J.; Yang, Y.; Zhang, C. Toward Biocompatible Semiconductor Quantum Dots: From Biosynthesis and Bioconjugation to Biomedical Application. *Chem. Rev.* **2015**, *115*, 11669−11717.

(8) Laurent, S.; Forge, D.; Port, M.; Roch, A.; Robic, C.; Vander Elst, L.; Muller, R. N. Magnetic Iron Oxide Nanoparticles: Synthesis, Stabilization, Vectorization, Physicochemical Characterizations, and Biological Applications. *Chem. Rev.* **2008**, *108*, 2064−2110.

(9) Astruc, D.; Boisselier, E.; Ornelas, C. Dendrimers Designed for Functions: From Physical, Photophysical, and Supramolecular Properties to Applications in Sensing, Catalysis, Molecular Electronics, Photonics, and Nanomedicine. *Chem. Rev.* **2010**, *110*, 1857−1959.

(10) Lee, C. C.; MacKay, J. A.; Fréchet, J. M. J.; Szoka, F. C. Designing Dendrimers for Biological Applications. *Nat. Biotechnol.* **2005**, *23*, 1517−1526.

(11) Kumari, A.; Yadav, S. K.; Yadav, S. C. Biodegradable Polymeric Nanoparticles Based Drug Delivery Systems. *Colloids Surf., B* **2010**, *75*, 1−18.

(12) Elsabahy, M.; Wooley, K. L. Design of Polymeric Nanoparticles for Biomedical Delivery Applications. *Chem. Soc. Rev.* **2012**, *41*, 2545−2561.

(13) Delplace, V.; Couvreur, P.; Nicolas, J. Recent Trends in the Design of Anticancer Polymer Prodrug Nanocarriers. *Polym. Chem.* **2014**, *5*, 1529−1544.

(14) Reisch, A.; Klymchenko, A. S. Fluorescent Polymer Nanoparticles Based on Dyes: Seeking Brighter Tools for Bioimaging. *Small* **2016**, *12*, 1968−1992.

(15) Kamaly, N.; Yameen, B.; Wu, J.; Farokhzad, O. C. Degradable Controlled-Release Polymers and Polymeric Nanoparticles: Mechanisms of Controlling Drug Release. *Chem. Rev.* **2016**, *116*, 2602−2663.

(16) Torchilin, V. P. Recent Advances with Liposomes as Pharmaceutical Carriers. *Nat. Rev. Drug Discovery* **2005**, *4*, 145−160.

(17) Mehnert, W.; Mäder, K. Solid Lipid Nanoparticles: Production, Characterization and Applications. *Adv. Drug Delivery Rev.* **2001**, *47*, 165−196.

(18) Anton, N.; Vandamme, T. F. The Universality of Low-Energy Nano-Emulsification. *Int. J. Pharm.* **2009**, *377*, 142−147.

(19) McClements, D. J. Nanoemulsions versus Microemulsions: Terminology, Differences, and Similarities. *Soft Matter* **2012**, *8*, 1719−1729.

(20) Yao, M.; Xiao, H.; McClements, D. J. Delivery of Lipophilic Bioactives: Assembly, Disassembly, and Reassembly of Lipid Nanoparticles. *Annu. Rev. Food Sci. Technol.* **2014**, *5*, 53−81.

DOI: 10.1021/acsami.8b22297
ACS Appl. Mater. Interfaces 2019, 11, 13079−13090

(21) Klymchenko, A. S.; Roger, E.; Anton, N.; Anton, H.; Shulov, I.; Vermot, J.; Mely, Y.; Vandamme, T. F. Highly Lipophilic Fluorescent Dyes in Nano-Emulsions: Towards Bright Non-Leaking Nano-Droplets. *RSC Adv.* **2012**, *2*, 11876−11886.
(22) Li, X.; Anton, N.; Zuber, G.; Vandamme, T. Contrast Agents for Preclinical Targeted X-Ray Imaging. *Adv. Drug Delivery Rev.* **2014**, *76*, 116−133.
(23) Anton, N.; Hallouard, F.; Attia, M. F.; Vandamme, T. F. Nano-Emulsions for Drug Delivery and Biomedical Imaging. In *Intracellular Delivery III: Market Entry Barriers of Nanomedicines*; Prokop, A., Weissig, V., Eds.; Fundamental Biomedical Technologies; Springer International Publishing: Cham, 2016; pp 273−300.
(24) Li, X.; Anton, N.; Zuber, G.; Zhao, M.; Messaddeq, N.; Hallouard, F.; Fessi, H.; Vandamme, T. F. Iodinated α-Tocopherol Nano-Emulsions as Non-Toxic Contrast Agents for Preclinical X-Ray Imaging. *Biomaterials* **2013**, *34*, 481−491.
(25) Attia, M. F.; Anton, N.; Chiper, M.; Akasov, R.; Anton, H.; Messaddeq, N.; Fournel, S.; Klymchenko, A. S.; Mély, Y.; Vandamme, T. F. Biodistribution of X-Ray Iodinated Contrast Agent in Nano-Emulsions Is Controlled by the Chemical Nature of the Oily Core. *ACS Nano* **2014**, *8*, 10537−10550.
(26) Kilin, V. N.; Anton, H.; Anton, N.; Steed, E.; Vermot, J.; Vandamme, T. F.; Mely, Y.; Klymchenko, A. S. Counterion-Enhanced Cyanine Dye Loading into Lipid Nano-Droplets for Single-Particle Tracking in Zebrafish. *Biomaterials* **2014**, *35*, 4950−4957.
(27) Texier, I.; Goutayer, M.; Da Silva, A.; Guyon, L.; Djaker, N.; Josserand, V.; Neumann, E.; Bibette, J.; Vinet, F. Cyanine-Loaded Lipid Nanoparticles for Improved in Vivo Fluorescence Imaging. *J. Biomed. Opt.* **2009**, *14*, No. 054005.
(28) Bouchaala, R.; Mercier, L.; Andreiuk, B.; Mély, Y.; Vandamme, T.; Anton, N.; Goetz, J. G.; Klymchenko, A. S. Integrity of Lipid Nanocarriers in Bloodstream and Tumor Quantified by Near-Infrared Ratiometric FRET Imaging in Living Mice. *J. Controlled Release* **2016**, *236*, 57−67.
(29) Ma, X.; Sun, R.; Cheng, J.; Liu, J.; Gou, F.; Xiang, H.; Zhou, X. Fluorescence Aggregation-Caused Quenching versus Aggregation-Induced Emission: A Visual Teaching Technology for Undergraduate Chemistry Students. *J. Chem. Educ.* **2016**, *93*, 345−350.
(30) Lainé, A.-L.; Gravier, J.; Henry, M.; Sancey, L.; Béjaud, J.; Pancani, E.; Wiber, M.; Texier, I.; Coll, J.-L.; Benoit, J.-P.; Passirani, C. Conventional versus Stealth Lipid Nanoparticles: Formulation and in Vivo Fate Prediction through FRET Monitoring. *J. Controlled Release* **2014**, *188*, 1−8.
(31) Reisch, A.; Didier, P.; Richert, L.; Oncul, S.; Arntz, Y.; Mély, Y.; Klymchenko, A. S. Collective Fluorescence Switching of Counterion-Assembled Dyes in Polymer Nanoparticles. *Nat. Commun.* **2014**, *5*, No. 4089.
(32) Huang, Y.; Zhang, G.; Hu, F.; Jin, Y.; Zhao, R.; Zhang, D. Emissive Nanoparticles from Pyridinium-Substituted Tetraphenylethylene Salts: Imaging and Selective Cytotoxicity towards Cancer Cells in Vitro and in Vivo by Varying Counter Anions. *Chem. Sci.* **2016**, *7*, 7013−7019.
(33) Greenspan, P.; Mayer, E. P.; Fowler, S. D. Nile Red: A Selective Fluorescent Stain for Intracellular Lipid Droplets. *J. Cell Biol.* **1985**, *100*, 965−973.
(34) Attia, M. F.; Dieng, S. M.; Collot, M.; Klymchenko, A. S.; Bouillot, C.; Serra, C. A.; Schmutz, M.; Er-Rafik, M.; Vandamme, T. F.; Anton, N. Functionalizing Nanoemulsions with Carboxylates: Impact on the Biodistribution and Pharmacokinetics in Mice. *Macromol. Biosci.* **2017**, *17*, No. 1600471.
(35) Collot, M.; Fam, T. K.; Ashokkumar, P.; Faklaris, O.; Galli, T.; Danglot, L.; Klymchenko, A. S. Ultrabright and Fluorogenic Probes for Multicolor Imaging and Tracking of Lipid Droplets in Cells and Tissues. *J. Am. Chem. Soc.* **2018**, 5401.
(36) Pfister, A.; Zhang, G.; Zareno, J.; Horwitz, A. F.; Fraser, C. L. Boron Polylactide Nanoparticles Exhibiting Fluorescence and Phosphorescence in Aqueous Medium. *ACS Nano* **2008**, *2*, 1252−1258.
(37) Contreras, J.; Xie, J.; Chen, Y. J.; Pei, H.; Zhang, G.; Fraser, C. L.; Hamm-Alvarez, S. F. Intracellular Uptake and Trafficking of Difluoroboron Dibenzoylmethane−Polylactide Nanoparticles in HeLa Cells. *ACS Nano* **2010**, *4*, 2735−2747.
(38) Kerr, C.; DeRosa, C. A.; Daly, M. L.; Zhang, H.; Palmer, G. M.; Fraser, C. L. Luminescent Difluoroboron β-Diketonate PLA−PEG Nanoparticle. *Biomacromolecules* **2017**, *18*, 551−561.
(39) Magde, D.; Rojas, G. E.; Seybold, P. G. Solvent Dependence of the Fluorescence Lifetimes of Xanthene Dyes. *Photochem. Photobiol.* **1999**, *70*, 737−744.
(40) Albota, M. A.; Xu, C.; Webb, W. W. Two-Photon Fluorescence Excitation Cross Sections of Biomolecular Probes from 690 to 960 Nm. *Appl. Opt.* **1998**, *37*, 7352−7356.
(41) Clamme, J. P.; Azoulay, J.; Mély, Y. Monitoring of the Formation and Dissociation of Polyethylenimine/DNA Complexes by Two Photon Fluorescence Correlation Spectroscopy. *Biophys. J.* **2003**, *84*, 1960−1968.
(42) Spingler, B.; Schnidrig, S.; Todorova, T.; Wild, F. Some Thoughts about the Single Crystal Growth of Small Molecules. *CrystEngComm* **2012**, *14*, 751−757.
(43) *"M86-E01078 APEX2 User Manual"*; Bruker AXS Inc.: Madison, 2006.
(44) Sheldrick, G. M. Phase Annealing in SHELX-90: Direct Methods for Larger Structures. *Acta Crystallogr., Sect. A: Found. Crystallogr.* **1990**, *46*, 467−473.
(45) Sheldrick, G. M. A Short History of SHELX. *Acta Crystallogr., Sect. A: Found. Crystallogr.* **2008**, *64*, 112−122.
(46) Anton, N.; Vandamme, T. F. The Universality of Low-Energy Nano-Emulsification. *Int. J. Pharm.* **2009**, *377*, 142−147.
(47) Reisch, A.; Heimburger, D.; Ernst, P.; Runser, A.; Didier, P.; Dujardin, D.; Klymchenko, A. S. Protein-Sized Dye-Loaded Polymer Nanoparticles for Free Particle Diffusion in Cytosol. *Adv. Funct. Mater.* **2018**, *28*, No. 1805157.
(48) Müller, P.; Schwille, P.; Weidemann, T. PyCorrFit-Generic Data Evaluation for Fluorescence Correlation Spectroscopy. *Bioinformatics* **2014**, *30*, 2532−2533.
(49) Karpenko, I. A.; Niko, Y.; Yakubovskyi, V. P.; Gerasov, A. O.; Bonnet, D.; Kovtun, Y. P.; Klymchenko, A. S. Push-Pull Dioxaborine as Fluorescent Molecular Rotor: Far-Red Fluorogenic Probe for Ligand-Receptor Interactions. *J. Mater. Chem. C* **2016**, *4*, 3002−3009.
(50) Gieseking, R. L.; Mukhopadhyay, S.; Risko, C.; Marder, S. R.; Brédas, J.-L. Effect of Bulky Substituents on Thiopyrylium Polymethine Aggregation in the Solid State: A Theoretical Evaluation of the Implications for All-Optical Switching Applications. *Chem. Mater.* **2014**, *26*, 6439−6447.
(51) Frischmann, P. D.; Würthner, F. Synthesis of a Non-Aggregating Bay-Unsubstituted Perylene Bisimide Dye with Latent Bromo Groups for C−C Cross Coupling. *Org. Lett.* **2013**, *15*, 4674−4677.
(52) Ozdemir, T.; Atilgan, S.; Kutuk, I.; Yildirim, L. T.; Tulek, A.; Bayindir, M.; Akkaya, E. U. Solid-State Emissive BODIPY Dyes with Bulky Substituents As Spacers. *Org. Lett.* **2009**, *11*, 2105−2107.
(53) Rosania, G. R.; Lee, J. W.; Ding, L.; Yoon, H.-S.; Chang, Y.-T. Combinatorial Approach to Organelle-Targeted Fluorescent Library Based on the Styryl Scaffold. *J. Am. Chem. Soc.* **2003**, *125*, 1130−1131.
(54) Yan, P.; Acker, C. D.; Zhou, W.-L.; Lee, P.; Bollensdorff, C.; Negrean, A.; Lotti, J.; Sacconi, L.; Antic, S. D.; Kohl, P.; Mansvelder, H. D.; Pavone, F. S.; Loew, L. M. Palette of Fluorinated Voltage-Sensitive Hemicyanine Dyes. *Proc. Natl. Acad. Sci. U.S.A.* **2012**, *109*, 20443−20448.
(55) Kuimova, M. K. Mapping Viscosity in Cells Using Molecular Rotors. *Phys. Chem. Chem. Phys.* **2012**, *14*, 12671−12686.
(56) Haidekker, M. A.; Theodorakis, E. A. Molecular Rotors–Fluorescent Biosensors for Viscosity and Flow. *Org. Biomol. Chem.* **2007**, *5*, 1669−1678.
(57) Su, D.; Teoh, C. L.; Wang, L.; Liu, X.; Chang, Y.-T. Motion-Induced Change in Emission (MICE) for Developing Fluorescent Probes. *Chem. Soc. Rev.* **2017**, *46*, 4833−4844.

DOI: 10.1021/acsami.8b22297
ACS Appl. Mater. Interfaces 2019, 11, 13079−13090

(58) Li, X.; Anton, N.; Ta, T. M. C.; Zhao, M.; Messaddeq, N.; Vandamme, T. F. Microencapsulation of nanoemulsions: novel Trojan particles for bioactive lipid molecule delivery. https://www.dovepress.com/microencapsulation-of-nanoemulsions-novel-trojan-particles-for-bioacti-peer-reviewed-article-IJN (accessed Oct 19, 2018).
(59) Bouchaala, R.; Anton, N.; Anton, H.; Vandamme, T.; Vermot, J.; Smail, D.; Mély, Y.; Klymchenko, A. S. Light-Triggered Release from Dye-Loaded Fluorescent Lipid Nanocarriers in Vitro and in Vivo. *Colloids Surf., B* **2017**, *156*, 414−421.
(60) Helmchen, F.; Denk, W. Deep Tissue Two-Photon Microscopy. *Nat. Methods* **2005**, *2*, 932−940.
(61) Svoboda, K.; Yasuda, R. Principles of Two-Photon Excitation Microscopy and Its Applications to Neuroscience. *Neuron* **2006**, *50*, 823−839.
(62) Piston, D. W. Imaging Living Cells and Tissues by Two-Photon Excitation Microscopy. *Trends Cell Biol.* **1999**, *9*, 66−69.

DOI: 10.1021/acsami.8b22297
ACS Appl. Mater. Interfaces 2019, 11, 13079−13090

Optimizing the Fluorescence Properties of Nanoemulsions for Single Particle Tracking in Live Cells

Supporting information

Xinyue Wang,[a] Nicolas Anton, [a,]* Pichandi Ashokkumar,[b] Halina Anton, [b] Tkhe Kyong Fam, [b] Thierry Vandamme,[a] Andrey S. Klymchenko, [b,]* Mayeul Collot [b,]*

[a] Université de Strasbourg, CNRS, CAMB UMR 7199, F-67000 Strasbourg, France

[b] Laboratory of Biophotonic and Pathologies, CNRS UMR 7021, Université de Strasbourg, Faculté de Pharmacie, 74, Route du Rhin, 67401 Illkirch, France

1. Synthesis

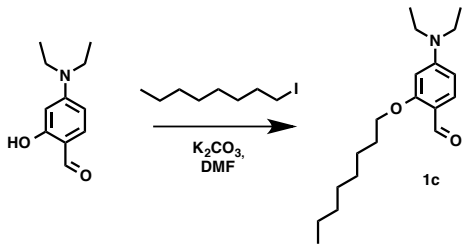

To a solution of 4-(Diethylamino)salicylaldehyde (1.00 g, 5.18 mmol) in degazed DMF (20 mL) were added 1-iodooctane (1.2 mL, 6.64 mmol, 1.3 eq) and grinded K_2CO_3 (2.10 g, 15.22 mmol, 3 eq). The heterogeneous solution was heated at 60°C for 4 h under argon. The solution was cooled down, water was added and the product was extracted with EtOAc (3 times), the organic phases were washed with brine (3 times) before being dried over anhydrous $MgSO_4$, filtered and evaporated. The crude was purified by column chromatography on silica gel (heptane/DCM: 5/5) to obtain 1.13 g of **1c** as a yellowish syrup (Yield = 71%). Rf = 0.49 (DCM). ^{1}H-NMR (400 MHz, $CDCl_3$): δ 10.20 (s, 1H, CHO), 7.73 (d, *J* = 8.9 Hz, 1H, CH Ar), 6.29 (dd, *J* = 9.0, 1.8 Hz, 1H, CH Ar), 6.03 (d, *J* = 2.0 Hz, 1H, CH Ar), 4.04 (t, *J* = 6.3 Hz, 2H, CH_2O), 3.43 (q, *J* = 7.1 Hz, 4H, $2C\underline{H_2}CH_3$), 1.85 (t, *J* = 7.5 Hz, 2H, CH_2), 1.52-1.48 (m, 2H, CH_2), 1.30 (s, 8H, $4CH_2$), 1.23 (t, *J* = 7.1 Hz, 6H, $2CH_2C\underline{H_3}$), 0.91 (dd, *J* = 8.8, 4.7 Hz, 3H, CH_3). ^{13}C-NMR (101 MHz, $CDCl_3$): δ 187.16, 163.89, 153.81, 130.09, 114.39, 104.23, 93.23, 68.08, 44.76, 31.79, 29.33, 29.22, 29.17, 26.14, 22.65, 14.08, 12.62. HRMS (ESI^+), calcd for $C_{19}H_{32}NO_2$ $[M+H]^+$ 306.2428, found 306.2432.

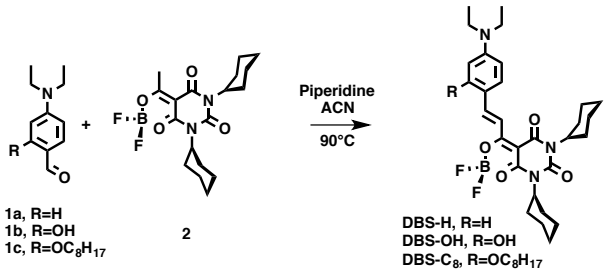

General procedure for the synthesis of DBS dyes. To a solution of aldehyde 1 (1.00 mmol) and barbiturate 2 (1.1 mmol) in dry ACN (8 mL) was added 3 drops of piperidine and the solution was warmed at 90°C for 4 h. The solution was evaporated and the crude was purified by column chromatography on silica gel using a mixture of heptane/EtOAc as eluent.

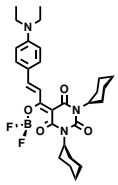

DBS-H. Purification: column chromatography on silica gel (heptane/EtOAc: 8/2). **DBS-H** was obtained as a violet syrup (Yield = 11%). Rf = 0.29 (heptane/EtOAc: 8/2). ^{1}H-NMR (400 MHz, $CDCl_3$): δ 8.31 (s, 2H, CH ethylene), 7.66 (d, *J* = 8.9 Hz, 2H, CH Ar), 6.68 (d, *J* = 9.0 Hz, 2H, CH Ar), 4.84 (dt, *J* = 7.9, 4.0 Hz, 2H, 2NCH CyHex), 3.49 (q, *J* = 7.1 Hz, 4H, $2C\underline{H_2}CH_3$), 2.38 (dd, *J* = 12.1, 2.3 Hz, 4H, CH_2 CyHex), 1.90-1.87 (m, 4H, CH_2 CyHex), 1.78 (dd, *J* = 10.9, 0.3 Hz, 2H, CH_2 CyHex), 1.71-1.66 (m, 4H, CH_2 CyHex), 1.42-1.38 (m, 4H, CH_2 CyHex), 1.26 (t, *J* = 7.1 Hz, 8H, $2CH_2$ CyHex, $2CH_2C\underline{H_3}$). ^{13}C-NMR (101 MHz, $CDCl_3$): δ 179.63, 179.61, 166.32, 159.96, 154.02, 152.10, 148.75, 134.05, 122.10, 112.16, 111.67, 91.74, 57.40, 54.86, 44.93, 29.37, 28.75, 26.41, 26.34, 25.29, 25.00, 12.61. ^{19}F-NMR (376 MHz, $CDCl_3$): δ -145.35 (20%), -145.41 (80%). HRMS (ESI^+), calcd for $C_{29}H_{39}BF_2N_3O_4$ $[M+H]^+$ 542.3002, found 542.3006.

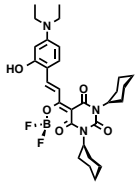

DBS-OH. Purification: column chromatography on silica gel (heptane/EtOAc: 8/2). **DBS-OH** was obtained as a dark violet solid (Yield = 23%). Rf = 0.08 (heptane/EtOAc: 8/2). ^{1}H-NMR (400 MHz, $CDCl_3$): δ 8.69 (d, *J* = 14.7 Hz, 1H, CH ethylene), 8.27 (d, *J* = 14.7 Hz, 1H, CH ethylene), 7.54 (d, *J* = 9.1 Hz, 1H, CH Ar), 6.26 (d, *J* = 9.3 Hz, 1H, CH Ar), 6.08 (s, 1H, CH Ar), 4.84 (s, 2H, 2NCH CyHex), 3.42-3.37 (m, 4H, CH_2 $2C\underline{H_2}CH_3$), 2.42-2.33 (m, 4H, CH_2 CyHex), 1.86 (s, 6H, CH_2 CyHex), 1.68-1.66 (m, 4H, CH_2 CyHex), 1.40-1.17 (m, 12H, $6CH_2$ CyHex, $2CH_2C\underline{H_3}$). ^{13}C-NMR (101 MHz, $CDCl_3$): δ 178.00, 165.79, 161.27, 160.38, 154.50, 149.59, 148.85, 133.35, 112.20, 110.55, 110.54, 106.82, 97.14, 91.16, 57.31, 54.90, 45.06, 29.40, 28.78, 26.39, 26.36, 25.27, 25.03, 12.71. ^{19}F-NMR (376 MHz, $CDCl_3$): δ -144.81 (21%), -144.87 (79%). HRMS (ESI^+), calcd for $C_{29}H_{39}BF_2N_3O_5$ $[M+H]^+$ 558.2951, found 558.2945.

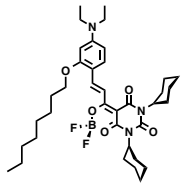

DBS-C_8.Purification: column chromatography on silica gel (heptane/EtOAc: 9/1). **DBS-C_8** was obtained as a dark violet amorphous solid (Yield = 26%). Rf = 0.24 (heptane/EtOAc: 8/2). ^{1}H-NMR (400 MHz, $CDCl_3$): δ 8.61 (d, *J* = 14.9 Hz, 1H, CH ethylene), 8.42 (d, *J* = 14.9 Hz, 1H, CH ethylene), 7.59 (d, *J* = 9.0 Hz, 1H, CH Ar), 6.32 (dd, *J* = 8.5, 0.7 Hz, 1H, CH Ar), 6.05 (s, 1H, CH Ar), 4.84-4.84 (m, 2H, 2NCH CyHex), 4.06 (t, *J* = 6.6 Hz, 2H, CH_2O), 3.48 (q, *J* = 6.9 Hz, 4H, $2C\underline{H_2}CH_3$), 2.40-2.34 (m, 4H, CH_2), 1.99-1.97 (m, 2H, CH_2), 1.89-1.86 (m, 4H, CH_2), 1.77 (m, 2H, CH_2), 1.70-1.65 (m, 4H, CH_2), 1.52-1.50 (m, 2H, CH_2), 1.41-1.25 (m, 20H, CH_2, $2CH_2C\underline{H_3}$), 0.90 (t, *J* = 6.5 Hz, 3H, CH_3).^{13}C-NMR (101 MHz, $CDCl_3$): δ 179.17, 165.98, 163.19, 159.86, 154.06, 149.89, 149.01, 134.86, 113.20, 111.95, 105.65, 93.71, 91.44, 68.66, 57.15,

54.74, 45.09, 31.78, 29.38, 29.24, 29.00, 28.78, 26.46, 26.41, 26.36, 26.19, 25.34, 25.03, 22.67, 22.64, 14.08, 12.74. ^{19}F-NMR (376 MHz, $CDCl_3$): δ -146.00 (19%), -146.06 (81%). HRMS (ESI^+), calcd for $C_{37}H_{55}BF_2N_3O_5$ $[M+H]^+$ 670.4203, found 670.4196.

2. Spectroscopy

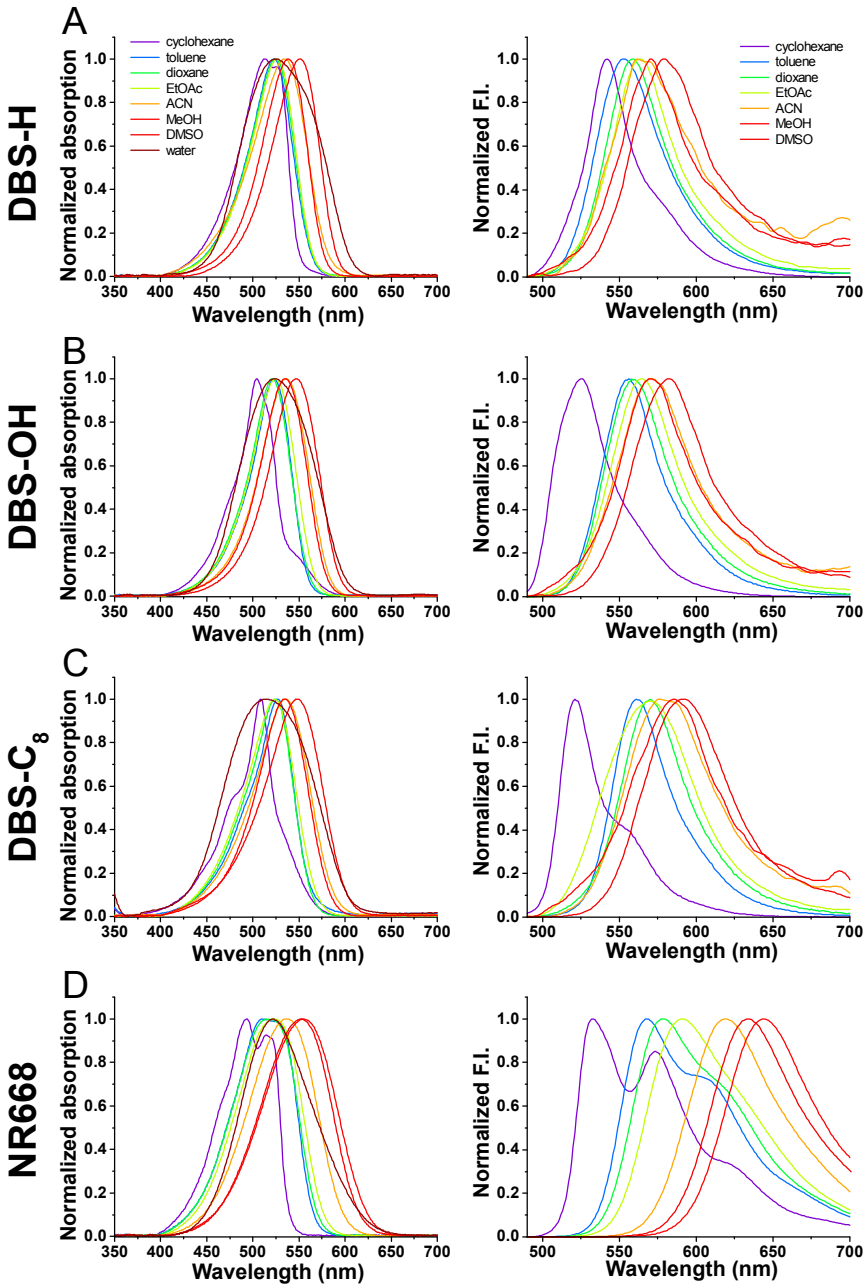

Figure S1. Normalized absorption (left) and emission (right) spectra of DBS dyes (A-C) and NR668 (D) in various organic solvents with increasing polarity. Emission spectra in water was not displayed due to poor solubility of dyes.

Table S1. Photophysical properties of the dyes in various solvents (concentration was 1 μM). Excitation wavelength was 480 nm.

DBS-H

Solvent	λ_{Abs} (nm)	ε ($M^{-1}.cm^{-1}$)	FWHM Abs (nm)	λ_{Em} (nm)	FWHM Em (nm)	Stokes shift (nm)	ϕ^{a} (QY)
Cyclohexane	508	78,070	50	521	32	13	0.13
Toluene	527	88,610	56	561	45	34	0.62
Dioxane	524	92,120	59	570	50	46	0.19
EtOAc	524	96,290	65	573	68	49	0.06
ACN	535	91,680	71	576	69	41	0.01
MeOH	535	81,630	64	585	70	50	0.01
DMSO	548	98,410	74	592	66	44	0.04
Water	517	45,280	108	N/A	N/A	N/A	N/A

DBS-OH

Solvent	λ_{Abs} (nm)	ε ($M^{-1}.cm^{-1}$)	FWHM Abs (nm)	λ_{Em} (nm)	FWHM Em (nm)	Stokes shift (nm)	ϕ^{a} (QY)
Cyclohexane	513	67,200	58	542	37	29	0.20
Toluene	523	79,230	56	553	51	30	0.08
Dioxane	525	90,600	56	558	47	33	0.08
EtOAc	526	99,120	57	563	49	37	0.03
ACN	534	60,500	68	562	94	28	0.01
MeOH	539	101,200	57	571	77	32	0.01
DMSO	551	94,000	60	579	59	28	0.03
Water	524	47,150	98	N/A	N/A	N/A	N/A

DBS-C_8

Solvent	λ_{Abs} (nm)	ε ($M^{-1}.cm^{-1}$)	FWHM Abs (nm)	λ_{Em} (nm)	FWHM Em (nm)	Stokes shift (nm)	ϕ^{a} (QY)
Cyclohexane	504	97,490	47	525	43	21	0.12
Toluene	523	111,610	50	556	45	33	0.50
Dioxane	521	119,710	52	558	49	37	0.20
EtOAc	524	112,350	56	564	52	40	0.05
ACN	536	115,510	61	571	60	35	0.01
MeOH	535	114,690	58	570	59	35	0.01
DMSO	547	125,840	62	582	59	35	0.03
Water	524	59,380	92	N/A	N/A	N/A	N/A

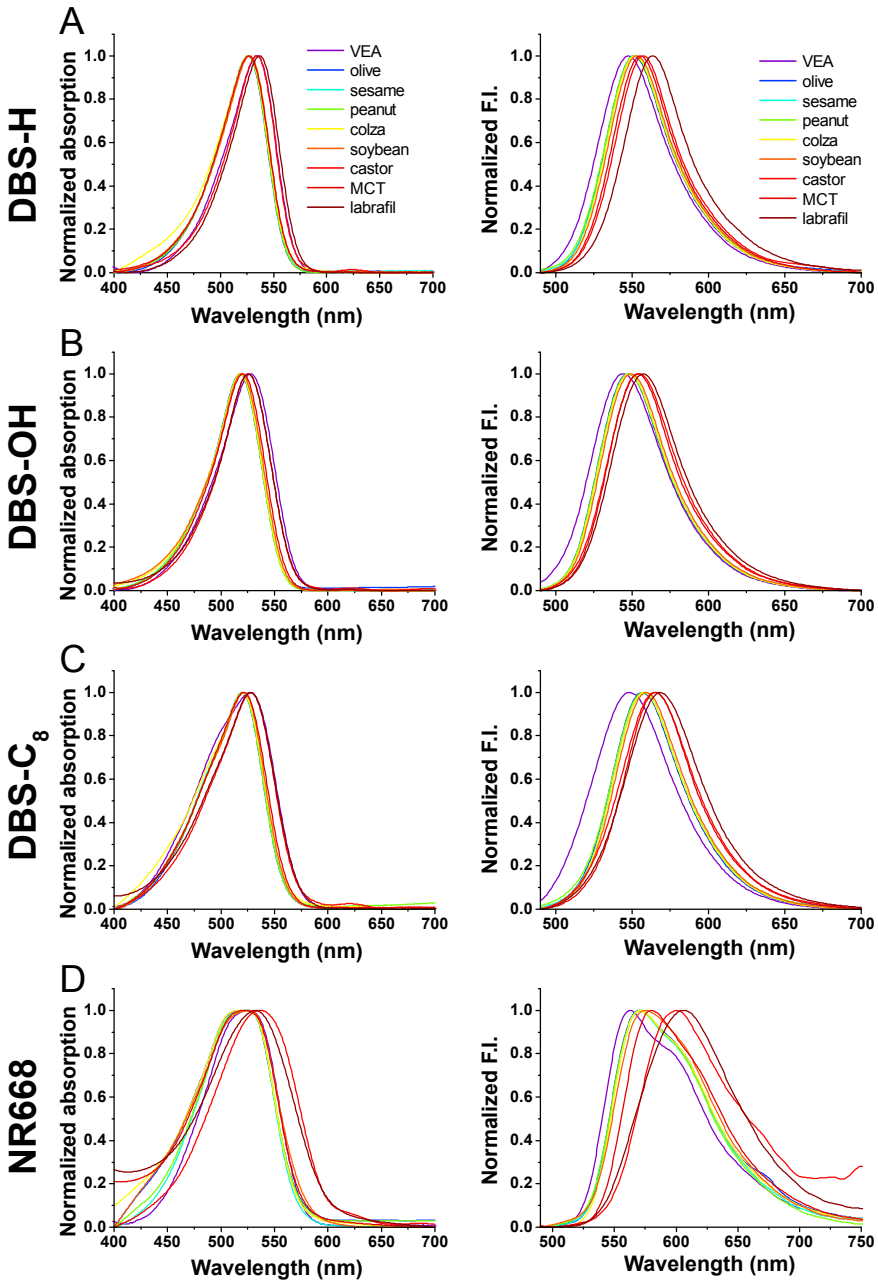

Figure S2. Normalized absorption (left) and emission (right) spectra of DBS dyes (A-C) and NR668 (D) in various oils. Excitation wavelength was 480 nm.

Table S2. Photophysical properties of the dyes in various oils (concentration was 1 μM). Excitation wavelength was 480 nm. MCT is medium chain triglyceride (Labrafac® WL), VEA is Vitamine E Acetate also called tocopherol acetate.

DBS-H

Oil	λ_{Abs} (nm)	ε ($M^{-1}.cm^{-1}$)	FWHM Abs (nm)	λ_{Em} (nm)	FWHM Em (nm)	Stokes shift (nm)	ϕ^a (QY)
MCT	521	76,260	68	566	54	45	0.42
labrafil	528	77,650	70	569	60	41	0.53
colza	520	78,130	70	558	54	38	0.40
peanut	520	70,260	65	558	56	38	0.42
sesame	520	71,990	66	559	55	39	0.40
soybean	521	73,090	71	557	55	36	0.49
olive	520	70,420	66	557	55	37	0.46
castor	528	76,690	69	557	59	29	0.80
VEA	527	59,080	81	548	63	21	0.62
mineral	512	73,370	56	525	34	13	0.22

DBS-OH

Oil	λ_{Abs} (nm)	ε ($M^{-1}.cm^{-1}$)	FWHM Abs (nm)	λ_{Em} (nm)	FWHM Em (nm)	Stokes shift (nm)	ϕ^a (QY)
MCT	527	87,150	55	555	49	28	0.38
labrafil	537	90,580	54	565	50	28	0.56
colza	526	85,730	58	553	50	27	0.44
peanut	527	83,900	53	553	52	26	0.49
sesame	527	83,980	54	554	51	27	0.44
soybean	527	81,050	56	552	50	25	0.45
olive	526	82,380	55	551	51	25	0.55
castor	534	98,430	54	559	49	25	0.87
VEA	534	68,940	55	548	53	14	0.95
mineral	516	68,380	60	545	45	29	0.37

DBS-C_8

Oil	λ_{Abs} (nm)	ε ($M^{-1}.cm^{-1}$)	FWHM Abs (nm)	λ_{Em} (nm)	FWHM Em (nm)	Stokes shift (nm)	ϕ^a (QY)
MCT	520	102,250	56	554	51	34	0.48
labrafil	526	95,590	56	559	54	33	0.73
colza	518	105,320	55	548	54	30	0.58
peanut	518	98,520	54	547	52	29	0.67
sesame	518	96,180	55	548	52	30	0.56
soybean	519	95,200	55	549	52	30	0.59
olive	518	100,790	55	548	52	30	0.60
castor	525	99,920	55	554	52	29	0.96
VEA	527	80,240	60	544	56	17	0.86
mineral	506	99,910	48	527	46	21	0.5

NR668

Oil	λ_{Abs} (nm)	ε ($M^{-1}.cm^{-1}$)	FWHM Abs (nm)	λ_{Em} (nm)	FWHM Em (nm)	Stokes shift (nm)	ϕ^a (QY)
MCT	525	40,090	87	583	84	58	0.98
labrafil	533	40,310	97	603	93	70	0.35
colza	524	41,610	87	572	86	48	0.53
peanut	524	38,950	82	571	88	47	0.48
sesame	524	38,720	82	574	87	50	0.44
soybean	526	35,120	92	572	90	46	0.46
olive	524	39,090	89	570	88	46	0.47
castor	537	41,790	94	602	98	65	0.10
VEA	525	41,440	79	563	85	38	0.86
mineral	496	40,780	74	537	79	41	0.44

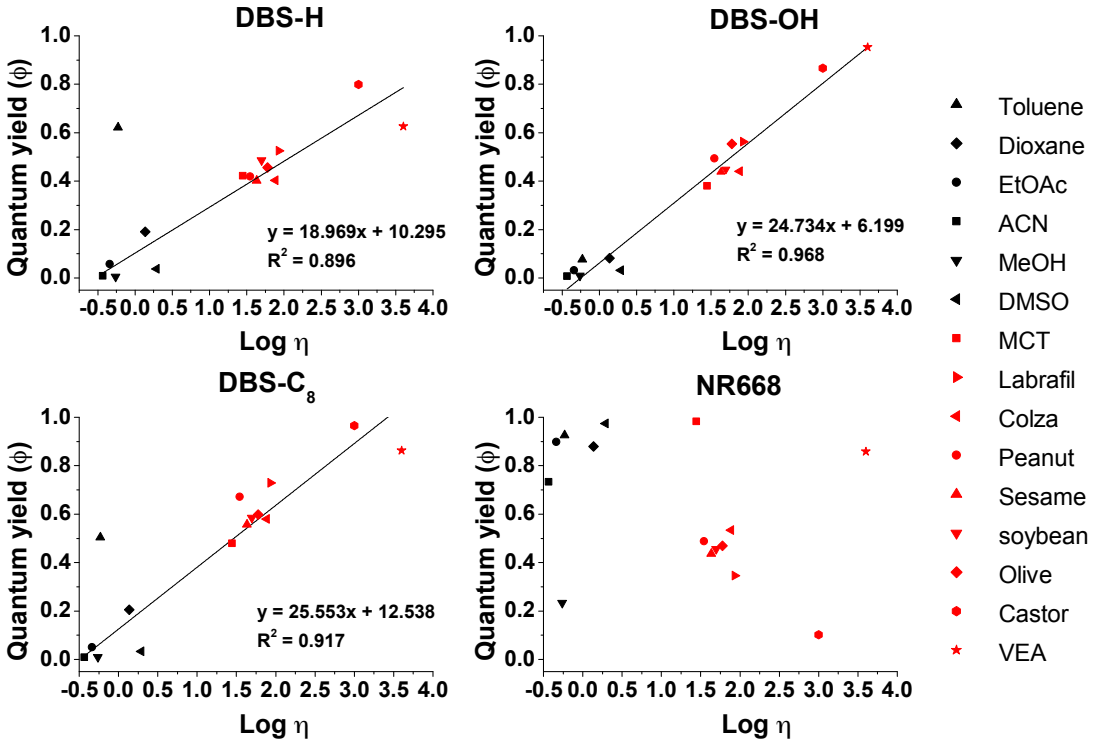

Figure S3. Correlation of the fluorescence quantum yield of DBS dyes and NR668 with the viscosity of the medium. η is the solvent viscosity expressed in mPa.s

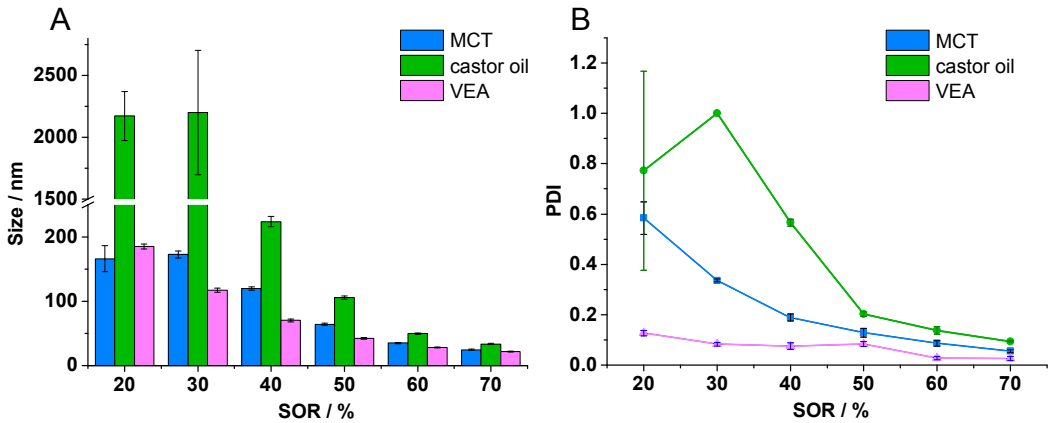

Figure S4. Size (A) and polydispersity index (B) obtained by DLS measurements for NEs formulated with various oils and increasing surfactant/oil ratios (SOR%). Surfactant is cremophore™.

Table S3. Solubility of DBS dyes in 3 different oils expressed in weight percentage.

Dye	MCT	castor oil	VEA
DBS-H	4.2	3.7	3.7
DBS-OH	2.7	2.6	2.7
DBS-C_8	0.3	2.9	7.6

Table S4. Sizes and polydispersity index of NEs (50% SOR, oil: VEA) with increasing dye loading: just prepared and after 10 days at room temperature.

Dye loading (wt% in oil)	Just prepared		10 days after	
	size (nm)	PDI	size (nm)	PDI
		DBS-H		
0.2%	40	0.038	43	0.055
0.5%	38	0.044	50	0.145
1.0%	45	0.045	48	0.066
1.5%	38	0.030	41	0.073
2.0%	44	0.043	56	0.214
2.5%	49	0.079	58	0.204
		DBS-OH		
0.2%	42	0.059	45	0.048
0.5%	40	0.044	44	0.104
1.0%	43	0.052	46	0.067
1.5%	45	0.041	48	0.047
2.0%	38	0.041	41	0.043
2.5%	43	0.051	46	0.050
		DBS-C_8		
0.2%	40	0.080	49	0.077
0.5%	49	0.080	53	0.067
1.0%	46	0.070	49	0.065
1.5%	44	0.084	47	0.065
2.0%	41	0.080	45	0.049
2.5%	39	0.064	43	0.060
		NR668		
0.2%	46	0.055	50	0.047
0.5%	39	0.038	42	0.042
1.0%	48	0.054	51	0.057
1.5%	51	0.038	54	0.057
2.0%	45	0.037	48	0.047
2.5%	40	0.033	42	0.049

Table S5. Sizes and zeta potentials of the neutral and negatively charged NEs

	Size (nm)	Size standard deviation	PDI	PDI standard deviation	zeta potential ξ (mV)	ξ standard deviation
Neutral NEs (no PMAO)	41	0.5	0.04	0.003	-7.4	0.7
Negatively charges NEs (1 wt.% PMAO)	41	0.4	0.05	0.006	-13.9	1.0

3. Cytotoxicity

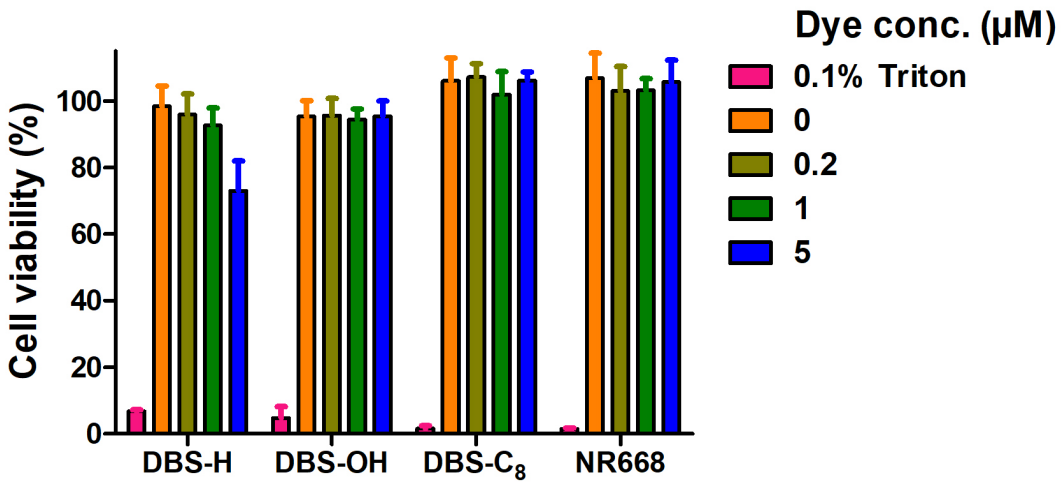

Figure S5. Cytotoxicity assay of the DBS and NR668 dyes at various concentrations using MTT test and HeLa cells. Triton X-100 that is cytotoxic was used as a positive control.

4. Two photon absorbance and imaging

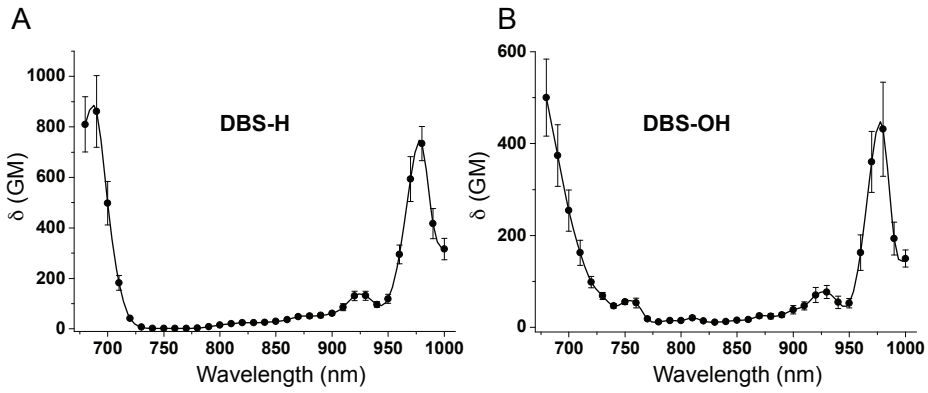

Figure S6. Two-photon excitation cross-section spectra of DBS-H (16 μM) (A) and DBS-OH (28 μM) (B) in dioxane.

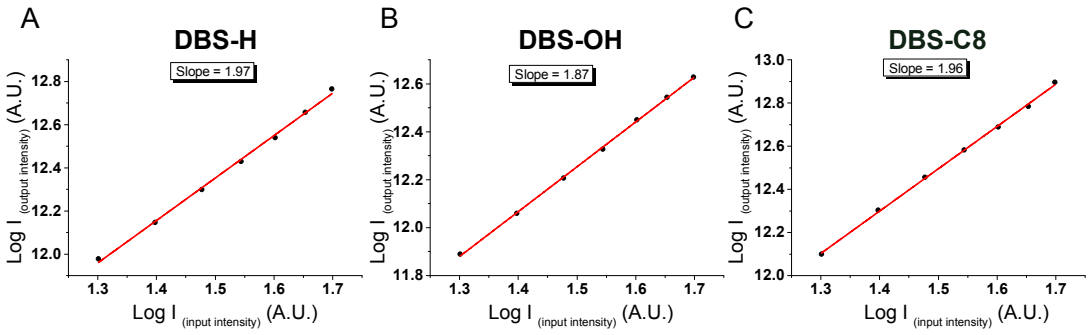

Figure S7. Quadratic intensity dependence plot for DBS dyes in dioxane. (A) DBS-H (16 μM, λ_{Ex}=700 nm), (B) DBS-OH (28 μM, λ_{Ex} =720 nm), (C) DBS-C8 (18 μM, λ_{Ex} =720 nm).

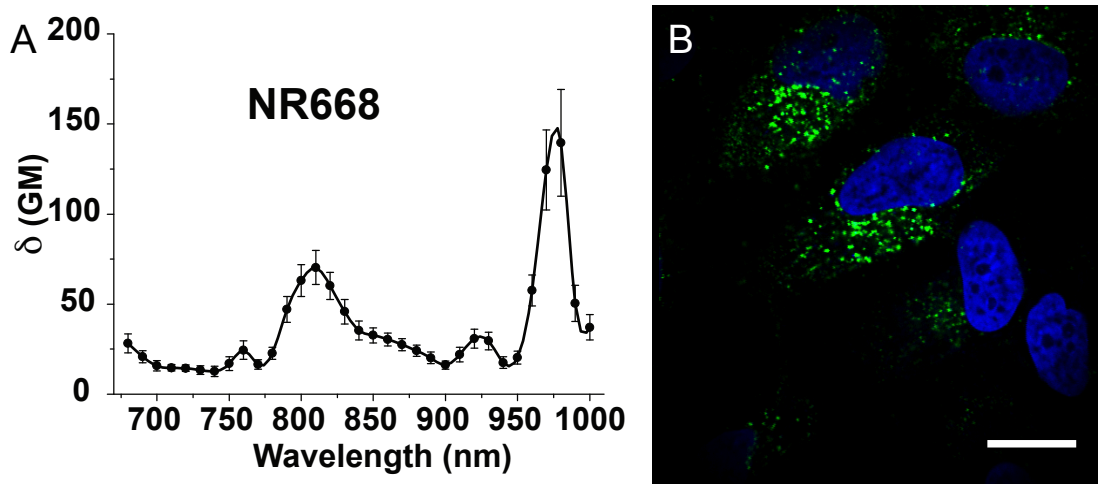

Figure S8. Two-photon excitation cross-section spectra NR668 (A) in dioxane (10 µM). Two-photon excitation imaging of HeLa cells incubated for 2 hours in the presence of NEs containing 1% PMAO and loaded with 1% NR668 (D). Concentration of dye was set at 1 µM. Nucleus was stained with Hoechst, NR668 and DBS-C_8 were excited at similar two-photon action cross-section ($\delta \times \Phi$) values: 930 nm for DBS-C_8 and 910 nm for NR668. Scale bar is 10 µm.

5. Single particle tracking

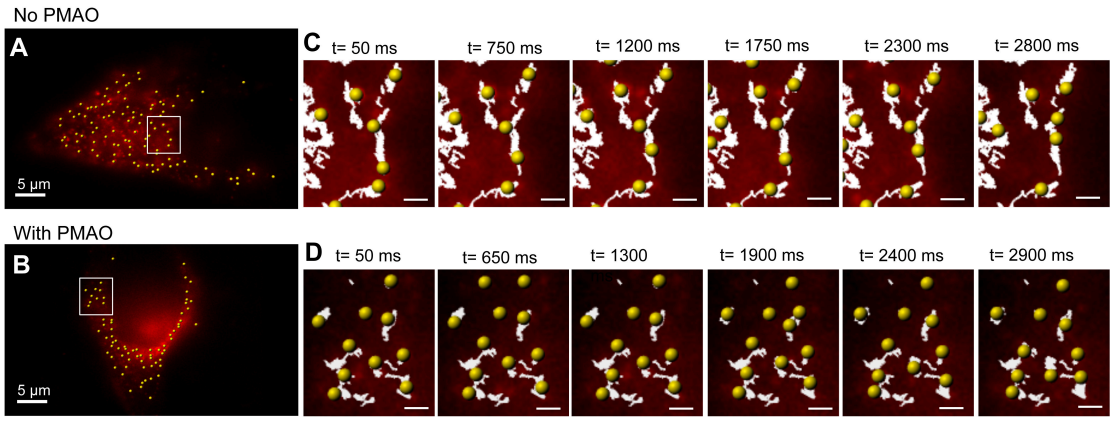

Figure S9. Time Lapse Images of single NEs tracking: A-B: Cells injected with neutral NEs or NEs covered with PMAO, yellow dots highlight single NEs detected in more than 10 consecutive frames. C-D: Time series of the displacement of the NEs along their trajectories (white lines). The images correspond to the inserts shown in the whole cell images A and B. Scale bars in C and D correspond to 2 µm.

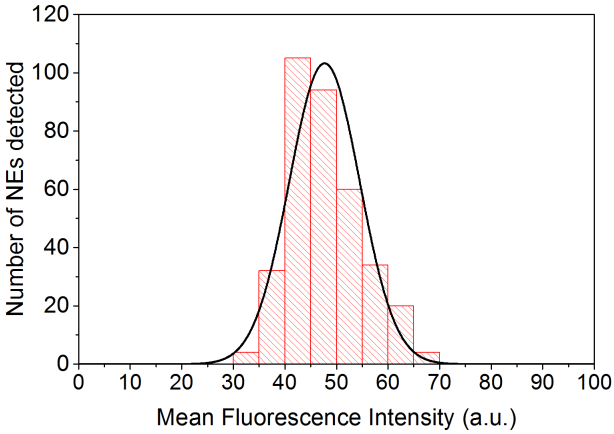

Figure S10. Distribution of the mean fluorescence intensity of the fluorescent NEs detected in the injected cell at 5 different time points. This distribution presents a single population of NEs (mean fluorescence intensity = 47.7+/-6.8 a.u.). For details see materials and methods section.

6. NMR and mass spectra

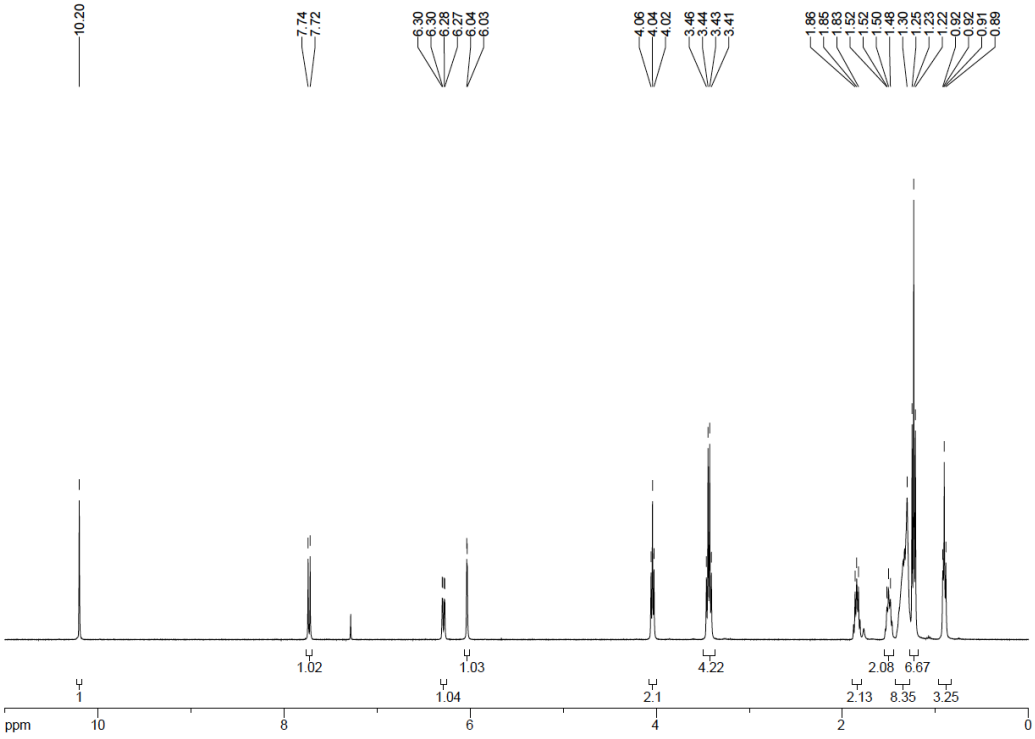

^{1}H NMR spectrum of 1c

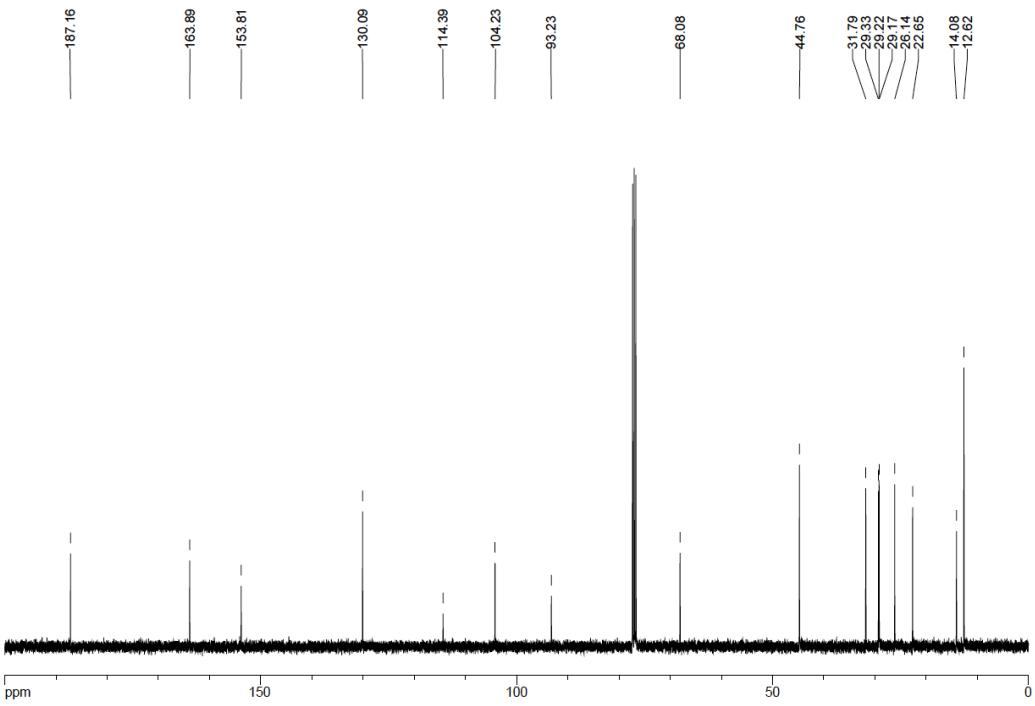

^{13}C NMR spectrum of 1c

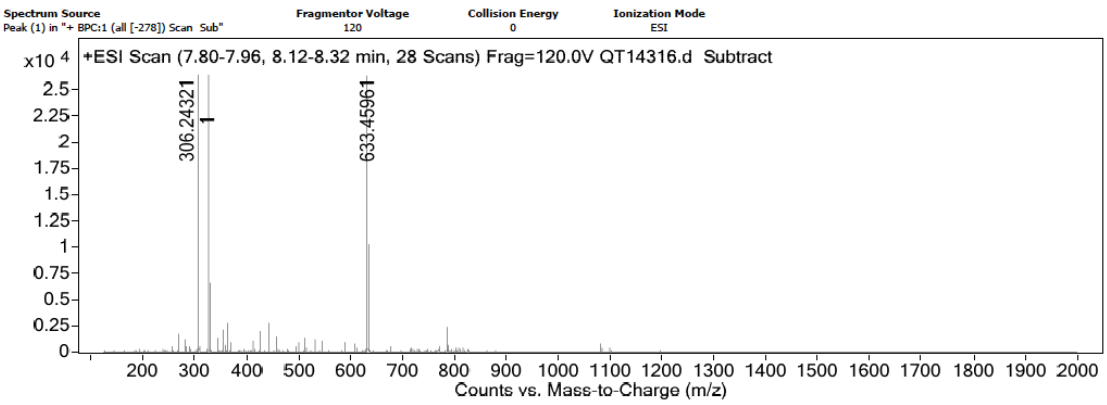

HRMS spectrum of 1c

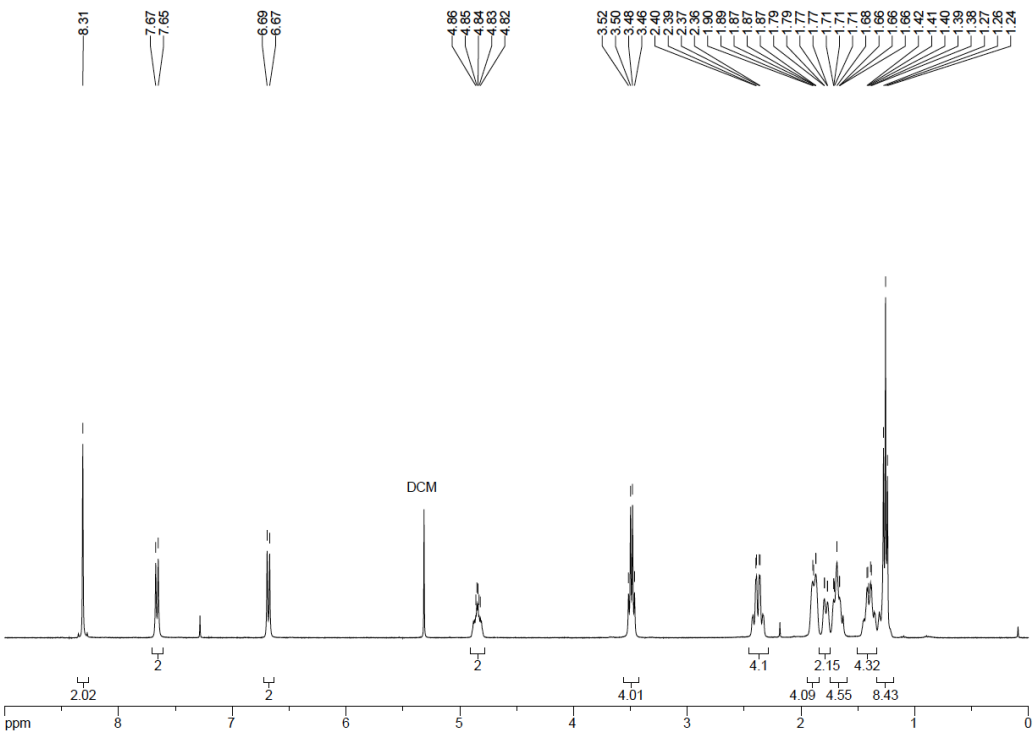

^{1}H NMR spectrum of DBS-H

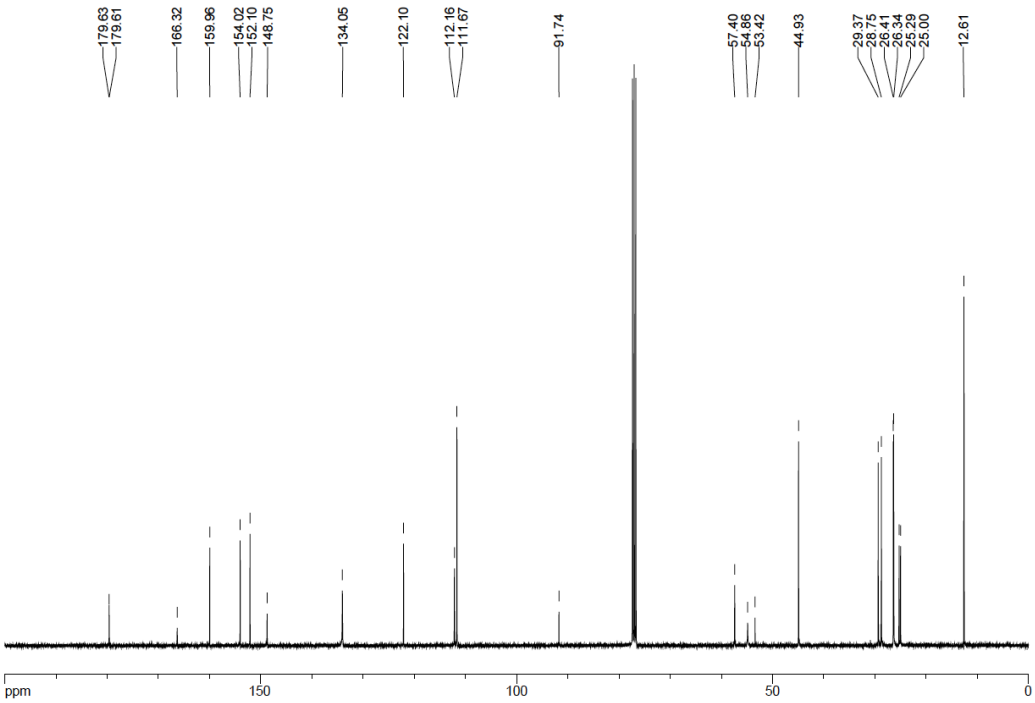

^{13}C NMR spectrum of DBS-H

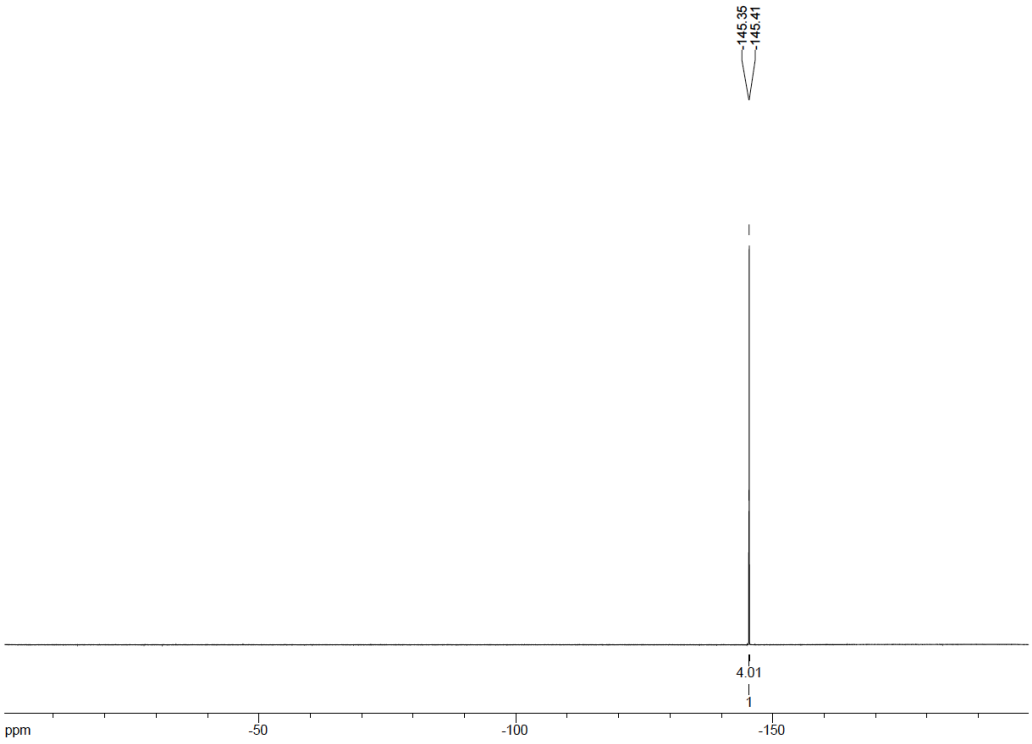

^{19}F NMR spectrum of DBS-H

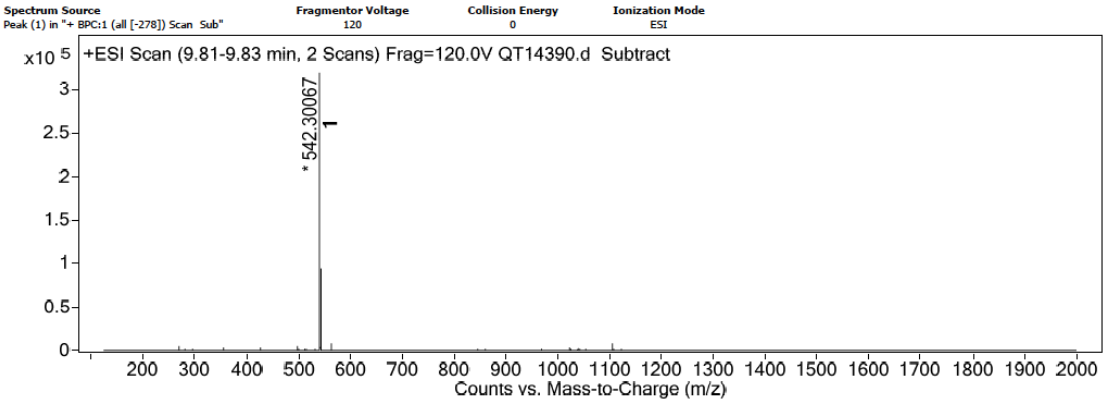

HRMS spectrum of DBS-H

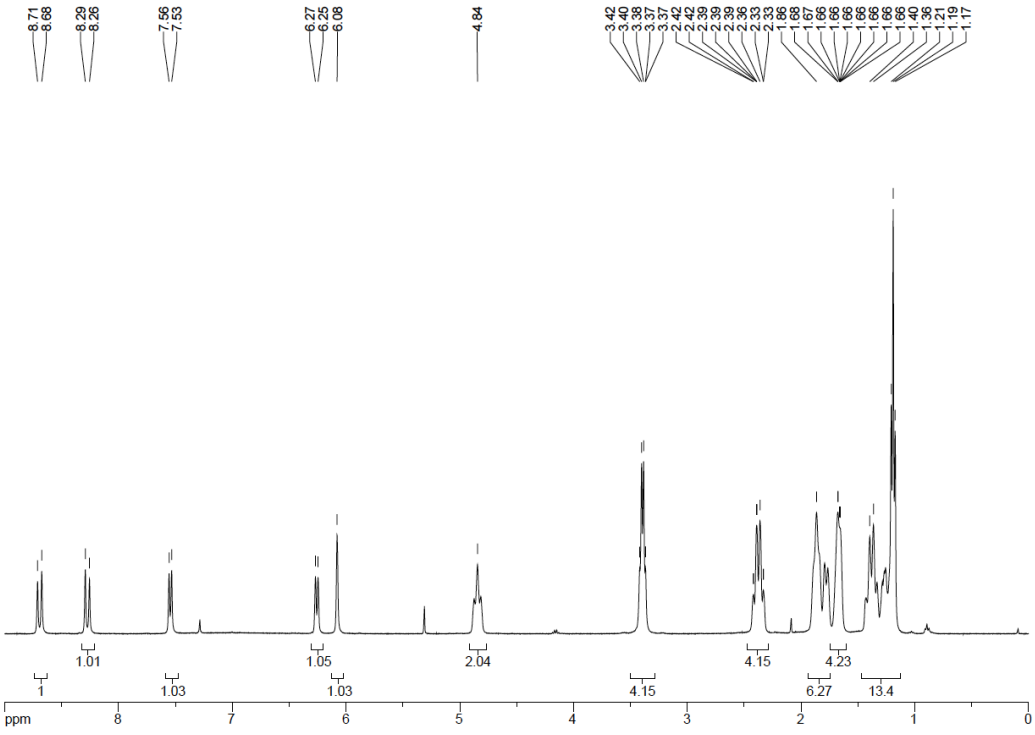

^{1}H NMR spectrum of DBS-OH

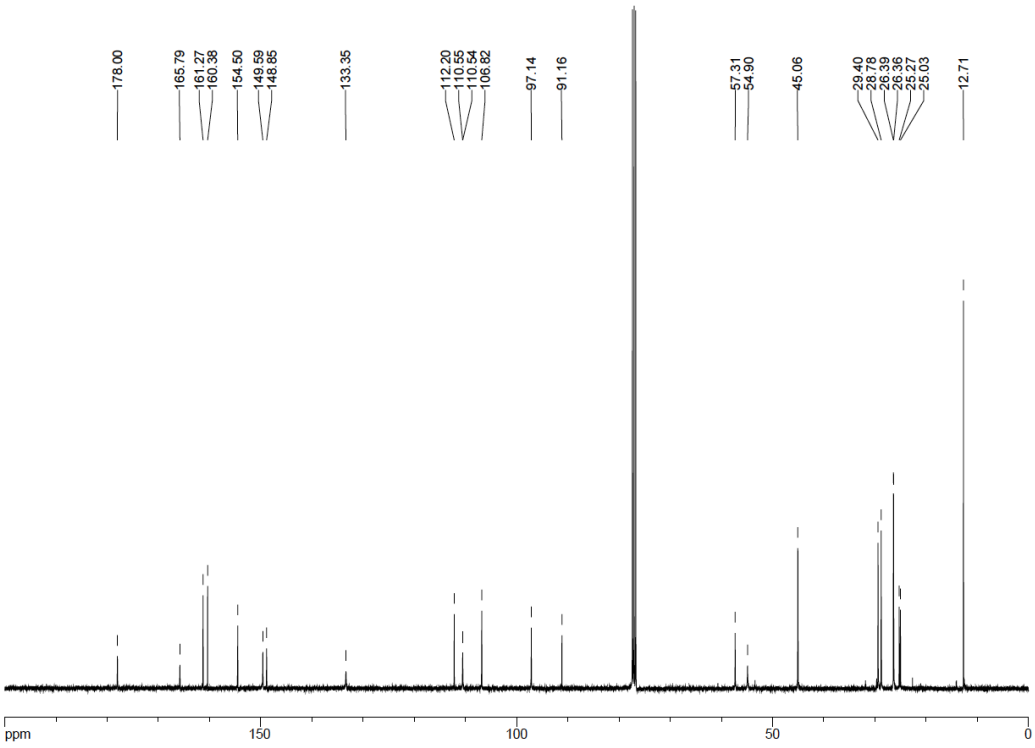

^{13}C NMR spectrum of DBS-OH

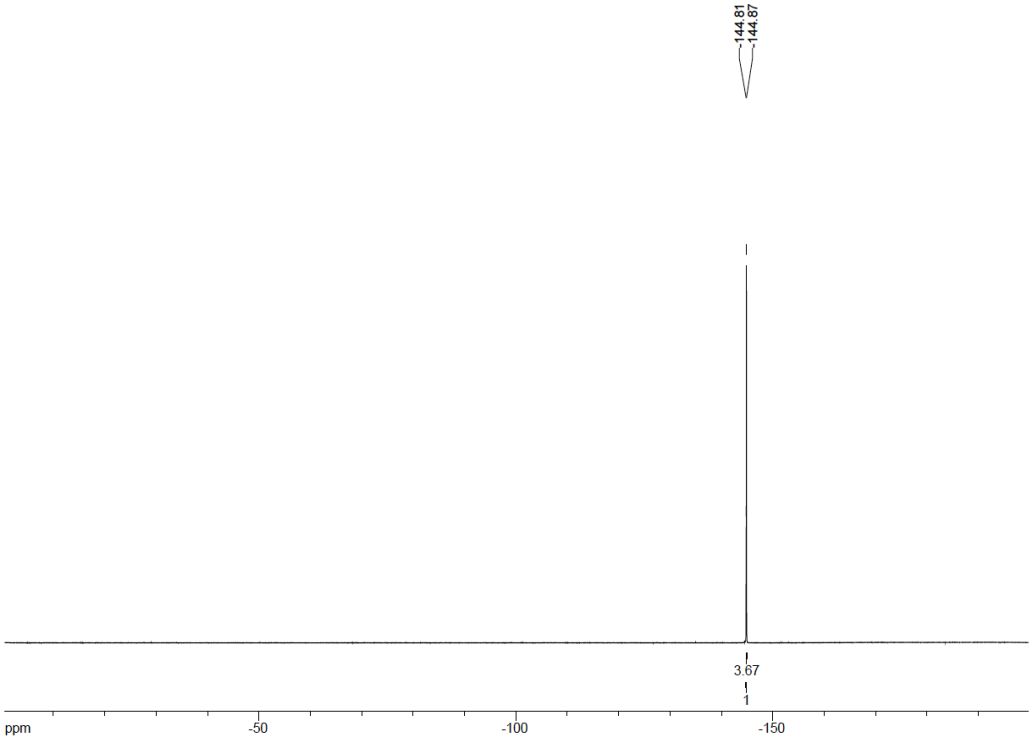

^{19}F NMR spectrum of DBS-OH

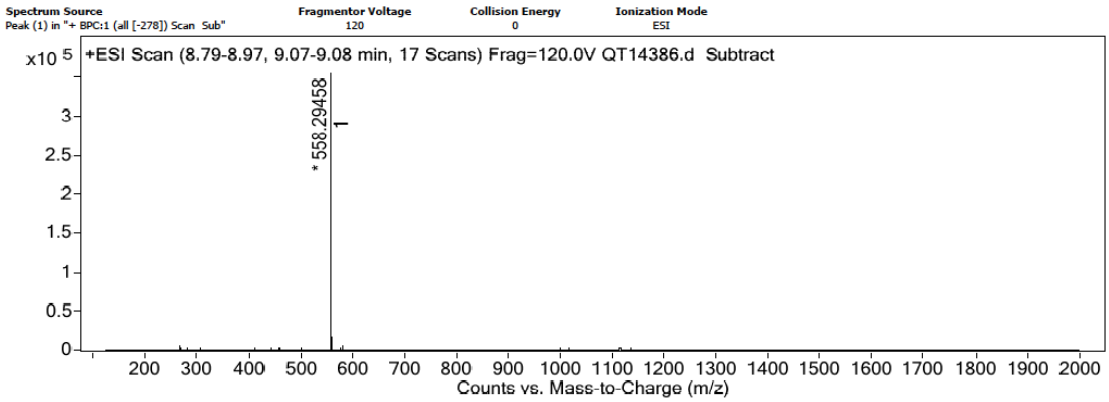

HRMS spectrum of DBS-OH

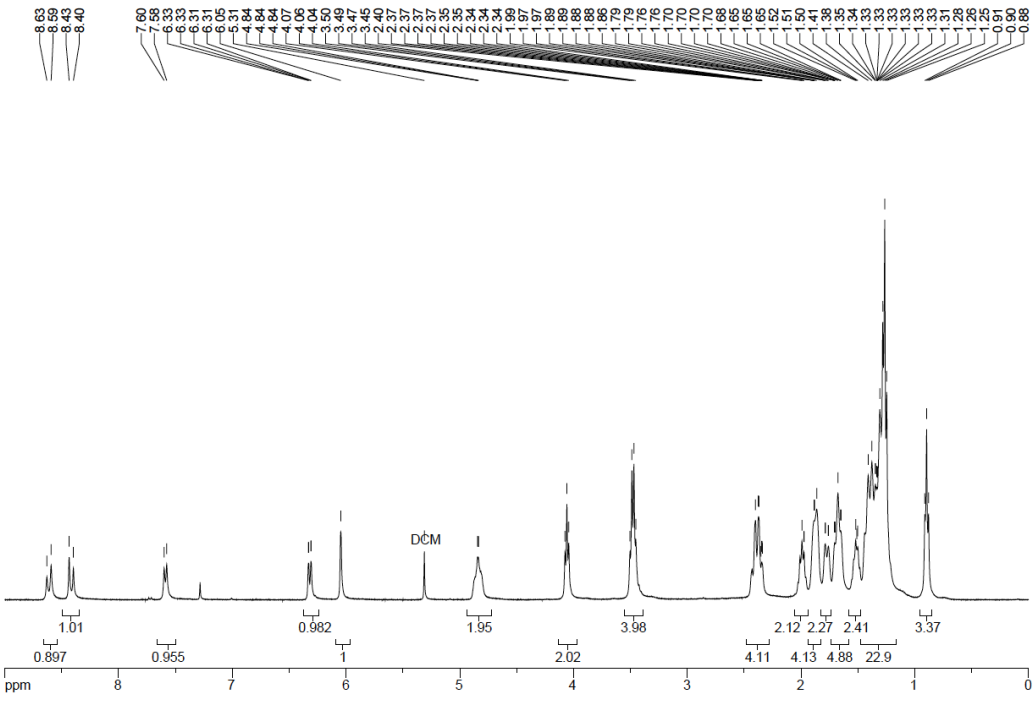

^{1}H NMR spectrum of DBS-C_8

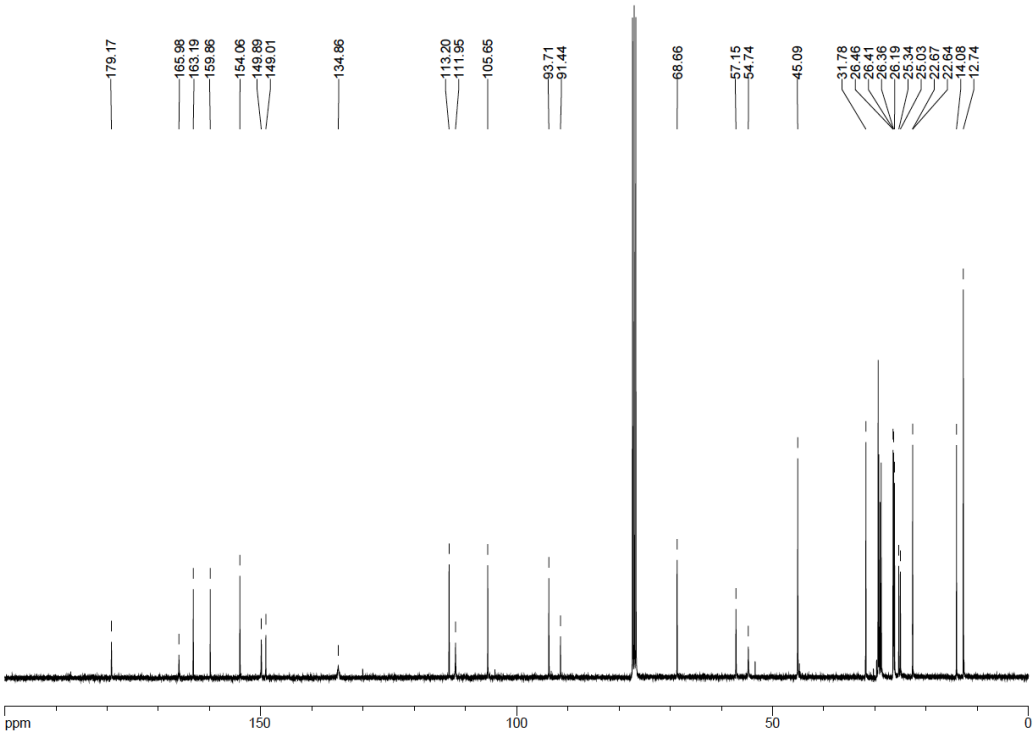

^{13}C NMR spectrum of DBS-C_8

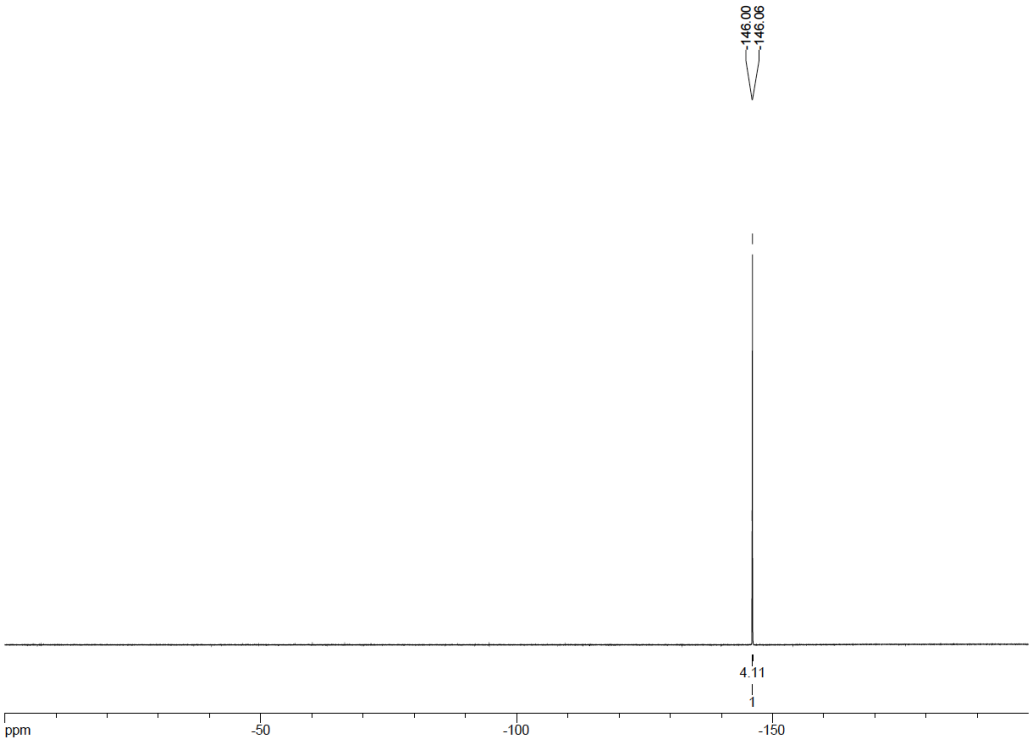

^{19}F NMR spectrum of DBS-C_8

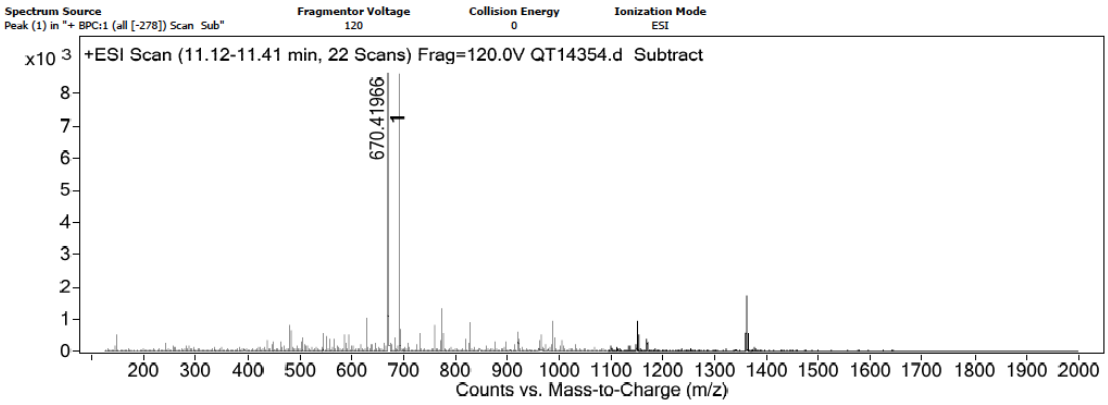

HRMS spectrum of DBS-C_8

Chapter 3

Further insights into release mechanisms from nano-emulsions

1 Introduction

Stability and drug release are both important properties for a therapeutic system, the former constitutes a prerequisite to clinical application, while the latter contributes to the rate and extent of active availability to the body. As a desirable delivery system, we would like to keep the stability during the storage, but release the loaded compounds completely and efficiently once it reaches the targeted point. The stability of drug-loaded nano-emulsion systems not just includes the time dependent physicochemical changes of the nanocarrier itself, but also refers to the integrity of the system and the location of the drug encapsulated, especially with the existence of biological molecules.

In this chapter, we focus on *Compositional ripening*, one of the destabilization manners commonly existed in emulsion systems but not that well studied due to the lack of a precise characterization method. In contrast to extensively studied phenomenon of Ostwald ripening, which is induced by a difference of size between two droplets and results in a change in particle size and distribution, the compositional ripening is induced by a difference of composition between two droplets and related to encapsulation stability, and the mass transfer from one droplet to another droplet can provide basic information of how the loaded compounds release to biological molecules.

Therefore, in this part, we established an aggregation-caused-quenching (ACQ)-based characterization method, by employing a hydrophobic modified Nile red (NR668), via the detection of quantum yield (QY) changes and the emission shifts (λ_{em}) of the mixture of dye-loaded and blank nano-emulsion systems, we studied how the formulation parameters (like the temperature and the dye concentration) impact the composition transfer between droplets. By investigating the dominant theory behind, we propose a new, simple and reliable characterization method for leakage from nano-emulsion systems.

This part of study has been published on *Journal of Colloid Interface and Science*, and the manuscript is enclosed as below.

Journal of Colloid and Interface Science 578 (2020) 768–778

Contents lists available at ScienceDirect

Journal of Colloid and Interface Science

journal homepage: www.elsevier.com/locate/jcis

Further insights into release mechanisms from nano-emulsions, assessed by a simple fluorescence-based method

Xinyue Wang [a], Mayeul Collot [b], Ziad Omran [c], Thierry F. Vandamme [a], Andrey Klymchenko [b], Nicolas Anton [a,*]

[a] Université de Strasbourg, CNRS, CAMB UMR 7199, F-67000 Strasbourg, France
[b] Université de Strasbourg, CNRS, LBP UMR 7021, F-67000 Strasbourg, France
[c] Department of Pharmaceutical Chemistry, College of Pharmacy, Umm AlQura University, 21955 Makkah, Kingdom of Saudi Arabia

GRAPHICAL ABSTRACT

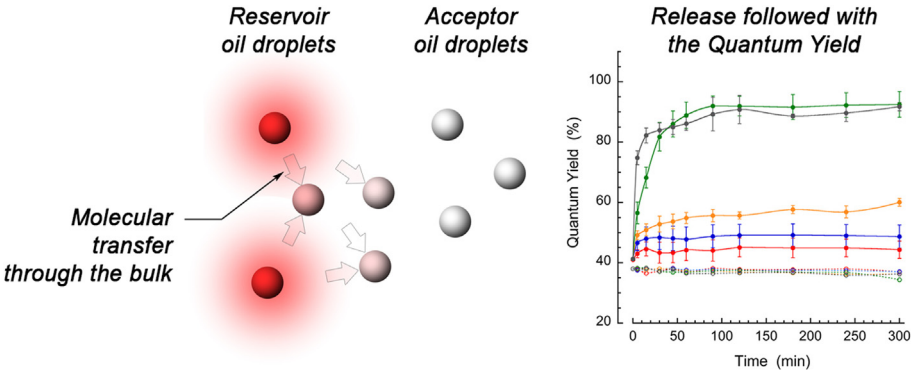

ARTICLE INFO

Article history:
Received 11 January 2020
Revised 4 June 2020
Accepted 7 June 2020
Available online 11 June 2020

ABSTRACT

Nano-emulsion consists of a dispersion of oil droplets sizing below 200 nm, in aqueous continuous phase, and generally stabilized by low-molecular-weight surfactants. These stable nano-carriers are able to encapsulate and transport lipophilic molecules poorly soluble in water. However, the question on the leakage and release mechanisms of an active pharmaceutical ingredient, from oil nano-droplets to an acceptor medium has not been clearly addressed. Herein, we developed a simple fluorescence approach based on self-quenching of lipophilic fluorophore-based on Nile Red (NR668) to monitor cargo transfer from lipid nano-droplets to the acceptor medium. In this method, the fluorophore release can be monitored by the increase in its fluorescence quantum yield and the blue shift in its emission spectrum. The studies of the release process allow emphasizing an important role of the bulk aqueous medium in controlling the droplet to droplet fluorophore transfer and the attained equilibrium. The developed methodology could be applied to monitor release of other lipophilic dyes and it could help to better understand the cargo release from nanocarriers.

1. Introduction

Nano-emulsion (NE) is nano-scaled biphasic dispersion of two immiscible liquids stabilized by amphiphilic molecules. Owing to the high surface area, good physico-chemical stability and

* Corresponding author.
E-mail address: nanton@unistra.fr (N. Anton).

https://doi.org/10.1016/j.jcis.2020.06.028
0021-9797/

non-toxicity, NEs are becoming a promising carrier in many application fields, such as the drug delivery, diagnostic, cosmetic, pesticide and food industries [1–5]. Compared to other types of nano-carriers, NEs have a real advantage to be a liquid reservoir for lipophilic active pharmaceutical ingredients (APIs), and thus, *a priori*, lipophilic fluorescent probes as models. This original feature has recently allowed the encapsulation of an outstanding number of fluorophores in a single droplet, making ultrabright nano-droplets enabling new possibilities such as single droplet tracking in cells or in small laboratory animals [6–8]. Although a large number of literature reports has shown that NE droplets themselves are intrinsically very stable, shown experimentally [9,10], and explained by the fact that droplets cannot enter in contact each other for steric reasons [11–13], the important question of the leakage of encapsulated APIs is still not clearly addressed.

Literature [6,14,15] showed that lipophilic APIs encapsulated in nano-emulsion can present very different release properties and stability, related to their chemical structure, lipophilicity, and affinities for the acceptor medium. In storage conditions, this leakage is generally negligible, as such lipophilic APIs are not soluble in aqueous medium. However, when the nano-carriers are brought into contact with an acceptor medium, such as serum, cells, biological tissues, or blank oil nano-droplets (oil droplets without API), a partitioning of the encapsulated molecules can occur, driving their leakage from the initial droplets to the acceptor reservoirs. Based on comparable phenomenon, at different concentration scales, this phenomenon can gather the so-called *compositional ripening* in which droplets of different compositions (like loaded and blank droplets) tend to equilibrate their concentration. In contrast to *Ostwald ripening*, *compositional ripening* has not been extensively investigated, likely due to the fact that its monitoring is not trivial on an experimental point of view [14,16]. However, understanding and controlling the stability of APIs encapsulation, up to the nano-carrier reaches the targeted site, is crucial, and it is not rare to see literature reports in which it is simply assumed, while a partial or complete leakage has already occurred.

In this study, we have considered that studying the stability of APIs encapsulated in nano-emulsion droplets can be extrapolated as a partial compositional ripening in which only APIs are able to release. The main mechanism at the origin of Ostwald and compositional ripening is the transfer of the dispersed phase through the continuous one, even if the oil is considered as *insoluble in* water, a very low solubility still allows such an inter-droplet molecular transfer. Indeed, in Ostwald ripening studies, the ripening rate was closely related to the solubility of the oil in water [17], and described by three possible mechanisms: a) a mechanism simply governed and limited by the molecular diffusion without any energy barrier [18,19]; b) the diffusion-limited mechanism can be helped by micelles formed in the aqueous bulk acting as the carriers of oil molecules [17,20]; c) the mass transfer between droplets is controlled by an energy barrier related to an interfacial resistance or to the bulk phase properties [21–24].

Recent works investigated the mass transfer between micrometric droplets focusing on complex emulsions like Pickering emulsions [25] and multiple emulsions [26], helped by developments of optical imaging with high-resolution cameras [27]. However, these experiments were conducted on macro or micro-scaled emulsions, but not adaptable on nano-emulsions reaching the limit of such experimental approach. Fluorescence techniques like Förster resonance energy transfer (FRET) are particularly suitable for studying molecular transfer of lipophilic cargo, where the dye leakage is identified as the loss of FRET between the donor and acceptor cargo molecules, however requiring a double fluorescence labelling of nano-emulsions [28]. Fluorescence correlation spectroscopy, a recently proposed strategy which uses a single fluorescent lipophilic cargo can detect the cargo transfer through changes in brightness and concentration of emissive species, as well as by monitoring standard deviation of fluorescence fluctuations [14], however, requires a dedicated fluorescence microscopy setup.

In this study, we propose a new approach to quantify and follow the stability, behavior and release of a model API (lipophilic fluoroprobe) based on the model of compositional ripening. The water-insoluble fluorescent NR668 (lipophilic Nile red derivative) encapsulated in nano-emulsion droplets, at a concentration high enough to induce a self-quenching of the probes due to molecular stacking, thus reducing its fluorescence quantum yield (QY). This phenomenon is reversible and decreases upon the dilution of the probes. Therefore, as their leakage towards an acceptor medium occurs, the QY increases and stabilizes when the concentration is equilibrated among all the donors and acceptors. The stability and robustness of this system will allow for clear identification of the conditions which can initiate the leakage, along with their respective impact. Herein, we propose a novel methodology to quantify the molecular leakage and kinetics from nano-carriers not subjected to Ostwald ripening, as well as give novel insights into the formulation parameters impacting on these phenomena.

2. Materials and methods

2.1. Materials

The oil phase, vitamin E acetate (VEA), was provided by Tokyo Chemical Industry (Tokyo, Japan). The surfactant, Kolliphor ELP®, was purchased from BASF (Ludwigshafen, Germany). NR668 is a homemade modified Nile red fluorophore on which was grafted lipophilic chains. Milli-Q water was obtained from a Millipore filtration system and used in all experiments.

2.2. Methods

2.2.1. Preparation of nano-emulsions and micelles

NR668-loaded NEs were prepared by spontaneous emulsification method. Firstly, NR668 was dissolved in VEA with different loadings of 1%, 2% and 3% in mass fraction. The dye-in-oil mixture was heated to 80 °C and mixed at 2,000 rpm with a thermomixer (Eppendorf), and vortexed (Bioblock Scientific) until the full solubilization and homogenization. After that, 200 mg of the mixture was centrifuged (Eppendorf) at 13,000 rpm for 1 min in case there could be some residues on the wall. Next, 200 mg Kolliphor ELP® was added, following the same mixing and vortex. With the addition of 600 µl Milli-Q water (at 80 °C) after mixing at room temperature for 10 min, the highly concentrated NEs were prepared. The choice of NR668 —a lipophilic version of Nile red (NR)— came from its greater stability against leakage compared to NR, when the water continuous phase is replaced by an acceptor medium like serum, cells or biological tissues like zebra-fish [6–8]. In addition, this choice was also driven by its fluorescent properties: when NR668 is dispersed in water there is almost no fluorescent signal, while it increases by 681-fold when solubilized in vitamin E acetate (structure and spectra of NR668 in water and VEA are reported in *Fig. S1 in Supplementary information* section).

Blank NEs were prepared with the same procedure above except that no dye was encapsulated. Blank micelles were prepared by mixing 200 mg Kolliphor ELP® with 800 mg Milli-Q water at the same condition.

Owing to the high percentage of surfactant used during the preparation of NEs, some micelles could be present in the bulk solution. In some cases, in order to eliminate the interference of micelles on droplet–droplet mass transfer and to compare the difference with or without micelles, dialysis was used to separate the large droplet from micelles. Regenerated cellulose dialysis

membrane with a molecular weight cut off 12–14 kDa was provided by Spectrumlabs® (Rancho Dominguez, USA). Dialysis was conducted for 48 h at room temperature with Milli-Q water as the outer phase, and it was changed every 24 h.

2.2.2. Mass transfer kinetics

Before the kinetic study, all the solutions were diluted with 100 times in ultrapure water to ensure a moderate transfer rate. The dilution and mixing process were shown in detail in Fig. 1. After that, the mixture was incubated in a thermomixer at the lowest speed (300 rpm) for 5 h. At each time point, 20 μl samples were taken, diluted again (10 times) and kept at 4 °C immediately to stop the transfer process. All the experiments were triplicated.

2.2.3. Absorption and fluorescence spectra

Absorption and fluorescence spectra were measured with a Cary 4000 HP ultraviolet–visible spectrophotometer (Agilent Technologies) and a Fluoromax-4 spectrofluorometer (Horiba Scientific), respectively. The absorption spectra were scanned from 400 nm to 700 nm, while the emission spectra were recorded from 490 nm to 700 nm with an excitation wavelength of 480 nm. All the solutions used for the spectral measurement were diluted to a dye concentration around 1 μM, where the absorption is below 0.1 for QY measurement.

When concentration of NR668 in nano-droplets is high, a phenomenon of *aggregation-caused quenching* (ACQ) occurs and results in a loss of the fluorescence efficiency. This consequences in decreasing the QY [30], and in a slight shift of the fluorescent spectra. Quantum yield is an important parameter to characterize fluorescent efficiency, which is defined as the ratio of the number of photons emitted to the number of photons absorbed:

$$\mathrm{QY} = \frac{OD_R \times I \times n^2}{OD \times I_R \times n_R^2} \times \mathrm{QY}_R \quad (1)$$

where QY represents quantum yield, OD is the optical density at excitation wavelength of 480 nm, I is the integrated fluorescence intensity, n is the refractive index of the solvent (*i.e.* water, n = 1.33). Quantum yield is a measure of the efficiency of photon emission and cannot reach more than 100%. It was measured using a reference, rhodamine 6G, defined with a QY of 95% in water [29]. Accordingly, the measured QY values were expressed in the scale range of 0 to 100%.

In our case, when dye molecules were transferred from a highly concentrated oily core to a blank emulsion droplet, the dilution will induce a reduction of the self-quenching and therefore an increase in the QY. By using this method based on the determination of the QY, the molecular mass transfer can be followed-up simply by fluorescence spectroscopy, and whatever the –micro or nano– scale of the dispersion. In addition, the fluorescence spectra can be shifted with the polarity of the acceptor medium (*i.e.* blank nano-droplets or micelles suspension), reflecting the transition before reaching the equilibrium.

2.2.4. Characterizing nanodroplet size distribution

After spectral measurement, size of all the samples were tested by Dynamic Light Scattering with the instrument Zetasizer® Nano ZS (Malvern). Both size distribution and polydispersity index (PDI) were recorded at a temperature of 25 °C. All the samples were performed in triplicate.

3. Results

As introduced in the previous sections, a new methodology was developed to study the encapsulation stability, the molecular leakage and transfer from the donor to the acceptor medium. This methodology involved following up the fluorescence QY and the shift of the emission maximum during the process.

3.1. Focus on the type of acceptor medium

In this section, the idea was to study the leakage of a model dye (NR668), comparing different lipid acceptor media for varied donor/acceptor ratios and temperatures. The donor nano-droplets were also varied as native and dialyzed NEs. The objective of this first screening is to understand general rules that can significantly impact the leakage mechanisms. Different types of acceptor media were studied: *(i)* native formulation of blank NEs, with an excess of surfactant in the bulk forming micelles (which is associated with the emulsification process); *(ii)* blank dialyzed NEs without micelles, where the excess of surfactant was removed by dialysis; *(iii)* acceptor media in form of only micelles; *(iv)* blank dialyzed NEs with micelles, where surfactant was reintroduced after dialysis at the same concentration as used in the formulation of blank nano-emulsion; and *(v)* control, where the acceptor medium is only distilled water. For all experiments, two donor/acceptor ratios were selected (1/1 and 1/2), and two temperatures were compared (60 °C and 80 °C). Similar experiments at room temperature do not show any release (these results will be shown and discussed below on the *focus on the effect of temperature* subsection). The presence of micelles in the continuous phase comes from the spontaneous emulsification process, involving a surfactant concentration largely higher than the CMC (0.02 wt% in water at 37 °C, given by the manufacturer BASF).

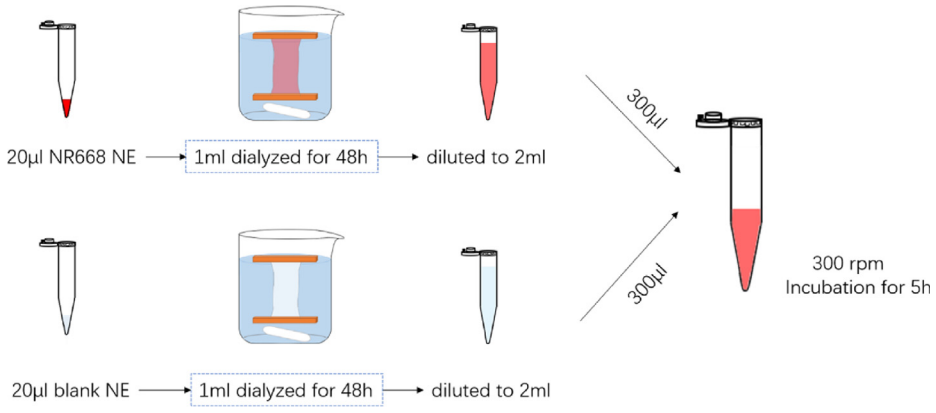

Fig. 1. Schematic representation of the preparation of loaded (top) and blank (bottom) droplets before mixing them together to study the dye molecular transfer between each other.

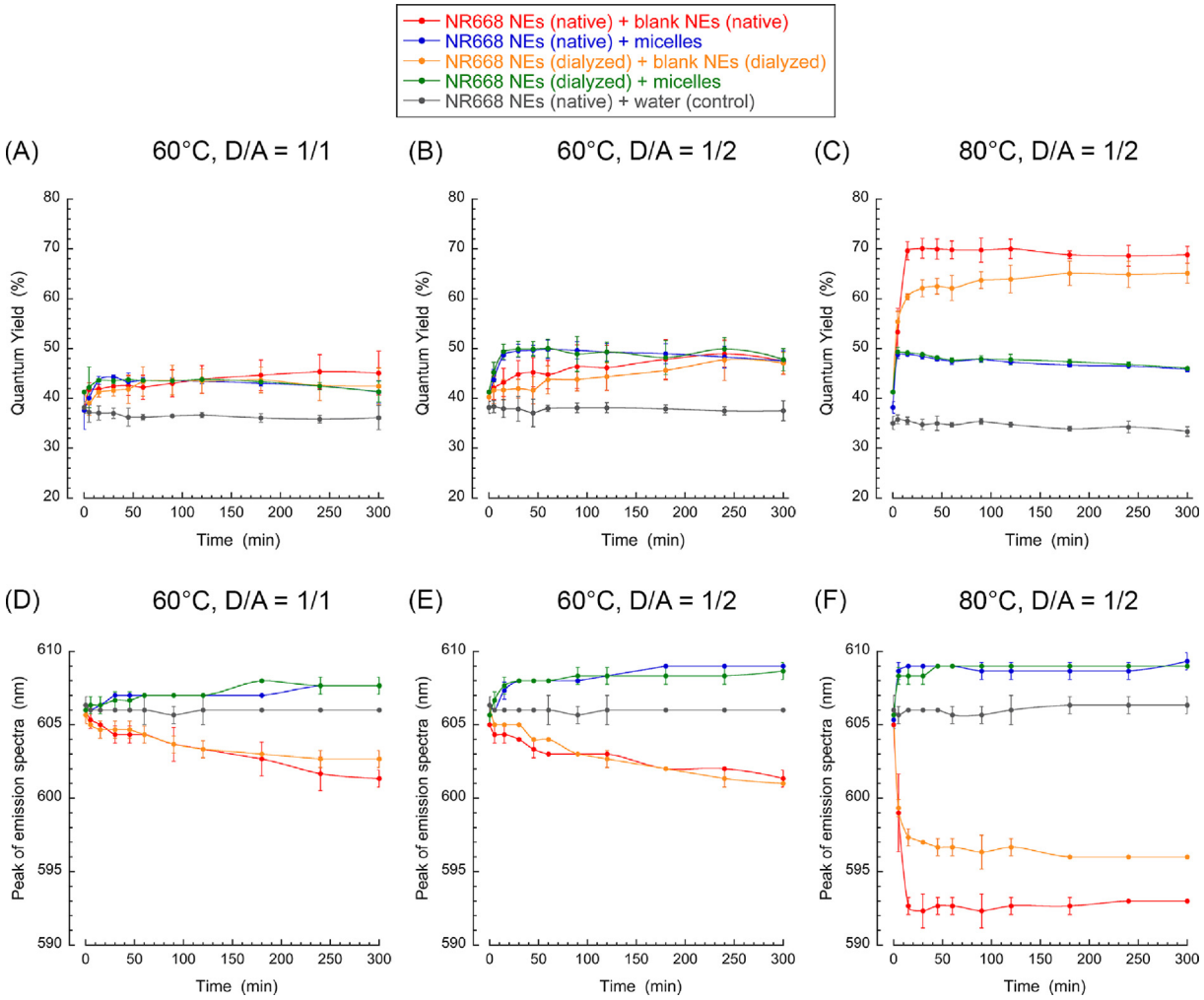

Fig. 2. Study of the quantum yield (A, B, C) and values of the peak of the fluorescence spectra (D, E, F) for different experimental conditions of temperature (60 °C and 80 °C) and donor-to-acceptor ratio (1/1 and 1/2), indicated in the figure, with the dye concentration in oil equal to 3 wt%.This experiment was conducted for different systems varying in the nature and composition of the acceptor (see details in the text). Data are mean values, and error bars indicate ± standard deviation, n = 3.

The results, reported in Fig. 2, show the evolution of QY and spectral shift (peak values are reported) over time. The corresponding spectra are reported in the *Supplementary information* section as Figs. S2, S3 and S4. The first remark concerns the control experiment with Milli-Q water (gray curves), where both QY and peak value remain constant all over the experiments whatever the temperatures are. In that case, we can consider that there is no acceptor medium, and these results confirm the stability of the NEs and also the conservation of the dye properties over the experiment. On the other hand, once acceptors are introduced in the medium, these stability profiles are significantly modified compared to the control with Milli-Q water.

The significant difference was obtained when comparing the acceptor medium composed of blank nano-emulsion droplets and micelles (without droplets), but indeed not in all the conditions studied. At first, in Fig. 2(A) (60 °C and D/A = 1/1), all acceptors induce a slight increase of the QY values at around 6% compared to the water control. This is confirmed by a slight shift of the peak values in Fig. 2(D), where the curves are shifted towards the blue (decreasing the wavelength) when the acceptor medium is a droplet suspension, and towards red (increasing the wavelength) when the acceptor medium is the micelles suspension. In contrast to variations of QY (related to dye self-quenching), the shift of the dye spectrum is due to its solvatochromism. This is thus revealing modifications of the polarity of the solubilizing medium [31]. A lose or increase of the acceptor polarity indicates that acceptor medium is the oil core of nano-droplets, or the micelles, respectively. Thus, the proper fact that polarity of acceptor medium has changed is also a confirmation of the leakage of the dyes.

The observed effects are enhanced when the concentration of acceptors is doubled, where for the same temperature, the QY values rapidly increases to stabilize around 10% compared to the water control, a value higher than for the previous conditions (Fig. 2(B), 60 °C and D/A = 1/2). Interestingly, when the acceptor medium is only made of micelles, the kinetics are faster compared to droplets, but the intensity values finally stabilize at the same above-mentioned value. As regards the spectral shifts (Fig. 2(E)), similar results to the previous conditions (Fig. 2(A), 60 °C and D/A = 1/1) were obtained, with blue and red shifts for droplets and micelles, respectively. Finally, raising the temperature up to 80 °C results in a clear additional effect on the QY (Fig. 2(C)) and spectral shift (Fig. 2(F)) for the acceptor medium made of droplets, reaching around 35% compared to the water control, while this temperature has no impact when the acceptor is only composed of micelles.

Interestingly, the NEs dialysis appears to have a significant inhibiting effect on the curves (difference between red and orange curves, native and dialyzed, respectively). This emphasize the

additional contribution of free micelles to the dye transfer. On the other hand, the leakage in free micelles for both dialyzed or native NEs (green and blue curves, respectively), appears strictly identical whatever the temperature and the D/A ratio.

Summarizing this first screening, the stability of the encapsulation of lipophilic molecules solubilized in the core of nano-emulsion droplets appears potentially modulated by environmental factors. In the presence of an acceptor medium containing a lipid phase (as blank nano-emulsions), the dye leakage will exclusively be spread into the lipid compartment even in the presence of micelles. In the presence of micelles without acceptor lipid phase, micelles will receive a part of the dye, rapidly saturated. The leakage into micelles is dependent of their concentration (D/A ratio) and independent of the modification of temperature. As a last remark, the kinetics of all these phenomena are quite fast and globally comparable, comprised within 30 min. This shows that the main factors that impacts on the equilibrium values are of thermodynamic origin rather than linked to kinetic phenomena. These first results are interesting since they disclose some important rules regarding the stability of nano-emulsions, which are in fact unstudied to date.

In order to confirm the relationship between color-shift and polarity of the acceptor observed above, NR668 was separately solubilized in all the systems studied: pure oil (VEA), solubilized in the core of NEs at different concentrations, in pure surfactant (Kolliphor® ELP), and in micellar suspension at different surfactant concentrations. The spectral properties (including values of the maximum of the peak, and the corresponding QYs, after an equilibration time of 300 min for all samples) are reported in Table 1. The spectra (normalized intensities are reported in the *Supplementary information* section as Fig. S5). These results confirm the color sensitivity of the NR668 towards the polarity of the solubilizing medium: solubilization in pure VEA appears as a low polarity limit with a peak around 550 nm, denoting a lipophilic environment. The emission spectra gradually shift to the red, first when formulated in nano-emulsions, and then in surfactants and in micelles, also affected by the concentration. These results confirm that the color shifts observed above in Fig. 2(D, E, F) are effectively due to the leakage of the dye to either droplets or micelles (blue or red shift, respectively). In addition, when comparing the NEs formulations with increasing dye concentrations, the spectra are red-shifted. This is attributed to a better interaction with the bulk through a part already leaked in micelles present in the bulk, and/or a redistribution of the dye from (apolar) oil core towards the (more polar) droplet interface [6]. The information provided by the QY values in different conditions presented in Table 1 shows an interesting difference between the pure oil and the NE, even at similar concentrations, which seems to indicate that a significant part cannot be considered as solubilized in pure oil, or even has leaked to interface or water. Pure surfactant seems to be a medium relatively neutral that allows a solubilization of the dye. Finally, considering the micelles, it shows the limitation in the solubility in such a medium, negligible when increasing the dye concentration above 1 wt%.

3.2. Focus on the donor-to-acceptor ratio (D/A)

As discussed above, the chosen D/A has an effect on the NEs leakage. In Fig. 2, only a slight effect was observed, and in this section, we propose to explore it in depth. The system herein studied was the dialyzed dye-loaded NEs (in order to eliminate the interfering effect from free micelles). The acceptor medium was blank NEs, also dialyzed in the same conditions. Five different D/A values were studied: 1/1, 1/2, 1/10, 1/20 and 1/50. All the experiments were conducted at 60 °C.

The results are presented in Fig. 3, showing, as a function of time, the QY (Fig. 3(A)), the shift of the fluorescent spectra (Fig. 3 (B)), and the nano-emulsion hydrodynamic diameter (Fig. 3(C)). The fluorescence emission spectra of different D/A ratio, against time, corresponding to Fig. 3(B) are reported in Fig. S6 in the *Supplementary information* section. In agreement with the observations above (Fig. 2), the QYs rose smoothly within a period of 100 min and then gradually stabilized within 300 min. It appears that the acceptor amounts significantly impacts on the kinetics and final stabilization values. The rise of QY values is accompanied by a significant blue-shift, indicating a migration towards the acceptor droplets. There are two reasons that explain this band shift in Fig. 3(B): first, at higher concentration, dye aggregation generally leads to formation of red shifted poorly emissive species; Second, at higher concentration, larger fraction of the dye is exposed to the interface of NEs. The latter increases environment polarity, which shifts to the red emission of NR668, because it is polarity sensitive probe [6]. Then, when the dye molecules are released into the acceptor oil droplets (*i.e.* diluted in oil), their local concentration in oil decreases and it results in a hypochromic shift (blue-shift) of the spectral peak. Thus, the higher the number of acceptor droplets, the higher the amount of dye molecules leaked. On the other hand, the droplet size was conserved all along the leakage monitoring (Fig. 3(C)), the PDI values being below 0.2 for all measurements; that is a direct evidence of the droplet stability, but also of the fact that such a dye leakage is not due to Ostwald ripening, but to compositional ripening. After 10 days (for NR668-loaded nano-emulsions, 3 wt% in oil), the QY value further increased by 6% and size increased by about 3 nm, coherent with the stabilization reported in the figures.

It follows therefrom that the encapsulated molecules leak towards the acceptor site up to an equilibrium state is reached. However, this final state does not mean that we have reached a similar concentration between donor and acceptor droplets, but rather that a metastable state is reached respective to the temperature of the sample. For example, in Fig. 2(B) and (C) for NEs, we can see that temperature impacts such an equilibrium. These saturating values with time indicate that an equilibrium is reached between donor and acceptor, and its variation with D/A ratio or temperature indicates that this equilibrium is modified. Thus, the concentrations of acceptor and donor, even at equilibrium, is not necessarily equalized. The dye leaking process seems to be limited by this final ratio between donor and acceptor, modulated by the temperature. To confirm this hypothesis, the effect of the temperature is specifically studied in the following section.

3.3. Focus on the effect of temperature

In the previous sections, temperature was shown to play an important role on the equilibrium between donor and acceptor. Herein we propose studying the leakage of NR668 from dialyzed

Table 1
Maximum emission wavelength and quantum yield of NR668 solubilized in different media for various composition.

	3% in Pure oil (VEA)	1% in NEs	2% in NEs	3% in NEs	3% in Pure Surfactant	1% in Micelles	2% in Micelles	3% in Micelles
λ_{em} (nm)	563	594	602	606	608	616	626	628
QY (%)	86	68	47	41	59	39	7	1

Note: All samples were diluted before measurement to finally have a similar dye concentration of 1 μM.

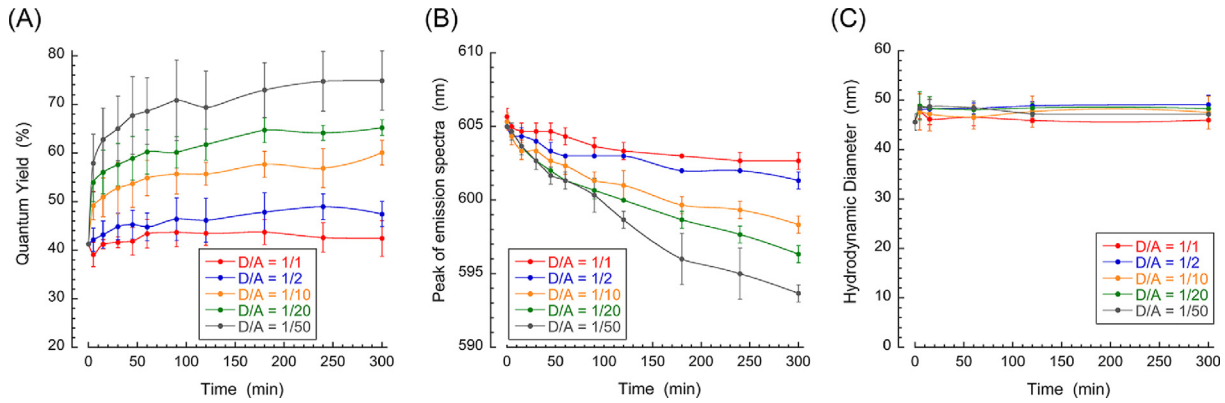

Fig. 3. Evolution of quantum yield, maximum emission wavelength and size changes over the time with different donor–acceptor ratios (at constant temperature equal to 60 °C, and dye concentration in oil equal to 3 wt%). Data are mean values, and error bars indicate ± standard deviation, n = 3.

loaded to dialyzed blank NEs (same conditions as in Fig. 3), but at different temperatures (25 °C, 37 °C, 60 °C, 70 °C and 80 °C) and for three different D/A ratios (1/1, 1/10 and 1/50).

As regards the QYs (Fig. 4(A, B, C)), the control in pure water remains very stable regardless of the temperature, up to 80 °C. This is an important point since it proves the temperature stability of the NEs and of the dyes, excluding that any partial release can occur in water. The increase in the temperature results in higher QY variations, and thus in higher dye release. Kinetics are stabilized after about 1 h-2 h. As seen above in Fig. 3, increasing the donor-to-acceptor ratio also impacts on the QY values and thus on the dye release extent. However, the relationship between temperature and release appears gradual for the lower donor-to-acceptor ratio (D/A = 1/1), but reveals unexpected and atypical behavior for D/A = 1/10 and 1/50. In these latter cases, the dye release seems to obey to energetical thresholds, driven by the temperature and in which the systems remain blocked before the threshold are reached. For instance, in the case of D/A = 1/10, QY gradually increases up to 60% for T = 60 °C, and jumps to 90% for 70 °C and 80 °C. This behavior is even more pronounced for 80 °C, since for 25 °C < T < 60 °C all the QY values are roughly similar around 60% and for T > 70 °C, they also jump up to 90%. As discussed in Fig. 2, all the kinetics are approximatively similar stabilized within 100 min whatever the D/A ratio and temperatures are, except the extreme point D/A = 50 or T > 70 °C for which the curves are stabilized within 15 to 25 min.

On the other hand, the peak shift of emission spectra, stabilized values and kinetics shown in Fig. 4(D, E, F), are consistent with the variation of QY discussed above (corresponding spectra are reported in the *Supplementary information* section as Figs. S7, S8 and S9). The blue-shift confirms the dye leakage towards blank nano-emulsions. In addition, the follow-up of the droplet size and polydispersity in these experiments (reported in Fig. S10 in the *Supplementary information* section) are stable, proving that Ostwald ripening does not interfere with the dye release.

To summarize, these results confirmed the important effect of the D/A ratio on the dye leaking, and also the strong impact of the temperature on the ability of the dye to leak. However, the D/A ratio is a limiting factor, for which a small value (*e.g.* D/A = 1) prevents the dye escape even at high temperature. It seems that the limitation is defined by the acceptance capability of acceptor droplets, where increasing the number of droplets increases the potential leakage. On the other hand, the fact that a temperature rise allows for increasing the release, with apparent thresholds (60 °C), seems to indicate that temperature favors the inter-droplet molecular transfer. This behavior is likely related to the modification of the partial solubility of NR668 in water with the change of temperature. Water solubility increased with a temperature rise due to the kinetics energy that favors their intermolecular interactions with the aqueous molecules and shifts their equilibrium towards the bulk. This phenomenon was also observed in the presence of micelles in the bulk water in addition to the acceptor droplets, for non-dialyzed NEs (Fig. 2 red curve), that resulted in increasing the dye solubility in water.

This impact of temperature on the bulk solubility is thus expected to be progressive, and this is why it cannot be attributed to the gap observed between 60 °C and 70 °C. A possible explanation of this sudden dye release at high temperature is a complete fusion and re-emulsification of the droplets, because of the fact that the *cloud point* (CP) of this nonionic surfactant, Kolliphor ELP® (therefore related to the phase inversion temperature) is equal to 72.5 °C (obtained for 1 wt% aqueous solution) [32]. It follows that for T > CP, as classically described in the phase inversion temperature, the whole oil phase merges, and when temperature is brought back to room temperature, it is re-emulsified, with the dye spread over all droplets, and thus involving the QY values reaching 100%.

3.4. Focus on the dye concentration in oil droplets

The study of the dye loading also remains an important parameter on which it is worthwhile to focus. In fact, the mechanisms disclosed seem to be limited by a ratio of concentrations between the donor and the acceptor NEs, defined by the accepting capability of acceptor droplets or the partial solubility of dye in the bulk water surrounding the loaded droplets. Herein, 1 wt%, 2 wt% and 3 wt% NR668-loaded NEs were prepared and used as donors, and two temperatures were compared, 60 °C and 70 °C.

Results are reported in Fig. 5, showing the QY and spectral peak shift variations (Fig. 5(A) and (B), respectively) as a function of time. Compared to all other results shown above, these ones present ΔQY and $\Delta\lambda_{em}$ (λ_{em} being the peak of emission spectra) as the difference between their measured values and the control in pure water. This representation is due to the fact that the baselines (values of the water control) is strongly impacted with the dye loading; thus, representing their relative variation allows a better comparison the dye leakages. Interestingly, in the case of these control experiments with pure water, increasing dye loading appears to have an important impact on both QY and spectral shift with any evolution over time (these raw data are reported in *Supplementary information* section, in Fig. S11). As a result, QYs are decreased (dashed lines in Fig. S11(A, B)), which could be likely attributed to the fact that self-quenching is accentuated with a concentration rise (*so-called* ACQ). The red-shift of the baselines

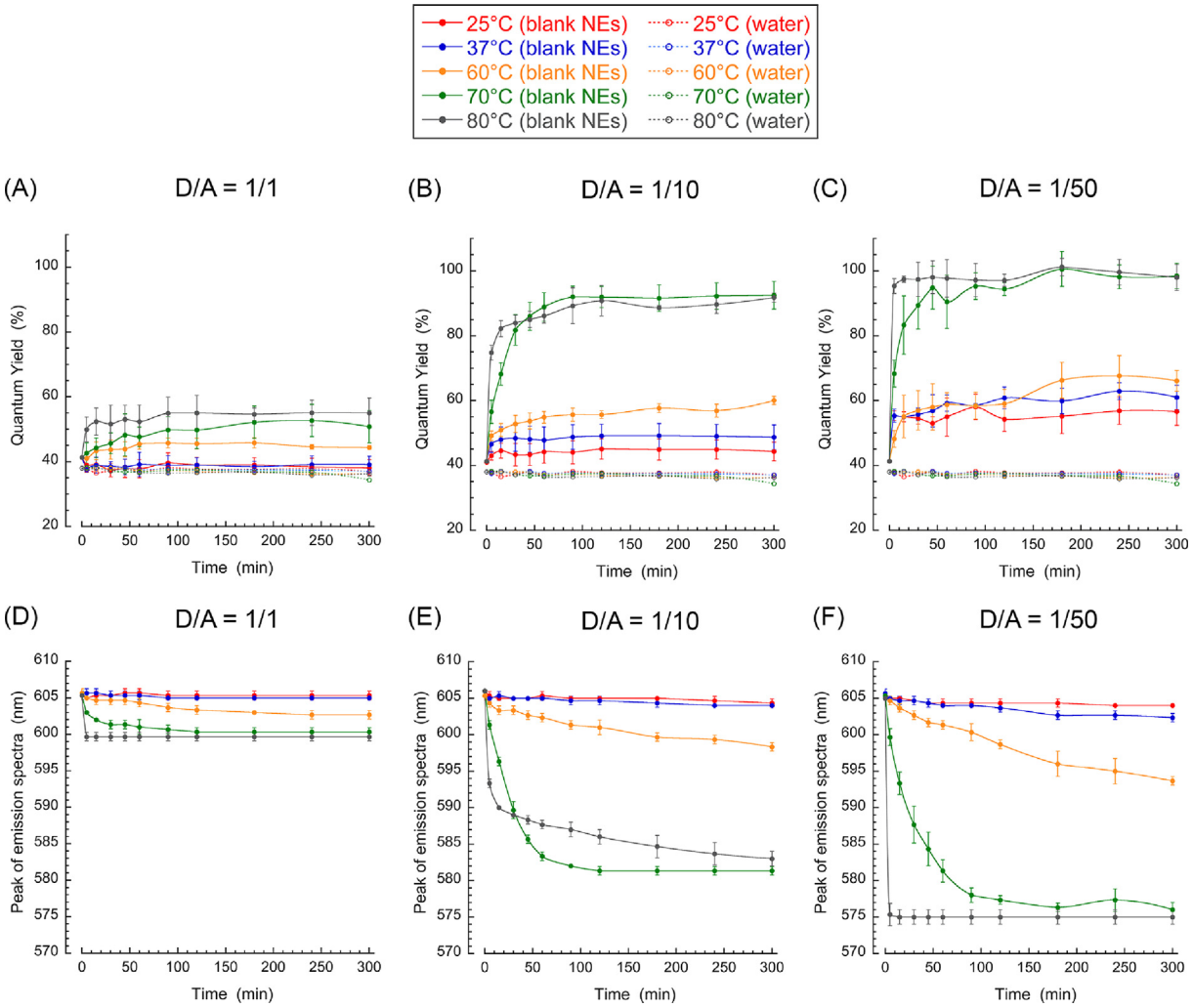

Fig. 4. Evolution of the quantum yield (A, B, C) and the maximum emission wavelength (D, E, F) over the time and for different temperature (varying from 25 °C to 80 °C) and for three donor-to-acceptor ratio (1/1, 1/10 and 1/50), indicated on the figure, and dye concentration in oil equal to 3 wt%. NR668 NEs (dialyzed) are brought in contact with blank NEs (dialyzed) or water (control). Data are mean values, and error bars indicate ± standard deviation, n = 3.

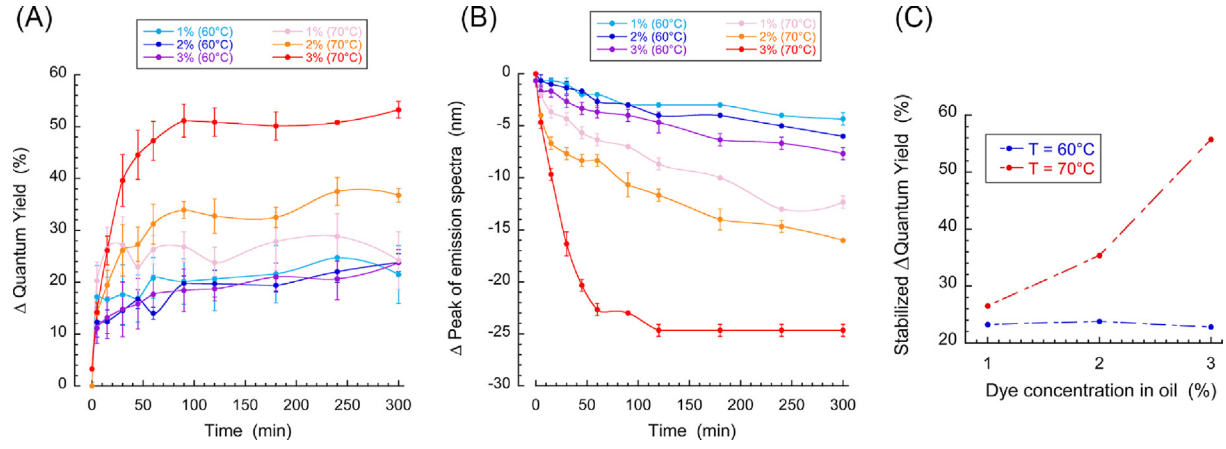

Fig. 5. Study of the quantum yield (A) and values of the peak of the fluorescence spectra (B) for different dye concentrations in the oil core of nano-emulsions, and for two different temperatures, 60 °C and 70 °C with a D/A of 1/10. Data are mean values, and error bars indicate ± standard deviation, n = 3. (C) Extrapolations of the data from (A) and (B), for $t \rightarrow \infty$ (shown in Fig. S12(E)).

is likely due to a higher dye localization to the droplets interface (excluding partition into micelles characterized by much higher environment polarity). Up to now, the dye concentrations were strictly identical for all experiments, and pure water as an acceptor media (as low as it is) was immediately saturated, and very stable, whatever the modifications of thermodynamic conditions.

In the presence of acceptor NEs, the spectroscopic changes depended on dye loading. As regards the values of ΔQYs (Fig. 5 (A)), the curves profiles gradually increase over time up to a plateau, indicating that the equilibrium of the dye redistribution was reached. Curves appear roughly similar for T = 60 °C (stabilizing around ΔQY = 20%), but appear significantly different when T = 70 °C, up to reaching ΔQY = 55% for 3 wt% of dye in oil. Summary of these difference between T = 60 °C and 70 °C are shown in Fig. 5(C), as the curves extrapolations for t →∞. When at 60 °C the dye release is independent of the dye concentration, it significantly increases with the reservoir concentration at 70 °C.

In the case of 60 °C, the amount of material released seems similar whatever the concentration of the reservoir droplets: capability of acceptor medium is clearly the limiting factor as it was the case for D/A ratio (observed in Figs. 2–4).

In contrast, at T = 70 °C, the amount of released materials growths with the dye concentration in the reservoirs. In line with the conclusion drawn in the last section above the gap between 60 °C and 70 °C (for T ≥ CP), this result is also consistent with a full repartition between all droplets, resulting in a re-emulsification of the droplets. The blue-shifts upon dye release followed similar trend as those for QY values (Fig. 5(B)).

In this last series of experiments, we confirm that two complementary effects seem to drive the release of lipophilic molecules from lipid nano-emulsions reservoirs. They are *(i)* established equilibrium of dye release depends on the number of acceptor sites; and *(ii)* the modulation of this equilibrium, likely induced by presence of micelles in the medium, by the temperature and/or the dye concentration in the reservoirs. We think that such a conclusion is an interesting advance in the understanding of the nano-emulsion stability, herein accessed by simple, powerful and reliable methodology based on recording QY and position of the emission maximum.

4. Discussion

By definition, nano-emulsions are very stable in suspension compared to micro-scale emulsions. Only a slow phenomenon involving the mass transfer of the oil through the bulk medium is able to destabilize nano-emulsions. Differences in size and in composition between droplets are the origin of such an inter-droplet molecular transfer, because they induce a different chemical potential of the solute in each environment. As discussed above, reaching equilibrium passes through the ripening of the droplet suspension, so-called Ostwald or compositional ripening (a difference in droplet size or in composition initiates the process, respectively) [21,33,34]. As a result, nano-emulsions are considered kinetically stable but thermodynamically unstable (as the energy barrier of destabilization is reached). Ostwald ripening is widely described, studied, and modelized [11], and, by changing the composition of the oil core, it can be modulated and inhibited. On the other hand, when composition of the droplets is not uniform, it is not the difference in size but the concentration gradient that governs the inter-droplet mass exchange, eventually inducing modification in the droplet size and composition up to equilibrium [35,36]. These both phenomena have been shown to be related to the mass transfer of the oil composing the droplets in the bulk, and to summarize, related to the droplet size distribution, composition distribution, solubility of the oil in the bulk, interfacial properties (*e.g.*, the barrier that inhibits the molecular transfer), but not related to the interfacial curvature (negligible effect on the difference in chemical potentials between two droplets) [11].

In addition to these considerations, Ostwald or compositional ripening implies that the own core of the droplets (oil phase), is released from one droplet, and able to migrate up to another droplet. On the other hand, nano-emulsions made with vegetable oils, natural products (like VEA as used in this study), or very viscous oil, present a much better stability upon Ostwald ripening, even over months [10]. This was attributed to their very low water solubility, and/or to the fact that they are often a mixture of several components, breaking the mass transfer (since increasing the difference in chemical potentials of the less soluble species remaining in the droplets).

In this study, droplets are made with a viscous and water-insoluble oil (VEA) solubilizing a dye (NR668), which is highly lipophilic water-insoluble analogue of Nile red. Thus, inter-droplet molecular transfer will only occur with the dye molecules (confirmed with the steadiness of the size over time when QY drastically changes, *e.g.*, in Fig. 3(C) or Fig. S10). Accordingly, this dye release can legitimately be considered as compositional ripening, as it is originated by the same phenomenon (difference in composition), and as it follows the same rules, diffusing through the bulk water from droplet to droplet. Even if the dye is considered insoluble in water, an extremely low solubility still exists [11].

As the solubility of the solute (dye) is the critical factor in the release mechanisms, in order to understand the different results on dye release shown throughout the present study, let us consider its general expression, often considered to explain Ostwald ripening [11]:

$$C(r) = c(\infty) \cdot \exp\left(\frac{2\gamma V_m}{rRT}\right) \quad (2)$$

where $C(r)$ is the solubility of the droplet material (oil or dye) in a particle of radius r, $c(\infty)$ is the solubility in the bulk phase, γ is the surface tension, and V_m is the molar volume of the mobile compound. The expression $(2\gamma V_m/rRT)$ is assimilated to a characteristic length of the penetration of the solute in the bulk, around 1 nm for oil phase, but can be increased in relation of the affinities between encapsulated molecules and bulk phase.

The release experiments can be schematically represented in Fig. 6 (A), showing the donor and acceptor medium and the partial solubility of the dye in the bulk and its extent and limitations. Fig. 6(B) shows the profile of solute concentrations in the reservoir droplets, through the interface (where interface does not induce resistance to mass transfer, as it is the case in nano-emulsions), and then, through the bulk where concentration decreases up to stabilize (as discussed in [35,36]). However, in the presence of acceptor droplets, NR668 is again solubilized in their oil core, and fluorescence rose because of the change in solubilizing medium. As a result, the global amount of dye molecules in the total oil (donor plus acceptor) appears diluted, thus leading to an increase of the QY. In fact, even if the oil phase is still the dispersed phase in the form of droplets, the release from donors to acceptors through the water results in the fact that dye is diluted in the oil phase, considered as a whole. This explains the effect of the D/A ratio revealed above in Figs. 2–4, when increasing the number of acceptors sites, the dilution increased. However, this also means that the concentration in the acceptor droplets is limited and different from the reservoir. This indicates that donor and acceptor droplets are not in equilibrium with each other, but rather that acceptor droplets are in equilibrium with the bulk water.

In addition, analyzing Eq. (2) provides interesting considerations that we can correlate with our experimental results: *(i)* increasing the temperature has an impact on the value of $c(\infty)$ (Fig. 6(C), effect of temperature) and thus on the concentration of the acceptor droplets (correlating with the representation of Fig. 6(B)), as seen in Fig. 4; and *(ii)* increasing the concentration inside the droplets increases the characteristic length of penetration in the bulk (Fig. 6(D), thus in line with the results of Fig. 5). It appears eventually that this theoretical representation of the

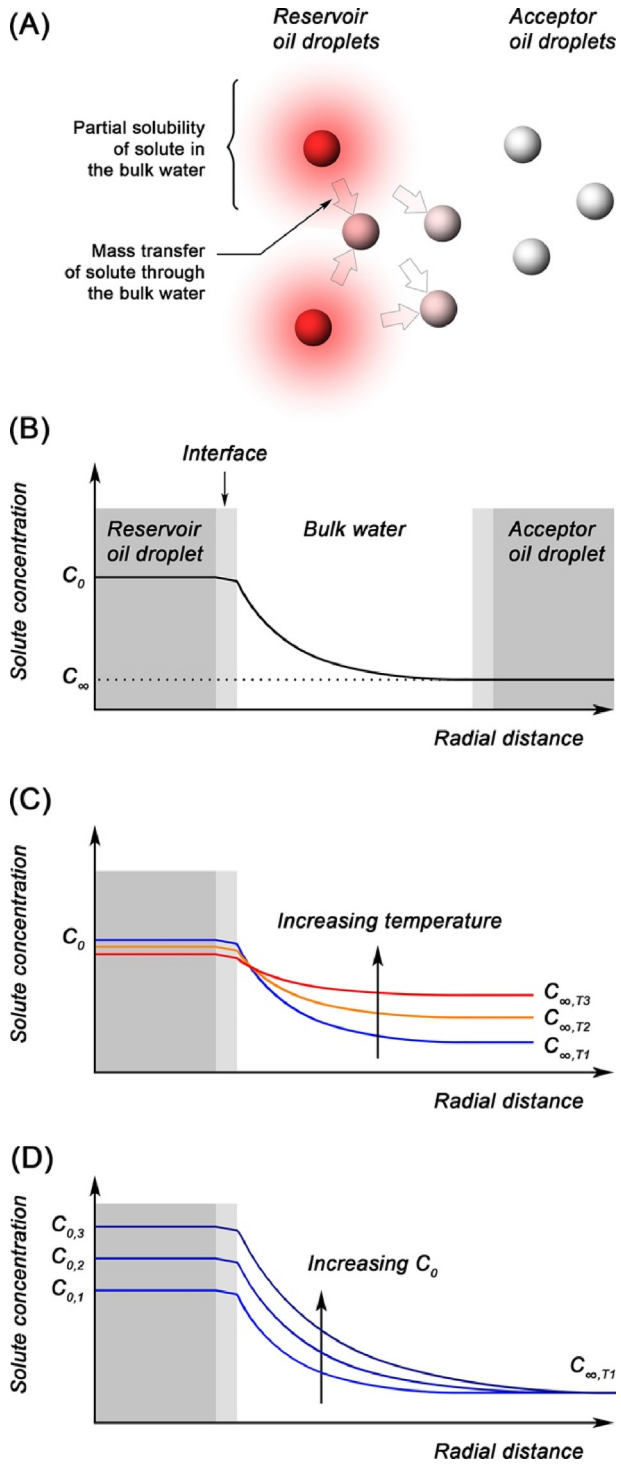

Fig. 6. (A) Schematic representation of the molecular transfer mechanisms of dye between loaded (red) and blank (gray) nano-emulsion droplets. (B) Representation of the molecular concentration through the droplet interface and the bulk surrounding water, up to the acceptor droplet. (C) Effect of the temperature and (D) of dye concentration on this schematic profile.

dye transfer through its solubility in the bulk arises in direct correlation with the experimental results, therefore confirmed. These two factors, temperature and dye loading, significantly impact on the concentration of the dye in the bulk, thus impacting the release from donor droplets, and finally the loading of acceptor droplets.

Interestingly, when reporting the stabilized values of QYs plotted against the increase of acceptor droplets (acceptor to donor ratio), *e.g.*, in Fig. 7(A) obtained from Fig. 3(A) at $t \rightarrow \infty$, it appears that the evolution of the values follows a rising monoexponential trend that stabilized for the higher possible number of acceptors (for D/A $\rightarrow \infty$), about 75.2%. Under this point of view, Fig. 7(B) shows the impact of temperature on the full release capabilities of the loaded/empty droplet system. This representation more clearly represents the release behavior for the temperatures below 60 °C, mainly considered as linked to the modification of the solubility in the bulk (unlike for T $\geq$ 70 °C for which another mechanism seems involved). Interestingly, in contrast to the conclusions drawn for Ostwald ripening that can link the ripening rates to the temperature with an Arrhenius law [37] (thus, relating kinetics of mass transfer to the temperature), in this case, the transfer seems to reach an equilibrium after a stabilization within 300 min, with a value depending on the temperature. Thus, the molecular transfer of NR668 can reach a multitude of equilibriums related to the thermodynamic conditions and nature of acceptor. This is why these parameters do not have impact on the kinetics, making difficult to correlate our observations with a classical model.

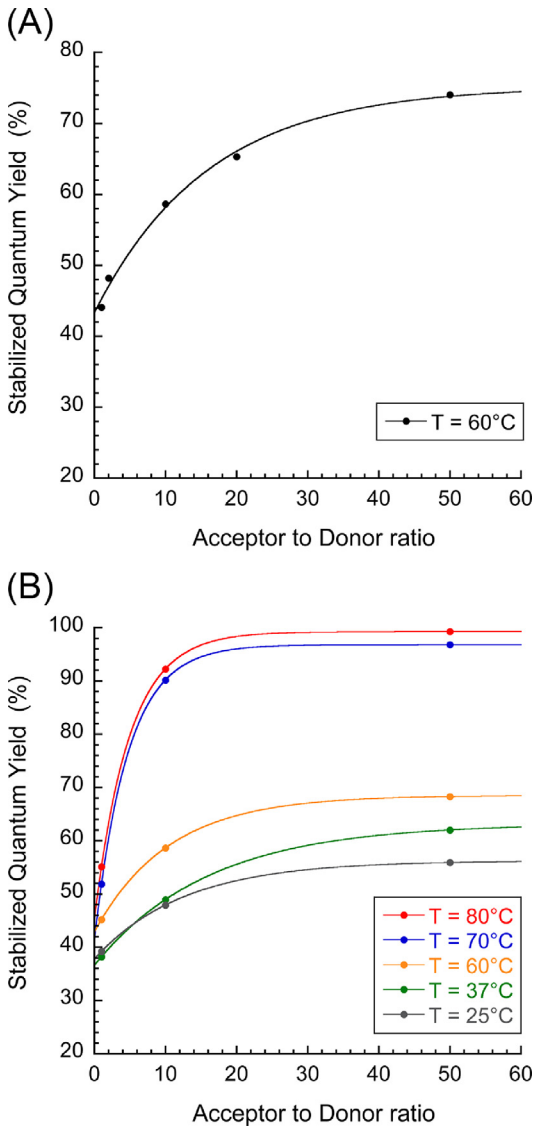

Fig. 7. Synthesis of the trends obtained from extrapolation experimental data according to simple mono-exponential fits. (A) Data from Fig. 3 (extrapolations for t$\rightarrow \infty$ shown in Fig. S12(A)). (B) Data from Fig. 4 (extrapolations for t$\rightarrow \infty$ shown in Fig. S12(B), (C) and (D)).

5. Conclusion

This study investigated the release mechanisms of a model fluorescent dye, from nano-emulsion droplets to acceptor media. Donor was nano-emulsions loaded with Nile red derivative NR668 and acceptor systems were pure water, micelles, or blank nano-emulsion droplets. Based on the aggregation-caused quenching (ACQ) that inhibits the dye brightness at high concentrations, our hypotheses were that, when released, the dyes will be diluted in the whole oil phase, improving their optical properties and thus the value of quantum yield of the sample. Thanks to this phenomenon, we proposed to elucidate the mechanisms driving the dye release from nano-emulsion droplets, and the potential impacts of the different formulation parameter on this release. Solvatochromism of NR668 revealed the modification of its solubilizing medium, as an additional indication of its release from donor nano-droplets. Innovation mainly lies in the combination of the simplicity of the experimental approach and its application to follow the inter-droplets interactions, which has never been reported to date. As key findings of this study, we showed that molecular transfer of encapsulated molecules follows the main rules of Ostwald or compositional ripening, and is mainly linked to the solubility of the solute in the bulk surrounding water. Acceptors solubilized a part of the dye, but at the bulk concentration, thus diluting the dye if we take the oil phase as a whole. This behavior disclosed that concentrations are not equalized between donors and acceptor droplets, but rather between bulk and acceptor droplets. Then, the modification of factors linked to the dye saturating concentration in the bulk (temperature or dye concentration) has a direct impact on the release from donor droplets towards water, and thus on the loading of acceptor droplets. To conclude, this study investigates the mechanisms governing the molecular transfer from nano-emulsion droplets, a theory based on the classical ripening but applied to a minor compound in the droplet composition. These results were often supposed [6–8,11,12,21] but, to the extent of our knowledge, never precisely studied to disclose the effective mechanisms in molecular transfer. Outlooks of such a work, beyond using blank nano-droplets as acceptor, would be applying this experimental approach to the study of dye release to living systems, biological membrane, cells or tissues.

CRediT authorship contribution statement

Xinyue Wang: Investigation, Conceptualization, Methodology, Writing - original draft. **Mayeul Collot:** Investigation, Conceptualization, Methodology, Writing - review & editing. **Ziad Omran:** Conceptualization, Validation, Writing - review & editing. **Thierry F. Vandamme:** Resources, Validation, Writing - review & editing. **Andrey Klymchenko:** Resources, Validation, Writing - review & editing. **Nicolas Anton:** Investigation, Conceptualization, Validation, Writing - original draft, Supervision.

Declaration of Competing Interest

The authors declare that they have no known competing financial interests or personal relationships that could have appeared to influence the work reported in this paper.

Acknowledgments

The authors would like to acknowledge the financial support provided by King Abdulaziz City for Science and Technology (KACST), Grant no. 14-MED1472-10, as well the support from ERC Consolidator grant BrightSens 648528 and ANR BrightRiboProbes (ANR-16-CE11-0010), and finally the China Scholarship Council Ph.D. fellowship (CSC No. 201706240033) for the funding of Xinyue Wang.

Appendix A. Supplementary data

Supplementary data to this article can be found online at https://doi.org/10.1016/j.jcis.2020.06.028.

References

[1] V.K. Rai, N. Mishra, K.S. Yadav, N.P. Yadav, Nanoemulsion as pharmaceutical carrier for dermal and transdermal drug delivery: formulation development, stability issues, basic considerations and applications, J. Control Release 270 (2018) 203–225.
[2] D. Pan, G.M. Lanza, S.A. Wickline, S.D. Caruthers, Nanomedicine: perspective and promises with ligand-directed molecular imaging, Eur. J. Radiol. 70 (2) (2009) 274–285.
[3] M.N. Yukuyama, D.D. Ghisleni, T.J. Pinto, N.A. Bou-Chacra, Nanoemulsion: process selection and application in cosmetics–a review, Int. J. Cosmet. Sci. 38 (1) (2016) 13–24.
[4] M. Kah, T. Hofmann, Nanopesticide research: current trends and future priorities, Environ. Int. 63 (2014) 224–235.
[5] Ş. Yalçınöz, E. Erçelebi, Potential applications of nano-emulsions in the food systems: an update, Mater. Res. Express 5 (6) (2018) 062001.
[6] A.S. Klymchenko, E. Roger, N. Anton, H. Anton, I. Shulov, J. Vermot, Y. Mely, T.F. Vandamme, Highly lipophilic fluorescent dyes in nano-emulsions: towards bright non-leaking nano-droplets, RSC Adv. 2 (31) (2012) 11876–11886.
[7] V.N. Kilin, H. Anton, N. Anton, E. Steed, J. Vermot, T.F. Vandamme, Y. Mely, A.S. Klymchenko, Counterion-enhanced cyanine dye loading into lipid nano-droplets for single-particle tracking in zebrafish, Biomaterials 35 (18) (2014) 4950–4957.
[8] X. Wang, N. Anton, P. Ashokkumar, H. Anton, T.K. Fam, T. Vandamme, A.S. Klymchenko, M. Collot, Optimizing the fluorescence properties of nanoemulsions for single particle tracking in live cells, ACS Appl. Mater. Interfaces 11 (14) (2019) 13079–13090.
[9] M. Maruno, P.A.d. Rocha-Filho, O/W Nanoemulsion After 15 Years of Preparation: A Suitable Vehicle for Pharmaceutical and Cosmetic Applications, J. Dispersion Sci. Technol. 31 (1) (2009) 17–22.
[10] F. Hallouard, N. Anton, G. Zuber, P. Choquet, X. Li, Y. Arntz, G. Aubertin, A. Constantinesco, T.F. Vandamme, Radiopaque iodinated nano-emulsions for preclinical X-ray imaging, RSC Adv. 1 (5) (2011) 792.
[11] T. Tadros, P. Izquierdo, J. Esquena, C. Solans, Formation and stability of nano-emulsions, Adv. Colloid Interface Sci. 108–109 (2004) 303–318.
[12] N. Anton, T.F. Vandamme, The universality of low-energy nano-emulsification, Int. J. Pharm. 377 (1–2) (2009) 142–147.
[13] N. Anton, T.F. Vandamme, Nano-emulsions and micro-emulsions: clarifications of the critical differences, Pharm. Res. 28 (5) (2011) 978–985.
[14] R. Bouchaala, L. Richert, N. Anton, T.F. Vandamme, S. Djabi, Y. Mely, A.S. Klymchenko, Quantifying release from lipid nanocarriers by fluorescence correlation spectroscopy, ACS Omega 3 (10) (2018) 14333–14340.
[15] C. Simonsson, G. Bastiat, M. Pitorre, A.S. Klymchenko, J. Béjaud, Y. Mély, J.-P. Benoit, Inter-nanocarrier and nanocarrier-to-cell transfer assays demonstrate the risk of an immediate unloading of dye from labeled lipid nanocapsules, Eur. J. Pharm. Biopharm. 98 (2016) 47–56.
[16] K.L. Markus Antonietti, Polyreactions in miniemulsions, Prog. Polym. Sci. 27 (4) (2002) 689–757.
[17] B.P. Binks, J.H. Clint, P.D. Fletcher, S. Rippon, Kinetics of swelling of oil-in-water emulsions, Langmuir 14 (1998) 5402–5411.
[18] W.I. Higuchi, M. Jagdish, Physical degradation of emulsions via the molecular diffusion route and the possible prevention thereof, J. Pharm. Sci. (1961) 459–466.
[19] I.M. Lifshitz, V.V. Slyozov, The kinetics of precipitation from supersaturated solid solutions, J. Phys. Chem. Solids 19 (1–2) (1961) 35–50.
[20] D.J. McClements, S.R. Dungan, J.B. German, J.E. Kinsella, oil exchange between oil-in-water emulsion droplets stabilised with a non-ionic surfactant, Food Hydrocolloids 6 (5) (1992) 415–422.
[21] A.A. Peña, C.A. Miller, Kinetics of compositional ripening in emulsions stabilized with nonionic surfactants, J. Colloid Interface Sci. 244 (1) (2001) 154–163.
[22] A.-H. Ghanem, W.I. Higuchi, A.P. Simonelli, Interfacial barriers in interphase transport: retardation of the transport of diethylphthalate across the hexadecane- water interface by an adsorbed gelatin film, J. Pharm. Sci. 58 (2) (1969) 165–174.
[23] A.-H. Ghanem, W.I. Higuchi, A.P. Simonelli, Interfacial barriers in interphase transport II: influence of additives upon the transport of diethylphthalate across the hexadecane-gelatin-water interface, J. Pharm. Sci. 59 (2) (1970) 232–237.
[24] A.-H. Ghanem, W.I. Higuchi, A.P. Simonelli, Interfacial barriers in interphase transport III: Transport of cholesterol and other organic solutes into hexadecane—gelatin—water matrices, J. Pharm. Sci. 59 (5) (1970) 659–665.
[25] B.P. Binks, P.D. Fletcher, B.L. Holt, O. Kuc, P. Beaussoubre, K. Wong, Compositional ripening of particle- and surfactant-stabilised emulsions: a comparison, Phys. Chem. Chem. Phys. 12 (9) (2010) 2219–2226.

[26] M.F. Haase, J. Brujic, Tailoring of high-order multiple emulsions by the liquid-liquid phase separation of ternary mixtures, Angew. Chem. Int. Ed. Engl. 53 (44) (2014) 11793–11797.
[27] J. Otero, S. Meeker, P.S. Clegg, Compositional ripening of particle-stabilized drops in a three-liquid system, Soft. Matter. 14 (19) (2018) 3783–3790.
[28] R. Bouchaala, L. Mercier, B. Andreiuk, Y. Mély, T. Vandamme, N. Anton, J.G. Goetz, A.S. Klymchenko, Integrity of lipid nanocarriers in bloodstream and tumor quantified by near-infrared ratiometric FRET imaging in living mice, J. Control. Release 236 (2016) 57–67.
[29] D. Magde, G.E. Rojas, P.G. Seybold, Solvent dependence of the fluorescence lifetimes of xanthene dyes, Photochem. Photobiol. 70 (5) (1999) 737–744.
[30] A. Reisch, A.S. Klymchenko, Fluorescent polymer nanoparticles based on dyes: seeking brighter tools for bioimaging, Small 12 (15) (2016) 1968–1992.
[31] A.S. Klymchenko, Solvatochromic and fluorogenic dyes as environment-sensitive probes: design and biological applications, Acc. Chem. Res. 50 (2) (2017) 366–375.
[32] R.C. Rowe, P.J. Sheskey, S.C. Owen, Handbook of pharmaceutical excipients, Pharmaceutical press London, 2006.
[33] P.C. Hiemenz, P.C. Hiemenz, Principles of colloid and surface chemistry, M. Dekker, New York, 1986.
[34] A.S. Kabalnov, E.D. Shchukin, Ostwald ripening theory: applications to fluorocarbon emulsion stability, Adv. Colloid Interface Sci. 38 (1992) 69–97.
[35] D.J. McClements, S.R. Dungan, Factors that affect the rate of oil exchange between oil-in-water emulsion droplets stabilized by a nonionic surfactant: droplet size, surfactant concentration, and ionic strength, J. Phys. Chem. 97 (28) (1993) 7304–7308.
[36] J. Weiss, D.J. McClements, Mass transport phenomena in oil-in-water emulsions containing surfactant micelles: solubilization, Langmuir 16 (14) (2000) 5879–5883.
[37] T. Delmas, H. Piraux, A.-C. Couffin, I. Texier, F. Vinet, P. Poulin, M.E. Cates, J. Bibette, How to prepare and stabilize very small nanoemulsions, Langmuir 27 (5) (2011) 1683–1692.

3 Supplementary information

Further insights into release mechanisms from nano-emulsions, assessed by a simple fluorescence-based method

Xinyue Wang,[a] Mayeul Collot,[b] Ziad Omran,[c] Thierry F. Vandamme,[a] Andrey Klymchenko,[b] Nicolas Anton [a,*]

[a] *Université de Strasbourg, CNRS, CAMB UMR 7199, F-67000 Strasbourg, France*

[b] *Université de Strasbourg, CNRS, LBP UMR 7021, F-67000 Strasbourg, France*

[c] *Department of Pharmaceutical Chemistry, College of Pharmacy, Umm AlQura University, 21955 Makkah, Kingdom of Saudi Arabia*

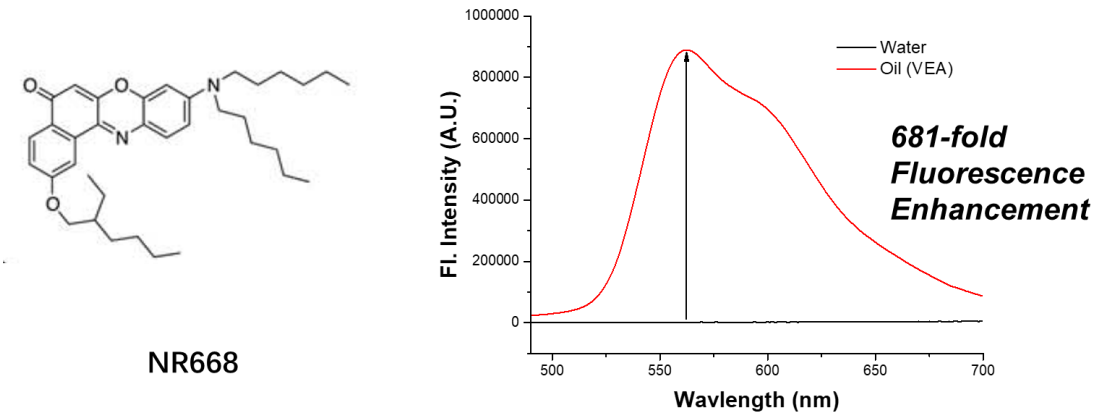

Figure S1: Structure and fluorescence enhancement of NR668, comparison between solubilizing/dispersing media: water and vitamin E acetate (VEA).

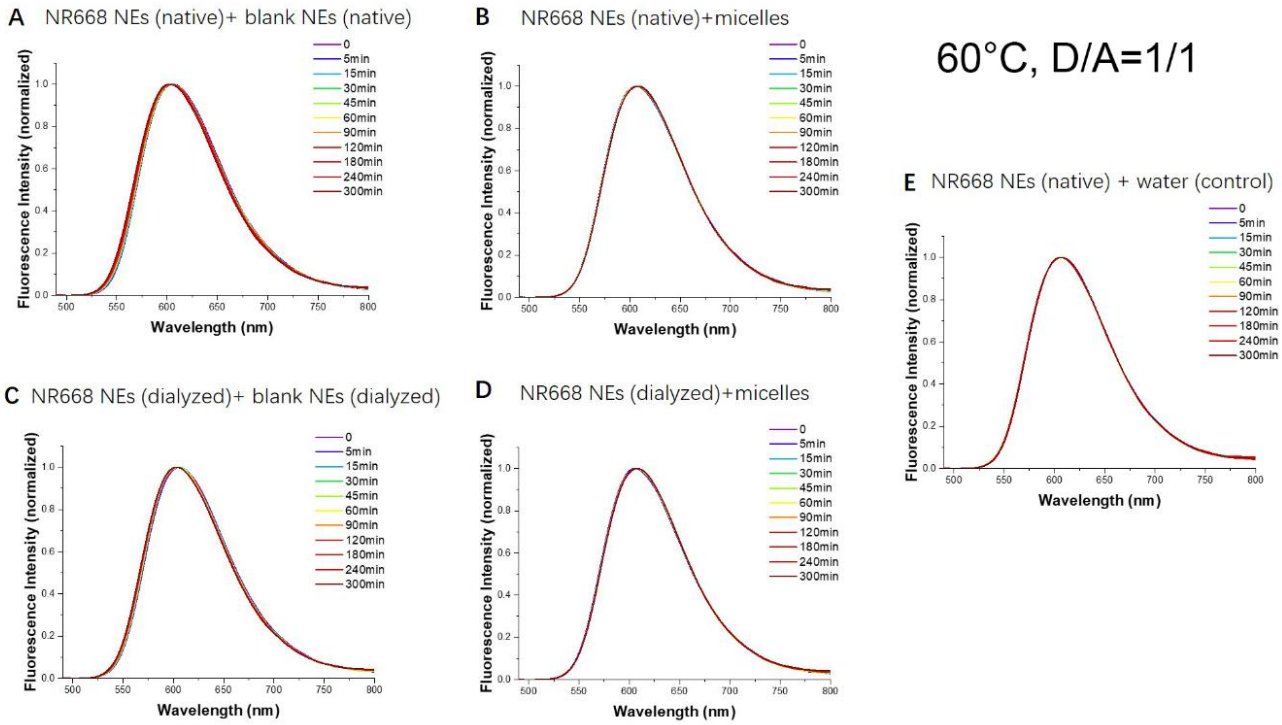

Figure S2: Fluorescence emission spectra of different system in function of time in correspondence of Fig. 2(D). This experiment was conducted for different systems varying in the nature and composition of the acceptor (see details in the text)

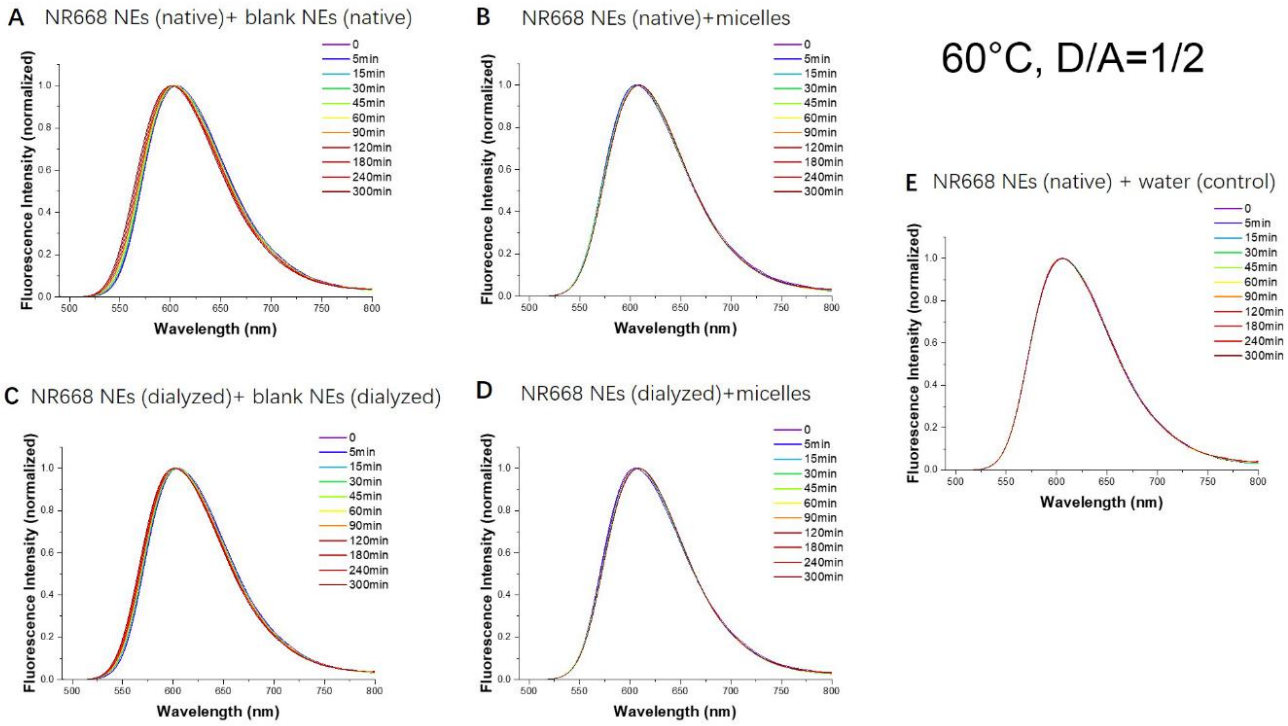

Figure S3: Fluorescence emission spectra of different system in function of time in correspondence of Fig. 2(E). This experiment was conducted for different systems varying in the nature and composition of the acceptor (see details in the text)

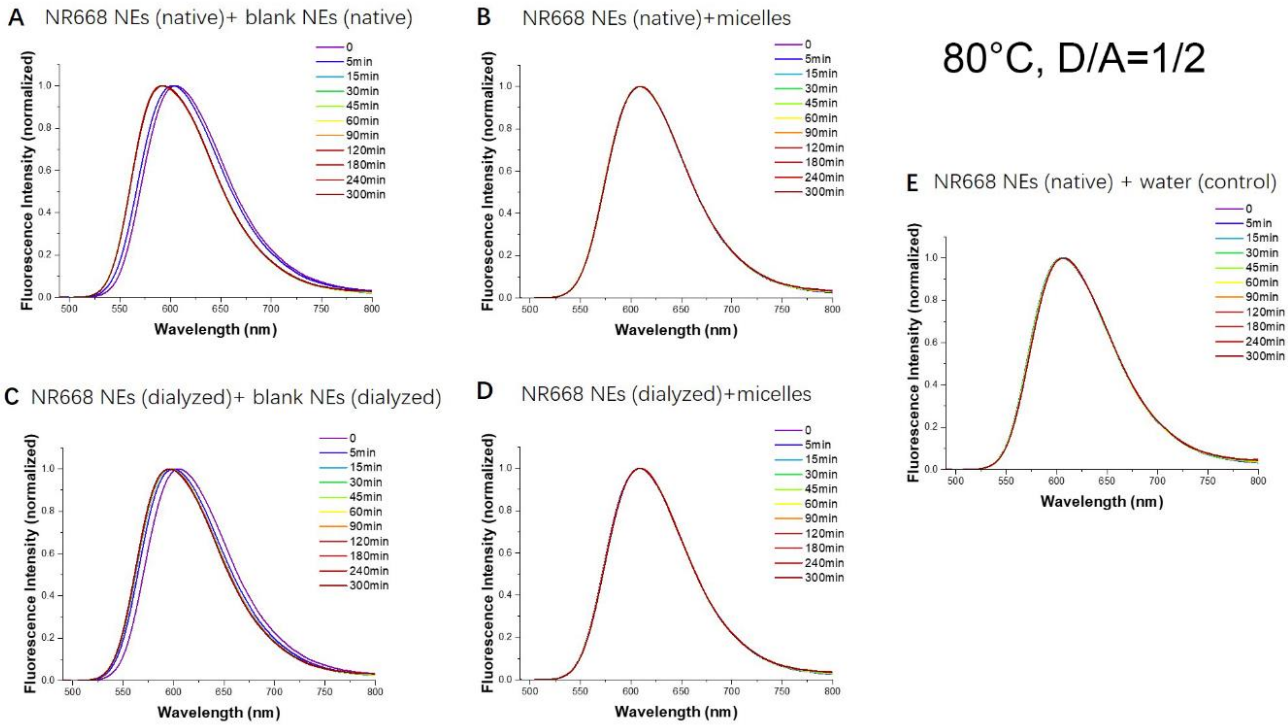

Figure S4: Fluorescence emission spectra of different system in function of time in correspondence of Fig. 2(F). This experiment was conducted for different systems varying in the nature and composition of the acceptor (see details in the text)

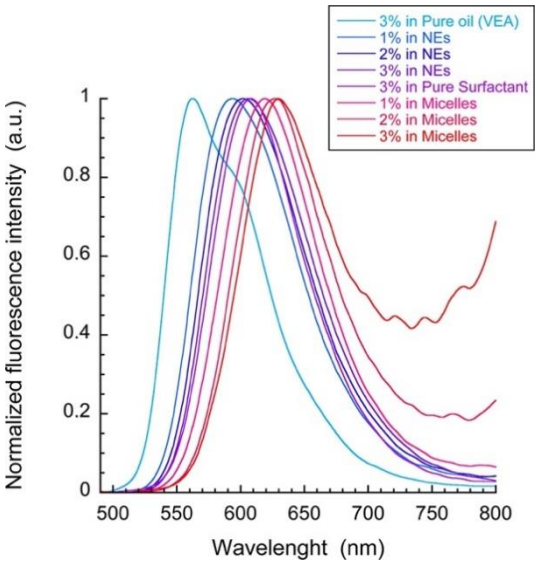

Figure S5: Normalized fluorescent spectra of NR668 solubilized in different media for various composition and concentrations in oil. All samples were diluted before measurement to finally have a similar dye concentration of 1 µM.

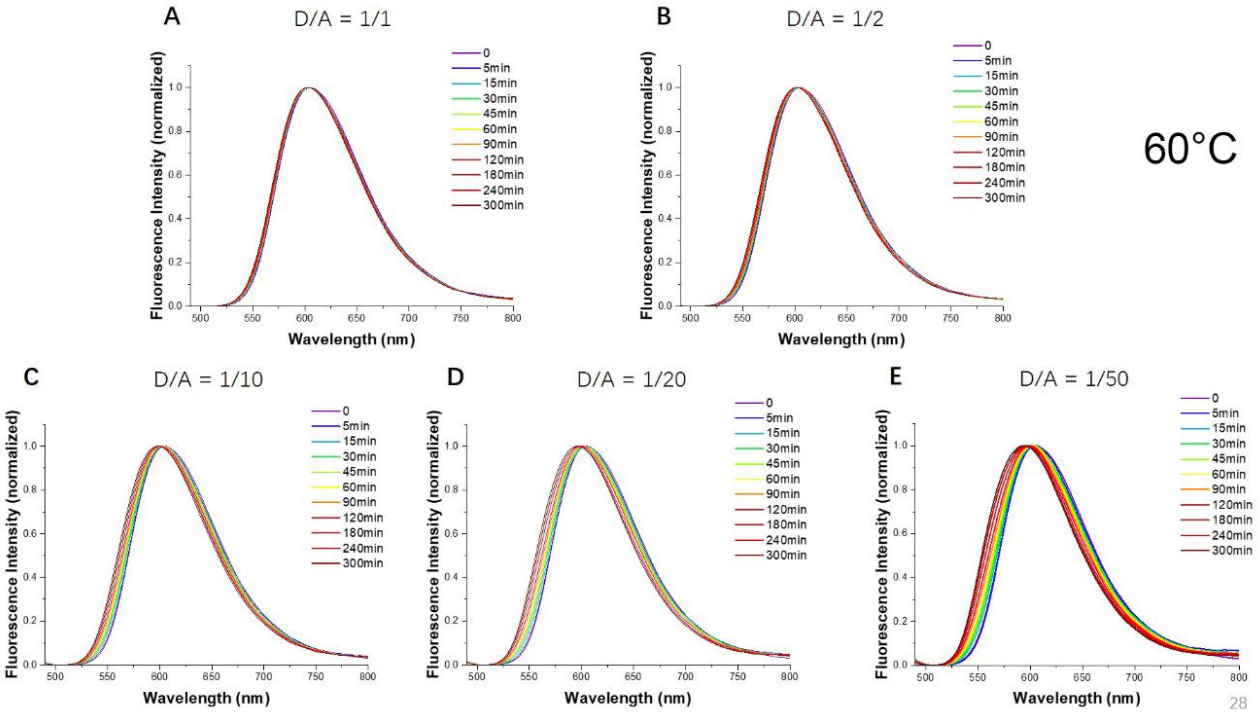

Figure S6: Fluorescence emission spectra of different D/A ratio in function of time in correspondence of Fig. 3(B).

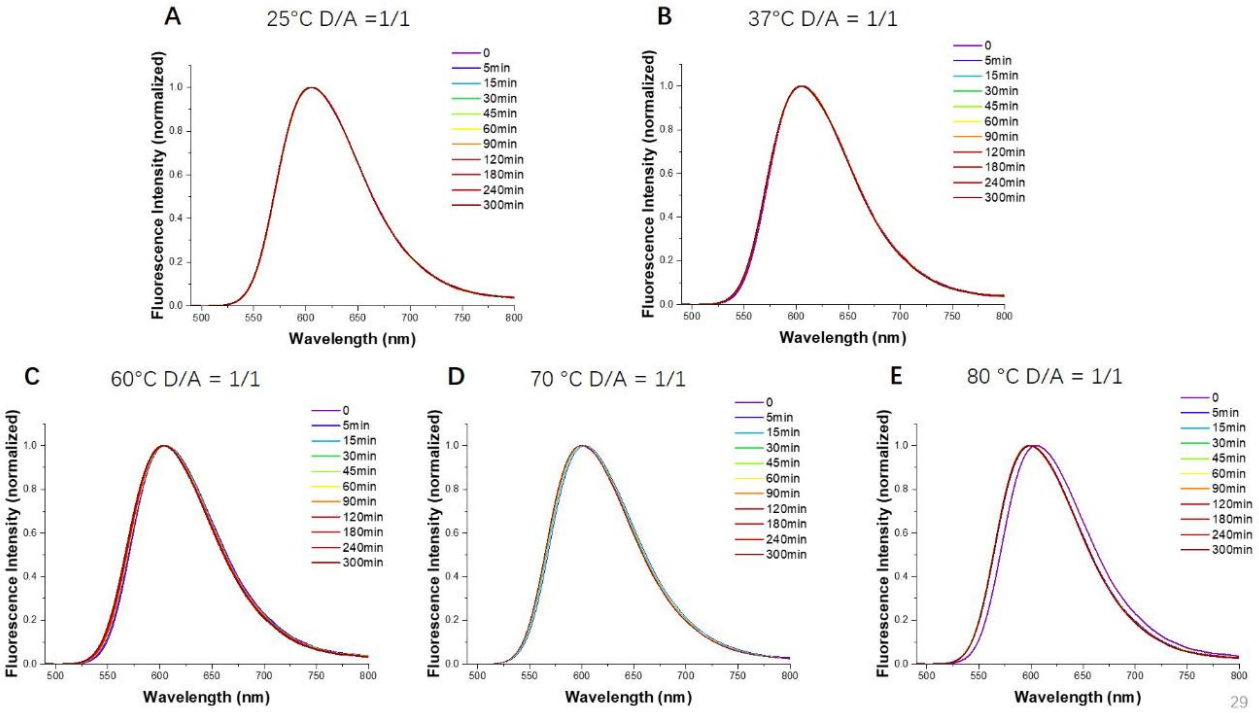

Figure S7: Fluorescence emission spectra of different temperature in function of time (with a D/A ratio of 1/1) in correspondence of Fig. 4(D).

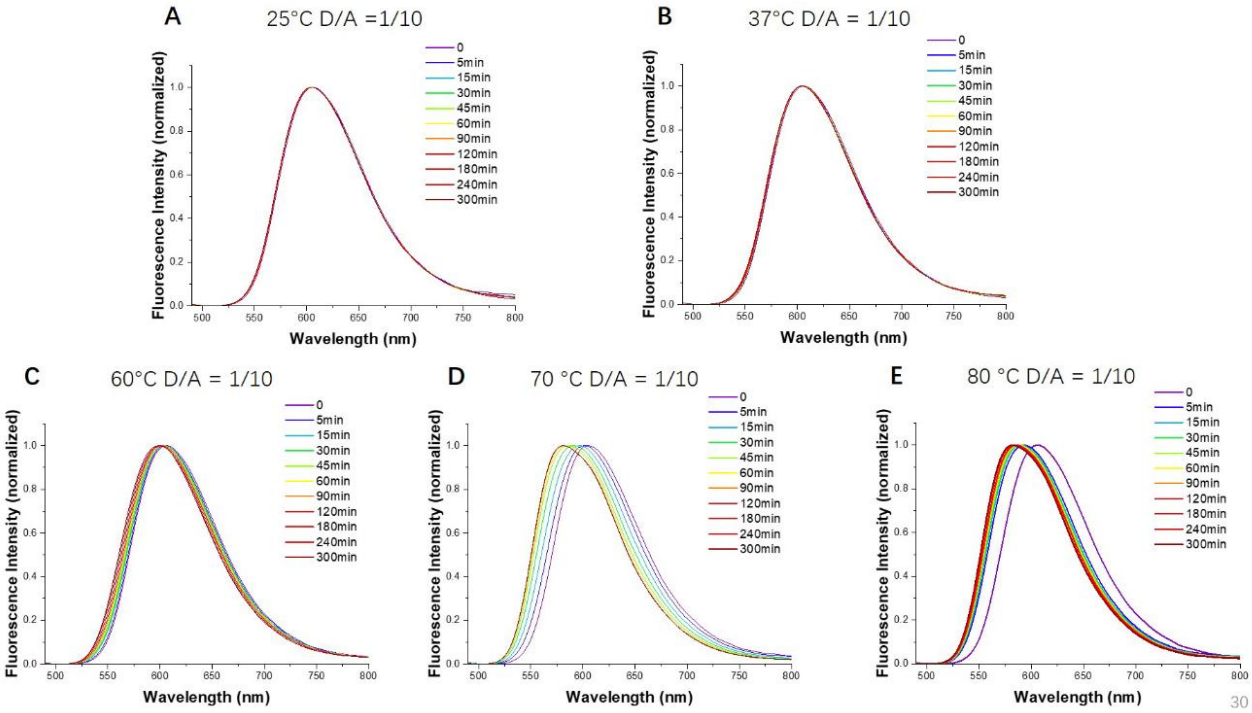

Figure S8: Fluorescence emission spectra of different temperature in function of time (with a D/A ratio of 1/10) in correspondence of Fig. 4(E).

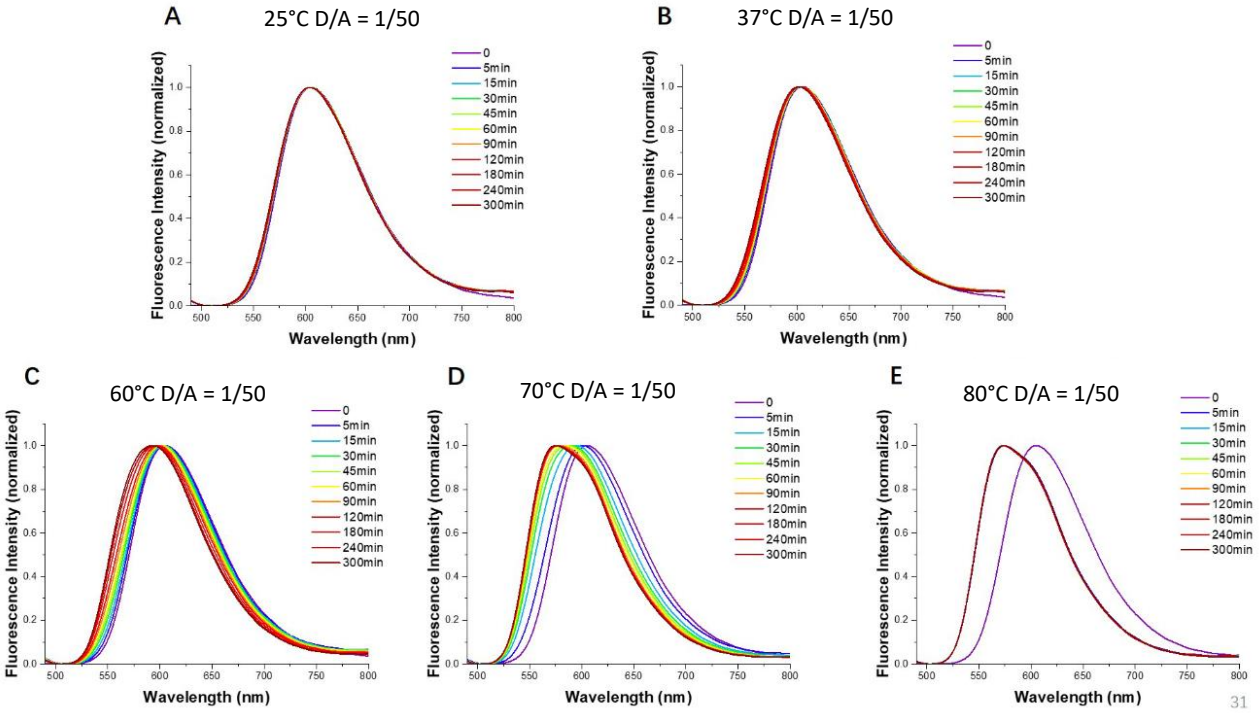

Figure S9: Fluorescence emission spectra of different temperature in function of time (with a D/A ratio of 1/50) in correspondence of Fig. 4(F).

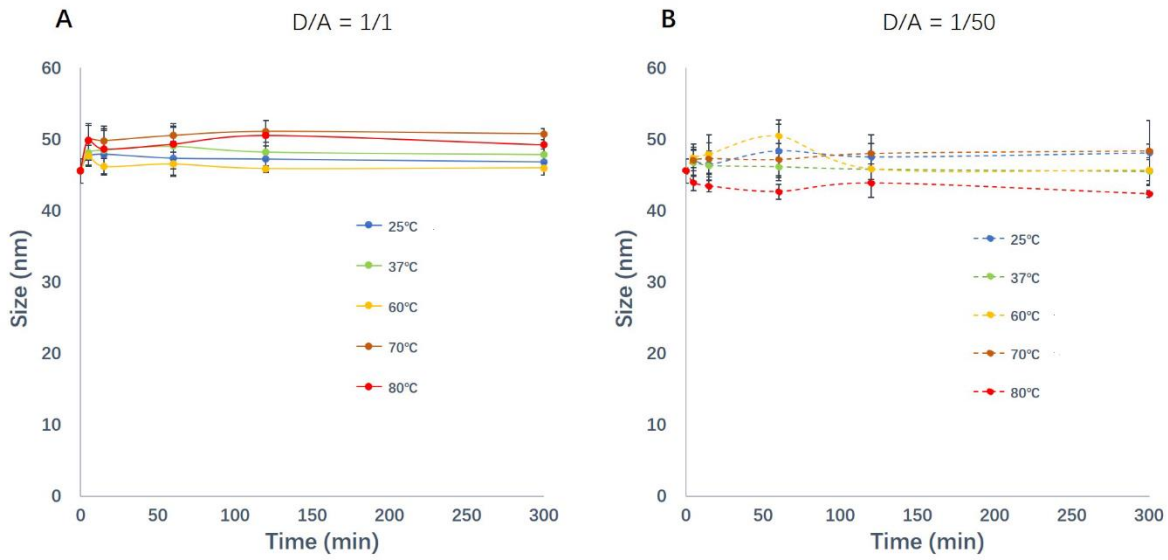

Figure S10: Size changes with incubation time in function of different temperature (varying from 25°C to 80°C) and for two donor-to-acceptor ratios (1/1 and 1/50). All the PDI values were below 0.2. Data are mean values, and error bars indicate ± standard deviation, n = 3.

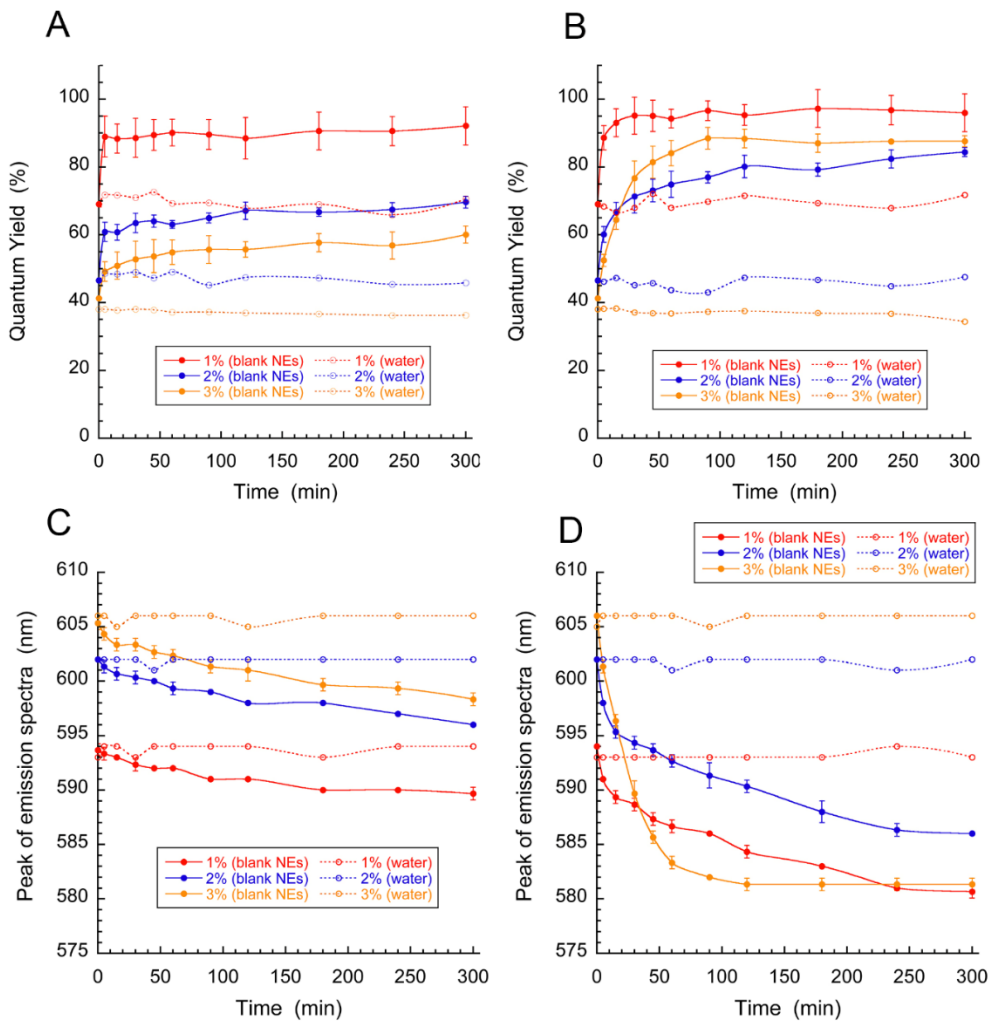

Figure S11: Quantum yield (A, B) and values of the peak of the fluorescence spectra (C, D) in function of different dye concentrations in the oil core of nano-emulsions, and for two different temperatures, 60°C and 70°C. Raw data corresponding to Fig. 5. Data are mean values, and error bars indicate ± standard deviation, n = 3.

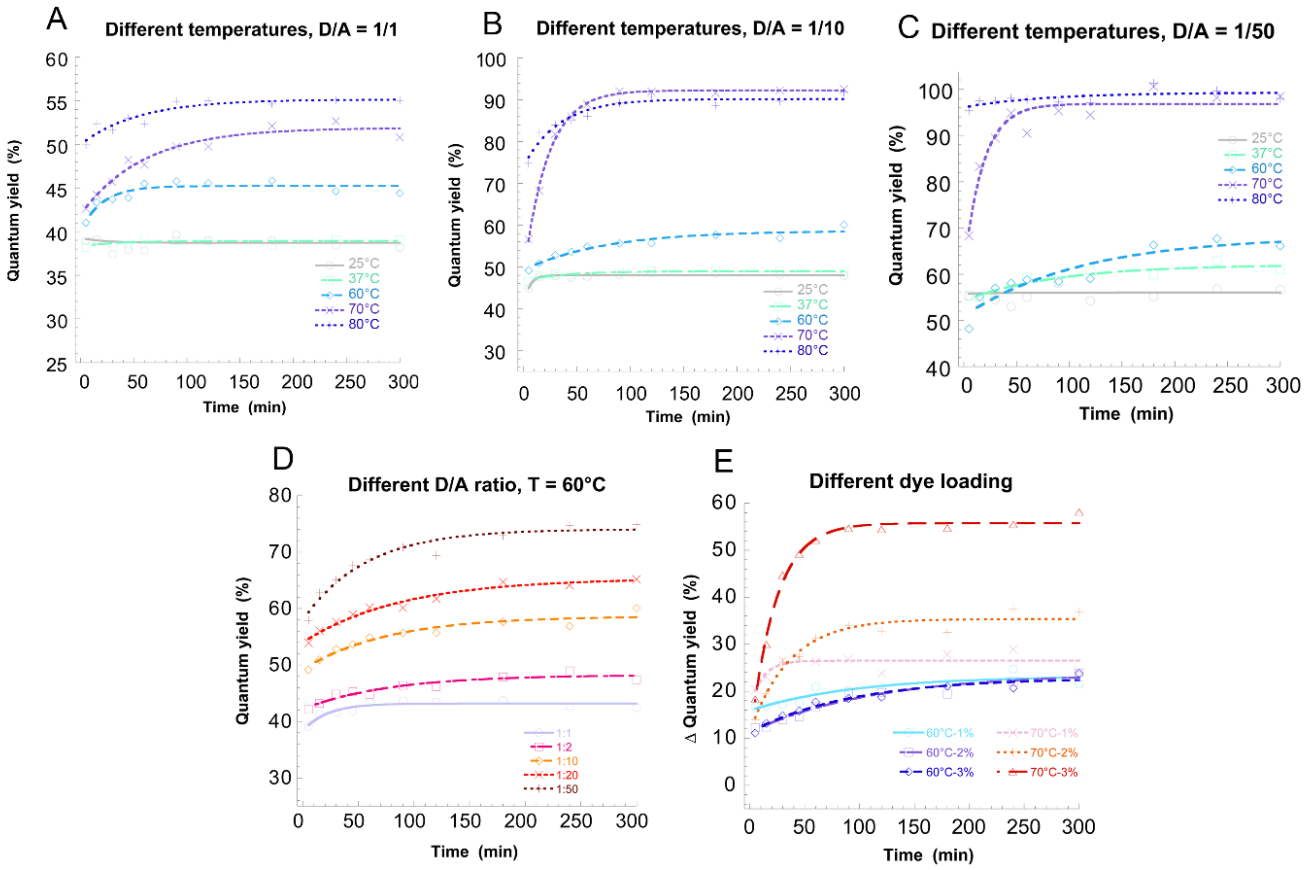

Figure S12: Mathematical fitting for quantum yield-time curves in different conditions (different D/A ratio, temperature and dye concentration). Extrapolation performed through a classical monoexponential rise, QY(t) = QY(t=0) + [QY(t → ∞) – QY(t=0)].[1-exp(-t/τ)], where QY(t=0) is the y-intercept, QY(t → ∞) is the QY after full stabilization, and τ a characteristic time. The values of interest, reported in Fig. 7, are eventually QY(t → ∞).

Chapter 4

Study of the spontaneous emulsification process, impact of the chemical nature and properties of surfactants

Chapter 5

Other participated projects

1 Introduction

In this chapter, three more applications of lipid-based fluorescent nanoparticles were introduced. Firstly, electrophoresis was introduced to evaluate the integration of polymer-stabilized nanodroplets by fluorescently labeling the oily core and the amphiphilic polymer with distinct colors at the same time. The migration provided an instinct discrimination of the different nanomaterials that can be obtained during the formulation, and it could be developed as a new method for the stability of the lipid nanomaterial. The scheme is shown in Fig. 5.1.

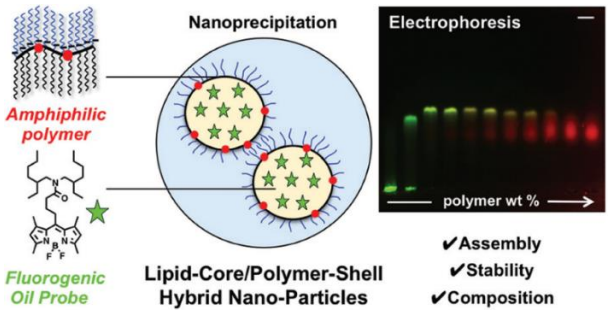

Figure 5.1 Two-color labeling electrophoresis used for lipid-based nanoparticles

Secondly, we introduced a chemical modified pro-dye encapsulated in nano-emulsion. By reversibly modifying the fluorescent dye into a non-fluorescent pro-dye, we achieved a non-leakage *in vitro* but an efficient delivery and release in cancer cells. The scheme is shown in Fig. 5.2.

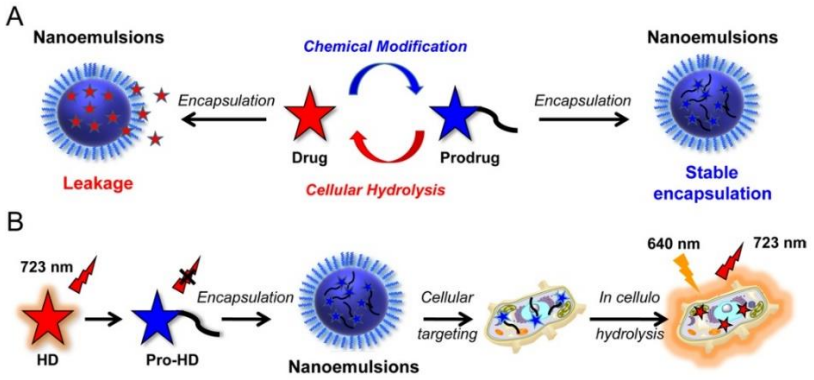

Figure 5.2 Schematic principle of a prodrug for enhanced encapsulation in NEs (A) and of the developed HD/Pro-HD system as a model to monitor the drug delivery by NEs (B).

Thirdly, fluorescence probe can also be used to characterize w/O/W double emulsion. Sulforhodamine 101 (SR101), which presents a fluorescent signal only when it is solubilized in water, was found still presenting the signal within the double emulsions after their separation from the continuous phase, and it can be a proof of the nano-scaled multi-structure of w/O/W. The scheme is shown in Fig. 5.3.

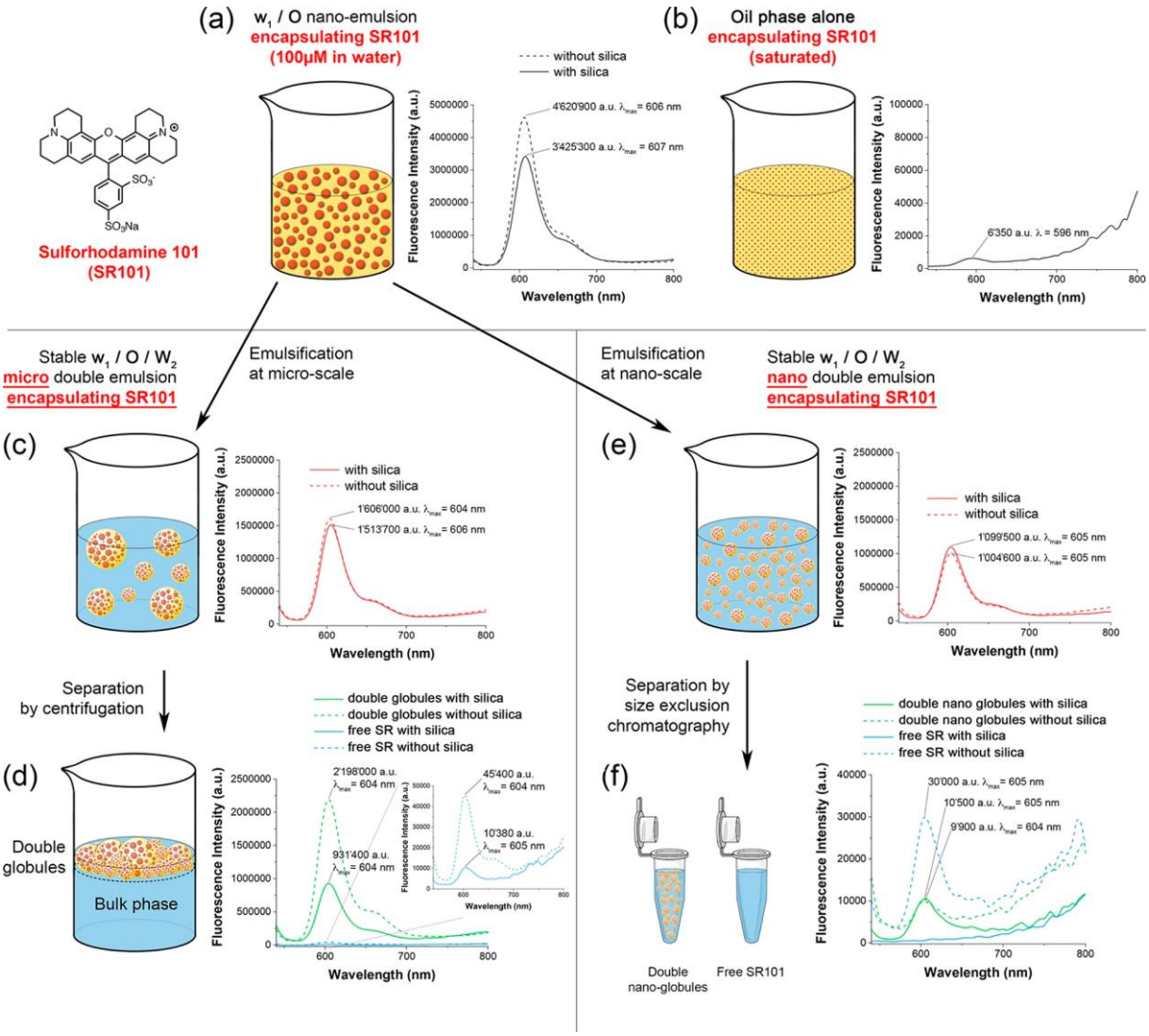

Figure 5.3 Schematic representation of the protocol followed to prove that liquid water is still presented inside the micro and nano double droplets, along with the corresponding fluorescence spectra.

The first part of study has been published on *Soft Matter*, the second has been published on *Journal of Materials Chemistry B*, and the third part has been published on *Langmuir*. The three articles are enclosed as below.

Soft Matter

ROYAL SOCIETY OF CHEMISTRY

PAPER

View Article Online
View Journal | View Issue

Cite this: *Soft Matter*, 2020, **16**, 4173

Lipid-core/polymer-shell hybrid nanoparticles: synthesis and characterization by fluorescence labeling and electrophoresis†

Sophie Bou,[a] Xinyue Wang,[b] Nicolas Anton,[b] Redouane Bouchaala,[a] Andrey S. Klymchenko[a] and Mayeul Collot*[a]

Received 13th January 2020,
Accepted 1st April 2020

DOI: 10.1039/d0sm00077a

rsc.li/soft-matter-journal

Among the lipid nanoparticles, lipid polymer hybrid nanoparticles (HNPs) composed of an oily core and a polymeric shell display interesting features as efficient drug carriers due to the high loading capability of the oil phase and the stability and surface functionalization of the polymer shell. Herein, we formulated lipid-core/polymer-shell hybrid nanoparticles (HNPs) using a simple nanoprecipitation method involving Vitamin E Acetate (VEA) as the oily core and a tailor-made amphiphilic polymer as a wrapping shell. The fluorescence labeling of the oil, using a newly developed green fluorogenic BODIPY tracker, and of the polymer using a covalent attachment of a red emitting rhodamine was done to assess the formation, the composition and the stability of these new hybrid nanoparticles using dual color electrophoresis gel analysis. This technique, combined to conventional DLS and electronic microscopy analysis, allowed us to quickly determine that 20 wt% of the polymer was an optimal ratio for obtaining stable HNPs by nanoprecipiation. Finally, we showed that using different polymeric shells, various HNPs can be obtained and finely discriminated using a combined approach of electrophoresis and two-color labeling.

1. Introduction

In the field of nanomaterials, lipid-based nanoparticles are drawing a growing interest especially as promising drug delivery systems, mainly due to the huge possibilities of lipophilic molecule loading.[1,2] Among these nanoparticles, nano emulsions (NEs),[3–5] solid lipid nanoparticles (SLNs)[6–8] and nanostructured lipid carriers (NLCs)[9,10] are composed of a lipid core that can serve as an efficient carrier of hydrophobic cargoes such as drugs or contrast agents. These lipid NPs are usually stabilized by monomeric surfactants or natural phospholipids with the reduced possibility of chemical modification, thus limiting the modification of their physico-chemical properties, their biodistribution, their circulation time in blood[11,12] or their targeting ability. Conversely, polymeric nanoparticles (PNPs) offer a wide diversity in their structures and functions due to accessible chemical modifications.[13–17] Consequently lipid polymer hybrid nanoparticles (HNPs) featuring the advantages of flexibility in the polymer design constitute promising new nanomaterials.[18] It is noteworthy that while polymeric core–lipid shell HNPs were extensively described,[19,20–22] those merging the advantage of an oily core with a polymeric shell, also called nanocapsules, remain poorly reported.[23–25] Therefore, a better comprehension on their formation and stability is required along with adapted analysis and characterization methods. Fluorescent labeling of lipid-based nanoparticles was used for bioimaging,[26,27] and for the *in cellulo*[28] and *in vivo*[29] tracking of single particles. In addition, it is also an efficient method of characterization using various fluorescence techniques including microscopy[29] and fluorescence correlation spectroscopy.[28,30] Although HNPs are generally characterized by dynamic light scattering (DLS) and by transmission electronic microscopy (TEM), these techniques do not provide fast and clear-cut information regarding their formation and composition. Conversely, electrophoresis relies on a simple and affordable setup and has already been reported as a reliable technique for analyzing and separating NPs of various sizes and shapes[31,32] and as a characterization method for nanomaterials including polymer wrapped inorganic nanoparticles[33] and upconverting nanoparticles.[34] When combined with fluorescence detection, electrophoresis enables the highly sensitive detection of fluorescently labeled nanomaterials[35] and nanoconjugates.[36] Consequently, the fluorescence labeling of HNPs combined with electrophoresis analysis would enable a precise assessment of their assembly and integrity.

Herein, we fluorescently labeled amphiphilic polymers in red and developed a green emitting fluorogenic oil tracker, thus

[a] *Laboratoire de Bioimagerie et Pathologies, UMR 7021 CNRS, University of Strasbourg, France. E-mail: mayeul.collot@unistra.fr*
[b] *Laboratoire de Conception et d'Applications de Biomolécules, UMR 7199 CNRS, University of Strasbourg, France*

† Electronic supplementary information (ESI) available. See DOI: 10.1039/d0sm00077a

allowing independent monitoring of the fate and colocalization of the polymer and the oil phase during the formulation of HNPs by nanoprecipitation. Electrophoresis revealed by fluorescence was successfully used as a monitoring method for the formation of HNPs and was found to be a valuable tool providing complementary information compared to DLS and TEM.

2. Results and discussion

2.1. Fluorescence labeling of HNP constituents

Herein we aimed at formulating new hybrid nanoparticles (HNPs) based on the wrapping of a lipid droplet by an amphiphilic polymer (Fig. 1C) as well as assessing their formation using a fluorescence technique involving simple methods. Firstly, an amphiphilic polymer was obtained from the chemical modification of a commercially available alternating polymer: poly(maleic anhydride-*alt*-1-octadecene) (PMAO), which is composed of a repeating unit consisting of a hydrophobic hydrocarbon chain (C16) and an amine reactive succinic anhydride function (Fig. 1A). These alternating amphiphilic polymers are widely used to wrap nanocrystals to obtain water soluble inorganic nanoparticles[33] and upconverting nanoparticles.[37] We also showed that PMAO, without any chemical modification, when incorporated at 1 wt% in oil can significantly modify the physicochemical properties of nanoemulsions.[24] PMAO can readily react with Jeffamine, an amine-terminated polypropylene glycol/polyethylene glycol copolymer mainly composed of PEG. Vitamin E acetate (VEA) is a biocompatible and viscous oil that was chosen to constitute the non-polar core of our HNPs as we recently demonstrated its ability to form small and monodisperse fluorescent lipid droplets by spontaneous nanoemulsification.[28] In order to assess the formation of HNPs, both constituents, namely the amphiphilic polymer and the oil, were fluorescently labeled. To this endeavor, 1% of the reactive anhydride sites of PMAO reacted with rhodamine-NH_2, a red emitting amino-rhodamine (Fig. 1A),[37] while the oil phase was labeled using a newly developed fluorogenic oil tracker consisting of a lipophilic green emitting BODIPY, BDP-$2C_8$. Indeed, this hydrophobic molecule displayed an impressive fluorescence enhancement at 507 nm from PBS to VEA (214-fold, Fig. 1B), and also when incorporated in VEA based nanoemulsions (130-fold, Table S1 and Fig. S1, ESI†). Thanks to its hydrophobicity, BDP-$2C_8$ possesses a high affinity towards lipid oil, as its calculated CLogP was found to be close to the log*P* of VEA (11.2 and 9.95, respectively). Consequently, two complementary color channels (green and red) can be used in fluorescence imaging to individually monitor both the oil phase and the polymer during the formulation of HNPs.

Once all the constituents are synthesized, two formulation methods were explored. (1) Rehydration of a dry organic film consisting of adding a non-solvent (PBS) on a film containing all the components (oil/polymer/BDP-$2C_8$). (2) A "nanoprecipitation" approach consisting of quickly adding a non-solvent (PBS) to a concentrated solution of the components in dioxane (Fig. 1C). While the rehydration approach led to flocculation and heterogeneous solutions, the nanoprecipitation method provided a visually clear nano-suspension and was thus adopted for the rest of our study.

2.2. Formulation & electrophoresis

In the first experiment, we used the amphiphilic polymer HP1 where all the anhydride functions reacted with Jeffamine-1000 and 1% of rhodamine-NH_2 (see the ESI†). This amphiphilic polymer thus displays hydrophobic hydrocarbon chains at one end, PEG chains at the other end and negatively charged carboxylate groups at the interface (Fig. 1A). We first assessed the formation of HNPs by varying the HP1/oil weight ratio (wt%). To this aim, a solution of VEA (2 mg mL^{-1} in dioxane) containing 1 wt% of BDP-$2C_8$ (as an oil tracker) and a solution of HP1 (2 mg mL^{-1} in dioxane) were mixed at various ratios, and PBS (95 vol% of the final volume) was vigorously added for

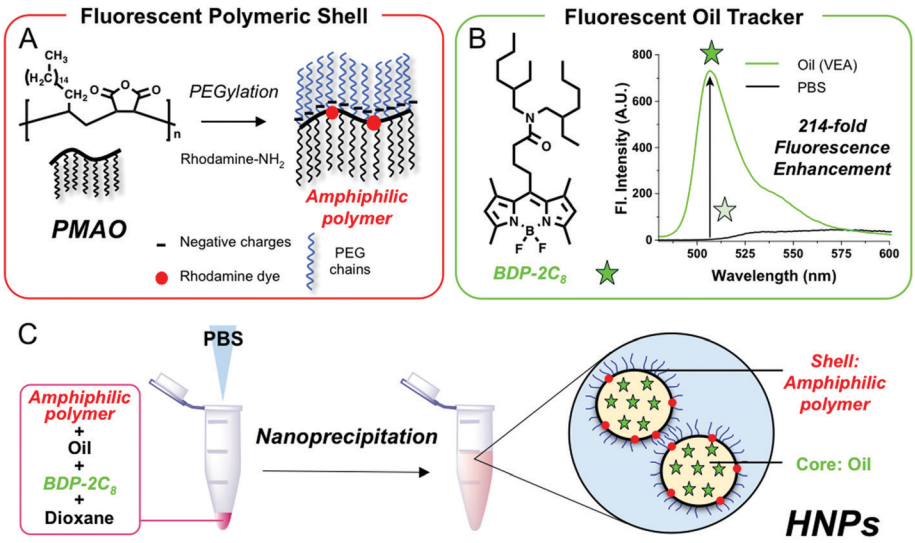

Fig. 1 (A) Synthesis of fluorescently labeled amphiphilic polymers. (B) Development of the fluorescent oil tracker based on BODIPY BDP-$2C_8$ and its fluorescent spectra at 1 μM in PBS and in oil. (C) Formulation of HNPs by nanoprecipitation and their schematic representation.

nanoprecipitation at room temperature. The formulations were then first analyzed by DLS. In absence of polymer, large and polydisperse (510 ± 307 nm, PDI 0.35) pure oil droplets were obtained (Fig. 2A).

Interestingly, at only 10 wt% HP1, dramatic effects were obtained as a smaller size (103 ± 11 nm) and improved dispersity (PDI = 0.15) (Fig. 2A). Upon the increase of HP1 wt%, the sizes gradually decreased (Fig. 2A) to finally reach pure polymer nanoparticles (PPNPs) with a size of 10.6 ± 0.6 nm. Although DLS provided information regarding the average size of the bulk formulation, it did not inform on the nature of the formed NPs. In order to provide a deeper characterization of the NP composition and taking advantages of our fluorescent labels, electrophoresis was performed, allowing for the individual tracking of the oil and polymer, using the green and red channels, respectively (Fig. 2B). Remarkably, the obtained gel displayed clear-cut and informative results. While in the absence of polymers the oil was unable to migrate to the anode, in the presence of 10 wt% HP1, the green signal was split up in two spots, one corresponding to the initial position (no migration), and the other one to the significant migration of the oil. At 20 wt% HP1, the pure oil spot was undetectable thus showing that this polymer/oil ratio was sufficient to uptake the entire amount of oil into new migrating species. At higher polymer wt%, the red and green fluorescence signals merged perfectly indicating that the new appearing spot might correspond to HNPs composed of both oil and the polymer. Interestingly, the use of larger polymer/oil ratios revealed the appearance of a new red fluorescent spot corresponding to pure polymeric NPs (PPNPs). This was confirmed by the formulation in the absence of oil that provided a red spot at the same migration distance (Fig. 2A, 100 wt% HP1). Compared to DLS, which provides the size distribution of the whole population whatever its composition, this experimental approach appeared much more informative on the composition of the NP suspension. The electrophoresis clearly discriminated the different populations and revealed the presence of hybrid NPs. According to these first results, the 20 wt% polymer was sufficient to formulate HNPs with full uptake of the oil.

In addition to this experiment, another series of formulations was studied, fixing the amount of oil in order to maintain a high green signal and the amount of the polymer was gradually increased, ranging from 10 to 50 wt% (results reported in Fig. S2, ESI†). The electrophoresis revealed that, upon an increase in the polymer wt%, the spots corresponding to the HNPs displayed the same yellow color (merging of green and red) with no significant change in their migration distance, whereas the intensity of spots corresponding to PPNPs gradually increased. These results indicated that the formulation of HNPs required a minimum amount of 20 wt% of the polymer and that the additional use of the polymer does not lead to its incorporation into HNPs but rather forms a second population of pure polymer nanoparticles (PPNPs).

At that point of our study several controls were used. First, we checked that the non-migrating and intense green signal obtained in the absence of the polymer was due to BDP-2C$_8$ dissolved in oil (Fig. 3B, formulation 1) and not to BDP-2C$_8$ itself in aqueous solution. Therefore, BDP-2C$_8$ was formulated alone in PBS at the same concentration as used in the presence of oil (Fig. 3, formulation 2). BDP-2C$_8$ formulated alone did not provide any signal at the level of pure oil. Instead, a dim orange signal was obtained at a higher migration distance. It is known that pure fluorophores can form aggregates at the nanoscale with a low brightness due to aggregation-caused quenching (ACQ).[38,39] Spectroscopic studies confirmed that BDP-2C$_8$, when formulated in PBS, forms dispersed aggregates. First, both absorption and emission spectra dramatically broadened (Fig. S1, ESI†). Then, emission spectra also revealed an important red shift. Indeed, while dissolved in oil BDP-2C$_8$ emitted at 500 nm with a high quantum yield (0.82), pure BDP-2C$_8$ NPs emitted at 577 nm with a notable quantum yield of 0.19 (Table S1, ESI†), explaining the dim orange spot obtained in electrophoresis (Fig. 3B, formulation 2).

This phenomenon was already reported for BODIPY fluorophores and was attributed to the formation of red shifted emissive J-aggregates.[40] In addition, DLS measurements corroborated that BDP-2C$_8$, when formulated in PBS, aggregated as monodisperse NPs (121 ± 1 nm, PDI = 0.08, Fig. 3A formulation 2). This experiment confirmed that the non-migrating green spot resulted from the oil droplets containing BDP-2C$_8$. Then, the

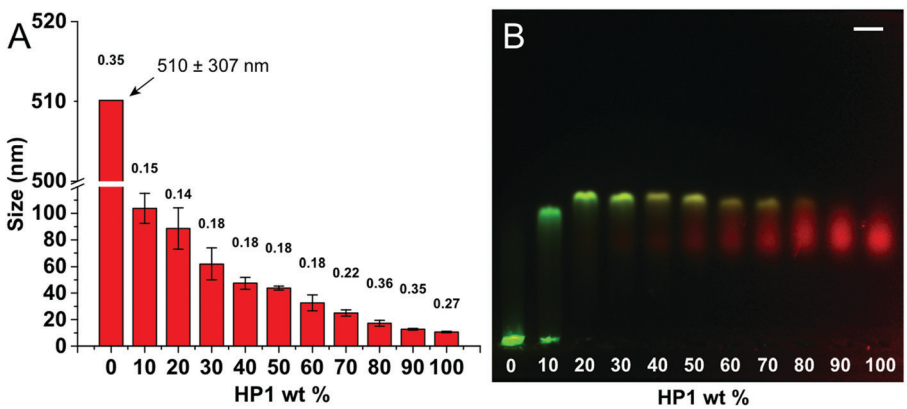

Fig. 2 Formulation of HNPs with various polymer/oil wt%. (A) Mean sizes measured by DLS resulting from at least 3 independent formulations. Numbers above the bars are the mean PDI values. (B) Merged green and red channels of the electrophoresis image. Scale bar is 0.5 cm.

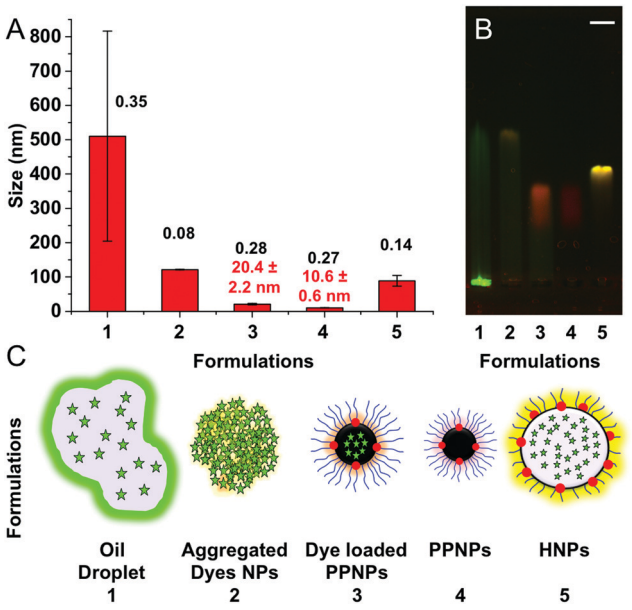

Fig. 3 Various formulations studied. (A) Mean sizes measured by DLS resulting from at least 3 independent formulations. (B) Merged green and red channels of the electrophoresis image. Scale bar is 0.5 cm. (C) Schematized structures assigned to the formulations. (1) VEA (100 μg mL^{-1} containing) + BDP-2C$_8$ (1 μg mL^{-1}); (2) BDP-2C$_8$ (1 μg mL^{-1}); (3) HP1 (100 μg mL^{-1}) + BDP-2C$_8$ (1 μg mL^{-1}); (4) HP1 (100 μg mL^{-1}); (5) VEA (80 μg mL^{-1} containing) + BDP-2C$_8$ (1 μg mL^{-1}) + HP1 (20 μg mL^{-1}).

polymer (HP1) was formulated in the presence of BDP-2C$_8$ and in the absence of oil (formulation 3) in order to verify whether the spots correspond to PPNPs or overlap with HNPs (Fig. 3, formulations 4 and 5, respectively). This control experiment showed that the migration spot of pure BDP-2C$_8$ NPs (formulation 2) disappeared, giving rise to an orange signal (formulation 3) that appeared at the same level as PPNPs (formulation 4), with similar small sizes (20 ± 2 nm and 11 ± 1 nm for formulations 3 and 4, respectively). This experiment showed the ability of PPNPs to efficiently entrap BDP-2C$_8$ providing a different spot than HNPs. Overall, these controls proved that an intense green signal is obtained only in the presence of the oil, and thus, that the colocalization of green and red signals (*i.e.* an intense yellow spot) was correctly assigned to HNPs (Fig. 3, formulation 5).

Since electrophoresis was used to monitor and optimize the formation of HNPs, we hypothesized that it could also serve to assess their stability. To this end, HNPs composed of HP1 (20 wt%) were formulated and submitted to a temperature of 60 °C over 4 h. Every 30 min the size was measured by DLS and a small aliquot was kept for electrophoresis (Fig. S3, ESI†). On the one hand, we note that although the size and the PDI only slightly increased over time, the electrophoresis showed clear signs of degradation. On the other hand, the migration distance of the spot corresponding to HNPs slightly decreased over time along with its red color probably denoting a partial erosion of the polymer leading to the destabilization of the HNPs. Finally, the green spots located at the deposition well, corresponding to pure oil, gradually appeared over time. Overall, the electrophoresis clearly depicted a phase separation between the oil and the polymer over time at 60 °C and thus appeared as an efficient method to assess the stability of the fluorescently labeled HNPs.

2.3. Transmission electronic microscopy (TEM)

According to the obtained results, electrophoresis when correlated to DLS, provided evidence that HNPs can be obtained by simple nanoprecipitation using the PMAO based amphiphilic polymer HP1. As complementary studies, HNPs composed of HP1 (20 wt%) were characterized by TEM.

The images revealed the presence of 2 populations of particles (Fig. 4A). The first population, present at a lower extent, displayed a spherical shape with a mean size of 503 ± 123 nm combined with a large polydispersity (Fig. 4D). This was in accordance with the DLS measurements of pure VEA droplets (Fig. 3A, formulation 1), probably resulting from the phase separation between oil and the polymer during the preparation

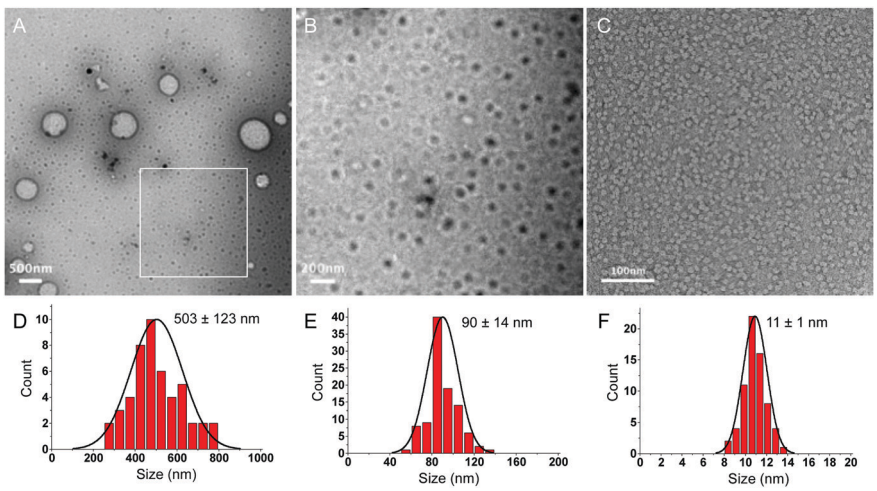

Fig. 4 (A) TEM images of HNPs composed of HP1 (20 wt%). (B) Zoomed region of interest in (A). (C) TEM image of PPNPs composed of HP1. (D–F) are the corresponding histograms of the measured particle sizes.

of the TEM sample under high vacuum. This type of image was already observed in TEM with nano-emulsions containing vitamin E-based compounds (or oils of similar viscosity), giving rise to spherical droplets that spread onto the carbon support.[41,42] The second population, present at a higher extent, displayed spherical shapes (Fig. 4B) with an average size of 90 ± 14 nm (Fig. 4E) and was attributed to the HNPs, as their size was similar to the DLS measurements (Fig. 3A, formulation 5). As a control, formulation involving only HP1 in the absence of oil was imaged. TEM images revealed that PPNPs formed a dense layer of spread particles (Fig. 4C) with an average size of 11 ± 1 nm (Fig. 4F), which was again in accordance with DLS (Fig. 3A, formulation 4).

2.4. Use of various amphiphilic polymers

We showed that the fluorescence labeling of oil and polymers in combination with electrophoresis analysis could be used to monitor the formation and degradation of HNPs. We then chemically modified the amphiphilic nature of PMAO-based polymers to assess their ability to form HNPs and used this new experimental approach to disclose the impact of their chemical structure on the formulations. To this end, various PMAO-based amphiphilic polymers were synthesized (Fig. 5A). Jeffamine-1000 and Jeffamine-2000 were used to modulate the PEG length and thus gave rise to HP1, HP1c, FP1 and HP2, HP2c and FP2, respectively. The negative charges brought by the remaining carboxylate groups (COO^-) were capped either by coupling with an excess of short ethanolamine molecules to give HP1c or HP2c, or by coupling supplementary Jeffamine PEG chains giving rise to fully PEGylated polymers, FP1 and FP2. According to our previous results, the formulations were performed with 20 wt% amphiphilic polymers and 80 wt% VEA in PBS. These formulations were analyzed by DLS (Fig. 5B) and electrophoresis (Fig. 5C). First, the electrophoresis showed that all of the polymers, when used at 20 wt%, were able to form HNPs. The obtained sizes by DLS spanned within a small range, from 71 ± 2 nm (HP1c) to 117 ± 6 nm (FP2) with larger sizes obtained with the fully PEGylated polymers. The slight difference in DLS size might be explained by the difference of molecular weight especially between the half PEGylated and the fully PEGylated polymers. Indeed although the wt% was kept at 20%, the molar polymer/oil ratio is significantly smaller in the case of "heavy" polymers that led to larger HNPs, this is consistent with our previous observations (Fig. 2A). In addition, while full PEGylation led to slightly lower migration distances compared to half PEGylation, the use of large PEG-2000 systematically led to an important decrease of migration. It is noteworthy that charge capping by ethanolamine, while it slightly enhanced the monodispersity of the obtained HNPs compared to the charged polymers, it hardly influenced their migration distance and their size. Although the efficiency of the chemical reactions performed on the polymer was confirmed by ^{1}H NMR (see the ESI†), the measured ζ potential displayed similar values (~26 mV, Table S2, ESI†). The correlation between electrophoretic migration and values of ζ potential obtained from charged and capped polymers suggests that the particles still present a significant surface potential, which can come from various origins, PEG chain conformations, dipoles and interactions of the ions present in the media. Overall, it appeared that the nature of the amphiphilic polymer, more precisely its PEGylation rate, but also the length of the PEG chains, significantly influenced the migration distance of the HNPs. To further support this hypothesis, a fully ethanolamine-capped polymer was used to study the influence of PEG groups on the formulation of HNPs (Fig. S4, ESI†). Interestingly the electrophoresis showed that neither the polymer nor the oil migrated indicating that this less polar polymer failed to form HNPs at any polymer/oil ratio. These results underline the major role of PEG chains in the formulation of HNPs. Eventually, the electrophoresis appeared to be a method of choice also adapted to characterize the surface modifications of these HNPs.

3. Conclusion

Herein, we aimed at developing new lipid-core/polymer-shell hybrid nanoparticles (HNPs) using a simple nanoprecipitation protocol. In order to facilitate the screening of the optimal conditions, both oil and polymer constituents were fluorescently labeled with distinct colors. To this end, the amphiphilic polymer was covalently labeled with a red emitting rhodamine

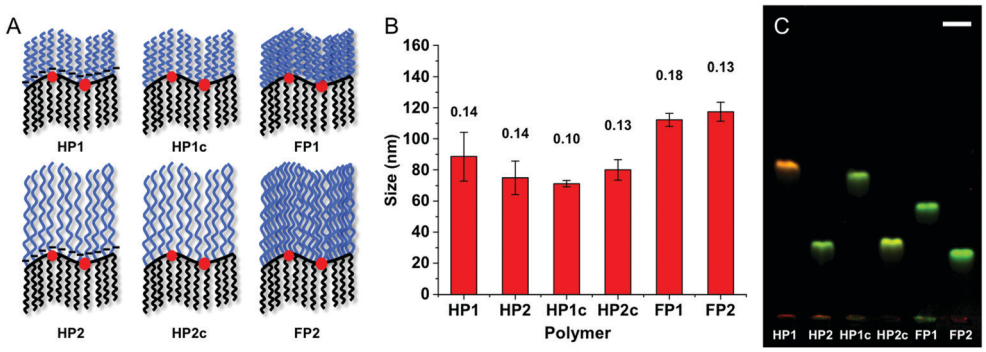

Fig. 5 Formulation of 20 wt% polymer HNPs with different amphiphilic polymers. (A) Schematic representation of the polymers used for the formulation. (B) Mean sizes measured by DLS resulting from at least 3 independent formulations. Numbers above the bars are the mean PDI values. (C) Merged green and red channels of the electrophoresis image. Scale bar is 0.5 cm.

and in parallel, an oil tracker was developed based on a hydrophobic fluorogenic BODIPY displaying a 214-fold fluorescence enhancement from PBS to oil. The obtained formulations were systematically analyzed by DLS and through an innovative experimental approach using dual color fluorescently revealed electrophoresis. We herein showed that, unlike DLS measurements and TEM imaging, electrophoresis provides unambiguous information by the discrimination of the different nanomaterials that can be obtained during the formulation. In addition, we showed that this technique could be used to assess the stability of the lipid nanomaterial, as well as to discriminate the relationships between particle composition and surface properties. We believe that, in the future, this method might facilitate the development of new lipid nanoparticles by accelerating the optimization of the formulation conditions. Finally, the herein presented hybrid nanomaterials present many advantages in terms of preparation and chemical modifications. Consequently, ongoing work is being performed by our group to develop hybrid particles able to be functionalized based on this approach.

4. Experimental section

4.1. Materials

Poly(maleic anhydride-*alt*-1-octadecene) (PMAO, average M_n 30 000–50 000), diisopropylethyl amine (DIEA), ethanolamine, tetrahydrofuran (THF) and dioxane were purchased from Sigma Aldrich. Jeffamine M-1000 (J-1000) and Jeffamine M-2070 (J-2000) were kindly offered by Huntsman Corporation (Texas, USA). Vitamin E acetate (VEA) was purchased from TCI Europe. The solvents were of analytical grade, and dimethylformamide (DMF) was anhydrous.

4.2. Synthesis

NMR spectra were recorded on a Bruker Avance III 400 MHz spectrometer. Mass spectra were obtained using an Agilent Q-TOF 6520 mass spectrometer. Spectra can be found in the ESI.† The cLogP value of BDP-2C_8 was obtained using ChemDraw (Cambridge software).

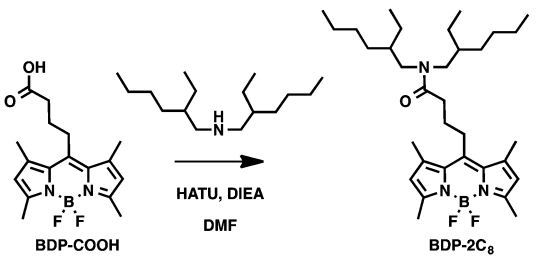

BDP-2C_8. To a solution of acid BDP-COOH (200 mg, 0.598 mmol, 1 eq.) in DMF (4 mL) under an argon atmosphere was added bis(2-ethylhexyl)amine (0.270 mL, 0.897 mmol, 1.5 eq.), followed by DIEA (0.313 mL, 1.790 mmol, 3 eq.) and HATU (273 mg, 0.718 mmol, 1.2 eq.). The reaction mixture was stirred for 1 h. The excess of solvent was evaporated. The crude product was extracted with DCM and washed with water (×2) and brine (×2). The organic phase was dried over anhydrous $MgSO_4$, filtered and evaporated. The product was purified on a chromatography column with silica gel using DCM/EtOAc (98/2). 159 mg of BDP-2C_8 was obtained (yield = 48%) as an orange powder. R_f = 0.25 (100% DCM). ^{1}H-NMR (400 MHz, $CDCl_3$): δ 6.07 (s, 2H, Hβ), 3.29 (ddd, J = 14.0, 7.4, 1.6 Hz, 2H, 2N-CH), 3.15 (d, J = 7.5 Hz, 2H, 2N-CH), 3.05–3.01 (m, 2H, CH_2), 2.53–2.47 (m, 14H, 4 CH_3, CH_2), 2.05–1.97 (m, 2H, CH_2), 1.67 (s, 1H, CH), 1.60 (s, 1H, CH), 1.36–1.19 (m, 16H, 8CH_2), 0.94–0.86 (m, 12H, 4CH_3). ^{13}C-NMR (101 MHz, $CDCl_3$): δ 171.9, 153.9, 145.7, 140.5, 131.5, 131.5, 121.6, 51.5, 48.9, 38.6, 37.0, 33.0, 30.6, 30.5, 28.8, 28.7, 28.7, 27.7, 27.4, 23.9, 23.8, 23.0, 23.0, 16.4, 14.4, 14.4, 14.4, 14.0, 14.0, 10.8, 10.6, 10.6. HRMS (ESI$^+$), calculated for $C_{33}H_{54}BF_2N_3ONa$ [M + Na]$^+$: 580.4426, found 580.4213. Calculated for $C_{33}H_{54}BFN_3O$ [M − F]$^+$: 538.4344, found 538.4329. Calculated for $C_{33}H_{54}BF_2N_3ONa$ [2M + Na]$^+$: 1137.8554, found 1137.8528.

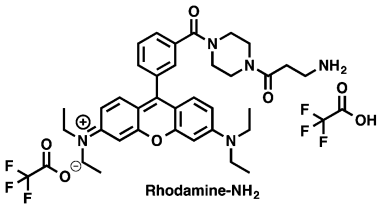

Rhodamine-NH_2. We described the synthesis of rhodamine-NH_2 elsewhere.[37]

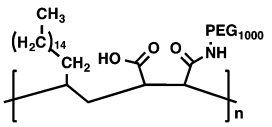

HP1. To a solution of PMAO (30 mg, 85.71 μmol of the repeating unit; see the ESI†) in degassed anhydrous DMF (3 mL) was added a solution of rhodamine-NH_2 (8.57 mol, 69 μL, C = 10 mg mL^{-1} in DMF) followed by DIEA (0.85 mmol, 200 mL, 10 eq.) and a solution of Jeffamine-1000 (1 mL, C = 100 mg mL^{-1} in DMF, 0.102 mmol, 1.2 eq.). The reaction mixture was stirred for 2 h before the addition of a few drops of water. The solvents were evaporated. The crude product was purified using a size exclusion column with DCM/MeOH (1/1). 61 mg of HP1 was obtained as a pink syrup (yield = 53%).

The synthesis of the other polymers can be found in the ESI.†

4.3. Spectroscopy

For spectroscopy, the concentration of BDP-2C_8 was 1 μM and the solvents were of spectroscopic grade. The water used was milliQ water. Absorption and emission spectra were recorded on a Cary 400 Scan ultraviolet-visible spectrophotometer (Varian) and a FluoroMax-4 spectrofluorometer (Horiba Jobin Yvon) equipped with a thermostated cell compartment, respectively. For the standard recording of fluorescence spectra, the emission was collected 10 nm after the excitation wavelength. All the spectra were corrected from the wavelength-dependent response of the detector. The quantum yields were determined by

comparison with fluorescein[43] (in NaOH 0.1 M, ϕ = 0.95) following eqn (1):

$$QY = QY_R \frac{I \times OD_R \times n^2}{I_R \times OD \times n_R^2} \quad (1)$$

where QY is the quantum yield, I is the integrated fluorescence intensity, n is the refractive index, and OD is the optical density at the excitation wavelength. R represents the reference.

4.4. Formulation of the HNPs

Preparation of stock solutions: first, the oil (VEA) was labeled by dissolving BDP-2C_8 at 1 wt%. The labeled oil was then dissolved in dioxane to reach a concentration of 2 mg mL^{-1}. Polymers were dissolved in dioxane at a concentration of 2 mg mL^{-1}. The HNPs were formulated using two different methods: (1) rehydration of films: in a round-bottom flask of 10 mL, 50 μL of premixed solutions of polymer and oil (according to the chosen ratio) were added before being slowly evaporated until a thin film was obtained. Then, 950 μL of PBS was vigorously added by back and forth pipetting using a 1 mL micropipette. (2) Nanoprecipitation: in an Eppendorf tube, stock solutions of polymers and oil (according to the chosen ratio) were added and mixed to reach a final volume of 50 μL. Then, 950 μL of PBS was vigorously added by back and forth pipetting using a 1 mL micropipette. The solution was immediately vortexed for 10 seconds.

4.5. Dynamic light scattering (DLS), and ζ potential

After the formulation, the size of HPNs was measured by dynamic light scattering using the instrument Zetasizer® Nano ZSP (Malvern, UK) involving the formulation solutions. Measurements were performed at 25 °C. Refractive indices were set to 1.33 for the continuous phase (water) and 1.49 for the dispersed phase (vitamin E acetate). Both size distribution and the polydispersity index (PDI) were recorded. The ζ potentials were measured from diluted solutions in distilled water (0.02 μg mL^{-1}) at a stable conductivity of 0.05 mS cm^{-1}.

4.6. Electrophoresis

Gel electrophoresis was prepared by dissolving agarose (0.5 wt%) in TAE (Tris acetate 40 mM, EDTA 1 mM). 13 μL of the formulation solutions were carefully added in the wells. The electrophoresis was run at 125 V for 1 h. The gels were visualized with an ImageQuant LAS 4000 system (GE Healthcare Life Sciences) using Cy2 (excitation: 473 nm) and Cy3 (excitation: 532 nm) channels and by acquiring successive images with an exposition time of 10 seconds. The images were prepared using ImageJ software.

4.7. Stability assay

HNPs composed of HP1 (20 wt%) were formulated as described in 4.4 and placed in a 1.6 mL cuvette for DLS measurement. The cuvette was then closed with the help of an adapted stopper and was warmed at 60 °C in a water bath. At each time point, the solution was rapidly cooled down to RT; then a DLS measurement was performed and 30 μL of the solution was taken off for electrophoresis.

4.8. Transmission electron microscopy (TEM)

5 μL of the formulation solution was deposited onto carbon-coated copper–rhodium electron microscopy grids that were used following amylamine glow-discharge. The grids were then treated for 1 min with a 2% uranyl acetate solution for staining and observed with a Philips CM120 transmission electron microscope equipped with a LaB_6 filament and operating at 100 kV. Areas covered with NPs of interest were recorded on a Peltier cooled CCD camera (Model 794, Gatan, Pleasanton, CA). Image analysis was performed using ImageJ software.

Conflicts of interest

The authors declare no conflicts of interest.

Acknowledgements

This work was supported by the European Research Council (ERC) Consolidator grant BrightSens 648528 and the French National Research Agency (ANR) BrightRiboProbes (ANR-16-CE11-0010). XW was founded by the China Scholarship Council PhD fellowship (CSC No. 201706240033). The authors would like to thank Dr Delphine Garnier from the Analytical platform (PACSI) for her assistance in the LC-MS and RMN analyses. We also thank the Huntsman Corporation for providing Jeffamine-M-1000 and Jeffamine-M-2070.

Notes and references

1 B. Mandal, H. Bhattacharjee, N. Mittal, H. Sah, P. Balabathula, L. A. Thoma and G. C. Wood, Core–shell-Type Lipid–polymer Hybrid Nanoparticles as a Drug Delivery Platform, *Nanomedicine*, 2013, **9**(4), 474–491, DOI: 10.1016/j.nano.2012.11.010.

2 A. A. Khan, J. Mudassir, N. Mohtar and Y. Darwis, Advanced Drug Delivery to the Lymphatic System: Lipid-Based Nanoformulations, *Int. J. Nanomed.*, 2013, **8**, 2733, DOI: 10.2147/IJN.S41521.

3 N. Anton and T. F. Vandamme, The Universality of Low-Energy Nano-Emulsification, *Int. J. Pharm.*, 2009, **377**(1–2), 142–147, DOI: 10.1016/j.ijpharm.2009.05.014.

4 D. J. McClements, Nanoemulsions versus Microemulsions: Terminology, Differences, and Similarities, *Soft Matter*, 2012, **8**(6), 1719–1729, DOI: 10.1039/C2SM06903B.

5 M. Yao, H. Xiao and D. J. McClements, Delivery of Lipophilic Bioactives: Assembly, Disassembly, and Reassembly of Lipid Nanoparticles, *Annu. Rev. Food Sci. Technol.*, 2014, **5**, 53–81, DOI: 10.1146/annurev-food-072913-100350.

6 W. Mehnert and K. Mäder, Solid Lipid Nanoparticles: Production, Characterization and Applications, *Adv. Drug Delivery Rev.*, 2001, **47**(2–3), 165–196.

7 N. Naseri, H. Valizadeh and P. Zakeri-Milani, Solid Lipid Nanoparticles and Nanostructured Lipid Carriers: Structure, Preparation and Application, *Adv. Pharm. Bull.*, 2015, **5**(3), 305, DOI: 10.15171/apb.2015.043.

8 S. Mukherjee, S. Ray and R. S. Thakur, Solid Lipid Nanoparticles: A Modern Formulation Approach in Drug Delivery System, *Indian J. Pharm. Sci.*, 2009, **71**(4), 349, DOI: 10.4103/0250-474X.57282.

9 Q. Li, T. Cai, Y. Huang, X. Xia, S. P. C. Cole and Y. Cai, A Review of the Structure, Preparation, and Application of NLCs, PNPs, and PLNs, *Nanomaterials*, 2017, **7**(6), 122, DOI: 10.3390/nano7060122.

10 M. A. Iqbal, S. Md, J. K. Sahni, S. Baboota, S. Dang and J. Ali, Nanostructured Lipid Carriers System: Recent Advances in Drug Delivery, *J. Drug Targeting*, 2012, **20**(10), 813–830, DOI: 10.3109/1061186X.2012.716845.

11 X. Li, N. Anton, G. Zuber, M. Zhao, N. Messaddeq, F. Hallouard, H. Fessi and T. F. Vandamme, Iodinated α-Tocopherol Nano-Emulsions as Non-Toxic Contrast Agents for Preclinical X-Ray Imaging, *Biomaterials*, 2013, **34**(2), 481–491, DOI: 10.1016/j.biomaterials.2012.09.026.

12 M. F. Attia, N. Anton, M. Chiper, R. Akasov, H. Anton, N. Messaddeq, S. Fournel, A. S. Klymchenko, Y. Mély and T. F. Vandamme, Biodistribution of X-Ray Iodinated Contrast Agent in Nano-Emulsions Is Controlled by the Chemical Nature of the Oily Core, *ACS Nano*, 2014, **8**(10), 10537–10550, DOI: 10.1021/nn503973z.

13 A. Kumari, S. K. Yadav and S. C. Yadav, Biodegradable Polymeric Nanoparticles Based Drug Delivery Systems, *Colloids Surf., B*, 2010, **75**(1), 1–18, DOI: 10.1016/j.colsurfb.2009.09.001.

14 M. Elsabahy and K. L. Wooley, Design of Polymeric Nanoparticles for Biomedical Delivery Applications, *Chem. Soc. Rev.*, 2012, **41**(7), 2545–2561, DOI: 10.1039/c2cs15327k.

15 V. Delplace, P. Couvreur and J. Nicolas, Recent Trends in the Design of Anticancer Polymer Prodrug Nanocarriers, *Polym. Chem.*, 2014, **5**(5), 1529–1544, DOI: 10.1039/C3PY01384G.

16 A. Reisch and A. S. Klymchenko, Fluorescent Polymer Nanoparticles Based on Dyes: Seeking Brighter Tools for Bioimaging, *Small*, 2016, **12**(15), 1968–1992, DOI: 10.1002/smll.201503396.

17 N. Kamaly, B. Yameen, J. Wu and O. C. Farokhzad, Degradable Controlled-Release Polymers and Polymeric Nanoparticles: Mechanisms of Controlling Drug Release, *Chem. Rev.*, 2016, **116**(4), 2602–2663, DOI: 10.1021/acs.chemrev.5b00346.

18 K. Raemdonck, K. Braeckmans, J. Demeester and S. C. D. Smedt, Merging the Best of Both Worlds: Hybrid Lipid-Enveloped Matrix Nanocomposites in Drug Delivery, *Chem. Soc. Rev.*, 2013, **43**(1), 444–472, DOI: 10.1039/C3CS60299K.

19 R. X. Zhang, T. Ahmed, L. Y. Li, J. Li, A. Z. Abbasi and X. Y. Wu, Design of Nanocarriers for Nanoscale Drug Delivery to Enhance Cancer Treatment Using Hybrid Polymer and Lipid Building Blocks, *Nanoscale*, 2017, **9**(4), 1334–1355, DOI: 10.1039/C6NR08486A.

20 K. Hadinoto, A. Sundaresan and W. S. Cheow, Lipid–polymer Hybrid Nanoparticles as a New Generation Therapeutic Delivery Platform: A Review, *Eur. J. Pharm. Biopharm.*, 2013, **85**(3 Part A), 427–443, DOI: 10.1016/j.ejpb.2013.07.002.

21 V. Dave, K. Tak, A. Sohgaura, A. Gupta, V. Sadhu and K. R. Reddy, Lipid-Polymer Hybrid Nanoparticles: Synthesis Strategies and Biomedical Applications, *J. Microbiol. Methods*, 2019, **160**, 130–142, DOI: 10.1016/j.mimet.2019.03.017.

22 L. Zhang and L. Zhang, Lipid–polymer Hybrid Nanoparticles: Synthesis, Characterization and Applications, *Nano LIFE*, 2010, **01**(01n02), 163–173, DOI: 10.1142/S179398441000016X.

23 K. S. Oh, K. E. Lee, S. S. Han, S. H. Cho, D. Kim and S. H. Yuk, Formation of Core/Shell Nanoparticles with a Lipid Core and Their Application as a Drug Delivery System, *Biomacromolecules*, 2005, **6**(2), 1062–1067, DOI: 10.1021/bm049234r.

24 M. F. Attia, S. M. Dieng, M. Collot, A. S. Klymchenko, C. Bouillot, C. A. Serra, M. Schmutz, M. Er-Rafik, T. F. Vandamme and N. Anton, Functionalizing Nanoemulsions with Carboxylates: Impact on the Biodistribution and Pharmacokinetics in Mice, *Macromol. Biosci.*, 2017, **17**(7), 1600471, DOI: 10.1002/mabi.201600471.

25 N. T. Huynh, C. Passirani, P. Saulnier and J. P. Benoit, Lipid nanocapsules: A New Platform for Nanomedicine, *Int. J. Pharm.*, 2009, **379**(2), 201–209, DOI: 10.1016/j.ijpharm.2009.04.026.

26 I. Texier, M. Goutayer, A. Da Silva, L. Guyon, N. Djaker, V. Josserand, E. Neumann, J. Bibette and F. Vinet, Cyanine-Loaded Lipid Nanoparticles for Improved in Vivo Fluorescence Imaging, *J. Biomed. Opt.*, 2009, **14**(5), 054005, DOI: 10.1117/1.3213606.

27 R. Bouchaala, L. Mercier, B. Andreiuk, Y. Mély, T. Vandamme, N. Anton, J. G. Goetz and A. S. Klymchenko, Integrity of Lipid Nanocarriers in Bloodstream and Tumor Quantified by Near-Infrared Ratiometric FRET Imaging in Living Mice, *J. Controlled Release*, 2016, **236**, 57–67, DOI: 10.1016/j.jconrel.2016.06.027.

28 X. Wang, N. Anton, P. Ashokkumar, H. Anton, T. K. Fam, T. Vandamme, A. S. Klymchenko and M. Collot, Optimizing the Fluorescent Properties of Nanoemulsions for Single Particle Tracking in Live Cells, *ACS Appl. Mater. Interfaces*, 2019, **11**, 13079–13090, DOI: 10.1021/acsami.8b22297.

29 V. N. Kilin, H. Anton, N. Anton, E. Steed, J. Vermot, T. F. Vandamme, Y. Mely and A. S. Klymchenko, Counterion-Enhanced Cyanine Dye Loading into Lipid Nano-Droplets for Single-Particle Tracking in Zebrafish, *Biomaterials*, 2014, **35**(18), 4950–4957, DOI: 10.1016/j.biomaterials.2014.02.053.

30 A. S. Klymchenko, E. Roger, N. Anton, H. Anton, I. Shulov, J. Vermot, Y. Mely and T. F. Vandamme, Highly Lipophilic Fluorescent Dyes in Nano-Emulsions: Towards Bright Non-Leaking Nano-Droplets, *RSC Adv.*, 2012, **2**(31), 11876–11886, DOI: 10.1039/C2RA21544F.

31 M. Hanauer, S. Pierrat, I. Zins, A. Lotz and C. Sönnichsen, Separation of Nanoparticles by Gel Electrophoresis According to Size and Shape, *Nano Lett.*, 2007, **7**(9), 2881–2885, DOI: 10.1021/nl071615y.

32 A. I. López-Lorente, B. M. Simonet and M. Valcárcel, Electrophoretic Methods for the Analysis of Nanoparticles, *TrAC, Trends Anal. Chem.*, 2011, **30**(1), 58–71, DOI: 10.1016/j.trac.2010.10.006.

33 A. Quarta, A. Curcio, H. Kakwere and T. Pellegrino, Polymer Coated Inorganic Nanoparticles: Tailoring the Nanocrystal Surface for Designing Nanoprobes with Biological Implications, *Nanoscale*, 2012, **4**(11), 3319–3334, DOI: 10.1039/C2NR30271C.

34 A. Hlaváček, A. Sedlmeier, P. Skládal and H. H. Gorris, Electrophoretic Characterization and Purification of

Silica-Coated Photon-Upconverting Nanoparticles and Their Bioconjugates, *ACS Appl. Mater. Interfaces*, 2014, **6**(9), 6930–6935, DOI: 10.1021/am500732y.

35 M. T. Fernández-Argüelles, A. Yakovlev, R. A. Sperling, C. Luccardini, S. Gaillard, A. Sanz Medel, J.-M. Mallet, J.-C. Brochon, A. Feltz and M. Oheim, *et al.*, Synthesis and Characterization of Polymer-Coated Quantum Dots with Integrated Acceptor Dyes as FRET-Based Nanoprobes, *Nano Lett.*, 2007, **7**(9), 2613–2617, DOI: 10.1021/nl070971d.

36 T. Pellegrino, R. A. Sperling, A. P. Alivisatos and W. J. Parak, Gel Electrophoresis of Gold-DNA Nanoconjugates, *J. Biomed. Biotechnol.*, 2007, **2007**, e26796, DOI: 10.1155/2007/26796.

37 O. Dukhno, F. Przybilla, M. Collot, A. Klymchenko, V. Pivovarenko, M. Buchner, V. Muhr, T. Hirsch and Y. Mély, Quantitative Assessment of Energy Transfer in Upconverting Nanoparticles Grafted with Organic Dyes, *Nanoscale*, 2017, **9**(33), 11994–12004, DOI: 10.1039/C6NR09706E.

38 I. Shulov, S. Oncul, A. Reisch, Y. Arntz, M. Collot, Y. Mely and A. S. Klymchenko, Fluorinated Counterion-Enhanced Emission of Rhodamine Aggregates: Ultrabright Nanoparticles for Bioimaging and Light-Harvesting, *Nanoscale*, 2015, **7**(43), 18198–18210, DOI: 10.1039/c5nr04955e.

39 K. Trofymchuk, J. Valanciunaite, B. Andreiuk, A. Reisch, M. Collot and A. S. Klymchenko, BODIPY-Loaded Polymer Nanoparticles: Chemical Structure of Cargo Defines Leakage from Nanocarrier in Living Cells, *J. Mater. Chem. B*, 2019, **7**(34), 5199–5210, DOI: 10.1039/C8TB02781A.

40 S. Choi, J. Bouffard and Y. Kim, Aggregation-Induced Emission Enhancement of a Meso-Trifluoromethyl BODIPY via J-Aggregation, *Chem. Sci.*, 2013, **5**(2), 751–755, DOI: 10.1039/C3SC52495G.

41 X. Li, N. Anton, G. Zuber, M. Zhao, N. Messaddeq, F. Hallouard, H. Fessi and T. F. Vandamme, Iodinated α-Tocopherol Nano-Emulsions as Non-Toxic Contrast Agents for Preclinical X-Ray Imaging, *Biomaterials*, 2013, **34**(2), 481–491, DOI: 10.1016/j.biomaterials.2012.09.026.

42 M. F. Attia, N. Anton, M. Chiper, R. Akasov, H. Anton, N. Messaddeq, S. Fournel, A. S. Klymchenko, Y. Mély and T. F. Vandamme, Biodistribution of X-Ray Iodinated Contrast Agent in Nano-Emulsions Is Controlled by the Chemical Nature of the Oily Core, *ACS Nano*, 2014, **8**(10), 10537–10550, DOI: 10.1021/nn503973z.

43 J. R. Lakowicz, *Principles of Fluorescence Spectroscopy*, Springer Science & Business Media, 2007.

2.2 Supplementary information

Synthesis

- Synthesis of BDP-2C_8

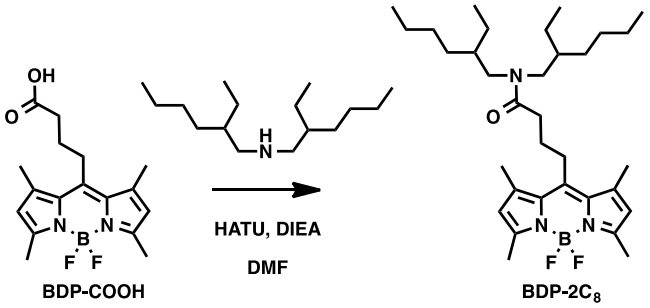

BDP-2C_8. To a solution of acid BDP-COOH[1] (200 mg, 0.598 mmol, 1 eq) in DMF (4 mL) under Ar atm, bis(2-ethylhexyl)amine (0.270 mL, 0.897 mmol, 1.5 eq) was added, followed by DIEA (0.313 mL, 1.790 mmol, 3 eq) and HATU (273 mg, 0.718 mmol, 1 .2 eq). The reaction mixture was allowed to stir for 1h. The excess of solvent was evaporated. The crude was extracted with DCM and washed with water (x2) and brine (x2). The organic phase was dried over anhydrous $MgSO_4$, filtered and evaporated. The product was purified by chromatography column on sicila gel using DCM/EtOAc (98/2). 159 mg of BDP-2C_8 was obtained (Yield= 48%) as an orange powder. Rf= 0.25 (100% DCM). ^{1}H-NMR (400 MHz, $CDCl_3$): δ 6.07 (s, 2H, H), 3.29 (ddd, *J* = 14.0, 7.4, 1.6 Hz, 2H, 2 N-CH), 3.15 (d, *J* = 7.5 Hz, 2H, 2 N-CH), 3.05-3.01 (m, 2H, CH_2), 2.53-2.47 (m, 14H, 4 CH_3, CH_2), 2.05-1.97 (m, 2H, CH_2), 1.67 (s, 1H, CH), 1.60 (s, 1H, CH), 1.36-1.19 (m, 16H, 8 CH_2), 0.94-0.86 (m, 12H, 4 CH_3). ^{13}C-NMR (101 MHz, $CDCl_3$): δ 171.9, 153.9, 145.7, 140.5, 131.5, 131.5, 121.6, 51.5, 48.9, 38.6, 37.0, 33.0, 30.6, 30.5, 28.8, 28.7, 28.7, 27.7, 27.4, 23.9, 23.8, 23.0, 23.0, 16.4, 14.4, 14.4, 14.4, 14.0, 14.0, 10.8, 10.6, 10.6. HRMS (ESI^+), calculated for $C_{33}H_{54}BF_2N_3ONa$ $[M+Na]^+$: 580.4426, found 580.4213. Calculated for $C_{33}H_{54}BFN_3O$ $[M-F]^+$: 538.4344, found 538.4329. Calculated for $C_{33}H_{54}BF_2N_3ONa$ $[2M+Na]^+$: 1137.8554, found 1137.8528.

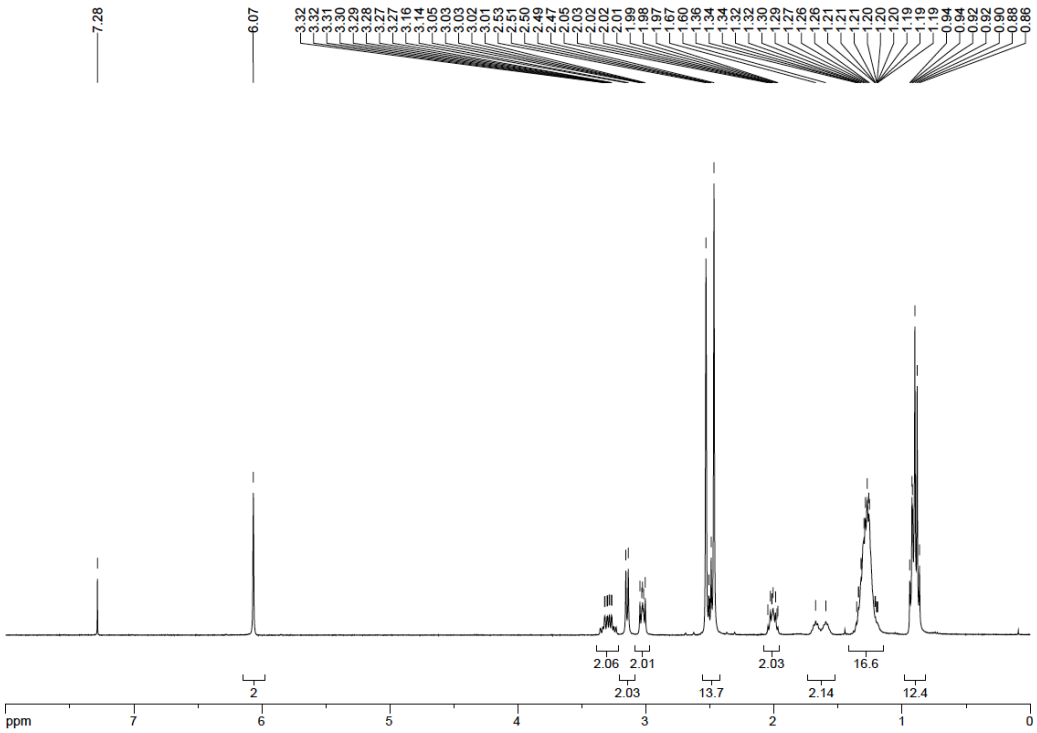

^{1}H NMR spectrum of BDP-2C$_8$

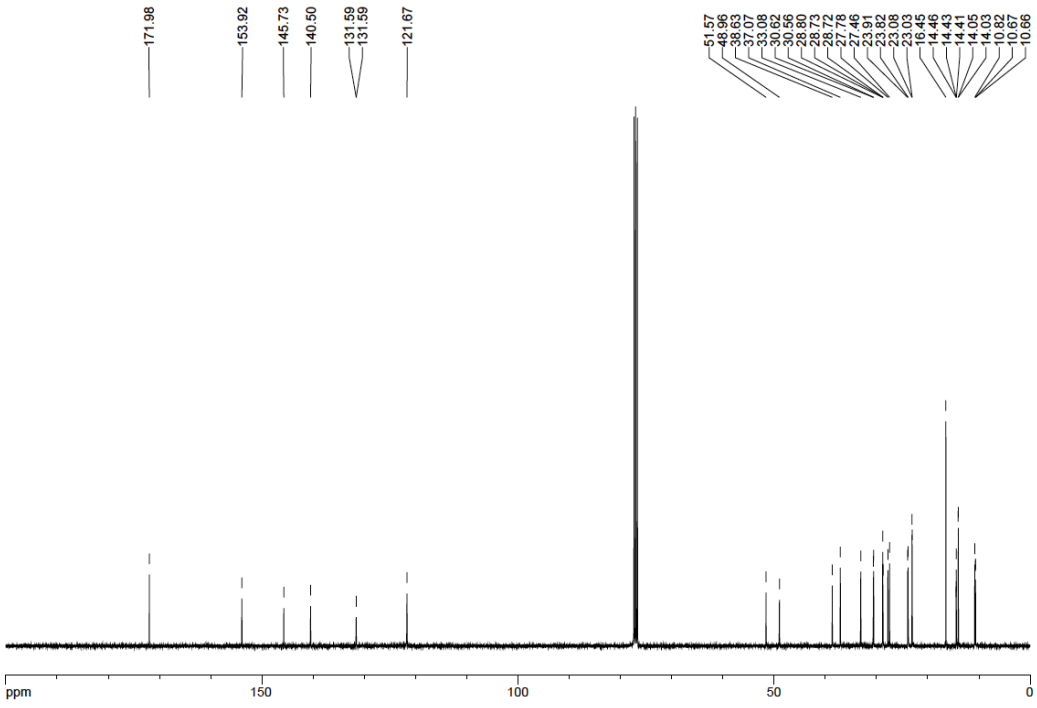

^{13}C NMR spectrum of BDP-2C$_8$

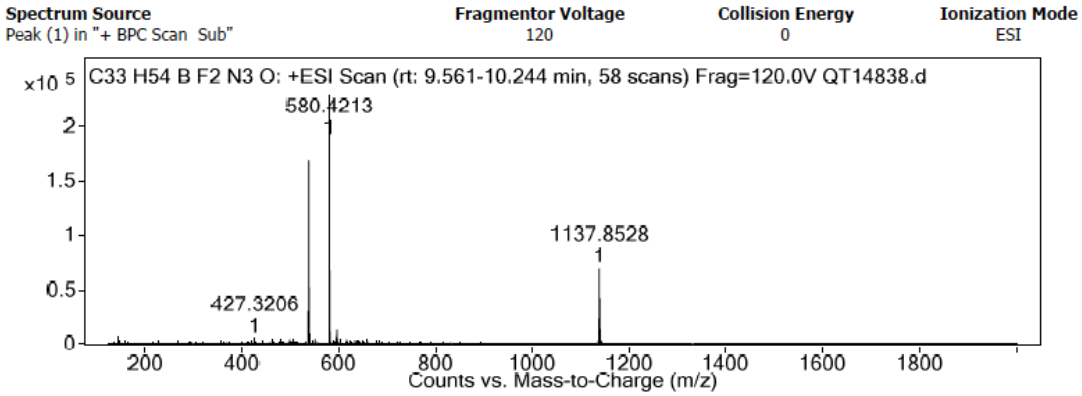

HRMS spectrum of BDP-2C$_8$

- Synthesis of Rhodamine-NH$_2$

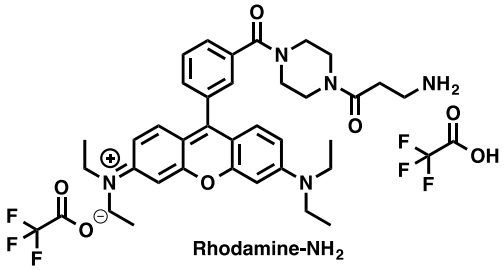

We described the synthesis of rhodamine-NH$_2$ elsewhere.[2]

- Synthesis of amphiphilic polymer

PMAO is sold with an average Mn of 30,000-50,000, which makes a polymer with ~100-140 repeating units per polymer molecule: M_n is the molecular weight of the repeating unit A.

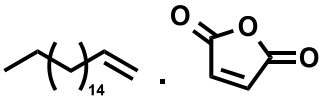

A
Repeating unit of PMAO
M= 350 g. mol^{-1}

For the synthesis, PMAO was considered as a single molecule of the repeating unit A with a molecular weight of 350 g.mol^{-1}.

Typical procedure

HP1. To a solution of PMAO (30 mg, 85.71 mol) in degased anhydrous DMF (3 mL) was added a solution of a Rhodamine-NH$_2$ (8.57 mol, 69 µL C=10 mg/mL in DMF) followed by DIEA (0.85 mmol, 200 mL, 10 eq) and a solution of Jeffamine-1000 (1 mL, C=100 mg/mL in DMF, 0.102 mmol, 1.2 eq). The reaction mixture was allowed to stir for 2h before the addition of few drops of water. The solvents were evaporated. The crude was purified by size exclusion column using DCM/MeOH (1/1). 61 mg of HP1 was obtained as a pink sirup (Yield= 53%).

The composition of the polymers were confirmed and characterization using ^{1}H NMR. The PEGylation yield was determined by dividing the integration value of the signal of the terminal methoxy group (OMe) of the PEG at 3.3 ppm with the CH_3 signal of the hydrocarbon chain at 0.8 ppm. The PEGylation yields were all above 80%.

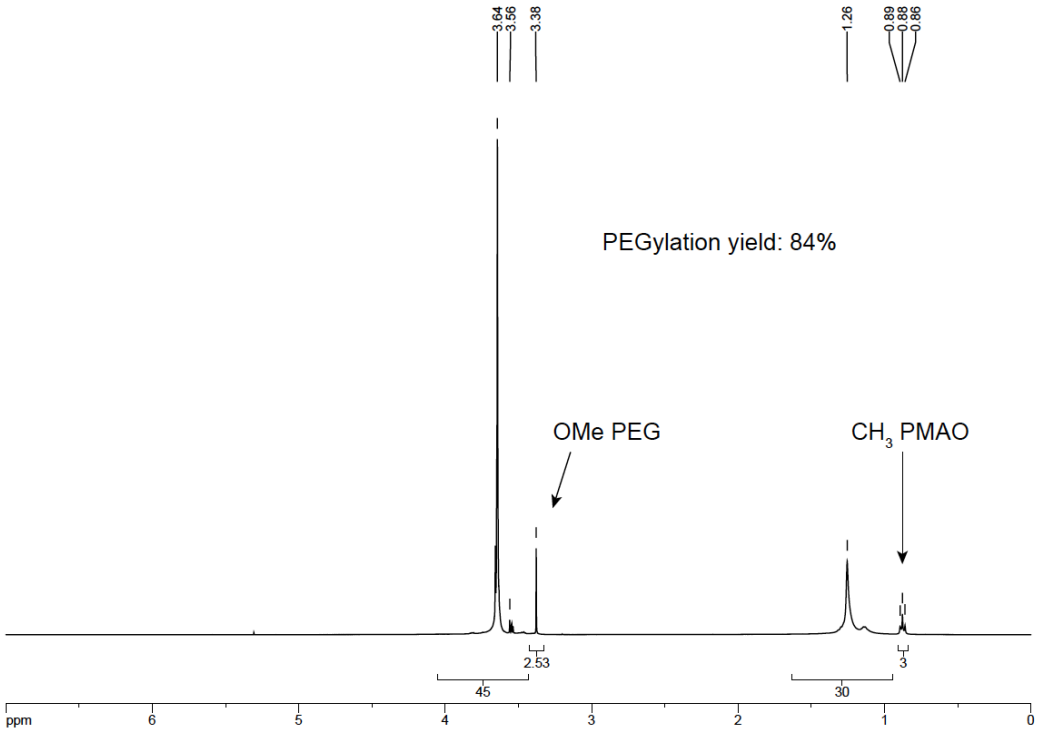

^{1}H NMR spectrum of HP1 ($CDCl_3$, 400 MHz)

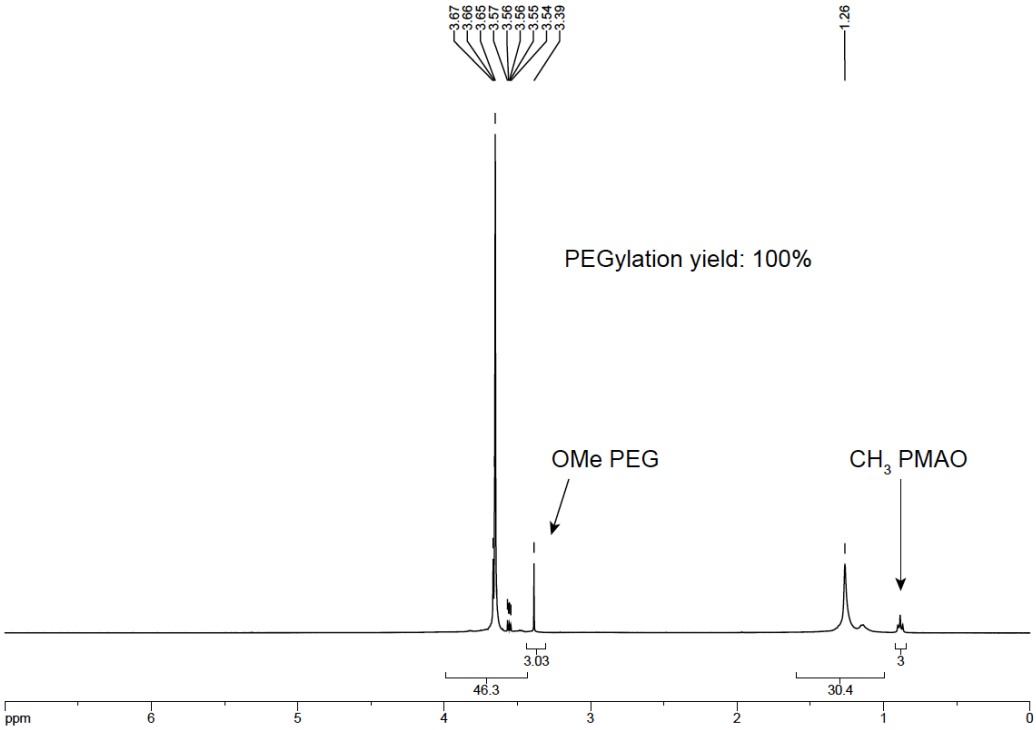

^{1}H NMR spectrum of HP1c ($CDCl_3$, 400 MHz)

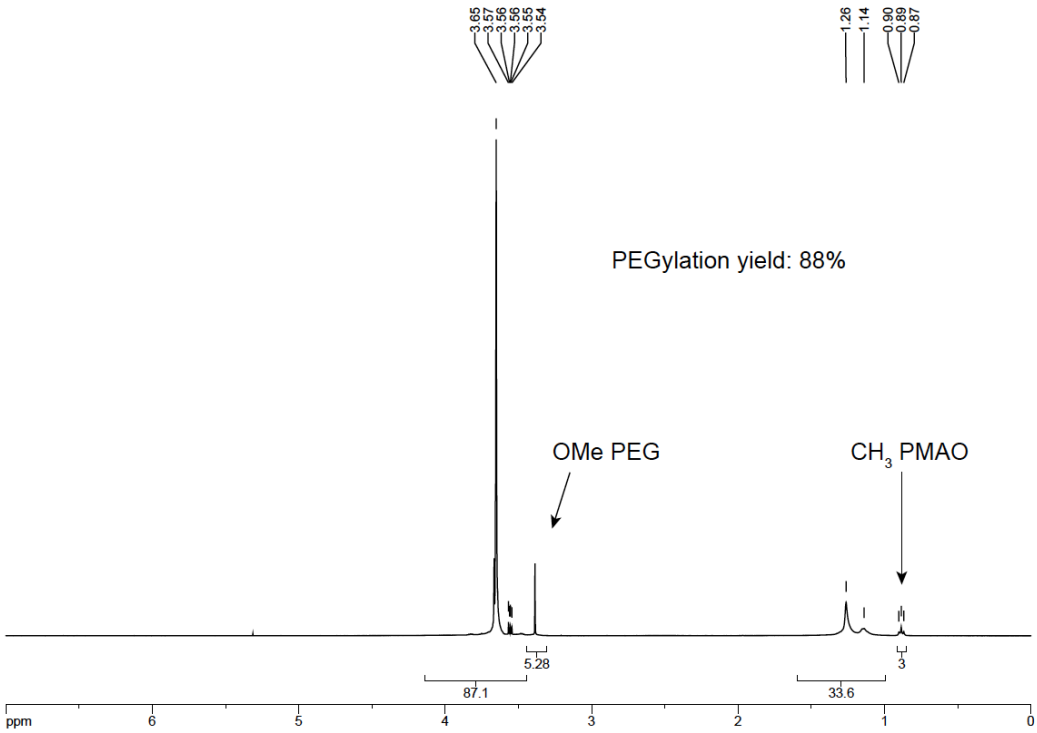

^{1}H NMR spectrum of FP1 ($CDCl_3$, 400 MHz)

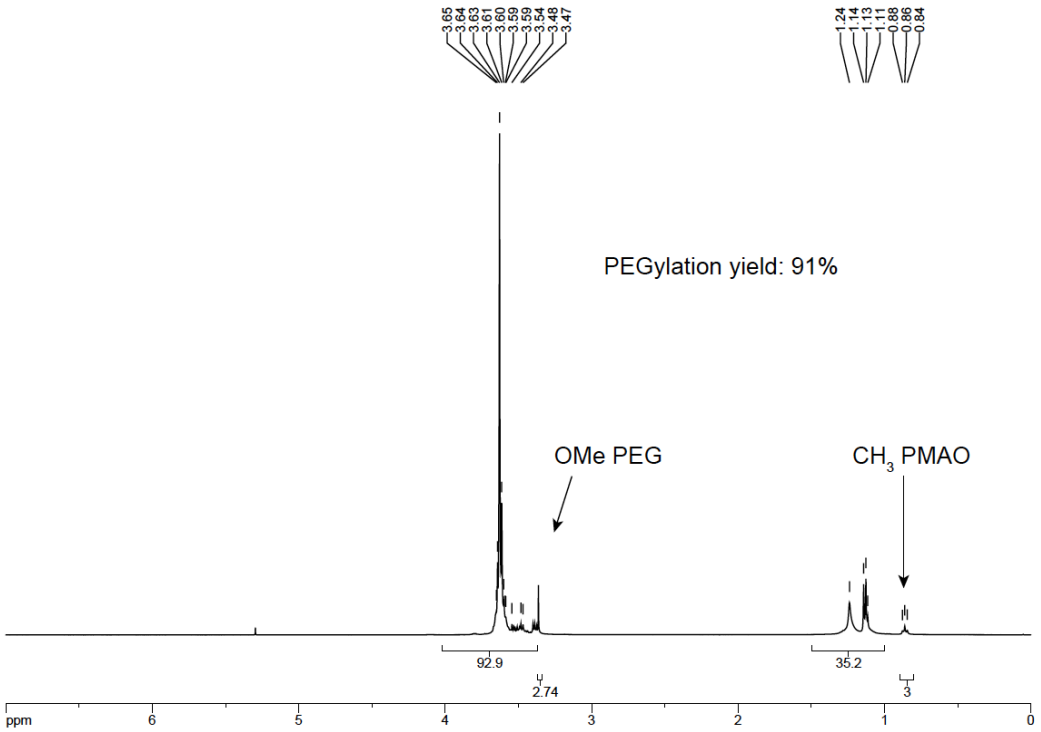

^{1}H NMR spectrum of HP2 ($CDCl_3$, 400 MHz)

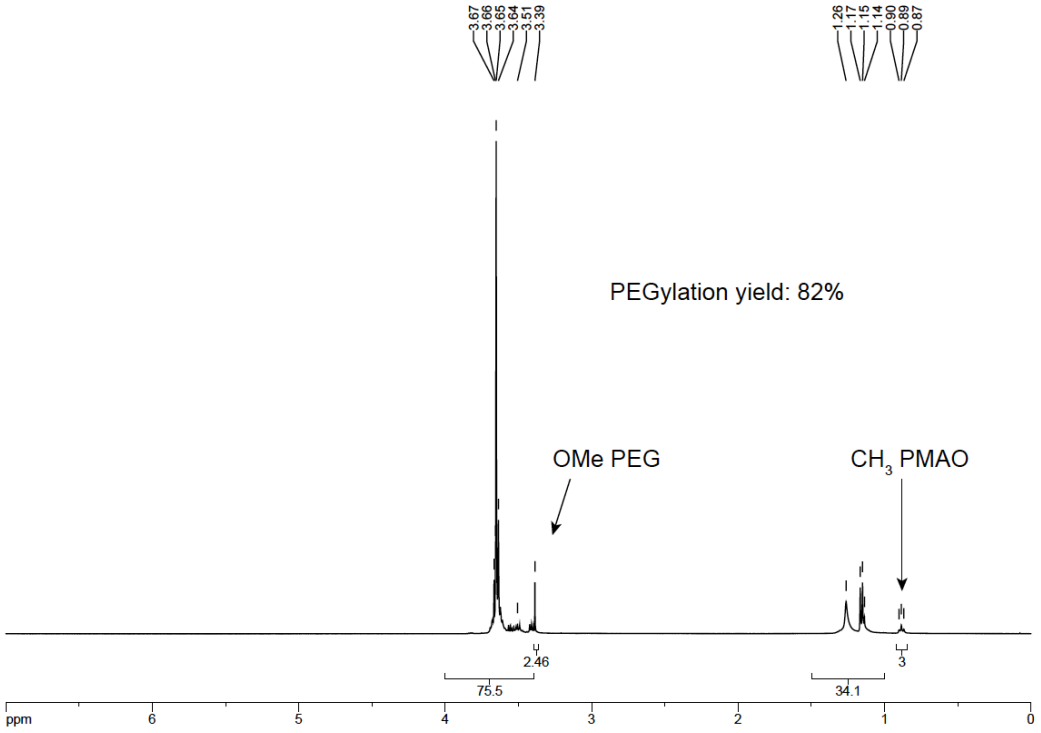

^{1}H NMR spectrum of HP2c ($CDCl_3$, 400 MHz)

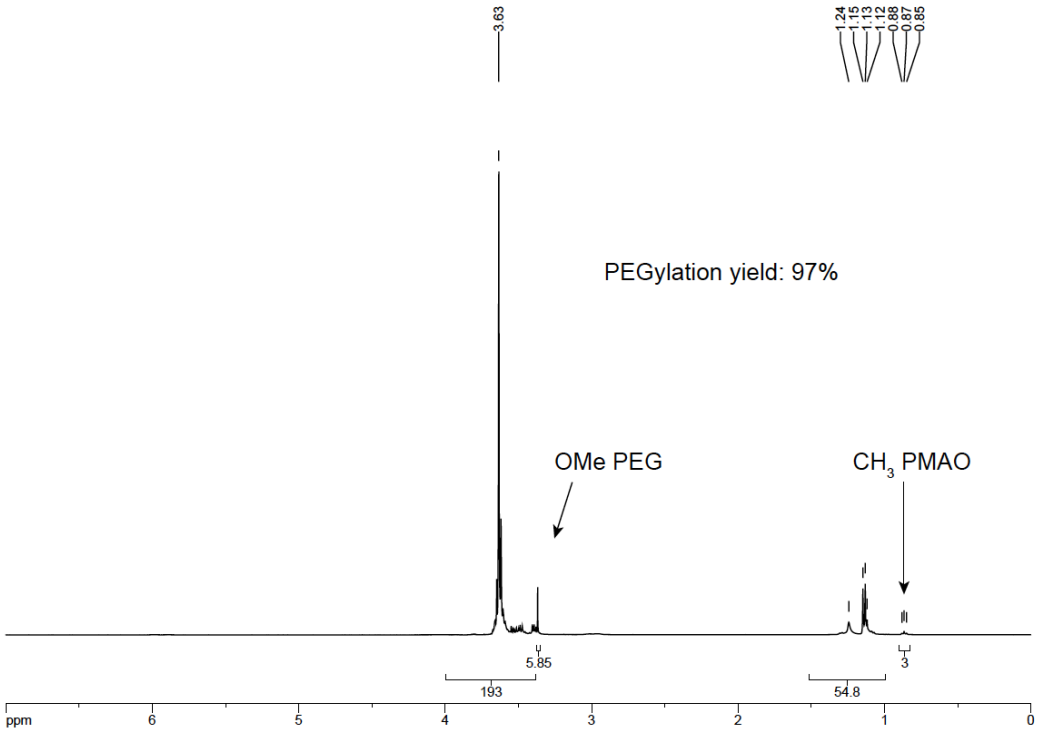

^{1}H NMR spectrum of FP2 ($CDCl_3$, 400 MHz)

Spectroscopic studies of BDP-2C$_8$

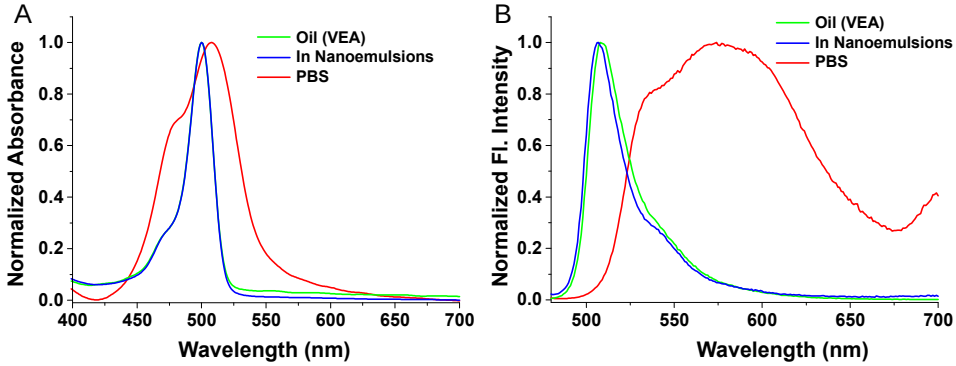

Figure S1. Normalized absorption (A) and emission (B) spectra of BDP-2C$_8$ at 1 µM in various media. In PBS (red lines), the broadening of the spectra and the red shift in emission are typical signs of aggregation. Excitation wavelength was 470 nm.

Table S1. Photophysical properties of BDP-2C$_8$.

	$\lambda_{ABS_{max}}$ (nm)	ε (M^{-1}.cm^{-1})	FWHM[b] (nm)	$\lambda_{Em_{max}}$ (nm)	FWHM[b] (nm)	f [c]
VEA	500	93,000	23	507	24	0.82
NE[a]	501	86,300	23	510	29	0.93
PBS	508	31,100	63	577	113	0.19

[a] Nano-emulsions (44 nm) obtained by spontaneous emulsification in PBS of 1 wt % BDP-2C$_8$ loaded-VEA in the presence of 50 wt % Kolliphor ELP® as surfactant.
[b] FWHM is the Full Width at Half maximum of the peak, this value depicts the broadness of the peak.
[c] Fluorescein (in 0.1 M naOH in water) was used as reference.

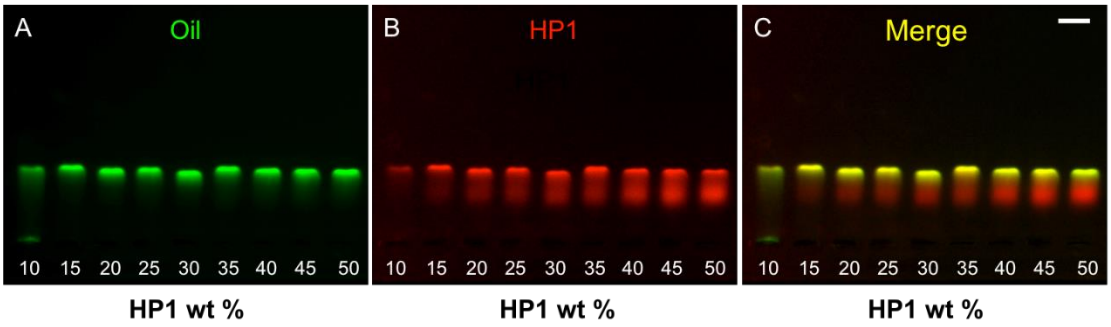

Figure S2. Electrophoresis revealed in the green channel (A) red channel (B) and the merged channel (C) of formulation obtained with various polymer/oil wt %. The concentration of oil (containing 1 wt % BDP-2C$_8$) was fixed at 80 μg/mL and the amount of HP1 was increased according to the indicated HP1 wt %. Scale bar is 0.5 cm.

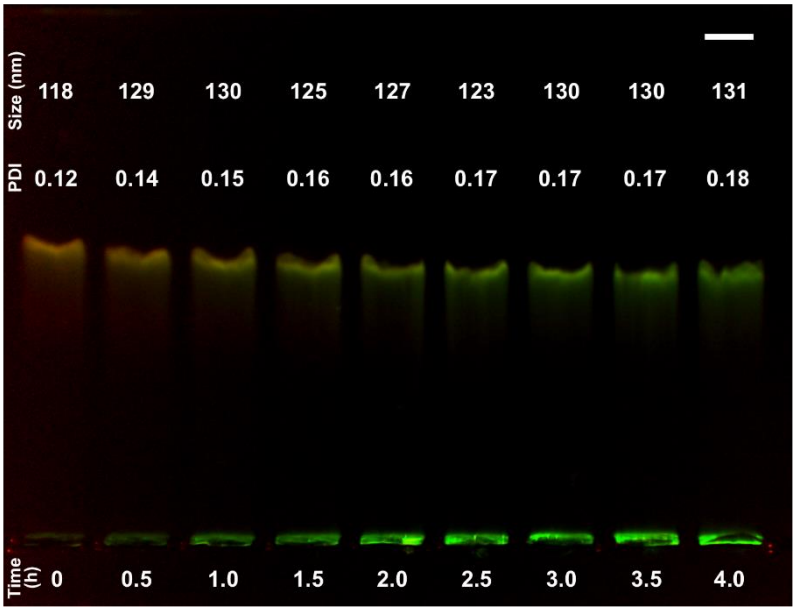

Figure S3. Stability of HNPs (20 wt %) over 4 h at 60°C. The figure features the merged green and red channels of the electrophoresis image as well as the size and PDI measured by DLS for each time points. Scale bar is 0.5 cm.

Table S2. Measured ζ potential of PMAO-based amphiphilic polymers formulated at 0.02 μg/mL in distilled water. Conductivity was at 0.05 mS/cm.

Polymer	HP1	HP2	HP1c	HP2c	FP1	FP2
ζ (mV)	-24	-29	-26	-21	-28	-28

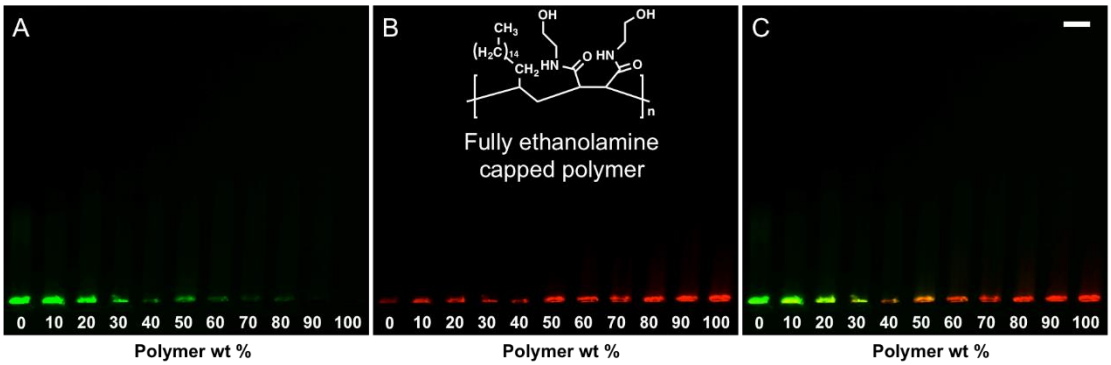

Figure S4. Electrophoresis revealed in the green channel (A) red channel (B) and the merged channel (C) of formulation obtained with various fully ethanolamine-capped polymer/oil wt %. Scale bar is 0.5 cm.

References

(1) Trofymchuk, K.; Valanciunaite, J.; Andreiuk, B.; Reisch, A.; Collot, M.; Klymchenko, A. S. BODIPY-Loaded Polymer Nanoparticles: Chemical Structure of Cargo Defines Leakage from Nanocarrier in Living Cells. *J. Mater. Chem. B* **2019**, *7* (34), 5199–5210. https://doi.org/10.1039/C8TB02781A.

(2) Dukhno, O.; Przybilla, F.; Collot, M.; Klymchenko, A.; Pivovarenko, V.; Buchner, M.; Muhr, V.; Hirsch, T.; Mély, Y. Quantitative Assessment of Energy Transfer in Upconverting Nanoparticles Grafted with Organic Dyes. *Nanoscale* **2017**, *9* (33), 11994–12004. https://doi.org/10.1039/C6NR09706E.

Journal of Materials Chemistry B

ROYAL SOCIETY OF CHEMISTRY

PAPER

View Article Online
View Journal

Cite this: DOI: 10.1039/d0tb00783h

Near infrared fluorogenic probe as a prodrug model for evaluating cargo release by nanoemulsions†

Sophie Bou,[a] Xinyue Wang,[b] Nicolas Anton,[b] Andrey S. Klymchenko[a] and Mayeul Collot*[a]

Received 23rd March 2020,
Accepted 1st May 2020

DOI: 10.1039/d0tb00783h

rsc.li/materials-b

Nanoemulsions (NEs) are biocompatible and stealth nanodroplets that can efficiently encapsulate hydrophobic cytoactive drugs in their oily core. NEs were shown to accumulate in tumors by enhanced permeability and retention (EPR) effect and thus display appealing features as nanocarriers to selectively deliver drugs to the tumors. However, to ensure efficient encapsulation with minimal early release, drugs must possess a high degree of lipophilicity. To circumvent this limitation, the latter could be transformed into prodrugs with enhanced hydrophobicity. In return, once delivered in the cell, the prodrug must be efficiently transformed into its active drug form. Herein we chemically and reversibly modified a near infrared Huda dye (HD) into pro-fluorophore (Pro-HD), a non-fluorescent and lipophilic prodrug model that was efficiently loaded in NEs. Thanks to the fluorogenecity of the system (fluorescence enhancement of 35-fold at 723 nm), we demonstrated that Pro-HD did not leak out of NEs, was efficiently delivered into cancer cells and was transformed *in cellulo* into HD. This proof of concept demonstrates the high potential of lipophilic "pro-fluorophore" approach for visualizing delivery of cargos using NEs as nanocarriers.

Introduction

Over the last 20 years nanoparticles (NPs) have drawn particular attention in medicine, especially in the field of cancers.[1,2] Indeed, NPs can improve three different aspects of cancer therapy: the tumor imaging, the diagnosis and the treatment.[3–7] The treatment of tumors can be achieved by specific drug delivery targeted by nanoparticles,[8] including polymeric NPs,[9,10] inorganic NPs,[11] hydrogels,[12] lipid polymer hybrid NPs,[13–15] liposomes[16] and solid lipid nanoparticles,[17] thus avoiding side effects of the conventional chemotherapy. Although inorganic NPs (*e.g.* quantum dots, iron oxide or gold NPs) and organic NPs (*e.g.* liposomes, polymeric NPs) can specifically target tumors by vectorization using ligands like RGD[18] or folic acid,[19,20] their drug loading remains overall limited.[21] Among NPs, nanoemulsions (NEs) that are composed of an oily core and a surfactant shell (see Fig. 1A) display attractive features: first, their lipid core enables the encapsulation of an impressive quantity of lipophilic cargos. Then NEs are stealth and constituted of biocompatible components that can be injected in the bloodstream. Finally, their preparation, based on spontaneous emulsification, is readily accessible.[22–24] Unlike polymeric NPs, the functionalization of NEs by specific ligands for vectorization remains difficult and is still limited to the cellular level.[25–28] However, it was recently shown using *in vivo* fluorescence imaging that, when injected in mice, NEs spontaneously accumulated in tumors by enhanced permeability and retention (EPR) effect.[29,30] This phenomenon was observed for solid tumors and it was shown that molecules/particles tend to preferentially accumulate in tumor tissues

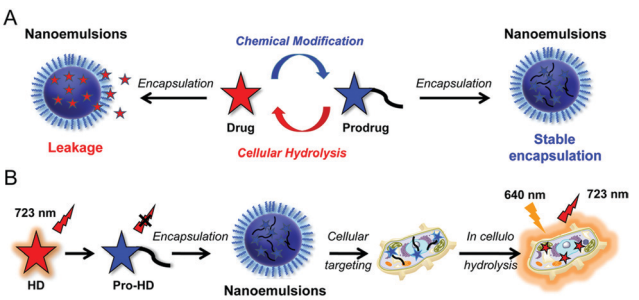

Fig. 1 Schematic principle of a prodrug for enhanced encapsulation in NEs (A) and of the developed HD/Pro-HD system as a model to monitor the drug delivery by NEs (B).

[a] *Laboratory of Biophotonic and Pathologies, CNRS UMR 7021, Université de Strasbourg, Faculté de Pharmacie, 74, Route du Rhin, 67401 Illkirch, France*
[b] *Université de Strasbourg, CNRS, CAMB UMR 7199, F-67000 Strasbourg, France. E-mail: mayeul.collot@unistra.fr*

† Electronic supplementary information (ESI) available. See DOI: 10.1039/d0tb00783h

allowing a faster growth of the tumor compared to other tissues. Consequently, NEs present appealing features to selectively deliver drugs to the tumors. However, loading NEs with cytoactive drugs requires the latter to be solubilized in the oily core and therefore is limited to highly lipophilic drugs. Previously, it was shown that Nile Red, a model of lipophilic drugs, should be modified with lipophilic groups to ensure efficient loading into NPs and to prevent its rapid leakage into biological media.[31] Unfortunately, most of the drugs do not display a sufficient lipophilic nature to fulfill this requirement. Indeed, common drugs used for chemotherapy medication to treat cancers including: docetaxel, bleomycin, vincristine, prednisolone or doxorubicin, possess several free polar hydroxyl groups. In order to circumvent this issue, a prodrug with a significantly enhanced hydrophobicity compared to its corresponding active drug could be used to be efficiently loaded in NEs.[32,33] In return, this chemical modification has to be reversible once the cell target reached in order to release the active drug (Fig. 1A).[34] In order to enhance the lipophilicity of the drugs, the above-mentioned hydroxyl functions can be used to introduce a hydrophobic vector. Carboxylic acids and alcohol functions are readily chemically transformed into esters that can be hydrolyzed *in cellulo* by specific enzymes called esterases.[35] It is noteworthy that this strategy is actually used for decades since the most famous drug, namely aspirin is the acetylated prodrug of salicylic acid.[36]

Although acetylation is a widely used prodrug strategy, it is not adapted for encapsulation in NEs due to the weak lipophilicity brought by the acetate group. Conversely, caprylic acid is a hydrophobic C_8 fatty acid, naturally present in mammals' milk and coconut oil. Moreover, unlike esters with longer chain, caprylic esters have been shown to be readily hydrolyzed by lipases and esterases.[35] Consequently, esterification of drugs into caprylic esters could be used to transform drugs into prodrugs with enhanced lipophilicity. In order to confirm this hypothesis, we herein developed Pro-HD, a fluorogenic drug model based on the esterification of a fluorescent probe (Fig. 1B). The esterified HD called Pro-HD is virtually non-fluorescent and upon hydrolysis releases HD that provokes a fluorescence enhancement of 35-fold in the near-infrared thus making it an efficient system to evaluate the cellular delivery of prodrug by NEs.

Results and discussion

Design and principle

In this work we aimed at developing a pro-fluorophore as a prodrug model in order to study by fluorescence imaging its ability to be efficiently delivered by NEs as biocompatible nanocarriers. In addition to its ability to be transformed into the corresponding drug, the encapsulated prodrug should possess two main features: (1) It has to be soluble in oil to be efficiently carried by NEs. (2) It should not leak out of the NE before reaching its cellular target (Fig. 1A).[31] Indeed, if leakage occurs, the uncontrolled release of the cytoactive molecule can lead to negative side effects on healthy cells. Our work relies on the chemical transformation of an emissive fluorescent dye into a hydrophobic and non-emissive pro-dye. The latter bears a hydrophobic vector that quenches or decreases the brightness. After delivery of the pro-fluorophore into the cells, the vector must be cleavable by a cellular process to reveal the fluorescence of the corresponding dye (Fig. 1B). This last step implies that the vector must be biocompatible, avoiding side effects after its cleavage. Dihydroxyxanthene hemicyanines also referred to "Huda dyes" (HD)[37] are recently developed fluorophores, featuring high brightness and narrow emission band in the near-infrared region (NIR).[38] Due to these interesting features these fluorophores served to develop efficient probes for hypoxia,[39] hydrazine,[40] pH,[41,42] calcium[43] and enzyme activity.[44] Moreover, their spectral properties, including emission in the NIR, make HD probes suitable for *in vivo* imaging.[39,45] For these reasons we intended to synthesize a fluorogenic probe based on HD that will display a high degree of hydrophobicity and that could be reversibly turned off by esterification (Scheme 1). To this aim, we designed Pro-HD that possesses several features: (1) the indoleninium moiety bears an octadecyl alkyl chain to maximize the hydrophobicity. (2) The phenolic moiety bears a chlorine atom at the *ortho* position to lower the pK_a of the probe as shown previously.[41,46] The addition of the chlorine atom leads to a probe with a reported pK_a of 6.2, thus ensuring formation of the brighter phenolate form of HD when exposed to the cytosol.[41] (3) The hydroxyl group was esterified into a caprylic ester as a lipophilic, biocompatible and cleavable vector.[35] (4) Finally, small hydrophobic counterion iodide was replaced with bulky hydrophobic counterion of tetraphenylborate family (F_5-TPB), which is important to further increase lipophilicity of cationic dyes.[47]

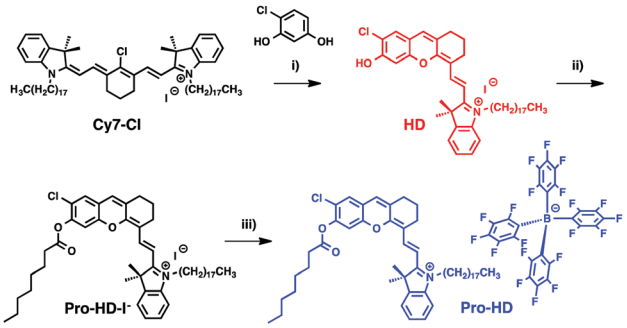

Scheme 1 Synthesis of HD and Pro-HD. (i) NEt_3, DMF, 75 °C, 2 h (ii) caprylic acid, EDC, DMAP, DCM, RT, overnight (iii) F_5-TPB-Li, DCM, RT, 5 min.

Synthesis of the probe

A common access to HD dyes consists in condensing an electron rich phenol on a carbocyanine 7-Cl.[38] Herein, Cy7-Cl bearing two octadecane chains was prepared (see ESI†) before being reacted with chlororesorcinol to obtain the NIR emitting HD. Then, caprylic acid was used to esterify HD into Pro-HD-I^-. Finally, the iodine counter anion of Pro-HD-I^- was easily exchanged for F_5-TPB (Scheme 1). This last step is further detailed in the section: encapsulation in NEs (see below).

Spectroscopic studies

In order to evaluate the performance of our system, spectroscopic studies of Pro-HD and HD were conducted. Due to the highly hydrophobic nature of HD and Pro-HD, spectroscopic studies could not be performed in aqueous solutions where aggregation occurred. Consequently, methanol was chosen as a polar and protic organic solvent that will mimic a cellular environment where these amphiphilic molecules are expected to end up, namely at the interface between biomembranes and cytosol. Oil (Middle Chain Triglycerides, MCT) was also used to study the properties of Pro-HD as it is its solvent when encapsulated in NEs.

First of all, the results showed that Pro-HD displayed similar properties in methanol and oil (Fig. 2A) with broad multi-peaks spectra with $\lambda_{\mathrm{Abs\,max}}$ at 585 and 595 nm, respectively with identical extinction coefficient (ε = 64 000 M^{-1} cm^{-1}) denoting similar solubility in both solvents at this concentration. Conversely to Pro-HD, HD displayed typical cyanine-shaped absorption spectra with $\lambda_{\mathrm{Abs\,max}}$ at 705 nm and a high extinction coefficient value (ε = 127 000 M^{-1} cm^{-1}) (Fig. 2A). Fluorescence spectroscopy showed that Pro-HD was found to be virtually non-fluorescent in methanol and oil (ϕ = 0.006), whereas HD emits in the NIR (723 nm) with a quantum yield of 0.2 (Fig. 2B). Interestingly, when excited at 640 nm, which is a common excitation wavelength in bioimaging, the fluorescence enhancement between Pro-HD and HD was 35-fold (Fig. 2B), making Pro-HD a promising fluorogenic probe to evaluate its hydrolysis by the cell machinery. In order to demonstrate the possible hydrolysis of Pro-HD towards HD, a base (NaOH) was added in the methanolic solution. The fluorescence intensity at 723 nm was monitored over the time (Fig. 2C) and showed that, in these conditions, a plateau was reached after ~15 min. It corresponded to a fluorescence enhancement of 32-fold which is in line with that between Pro-HD and HD (Fig. 2C). After hydrolysis of Pro-HD, the absorption and emission spectra were recorded and corresponded to those of HD (Fig. S1, ESI†). As discussed above, a chlorine atom was introduced to the structure of HD to lower its pK_a and thus to ensure an emissive specie when exposed to cytosolic environment (pH 7.4). Moreover, a lower pK_a would also limit the acidification of HD in acidic environment like in early endosomes (pH ~ 6). Indeed, in methanol and in the presence of acid, HD was found to be virtually non-emissive with a fluorescence intensity at 723 nm drastically reduced by 60-fold. Conversely, in the presence of a base (triethylamine), the fluorescence of HD was not significantly affected (Fig. S2, ESI†). In the light of these results, the Pro-HD/HD system was considered as a promising probe for encapsulation in NEs.

Encapsulation in NEs

Efficient encapsulation of a molecule in NEs requires a high lipophilicity in order to: (1) ensure a high solubility in the oil phase and (2) avoid its leakage out of the NEs.[29,31,47,48] As shown in the synthesis section, the iodine counter-ion of Pro-HD-I^- was exchanged to F_5-TPB to obtain Pro-HD using TPB-F_5Li (Fig. 3A). Indeed, modifying the salt forms of active pharmaceutical ingredients is a common approach to efficiently modulate their physicochemical and biological properties.[49] This approach was successfully used for enhancing the encapsulation of a potent antituberculosis drug in poly(lactide) microspheres by replacing the polar sodium counterion ion by a lipophilic tetraheptylammonium one.[50]

Although Pro-HD-I^- already displayed a hydrophobic structure with a C_{18} chain combined with a caprylic (C_8) ester, its cationic nature combined to the relatively polar iodine counter ion may lead to poor solubility of the dye and potential leakage into biological media.[47] As shown in Fig. 3A, the calculated log P (Clog P) of Pro-HD-I^- is drastically increased when transformed in Pro-HD bearing F_5-TPB, from −1.3 to 9.6, respectively. As an illustration of the counterion exchange's effect, the TLC plate is displayed on Fig. 3A and shows the impressive difference of migration distance on silica (from R_F 0.06 to 0.96), in line with earlier reports for other dyes.[51] After solubilization of Pro-HD in oil at 0.5 wt% (corresponding to 3.4 mM), two types of NEs were formulated: (1) stealth NEs (Fig. 3B), with highly PEGylated surface that prevents from non-specific interactions and thus do not interact with cells. They will be used as control to check whether Pro-HD leaks out of the NEs in the presence of cells. (2) Cell-penetrating NEs, cpNEs (Fig. 3B) that we recently reported,[25] to deliver the cargo to the cells.

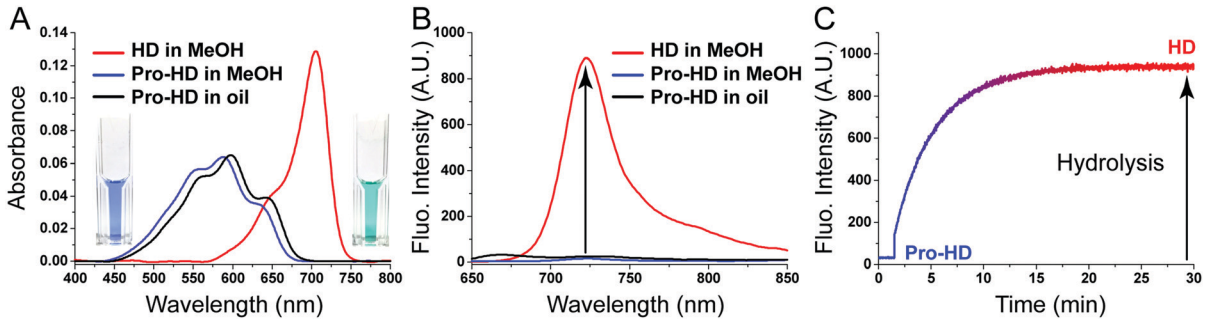

Fig. 2 Spectroscopic studies of Pro-HD and HD (1 μM). Absorption (A) and emission (B) spectra of HD in methanol and Pro-HD in oil (MCT) and in methanol. (C) *In situ* hydrolysis of Pro-HD to HD (1 μM in MeOH), evolution of the fluorescence intensity at 723 nm over 30 min and after addition of aqueous NaOH (at 90 s, 5 μL added in 1 mL, final NaOH concentration was 250 μM). Excitation wavelength was 640 nm. Pictures of cuvettes are Pro-HD (left) and HD (right) in methanol.

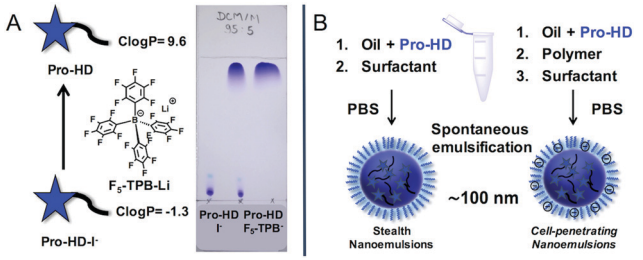

Fig. 3 (A) Anion exchange using F_5-TPB as a lipophilic counter-ion, TLC (DCM/MeOH, 95 : 5) depicted the efficiency in decreasing the polarity from Pro-HD-I^- to Pro-HD (F_5-TPB^-). (B) Formulation by spontaneous nanoemulsification of Pro-HD loaded stealth NEs (NEs) and cell-penetrating NEs (cpNEs) using poly(maleic anhydride-*alt*-1-octadecene) (PMAO) as polymer.[25]

The cpNEs are obtained by dissolving poly(maleic anhydride-*alt*-1-octadecene) (PMAO) in the oil prior to formulation. This alternating polymer is composed of lipophilic carbon chains and cyclic anhydride functions. Upon formulation the latter get hydrolyzed to finally display negative charges at the oil–water interface. We reported that the negative charges lead to cell-penetration by endocytosis mediated by non-specific electrostatic interactions.[25] After formulation, their sizes were measured by DLS and were found to be similar: 97 and 91 nm, respectively (see Fig. S3, ESI†). Absorption spectra confirmed the efficient encapsulation of Pro-HD in NEs as the optical density of Pro-HD (after correction of the scattering) was similar to those of Pro-HD in methanol at the same targeted concentration (Fig. S4, ESI†). Fluorescence spectra, acquired in the same conditions, indicated that Pro-HD was not emissive in both NEs and cpNEs. In order to assess the potential leakage of Pro-HD out of the NEs, the latter were put in the presence of a base, similarly to Fig. 2C. Indeed, if the Pro-HD leaks out of the NEs in the presence of NaOH, HD should be formed and should emit at 723 nm. In these conditions no fluorescence enhancement was obtained for both NEs and cpNEs denoting a strong encapsulation of Pro-HD without any apparent leakage (Fig. S5, ESI†).

Evaluation in cellular experiments

Initially, Pro-HD was incubated for 2 h in the presence of HeLa cells as a positive control to evaluate the ability of Pro-HD to be hydrolyzed into fluorescent HD *in cellulo*. Indeed, due to its high hydrophobicity, Pro-HD was expected to spontaneously penetrate the cells in a fast manner. After incubation for 2 h the cells were washed and presented only a dim signal in the near-infrared channel. However, upon longer incubation, an increasing fluorescence signal was observed in the cytoplasm of cells, reaching a plateau of intensity after 3 h (Fig. S6, ESI†). This control experiment suggested that Pro-HD can be efficiently hydrolyzed *in cellulo* and that this conversion is not immediate, requiring several hours to occur. In a second time, both Pro-HD (0.5 wt%) loaded NEs and cpNEs were incubated in the presence of cells for 2 h before being washed. Fluorescence imaging showed that whereas cells incubated with stealth NEs displayed no red fluorescence over the time (Fig. 4A–D), those incubated with cell-penetrating NEs showed the progressive appearance of the red fluorescence over the time (Fig. 4E–H).

Quantification of fluorescence intensity confirmed these observations and showed that the maximum signal is reached after 6 h post incubation (Fig. 5). After 24 h the signal decreased

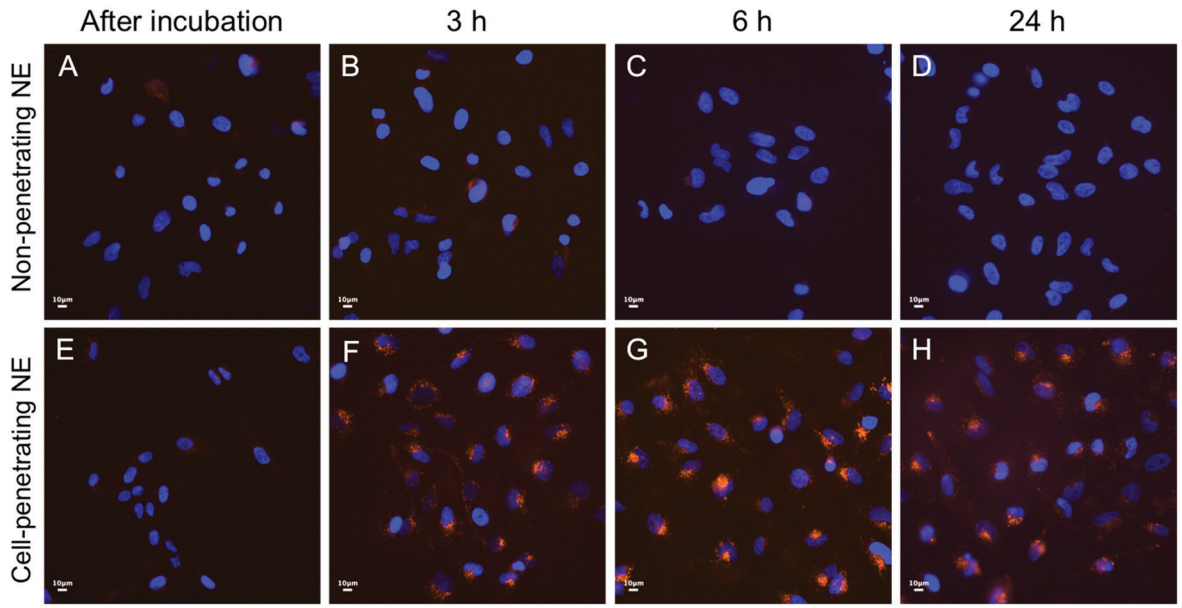

Fig. 4 Epi-fluorescence microscopy imaging of fixed HeLa cells pre-incubated for 2 h in the presence of 0.5 wt% Pro-HD loaded NEs (top images) and 0.5 wt% Pro-HD loaded cell-penetrating NEs (bottom images). Final concentration of loaded Pro-HD was set to 1 µM and the images were acquired in the same conditions of illumination, recording and processing. HD was excited at 641 nm. The nucleus was stained with Hoechst (5 µg mL^{-1}). Scale bar is 10 µm.

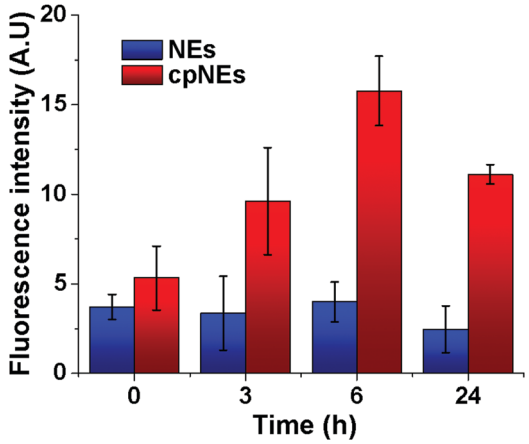

Fig. 5 Mean fluorescence intensity of cells at various time points post incubation with NEs and cpNEs. Error bars are the standard deviation between images (10 images per condition, 10 cells per image).

probably due to the repartition of the probe during cell division. This experiment confirmed that Pro-HD is tightly confined in the NEs and does not leak out from the latter ensuring a controlled delivery. It also showed that cpNEs successfully delivered Pro-HD into cells. It was noteworthy that when Pro-HD was delivered by cpNEs, the fluorescence signal was lower in comparison with direct incubation of Pro-HD and required more time to reach a plateau of fluorescence intensity. Indeed, unlike free Pro-HD, the Pro-HD loaded cpNEs need to: first interact with cells in a non-specific manner and then internalize before being disintegrated to gradually liberate Pro-HD within the cell. The summary of our experiments and the mechanism of release is presented in Fig. S7 (ESI†).

Conclusion

Visualization of prodrug delivery and release of active drug from nanocarriers is important for better understanding of the bottlenecks in nanomedicine. In particular, it concerns moderately hydrophobic cargos that could be reversibly modified into lipophilic prodrug in order to be loaded in nanoemulsions for controlled drug delivery. Here, we developed Pro-HD, a lipophilic near infrared fluorogenic probe as a model of prodrug to assess the controlled cargo delivery and release by nanoemulsions into cells. For this purpose, HD, our fluorescent drug model, was esterified with the hydrophobic and biocompatible caprylic acid, and its counter ion was exchanged for the hydrophobic F_5-TPB giving rise to Pro-HD, a highly lipophilic fluorogenic prodrug model. We demonstrated that Pro-HD, which is virtually non-fluorescent, could be hydrolyzed into HD in cuvette as well as *in cellulo*, provoking a fluorescence enhancement of 35-fold in the near infrared region (λ_{Em} = 723 nm). Due to its high lipophilicity, Pro-HD was efficiently loaded into NEs with no leakage thus avoiding undesired premature delivery. Using cell-penetrating NEs, we were able to show that Pro-HD was delivered to cells and transformed into HD within ~6 h. We believe that this proof of concept can lead to the development of efficient prodrugs based on similar modifications of drugs requiring NEs as nanocarriers for efficient administration to target and treat tumors. As perspective, and taking advantage of the near infrared emission of HD, we also believe that this system is amenable to fluorescence *in vivo* imaging experiments, this will be the subject of a dedicated study.

Experimental

Materials

The solvents were of analytical grade and dry, reagents and starting materials were purchased form TCI, Alfa Aesar or Merck Millipore. Labrafac WL® 1349 (medium chain triglycerides, MCT) was obtained from Gattefossé (Saint-Priest, France). Kolliphor ELP®, was from BASF (Ludwigshafen, Germany). Poly(maleic anhydride-*alt*-1-octadecene) (PMAO) was purchased from Sigma Aldrich (St. Louis, USA). Phosphate buffered saline (PBS) was from Eurobio (Gourtaboeuf, France) and fetal bovine serum (FBS) from Lonza.

Synthesis

Protocols and characterizations can be found in the ESI.† NMR spectra were recorded on a Bruker Avance III 400 MHz spectrometer. Mass spectra were obtained using an Agilent Q-TOF 6520 mass spectrometer.

Spectroscopic studies

All the solvents were spectro grade. Absorption and emission spectra were recorded on a Cary 400 Scan ultraviolet-visible spectrophotometer (Varian) and a FluoroMax-4 spectrofluorometer (Horiba Jobin Yvon) respectively. For standard recording of fluorescence spectra, the emission was collected 10 nm after the excitation wavelength. All the spectra were corrected from wavelength-dependent response of the detector. Quantum yields were determined by comparison with Rhodamine 800 in EtOH (QY = 0.25)[52] as reference using the following equation:

$$QY = QY_R \times \frac{I \times OD_R \times n^2}{I_R \times OD \times n_R^2}$$

where QY is the quantum yield, I is the integrated fluorescence intensity, n is the refractive index, and OD is the optical density at the excitation wavelength. R represents the reference.

Formulation of NEs

Nano-emulsions (NEs) were formulated with spontaneous emulsification method, as described previously.[25] In 100 mg of Medium Chain Triglyceride oil (MCT), Pro-HD (0.5 mg) in acetone was added before being heated at 80 °C until complete evaporation of acetone and solubilization of Pro-HD in MCT. 67 mg of Kolliphor (surfactant) was then added at 80 °C and after mixing for 10 min, 0.25 mL of pre-heated PBS was added to form nanoemulsions. For cell-penetrating NEs, PMAO (1 mg) was first dissolved in MCT prior to the addition of Pro-HD. The size of the obtained NEs was measured by Dynamic Light Scattering (DLS) using a Malvern Zetasizer Nano ZSP

(Malvern, U.K.). For the size measurement, all the emulsions were diluted by 100 times and measured at a temperature of 25 °C. Both size distribution and polydispersity index (PDI) were recorded.

Cellular imaging

HeLa cells (ATCC® CCL-2™) were grown in Dulbecco's Modified Eagle Medium without phenol red (DMEM, Gibco-Invitrogen) supplemented with 10% fetal bovine serum (FBS, Lonza), 1% L-glutamine (Sigma Aldrich) and 0.1% antibiotic solution (gentamicin, Sigma-Aldrich) at 37 °C in humidified atmosphere containing 5% CO_2. Cells were seeded onto a 35 mm glass-bottomed imaging dish (Ibidi®) at a density of 5×10^4 cells per well 24 h before incubation experiments. The cells were then washed 3 times with PBS and incubated 2 h in opti-MEM in the presence of Pro-HD, Pro-HD loaded NEs and Pro-HD loaded cpNEs (1 μM based on absorbance of Pro-HD) before being washed again 3 times with PBS. The cells were then incubated at various times in Dulbecco's modified Eagle medium (DMEM, Gibco-Invitrogen), supplemented with 10% fetal bovine serum (FBS, Lonza) and 1% antibiotic solution (penicillin–streptomycin, Gibco-Invitrogen) at 37 °C in humidified atmosphere containing 5% CO_2. Prior to imaging, nucleus was stained with Hoechst (5 μg mL^{-1}) and the cells were washed with PBS and fixed with 4% PFA at room temperature for 5 minutes before being washed 3 times with PBS. The images were acquired with a Nikon Ti-E inverted epi-fluorescence microscope, using CFI Plan Apo ×60 oil (NA = 1.4) or CFI Plan Apo ×20 air (NA = 0.75) objective, and a Hamamatsu Orca Flash 4 sCMOS camera. Hoechst and HD were excited at 395 and 641 nm, respectively, using light-emitting diode (SpectraX, Lumencor). The images were recorded using NIS Elements and then processed with Icy software.

Conflicts of interest

There are no conflicts to declare.

Acknowledgements

This work was supported by ERC Consolidator grant BrightSens 648528. XW was founded by the China Scholarship Council PhD fellowship (CSC No. 201706240033). We acknowledge Dr Delphine Garnier and Dr Estefania Oliva from the Service de Chimie Analytique (SCA) for their assistance in the LC-MS and NMR analyses.

References

1 J. Shi, P. W. Kantoff, R. Wooster and O. C. Farokhzad, *Nat. Rev. Cancer*, 2017, **17**, 20–37.
2 K. Cho, X. Wang, S. Nie, Z. (Georgia) Chen and D. M. Shin, *Clin. Cancer Res.*, 2008, **14**, 1310–1316.
3 M. V. Yigit, A. Moore and Z. Medarova, *Pharm. Res.*, 2012, **29**, 1180.
4 X. Huang and M. A. El-Sayed, *J. Adv. Res.*, 2010, **1**, 13–28.
5 R. A. Revia and M. Zhang, *Mater. Today*, 2016, **19**, 157–168.
6 N. Rapoport, Z. Gao and A. Kennedy, *JNCI, J. Natl. Cancer Inst.*, 2007, **99**, 1095–1106.
7 X.-H. Peng, X. Qian, H. Mao, A. Y. Wang, Z. (Georgia) Chen, S. Nie and D. M. Shin, *Int. J. Nanomed.*, 2008, **3**, 311.
8 A. H. Faraji and P. Wipf, *Bioorg. Med. Chem.*, 2009, **17**, 2950–2962.
9 J. M. Chan, P. M. Valencia, L. Zhang, R. Langer and O. C. Farokhzad, *Methods Mol. Biol.*, 2010, **624**, 163–175.
10 K. M. El-Say and H. S. El-Sawy, *Int. J. Pharm.*, 2017, **528**, 675–691.
11 M. Liong, J. Lu, M. Kovochich, T. Xia, S. G. Ruehm, A. E. Nel, F. Tamanoi and J. I. Zink, *ACS Nano*, 2008, **2**, 889.
12 M. Hamidi, A. Azadi and P. Rafiei, *Adv. Drug Delivery Rev.*, 2008, **60**, 1638–1649.
13 B. Mandal, H. Bhattacharjee, N. Mittal, H. Sah, P. Balabathula, L. A. Thoma and G. C. Wood, *Nanomedicine*, 2013, **9**, 474–491.
14 K. Hadinoto, A. Sundaresan and W. S. Cheow, *Eur. J. Pharm. Biopharm.*, 2013, **85**, 427–443.
15 L. Zhang, J. M. Chan, F. X. Gu, J.-W. Rhee, A. Z. Wang, A. F. Radovic-Moreno, F. Alexis, R. Langer and O. C. Farokhzad, *ACS Nano*, 2008, **2**, 1696.
16 V. P. Torchilin, *Nat. Rev. Drug Discovery*, 2005, **4**, 145–160.
17 W. Mehnert and K. Mäder, *Adv. Drug Delivery Rev.*, 2001, **47**, 165–196.
18 H.-Y. Lee, Z. Li, K. Chen, A. R. Hsu, C. Xu, J. Xie, S. Sun and X. Chen, *J. Nucl. Med.*, 2008, **49**, 1371–1379.
19 S. Mohapatra, S. K. Mallick, T. K. Maiti, S. K. Ghosh and P. Pramanik, *Nanotechnology*, 2007, **18**, 385102.
20 Z. Zhang, J. Jia, Y. Lai, Y. Ma, J. Weng and L. Sun, *Bioorg. Med. Chem.*, 2010, **18**, 5528–5534.
21 C. Yan, Z. Guo, Y. Shen, Y. Chen, H. Tian and W.-H. Zhu, *Chem. Sci.*, 2018, **9**, 4959–4969.
22 N. Anton and T. F. Vandamme, *Int. J. Pharm.*, 2009, **377**, 142–147.
23 D. J. McClements, *Soft Matter*, 2012, **8**, 1719–1729.
24 M. Yao, H. Xiao and D. J. McClements, *Annu. Rev. Food Sci. Technol.*, 2014, **5**, 53–81.
25 M. F. Attia, S. M. Dieng, M. Collot, A. S. Klymchenko, C. Bouillot, C. A. Serra, M. Schmutz, M. Er-Rafik, T. F. Vandamme and N. Anton, *Macromol. Biosci.*, 2017, **17**, 1600471.
26 M. F. Attia, N. Anton, R. Bouchaala, P. Didier, Y. Arntz, N. Messaddeq, A. S. Klymchenko, Y. Mély and T. F. Vandamme, *RSC Adv.*, 2015, **5**, 74353–74361.
27 D. A. Estabrook, A. F. Ennis, R. A. Day and E. M. Sletten, *Chem. Sci.*, 2019, **10**, 3994–4003.
28 A. Saito, S. Yamamoto, R. Ochi, K. Inoue, S. Hadano, S. Watanabe, T. Nakayama and Y. Niko, *Bull. Chem. Soc. Jpn.*, 2020, **93**, 568–575.
29 R. Bouchaala, L. Mercier, B. Andreiuk, Y. Mély, T. Vandamme, N. Anton, J. G. Goetz and A. S. Klymchenko, *J. Controlled Release*, 2016, **236**, 57–67.
30 M. A. Radicchi, J. V. de Oliveira, A. C. P. Mendes, D. M. de Oliveira, L. A. Muehlmann, P. C. Morais, R. B. Azevedo and J. P. F. Longo, *J. Mater. Chem. B*, 2018, **6**, 7306–7316.

31 A. S. Klymchenko, E. Roger, N. Anton, H. Anton, I. Shulov, J. Vermot, Y. Mely and T. F. Vandamme, *RSC Adv.*, 2012, **2**, 11876–11886.
32 A. L. Dos Santos Câmara, G. Nagel, H. R. Tschiche, C. M. Cardador, L. A. Muehlmann, D. M. de Oliveira, P. Q. Alvim, R. B. Azevedo, M. Calderón and J. P. Figueiró Longo, *Nanomedicine*, 2017, **12**, 1751–1765.
33 J.-J. Wang, K. C. Sung, O. Y.-P. Hu, C.-H. Yeh and J.-Y. Fang, *J. Controlled Release*, 2006, **115**, 140–149.
34 R. K. Keservani and A. K. Sharma, *Nanoconjugate Nanocarriers for Drug Delivery*, CRC Press, 2018.
35 T. D. Nalder, T. D. Ashton, F. M. Pfeffer, S. N. Marshall and C. J. Barrow, *Biochimie*, 2016, **128–129**, 127–132.
36 H. Dreser, *Pflugers Arch.*, 1899, **76**, 306–318.
37 L. Yuan, W. Lin, K. Zheng, L. He and W. Huang, *Chem. Soc. Rev.*, 2012, **42**, 622–661.
38 L. Yuan, W. Lin, S. Zhao, W. Gao, B. Chen, L. He and S. Zhu, *J. Am. Chem. Soc.*, 2012, **134**, 13510–13523.
39 Y. Liu, L. Teng, L. Chen, H. Ma, H.-W. Liu and X.-B. Zhang, *Chem. Sci.*, 2018, **9**, 5347–5353.
40 S. Zhu, W. Lin and L. Yuan, *Anal. Methods*, 2013, **5**, 3450–3453.
41 Y. Li, Y. Wang, S. Yang, Y. Zhao, L. Yuan, J. Zheng and R. Yang, *Anal. Chem.*, 2015, **87**, 2495–2503.
42 Q. Wan, S. Chen, W. Shi, L. Li and H. Ma, *Angew. Chem., Int. Ed.*, 2014, **53**, 10916–10920.
43 M. Collot, F. Ponsot and A. S. Klymchenko, *Chem. Commun.*, 2017, **53**, 6117–6120.
44 Z. Luo, L. Feng, R. An, G. Duan, R. Yan, H. Shi, J. He, Z. Zhou, C. Ji, H.-Y. Chen and D. Ye, *Chem. – Eur. J.*, 2017, **23**, 14778–14785.
45 H. Chen, W. Lin, H. Cui and W. Jiang, *Chem. – Eur. J.*, 2015, **21**, 733–745.
46 G. Despras, A. I. Zamaleeva, L. Dardevet, C. Tisseyre, J. G. Magalhaes, C. Garner, M. D. Waard, S. Amigorena, A. Feltz, J.-M. Mallet and M. Collot, *Chem. Sci.*, 2015, **6**, 5928–5937.
47 V. N. Kilin, H. Anton, N. Anton, E. Steed, J. Vermot, T. F. Vandamme, Y. Mely and A. S. Klymchenko, *Biomaterials*, 2014, **35**, 4950–4957.
48 X. Wang, N. Anton, P. Ashokkumar, H. Anton, T. K. Fam, T. Vandamme, A. S. Klymchenko and M. Collot, *ACS Appl. Mater. Interfaces*, 2019, **11**, 13079–13090.
49 D. Gupta, D. Bhatia, V. Dave, V. Sutariya and S. Varghese Gupta, *Molecules*, 2018, **23**, 1719.
50 H. Zhou, C. Lengsfeld, D. J. Claffey, J. A. Ruth, B. Hybertson, T. W. Randolph, K. Ng and M. C. Manning, *J. Pharm. Sci.*, 2002, **91**, 1502–1511.
51 B. Andreiuk, A. Reisch, E. Bernhardt and A. S. Klymchenko, *Chem. – Asian J.*, 2019, **14**, 836–846.
52 A. Alessi, M. Salvalaggio and G. Ruzzon, *J. Lumin.*, 2013, **134**, 385–389.

Electronic Supplementary Material (ESI) for Journal of Materials Chemistry B.

Near Infrared Fluorogenic Probe as a Prodrug Model for Evaluating Cargo Release by Nanoemulsions

Supplementary information

- Synthesis of Cy7-Cl

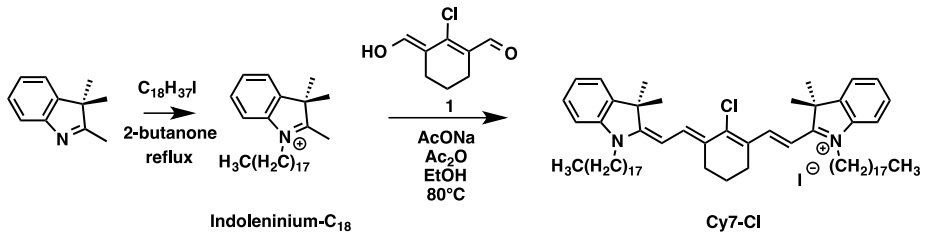

Indoleninium-C_{18} was synthesized according to a described protocol.[1]

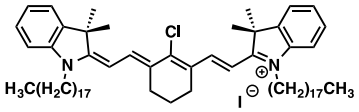

Cy7-Cl. To a solution of 2-chloro-3-(hydroxymethylene) cyclohexene-1-carbaldehyde **1** (164 mg, 0.950 mmol) and Indolenine-C_{18} (1.023 g, 1.900 mmol, 2 eq) in EtOH (5 mL) was added sodium acetate (78 mg, 0.95 mmol, 1 eq) and acetic anhydride (1 mL). The mixture was heated at 80°C for 30 min. The reaction was monitored by TLC: DCM/MeOH (95/5). After cooling down, EtOH (5 mL) was added and the product was allowed to crystallize overnight. The solution was filtered and washed with EtOH and Et_2O and dried under vacuum to obtain 370 mg (Yield=36%) of **Cy7-Cl** as a shiny green powder. **Cy7-Cl** was found to be insoluble in various deuterated solvents and thus could not be characterized by NMR spectroscopy. Therefore it was involved in the next step without further characterizations. HRMS (ESI^+), calcd for $C_{66}H_{104}ClN_2^+$ $[M]^+$: 959,7883, found 959.7909.

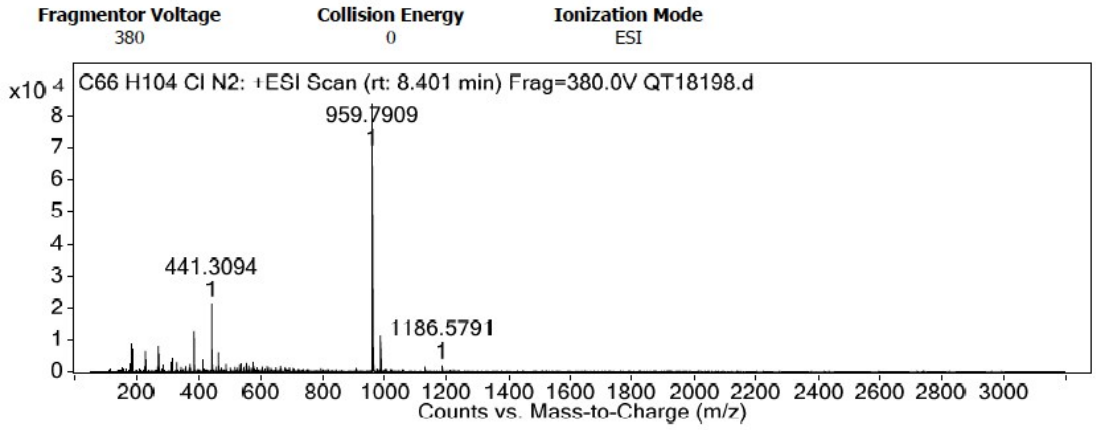

HRMS spectrum of Cy7-Cl

- Characterizations of products

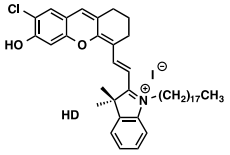

HD. To a solution of **Cy7-Cl** (368.2 mg, 0.338 mmol) and 4-chlororesorcin (195.4 mg, 4 eq, 1.352 mmol) in dry DMF (3 mL) was added triethylamine (0.5 mL). The solution was allowed to stir under argon at 75°C for 2 h. The solvents were evaporated. The product was extracted with DCM and washed with water and brine. The organic phase was dried over anhydrous $MgSO_4$, filtered and evaporated. The crude was purified by column chromatography on silica gel using DCM/MeOH, 95:5 to obtain 111 mg of HD (Yield= 42%) as a blue powder. Rf = 0.25, DCM/MeOH, 95:5. ^{1}H-NMR (400 MHz, $CDCl_3$): δ 8.11 (d, *J* = 13.4 Hz, 1H, H Ar), 7.43 (s, 1H, H Ar), 7.31-7.29 (m, 2H, H Ar), 7.08 (td, *J* = 7.4, 0.6 Hz, 1H, H Ar), 6.84 (d, *J* = 7.8 Hz, 1H, H Ar), 6.71 (s, 1H, HC=C), 5.65 (d, *J* = 13.5 Hz, 1H, HC=C), 3.79 (t, *J* = 7.5 Hz, 2H, H_2C-N), 2.72-2.69 (m, 2H, CH_2), 2.64-2.61 (m, 2H, CH_2), 1.96-1.90 (m, 2H, CH_2), 1.77 (t, *J* = 6.8 Hz, 2H), 1.69 (s, 6H, 2 CH_3), 1.44-1.27 (m, 32H, 19 CH_2), 0.90 (m, *J* = 6.9 Hz, 3H, CH_3). ^{13}C-NMR (126 MHz, $CDCl_3$): δ 160.19 (CN^+), 157.83 (C-O), 143.30, 139.74, 139.45, 133.14, 132.16, 128.11, 127.19, 122.39, 122.14, 116.47, 115.68, 115.36, 108.06, 103.80, 94.37, 94.34, 47.59, 43.20, 31.93, 29.70, 29.36, 28.65, 27.96, 27.10, 26.51, 24.41, 22.70, 21.30, 14.13. HRMS (ESI^+), calcd for $C_{43}H_{59}NO_2Cl$ $[M]^+$: 656.4229, found 656.4224.

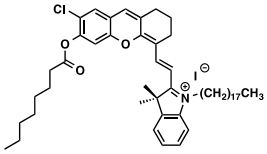

pro-HD-I$^-$. To a solution of caprylic acid (37.4 g, 3 eq, 0.230 mmol), EDC (47.5 mg, 4 eq, 0.306 mmol) and DMAP (3.66 mg, 0.13 eq, 0.03 mmol) in DCM (3 mL) was added **HD** (60 mg, 1 eq, 0.076 mmol) in DCM (2mL). The reaction was allowed to stir overnight at room temperature. The solvents were evaporated and the crude was purified by column chromatography on silica gel using DCM/MeOH, (95:5) to obtain 28 mg of **pro-HD** (Yield= 14%) as a blue syrup. Rf = 0.1, DCM/MeOH, (95:5). ^{1}H-NMR (400 MHz, $CDCl_3$, MeOD): δ 8.73 (d, *J* = 15.2 Hz, 1H, HC=C), 7.71-7.51 (m, 5H, H Ar), 7.38 (s, 1H, H Ar), 7.20 (s, 1H, H Ar), 6.68 (d, *J* = 15.3 Hz, 1H, HC=C), 4.46 (t, *J* = 7.3 Hz, 2H, CH_2N^+), 2.79-2.67 (m, 6H, 2 CH_2), 1.95-1.93 (m, 4H, 2 CH_2), 1.82-1.77 (m, 8H, 1 CH_2, 2 CH_3), 1.47-1.23 (m, 38H, 19 CH_2), 0.93-0.87 (m, 6H, 2 CH_3). ^{13}C-NMR (126 MHz, $CDCl_3$): δ 179.0 (CN^+), 171.0 (C Ar), 158.2, 151.30, 148.35, 146.12, 142.43, 141.38, 131.69, 129.40, 128.26, 128.21, 127.61, 123.44, 122.49, 120.79, 116.29, 113.82, 111.43, 108.51, 51.14, 47.08, 34.06, 31.91, 31.64, 29.69, 29.67, 29.65, 29.61, 29.57, 29.41, 29.38, 29.34, 29.04, 28.87, 28.45, 28.07, 26.88, 24.76, 24.61, 22.67, 22.58, 20.19, 14.10, 14.06. HRMS (ESI^+), calcd for $C_{51}H_{73}NO_3Cl$ $[M]^+$: 782.5273, found 782.5294.

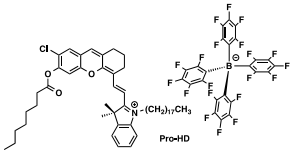

Pro-HD. To a solution of pro-HD-I$^-$ (20 mg, 0.025 mmol) in DCM (2 mL) was added Lithium tetrakis(pentafluorophenyl)borate lithium salt (TPB-F_5-Li) (51 mg, 0.075 mmol, 3 eq). The solution was allowed to stir at room temperature for 5 min and, after a control TLC, the product was purified by column chromatography on silica gel (DCM/MeOH, 95:5) to give 33 mg of Pro-HD with a quantitative yield. Pro-HD displayed similar ^{1}H and ^{13}C NMR and HRMS spectra than Pro-HD-I$^-$.^{19}F-NMR (376 MHz, $CDCl_3$): δ -132.52 (d, *J* = 10.5 Hz, 1F), -163.07 (t, *J* = 20.6

Hz, 1F), -166.81 (t, *J* = 17.8 Hz, 1F). ^{11}B-NMR (128 MHz, $CDCl_3$): δ -16.69 (s, 1B). HRMS (ESI^+), calcd for $C_{51}H_{73}NO_3Cl$ $[M]^+$: 782.5273, found 782.5287.
^{1}H, ^{13}C, ^{19}F and ^{11}B NMR spectra as well as HRMS can be found below.

- NMR and mass spectra

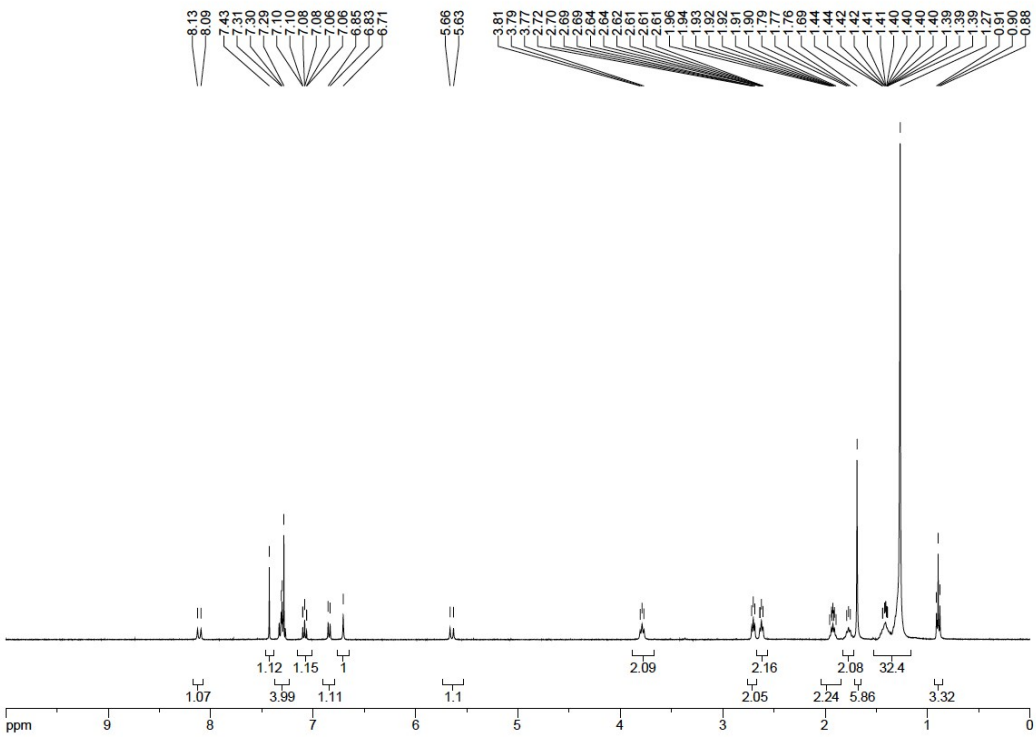

^{1}H NMR spectrum of HD ($CDCl_3$)

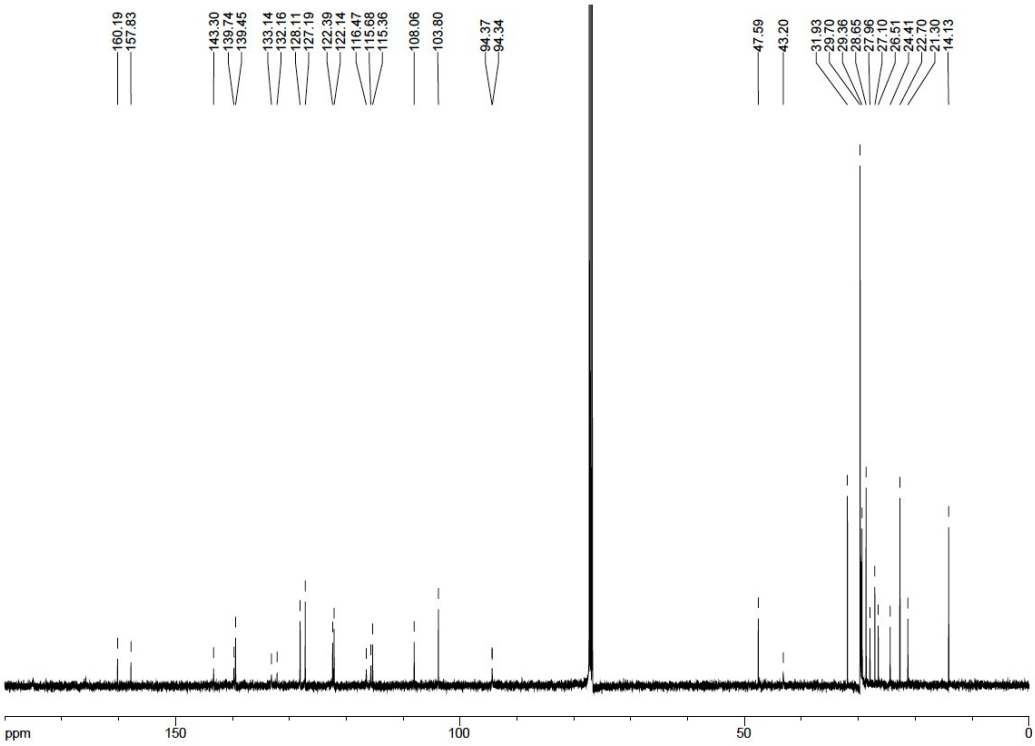

^{13}C NMR spectrum of HD ($CDCl_3$)

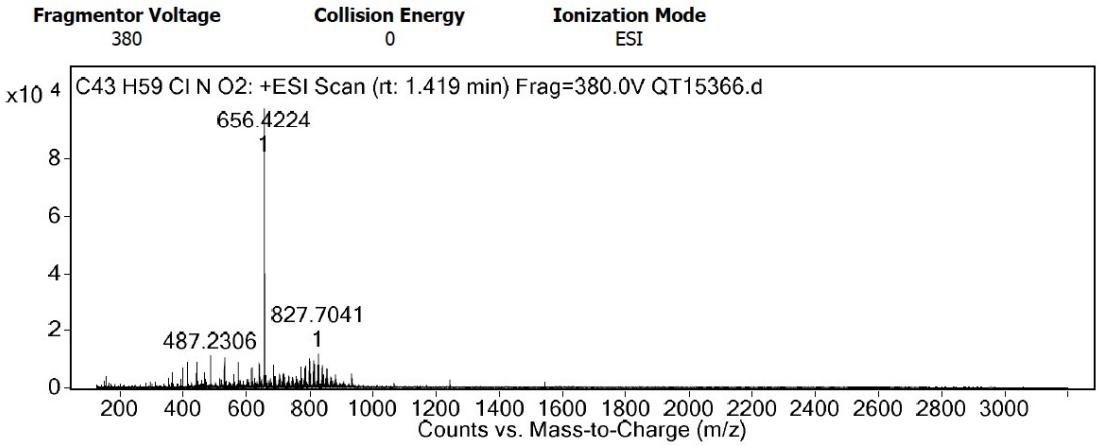

HRMS spectrum of HD (by infusion)

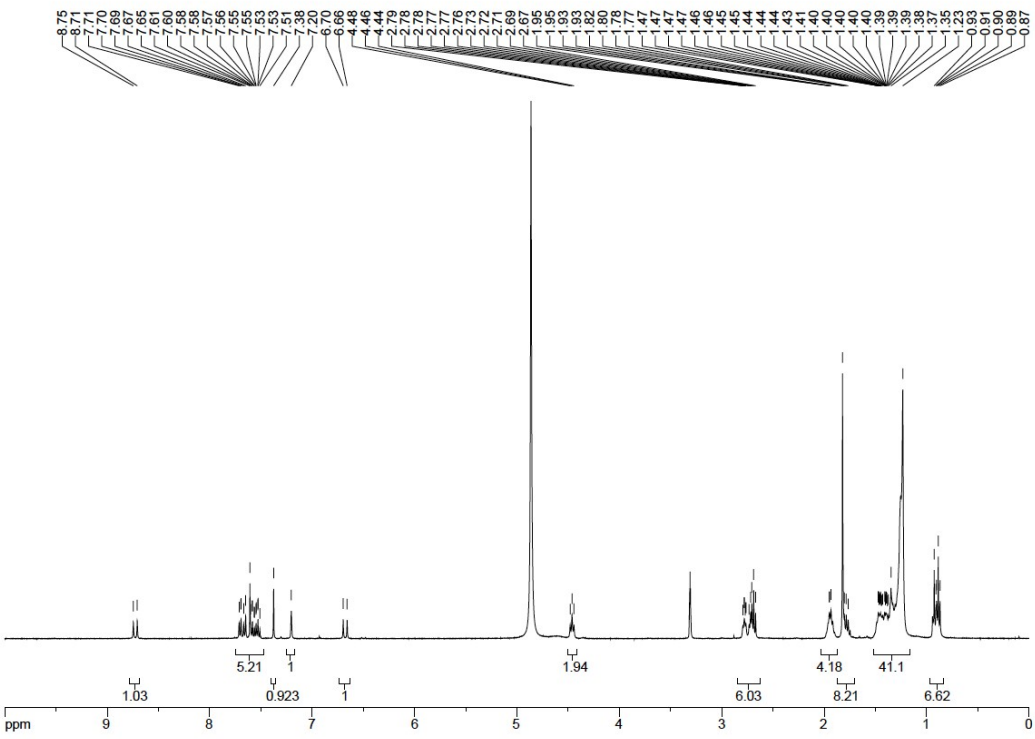

^{1}H NMR spectrum of Pro-HD-I^{-} ($CDCl_3$)

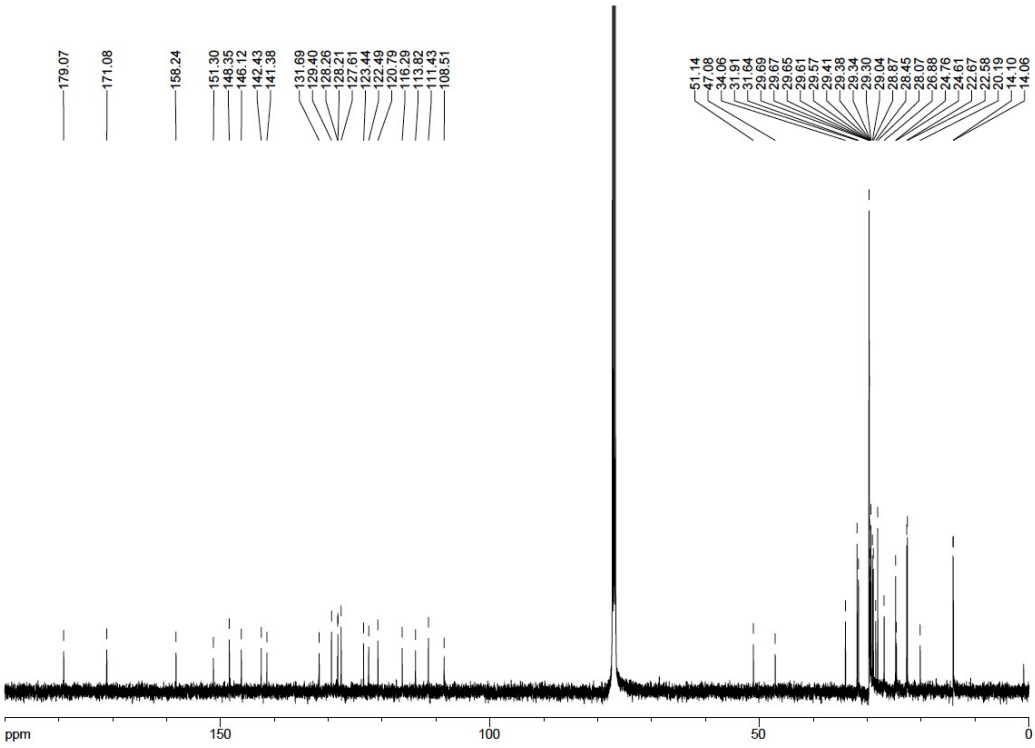

^{13}C NMR spectrum of Pro-HD-I^{-} ($CDCl_3$)

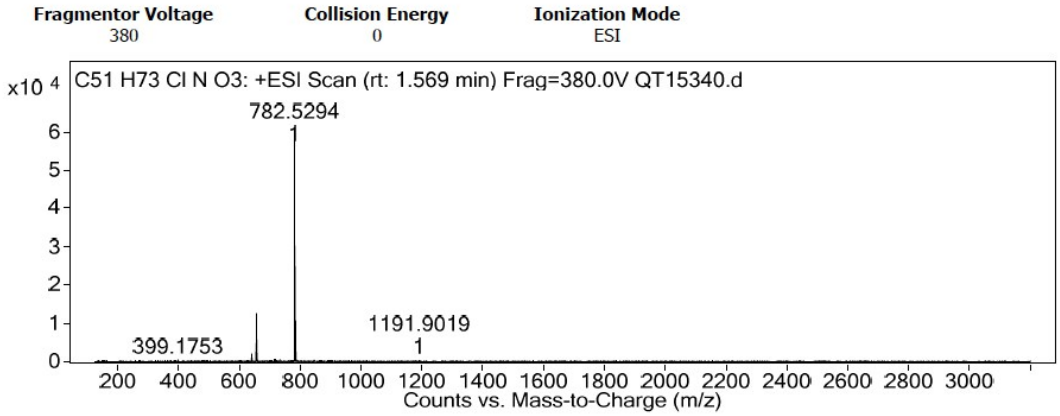

HRMS spectrum of Pro-HD-I^- (by infusion)

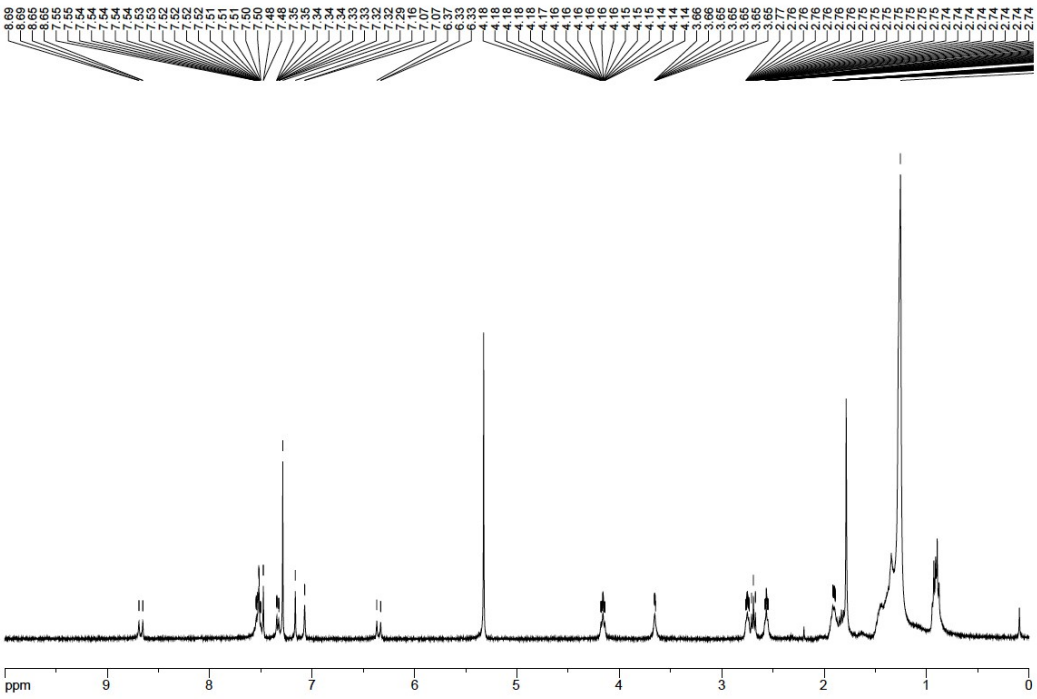

^{1}H NMR spectrum of Pro-HD ($CDCl_3$)

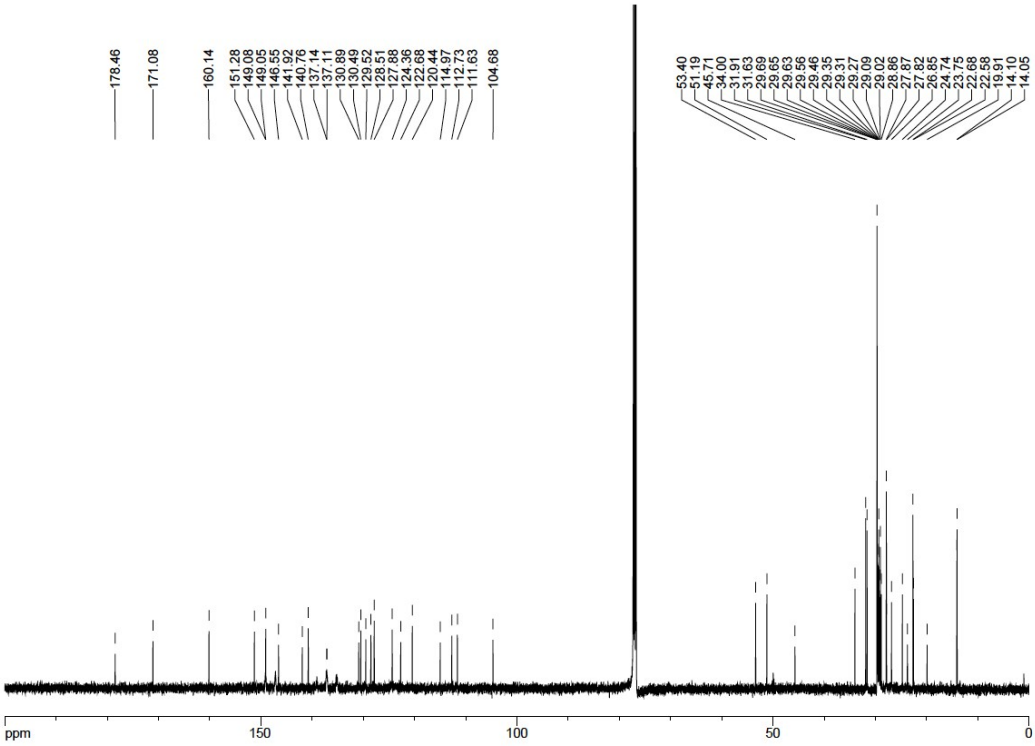

^{13}C NMR spectrum of Pro-HD ($CDCl_3$)

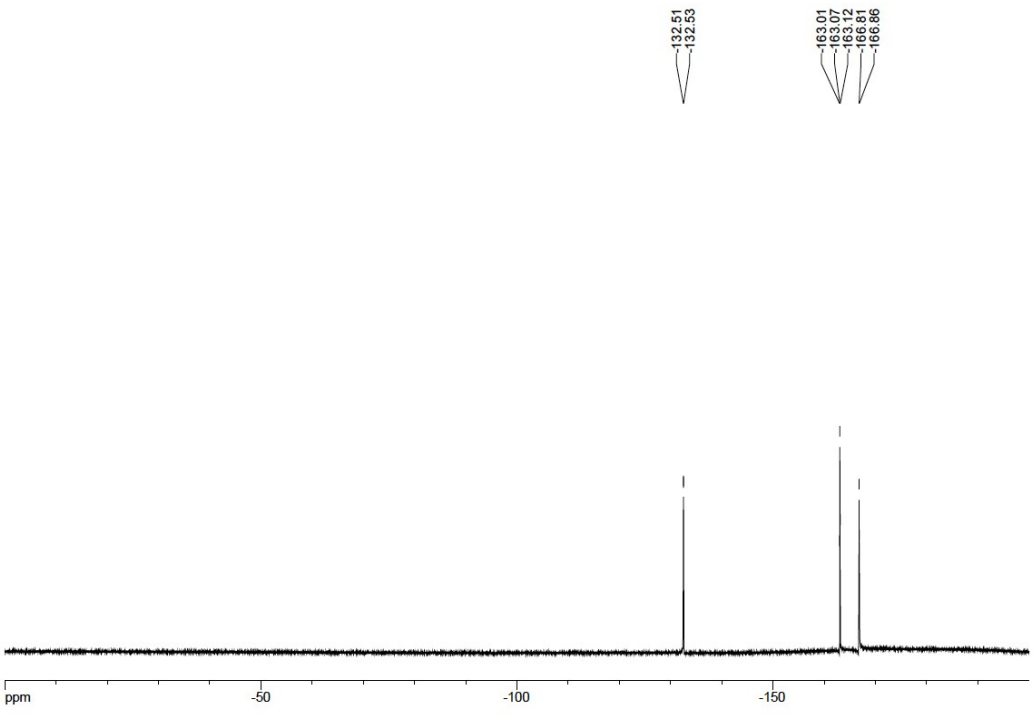

^{19}F NMR spectrum of Pro-HD ($CDCl_3$)

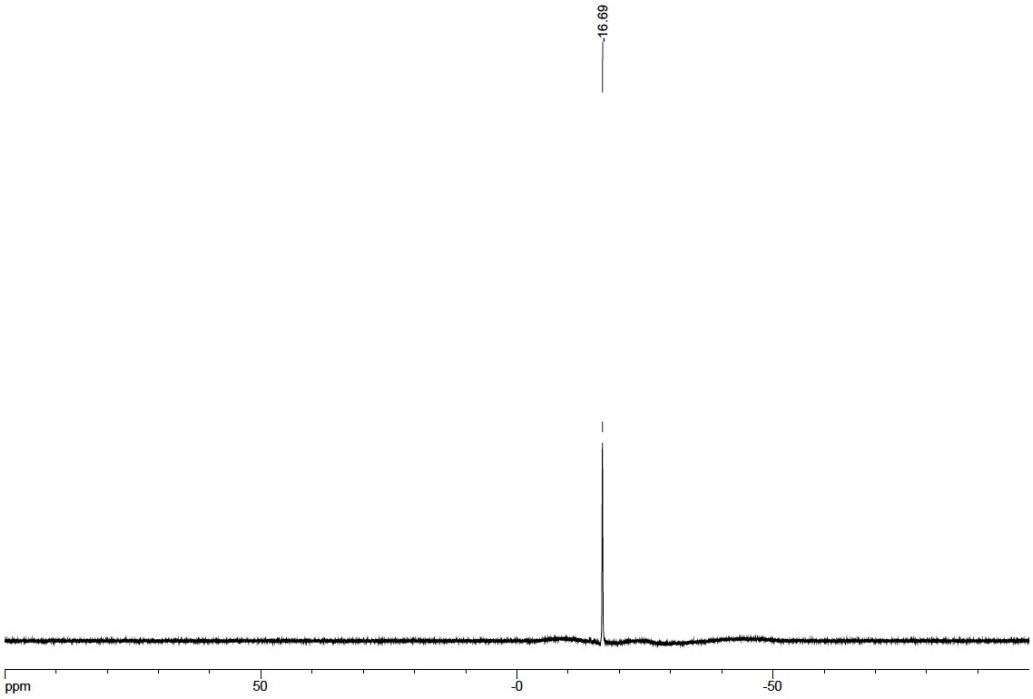

^{11}B NMR spectrum of Pro-HD ($CDCl_3$)

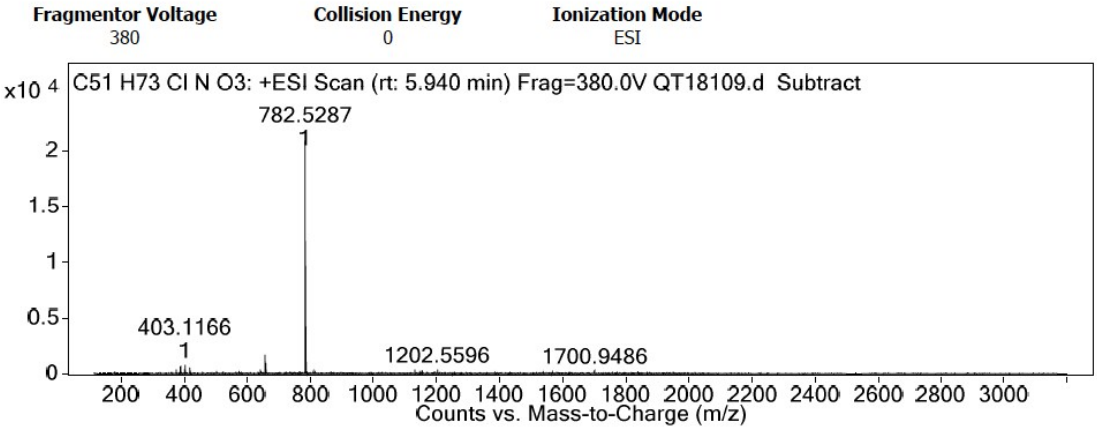

HRMS spectrum of Pro-HD-$TPBF_5$ (by infusion)

Spectroscopy

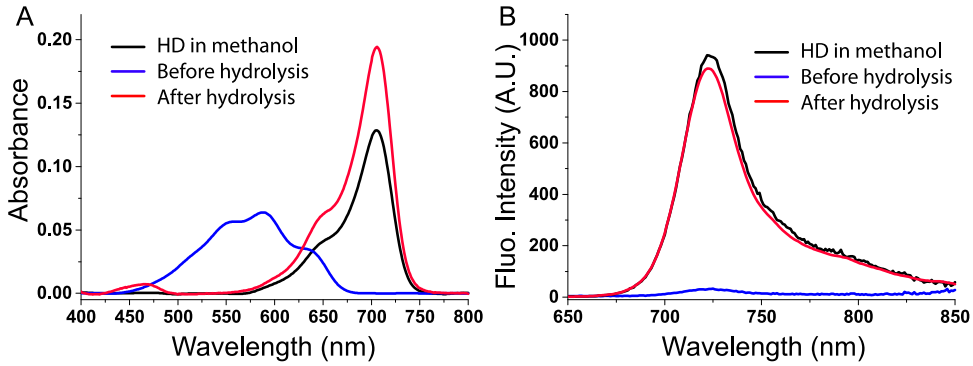

Figure S1. Absorption (A) and emission spectra (B) of Pro-HD before and after hydrolysis compared to HD in pure methanol. After hydrolysis of Pro-HD, HD displayed and enhanced absorption due to the presence of NaOH that favors the phenolate form of HD.

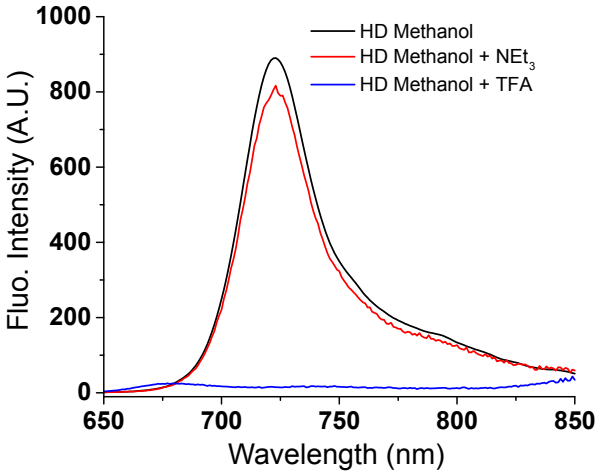

Figure S2. Fluorescence spectra of HD in methanol and in the presence of a base (triethylamine, 5 µL in 1 mL MeOH, 69 ?M) and an acid (TFA, 5 µL in 1 mL MeOH: 29 mM).

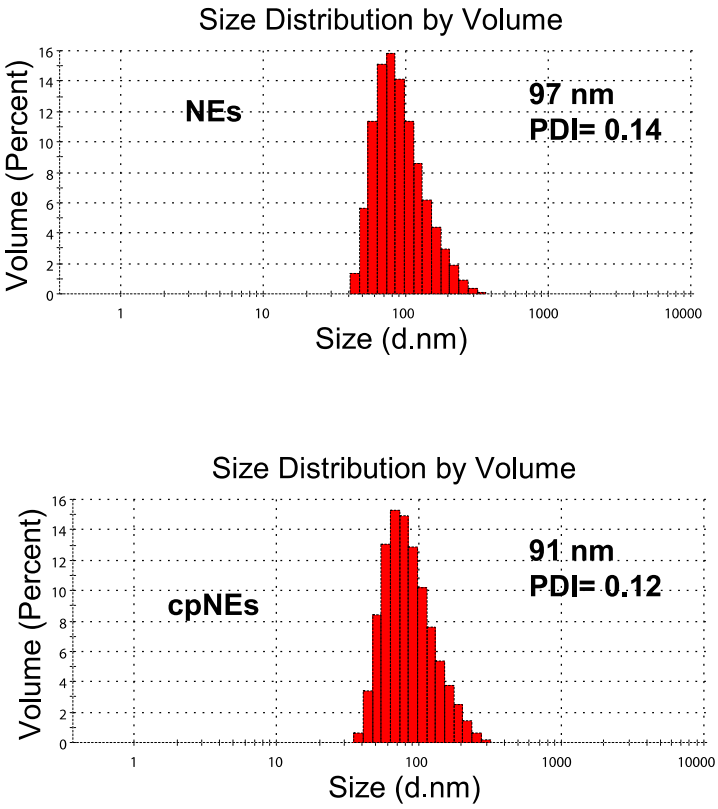

Figure S3. Histogram of size distribution of Pro-HD loaded NEs and cpNEs obtained by DLS measurements.

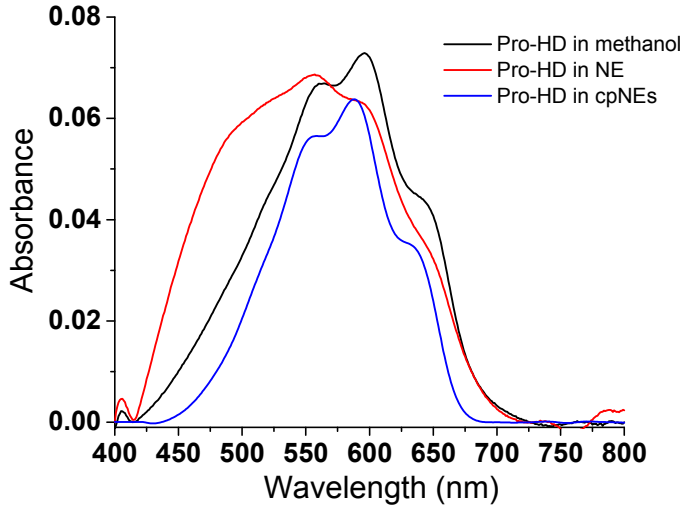

Figure S4. Absorption spectra of Pro-HD (1 μM) in methanol and in NEs and cpNEs loaded at 0.5 wt %.

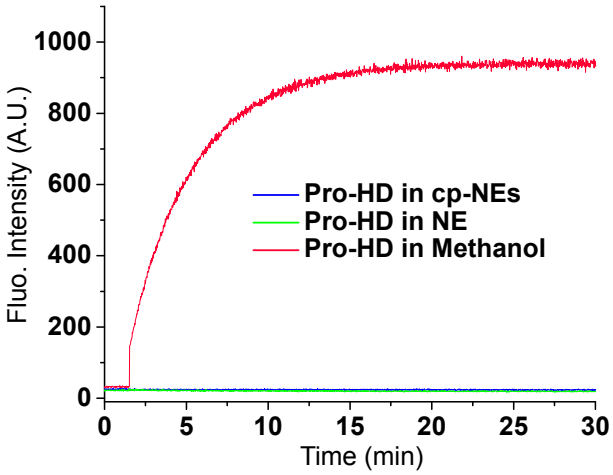

Figure S5. Evolution of the fluorescence intensity at 723 nm over 30 min and after addition of aqueous NaOH (at 90 s, final concentration was 250 μM). Whereas Pro-HD is hydrolyzed in methanol, it is protected in NEs. Excitation wavelength was 640 nm.

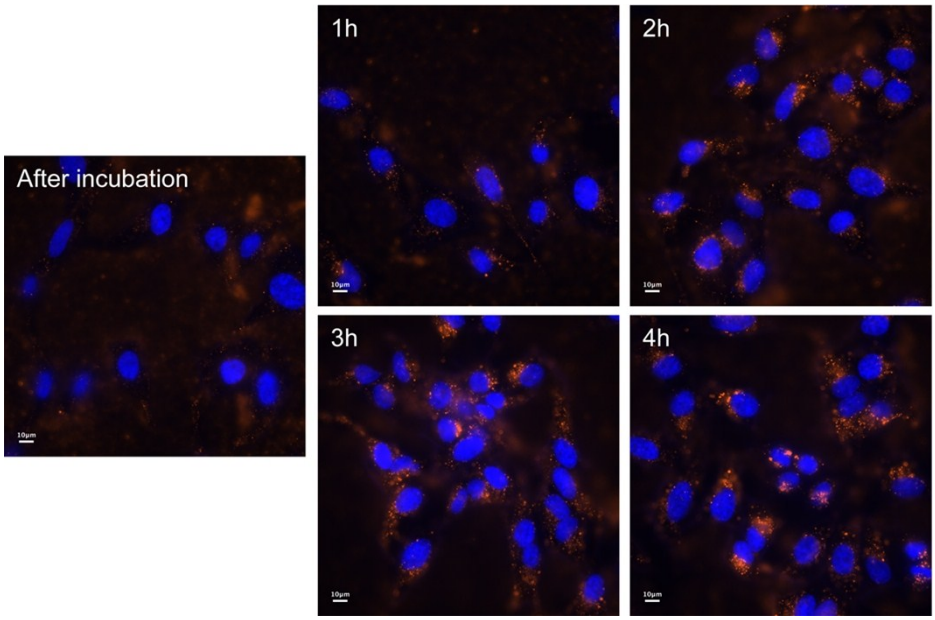

Figure S6. Epi-fluorescence microscopy imaging of fixed HeLa cells after pre-incubated for 2 h in the presence of pro-HD (1 μM) and after washing and 1, 2, 3 and 4h of further incubation. **HD** was excited at 641 nm. The nucleus was stained with Hoechst (5 μg.mL^{-1}). Scale bar is 10 μm.

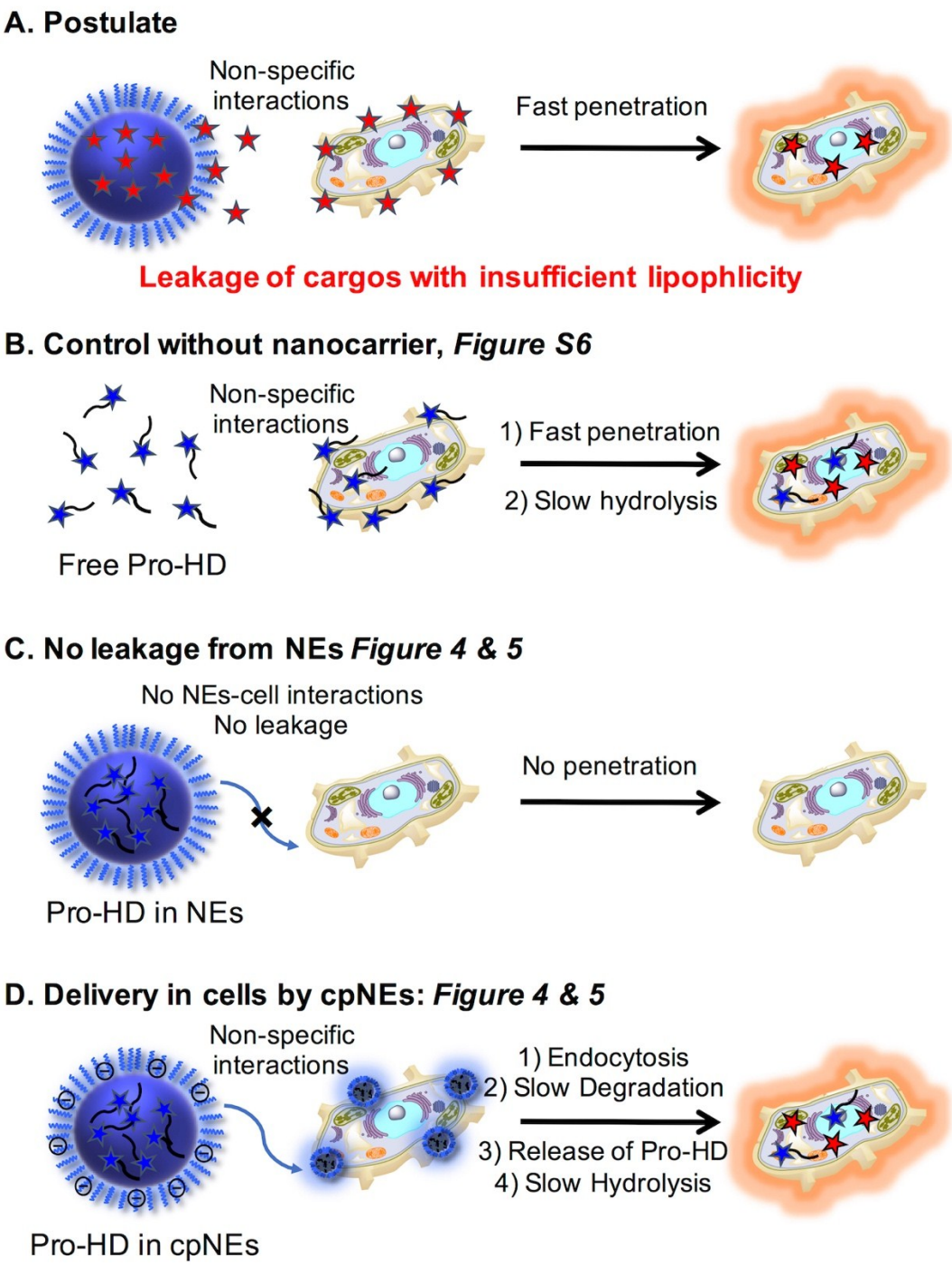

Figure S7. Summary scheme. (A) Initial postulate: cargos with insufficient lipophilic nature leak out from NEs but is sufficiently lipophilic to interact and penetrate the cells.[2, 3, 4, 5] (B) Pro-HD is lipophilic and penetrate quickly in cells by non-specific interactions, within 2 h the maximum fluorescence is obtained proving that Pro-HD can be hydrolysed in cells. (C) Similarly to our previous work,[2] Pro-HD when encapsulated in NEs is stable and does not leak out from NEs. (D) As already demonstrated,[6] similarly to NEs, cpNEs are able to retain lipophilic cargos but can penetrate in cells by non-specific interactions. Consequently, the mechanism of release is not controlled by diffusion (leakage) but by subsequent: endocytosis, degradation of the NEs' matrix, release of Pro-HD and finally hydrolysis into HD.

References

(1) Crystalline-State Photochromism and Thermochromism of New Spiroxazine. *Dyes Pigments* **2002**, *53* (3), 251–256. https://doi.org/10.1016/S0143-7208(02)00022-0.
(2) Kilin, V. N.; Anton, H.; Anton, N.; Steed, E.; Vermot, J.; Vandamme, T. F.; Mely, Y.; Klymchenko, A. S. Counterion-Enhanced Cyanine Dye Loading into Lipid Nano-Droplets for Single-Particle Tracking in Zebrafish. *Biomaterials* **2014**, *35* (18), 4950–4957. https://doi.org/10.1016/j.biomaterials.2014.02.053.
(3) Klymchenko, A. S.; Roger, E.; Anton, N.; Anton, H.; Shulov, I.; Vermot, J.; Mely, Y.; Vandamme, T. F. Highly Lipophilic Fluorescent Dyes in Nano-Emulsions: Towards Bright Non-Leaking Nano-Droplets. *RSC Adv.* **2012**, *2* (31), 11876–11886. https://doi.org/10.1039/C2RA21544F.
(4) Andreiuk, B.; Reisch, A.; Pivovarenko, V. G.; Klymchenko, A. S. An Aluminium-Based Fluorinated Counterion for Enhanced Encapsulation and Emission of Dyes in Biodegradable Polymer Nanoparticles. *Mater. Chem. Front.* **2017**, *1* (11), 2309–2316. https://doi.org/10.1039/C7QM00248C.
(5) Andreiuk, B.; Reisch, A.; Bernhardt, E.; Klymchenko, A. S. Fighting Aggregation-Caused Quenching and Leakage of Dyes in Fluorescent Polymer Nanoparticles: Universal Role of Counterion. *Chem. – Asian J.* **2019**, *14* (6), 836–846. https://doi.org/10.1002/asia.201801592.
(6) Attia, M. F.; Dieng, S. M.; Collot, M.; Klymchenko, A. S.; Bouillot, C.; Serra, C. A.; Schmutz, M.; Er-Rafik, M.; Vandamme, T. F.; Anton, N. Functionalizing Nanoemulsions with Carboxylates: Impact on the Biodistribution and Pharmacokinetics in Mice. *Macromol. Biosci.* **2017**, *17* (7), 1600471. https://doi.org/10.1002/mabi.201600471.

LANGMUIR Article
Cite This: Langmuir 2019, 35, 2313−2325
pubs.acs.org/Langmuir

Toward the Formulation of Stable Micro and Nano Double Emulsions through a Silica Coating on Internal Water Droplets

Salman Akram,[†] Xinyue Wang,[†] Thierry F. Vandamme,[†] Mayeul Collot,[‡] Asad Ur Rehman,[†] Nadia Messaddeq,[§] Yves Mély,[‡] and Nicolas Anton*[,†]

[†]CNRS, CAMB UMR 7199, [‡]CNRS, LBP UMR 7021, and [§]IGBMC, Inserm U964, CNRS UMR7104, Université de Strasbourg, F-67000 Strasbourg, France

ABSTRACT: Delivery systems able to coencapsulate both hydrophilic and hydrophobic species are of great interest in both fundamental research and industrial applications. Water-in-oil-in-water ($w_1/O/W_2$) emulsions are interesting systems for this purpose, but they suffer from limited stability. In this study, we propose an innovative approach to stabilize double emulsions by the synthesis of a silica membrane at the water/oil interface of the primary emulsion (i.e., inner w_1/O emulsion). This approach allows the formulation of stable double emulsions through a two-step process, enabling high encapsulation efficiencies of model hydrophilic dyes encapsulated in the internal droplets. This approach also decreases the scale of the double droplets up to the nanoscale, which is not possible without silica stabilization. Different formulation and processing parameters were explored in order to optimize the methodology. Physicochemical characterization was performed by dynamic light scattering, encapsulation efficiency measurements, release profiles, and optical and transmission electron microscopies.

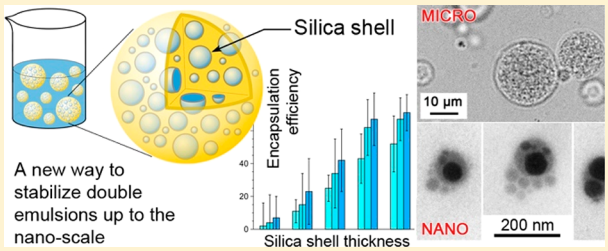

INTRODUCTION

Scientific challenges in the fields of agrofoods and cosmetic or pharmaceutical sciences have often found innovative solutions in the form of optimized delivery systems. With the unique properties to encapsulate hydrophilic molecules in lipid emulsions, the double emulsions have gained an important place in this research.[1] In the field of pharmaceuticals, double emulsions can be used as oral delivery systems for vaccines, drugs, and plant bioactives,[2,3] while in the food industry they can be used as carriers for probiotics, vitamins, seasoning agents, and extracts.[4−8] In the field of nanomedicine, nanoscale double emulsions could solve important challenges, like the targeted delivery of hydrophilic molecules.

When aiming for a globule dispersion in the aqueous continuous phase (e.g., in most pharmaceutical formulations), double emulsions are formulated to be in the water-in-oil-in-water type (w/O/W). These systems can be made through either a single-step[9,10] or a two-step process.[11,12] In the one-step method, internal and external water phases have the same composition. Moreover, this method may require an additional step of bulk purification (e.g., through a desalination column in the case of nanosized carriers). This method is not optimized for the encapsulation of high-added-value active compounds and for obtaining high encapsulation efficiencies. On the contrary, in the two-step processes (which we followed), the internal water may be different from the external water, which makes them more suited for optimizing the encapsulation efficiency.[13−15]

The primary w_1/O emulsion must be very small, preferably a nanoemulsion stabilized by a low HLB surfactant. Reverse emulsion is generally obtained by a high-energy method, using a high-pressure homogenizer or ultrasound. For the second emulsification, several approaches can be used, but a low-energy method may be privileged in order to prevent the premature release of the hydrophilic material solubilized in the internal water droplets. Indeed, high-energy methods can destroy the primary emulsion, giving rise to simple O/W emulsions.[16]

For many years, double emulsions have been considered to be an emerging technology with high potential and high interest. Therefore, a huge research effort was undertaken to optimize double emulsions for industrial applications and scale-up. However, to date, only a few products based on these emulsions are on the market.[4] The main issue is that their limited stability (i.e., formulating robust double emulsions able to conserve its specifications with respect to storage time, appearance, texture, and taste) involves long-term physical and chemical stability. This stability is very difficult to control in double emulsions due to the difference in osmotic pressure between the inner and outer water phases that should be equalized, and the difference in Laplace hydrodynamic pressure that tends to vanish with time and modify the morphology of the double structure. These equilibration phenomena are also favored by the surfactants used for the first emulsification, which destabilize the thin liquid films between internal water droplets. As a result, the stability

Received: November 22, 2018
Revised: January 8, 2019
Published: January 10, 2019

DOI: 10.1021/acs.langmuir.8b03919
Langmuir 2019, 35, 2313−2325

equation is complex and highly challenging. At this point, using a nanoemulsion as a primary w_1/O emulsion can be an interesting option as a result of the strong stability of the nanodroplets.

On the other hand, stable double emulsions of nanometric size (<200 nm) are difficult to obtain because the second nanoemulsification process is very drastic in this case and the reduced dimensions of the oil film between internal droplets and the bulk can facilitate water transfer. Reducing the scale of the double emulsions should allow the nanoencapsulation of hydrophilic and lipophilic species in a single particle, compatible with parenteral and i.v. administration. For example, such a coencapsulation of drugs is critical for optimizing targeted therapies by the simultaneous codelivery of anticancer species with another complementary cytotoxic molecule, anti-inflammatory agent, or adjuvant. Double-emulsion formulations at the nanoscale have already been reported,[12−15,17,18] but always by turning one of the liquid phase (i.e., internal water or oil) into a polymerized matrix. Herein, we present for the first time a liquid/liquid/liquid system keeping all advantages of double emulsions in terms of encapsulation and release properties, along with the advantages of nanoemulsions that allow homogeneous dispersion and compatibility with parenteral administration and targeted drug delivery.

In this context, the objective of the present study was to understand the formation of double emulsions obtained with a reverse nanoemulsion as a primary w_1/O emulsion and to explore how to improve their stability, keeping the liquid/liquid/liquid morphology even on the nanoscale. To improve the double emulsion stability, the internal water/oil interface was reinforced by a silica-based membrane synthesized in situ.[19−28] It is noteworthy that silica material as well as silica nanomaterials are, in general, widely used in biomedical applications because they are considered to be biocompatible and safe.[29−31] In the first part, micrometric-scale double emulsions were formulated to understand the impact of the formulation parameters on the integrity of the droplets, as monitored by the encapsulation efficiency and leakage of a water-soluble dye (methylene blue). The second part of the study aimed to transpose the optimized formulation to the nanoscale, by modifying the secondary emulsification. Double nanoemulsions were characterized by dynamic light scattering (DLS) and transmission electron microscopy (TEM) as well as by measuring the encapsulation efficiencies (EE) and release profile of hydrophilic model species encapsulated in the internal aqueous droplets.

EXPERIMENTAL SECTION

Materials. Oil compatible with parenteral administration (Labrafac WL 1349) was obtained from Gattefossé S.A., Saint-Priest, France. This is a mixture of capric and caprylic acids that we used throughout this study as the oil phase and thus as continuous phase in the primary w_1/O nanoemulsion. Polyglycerol polyricinoleate (PGPR) was kindly gifted by Stéarinerie Dubois (Boulogne-Billancourt, France), and served as a lipophilic surfactant (HLB around 1.5) for the preparation of a primary w_1/O nanoemulsion. This emulsifier is largely used for human consumption, being approved for food formulation by the FDA (Food and Drug Administration) and the JECFA (Joint FAO/WHO Expert Committee on Food Additives). Kolliphor ELP (BASF, Ludwigshafen, Germany) is a hydrophilic nonionic surfactant (HLB around 13) compatible with parenteral administration that was used as a hydrophilic surfactant for the second emulsification step in the formulation of double droplets. Methylene blue, tetra ethyl orthosilicate (TEOS), (3-aminopropyl) triethoxysilane (APTES), and sulforhodamine 101 were purchased from Sigma (St. Louis, MO, USA).

Methods. *Formation of a Primary w_1/O Nanoemulsion.* The oil phase (4.8 g) consists of Labrafac WL 1349 containing PGPR (from 1 to 35 wt %) and the silica precursor (the quantity of TEOS ranging from 5 to 25 wt % or the quantity of APTES ranging from 2.5 to 10 wt %). The oil phase was mixed with the aqueous phase w_1 (1.2 g) made of distilled water containing $CaCl_2$ (5 wt %). This mixture was first vortex mixed for 1 min and then adjusted at 50 °C with gentle mixing at 100 rpm in a ThermoMixer C (Eppendorf) for 5 min. This choice of 50 °C simply comes from the experiment: compared to a similar experiment at room temperature, stirring the premix at 50 °C before the stage of nanoemulsification by ultrasonication is highly beneficial to the properties of the resulting dispersion. The size distribution is thinner, and the sample homogeneity and stability are improved. The reason could be linked to the modification of the phase viscosities lowered at higher temperature, impacting the phase viscosities ratio and thus impacting the critical Weber number (We_c) (cf., the classical so-called Grace curve). As a result, viscous forces may prevail over capillary forces, and the droplet fractionation is increased. Next, this coarse dispersion was nanoemulsified by ultrasonication (Bio block 75043, Sonics Materials, Newtown, MA, USA) operating at 400 W, 20 kHz, 3 mm sonotrode with total operating times of 5 to 20 min (cycles of 30 s carried out in a succession of 10 s of sonication and 20 s off).

Preparation of the Micrometric Double Emulsions $w_1/O/W_2$. The $w_1/O/W_2$ double emulsions of micrometric size were prepared by mixing the aqueous phase W_2 (4.8 g) made of distilled water and Kolliphor ELP solubilized at concentrations ranging from 15 to 25 wt % with the primary emulsion w_1/O (1.2 g) playing the role of the oil phase in the second emulsification. This mixture was vortex mixed for 30 s and emulsified with an UltraTurrax high-speed rotor/stator homogenizer (IKA T25 M Germany) operating at 15 000 rpm for 5 min.

Preparation of Nanometric Double Emulsions $w_1/O/W_2$. To formulate double emulsions in the nanometric range, the second emulsification step must be a nanoemulsification process. The oil phase is the primary emulsion w_1/O (1.2 g) directly mixed with Kolliphor ELP at different surfactant-to-oil weight ratios (SORs) ranging from 25 to 45%. This mixture was vortex mixed for 30 s, and the second aqueous phase W_2 (4.8 g of distilled water) was suddenly added before final vortex mixing (3 min). This immediately generates the double nanoemulsion according to the spontaneous emulsification method.[32−34]

Characterization of Primary Emulsions. All of the characterizations of primary and double emulsions, size, encapsulation efficiency, and release were carried out in triplicate on different formulations.

Hydrodynamic Diameter and PDI. The hydrodynamic diameter, size distribution, and PDI of the primary emulsions were determined by dynamic light scattering (Malvern ZS 90, Malvern Instruments, Orsay, France). Measurements were performed after a suitable dilution of the sample with oil, up to the point where the milky aspect of the sample becomes transparent, allowing the DLS measurement. In the case of primary emulsions, the diluent was exactly the same oil (medium-chain triglycerides, Labrafac WL 1349) used to prepare these primary w_1/O nanoemulsions. In the second case, $w_1/O/W_2$, dilution was performed only with distilled water. The effect of dilution on the droplet size distributions was checked by different assays at different dilutions, and (data not shown) in both cases, the dilution does not affect the results. Each formulation and measurement was repeated three times.

Encapsulation Efficiency. The encapsulation efficiency of primary emulsions was measured to confirm that the methylene blue dyes are effectively encapsulated in the primary nanoemulsion and can be totally released. The primary emulsion is destabilized by mixing with a large amount of Kolliphor ELP (with a weight ratio of 50:50 with respect to the primary emulsion) and held at 90 °C for 1 h

DOI: 10.1021/acs.langmuir.8b03919
Langmuir 2019, 35, 2313−2325

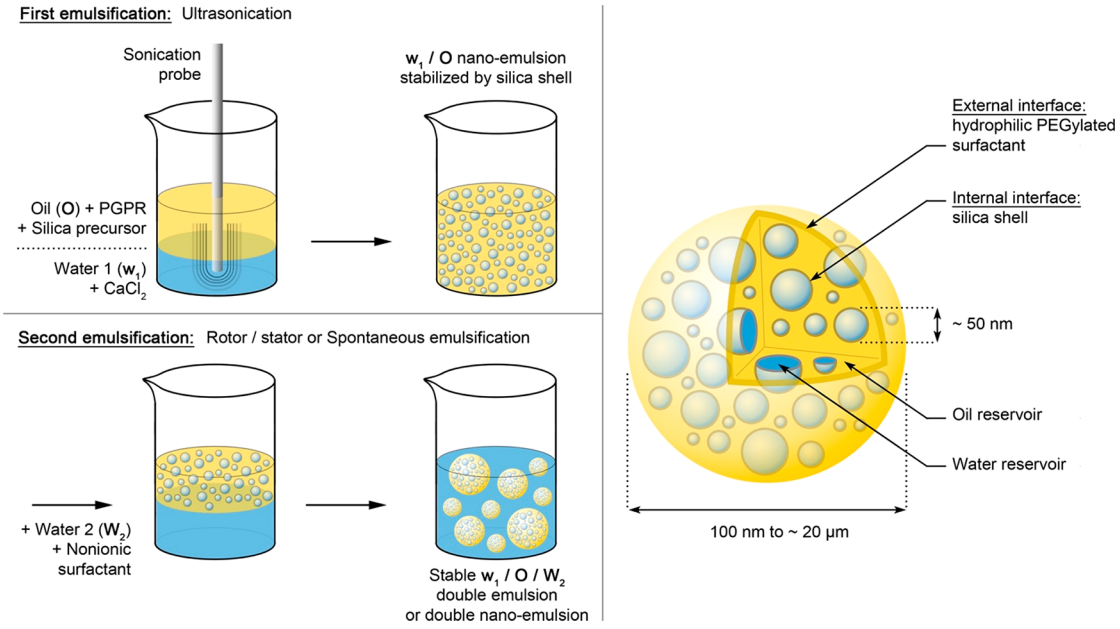

Figure 1. Formulation of the micrometric and nanometric double droplets stabilized by a silica shell. The first emulsification provides the primary reverse nanoemulsion by which the water/oil interface is stabilized by both PGPR and the silica shell. The second emulsification is performed either by a rotor/stator apparatus (Ultraturrax) for micrometric double emulsions or by spontaneous emulsification for double nanoemulsions.

(ThermoMixer C, Eppendorf). Then, the mixture is centrifuged for 30 min at 13 500 rpm to complete the destabilization of the w_1/O nanoemulsion and induce a phase separation. This allows the collection of the aqueous phase at the bottom of the tube. The supernatant was removed, and the aqueous phase was washed with dichloromethane three times. Finally, dichloromethane was evaporated, and the methylene blue was dissolved in distilled water and quantified by absorption spectroscopy after a controlled dilution (plate reader Safas Xenius XM). The process was repeated three times, and averages of the encapsulation efficiency were reported as final values.

Characterization of Micrometric Double Emulsions. Optical Microscopy. The micrometric double emulsions were visually characterized by optical microscopy (AXIO Imager.A1, Carl Zeiss, Marly le-Roi, France). Different samples and controls were selected: emulsions without a primary emulsion, double emulsions without silica precursors, and double emulsions with silica precursors at 2.5 and 10 wt % in oil. (See the details in the text below.) A little drop of the suspension was deposited on the glass slide, covered with a coverslip, and observed at a magnification of 40× (recorded with an Axiocam camera). This optical characterization reveals the global morphology of the droplets (evidencing the double structure) and their size distribution through size analysis with ImageJ (done on around 100 droplets).

Encapsulation Efficiency Study. The ability of the double emulsions to encapsulate hydrophilic molecules was evaluated through the encapsulation efficiency (EE) value that was determined by comparing the dye encapsulated in the emulsions with the free dye in the bulk aqueous phase. To this end, 1 mL double emulsion samples were taken in Eppendorf tubes and centrifuged at 13 400 rpm for 30 min. As the size of these double droplets is micrometric, their separation is effective by a simple centrifugation. Bulk water was then collected with a syringe, filtered on 0.45 μm filters, diluted with distilled water, and analyzed by spectrophotometry.

Stability Studies at High Temperature. To evaluate their stability, the micrometric double emulsions were exposed to 90 °C (1 mL samples in Eppendorf tubes set in a boiler). Stability was assessed by following the EE loss for 30 min and 1 h, as described above.

Characterization of Nanometric Double Emulsions. Physicochemical Characterization. The hydrodynamic diameter and PDI were determined by dynamic light scattering (NanoZS, Malvern), as described above. In transmission electron microscopy, the double structure of the double emulsion shows a good contrast mainly because the silica capsules and the oil have two distinct electron attenuations and thus a distinct contrast. Samples were used without any staining agent and were diluted (1/10) with Milli-Q water. A drop of suspension was placed on a carbon grid (carbon type-A, 300 mesh, copper, Ted Pella Inc. Redding, PA, USA) and dried at 60 °C for 30 min. Observations were carried out using a Philips Morgagni 268D electron microscope operating at 70 kV. It is noteworthy that the operating conditions we used (70 kV) are very low compared to TEM experimental conditions generally followed in material science (e.g., 200 kV). This was chosen to minimally affect the samples.

Encapsulation Efficiency. As described above for micrometric double emulsions, EE values were determined by quantifying the dye concentration in the external bulk phase. However, as centrifugation is not efficient for separating such nanodroplets, they were separated from free dyes by size exclusion chromatography using a desalting column (PD-10 Sephadex G-25 M, GE Healthcare). One milliliter of sample was introduced into the prepacked column and then eluted using distilled water. (About 30 mL of distilled water was first introduced into the column for equilibration.) The elution showed that double nanodroplets came first and then a clear boundary was observed, finally eluting free dye. The free dye fractions were quantified by spectrophotometry. Each formulation and measurement was repeated three times.

Dye Release Studies. The release studies were performed by dialysis. One milliliter of sample was introduced into a dialysis tube (Spectrum Laboratories, 12−14 kDa) and dialyzed against distilled water at 37 °C, under gentle stirring at 500 rpm, in a volume of 500 mL. The samples were collected after 0.5, 1, 2, 4, and 6 h. EE values were determined by separating and quantifying free dyes (by spectrophotometry) and expressed as cumulative release as a function of time.

Spectroscopy. Emission spectra were recorded on a FluoroMax-4 spectrofluorometer (Horiba Jobin Yvon) equipped with a thermostated cell compartment. For the standard recording of fluorescence spectra, the emission was collected 10 nm after the excitation wavelength. All of the spectra were corrected from the wavelength-dependent response of the detector. Fluorescent behavior of SR101, in Milli-Q water, was recorded as a function of its concentration (data not shown) and exhibited linear behavior up to 10−20 μM, which was then attenuated at higher concentrations due to a partial quenching of

DOI: 10.1021/acs.langmuir.8b03919
Langmuir 2019, 35, 2313−2325

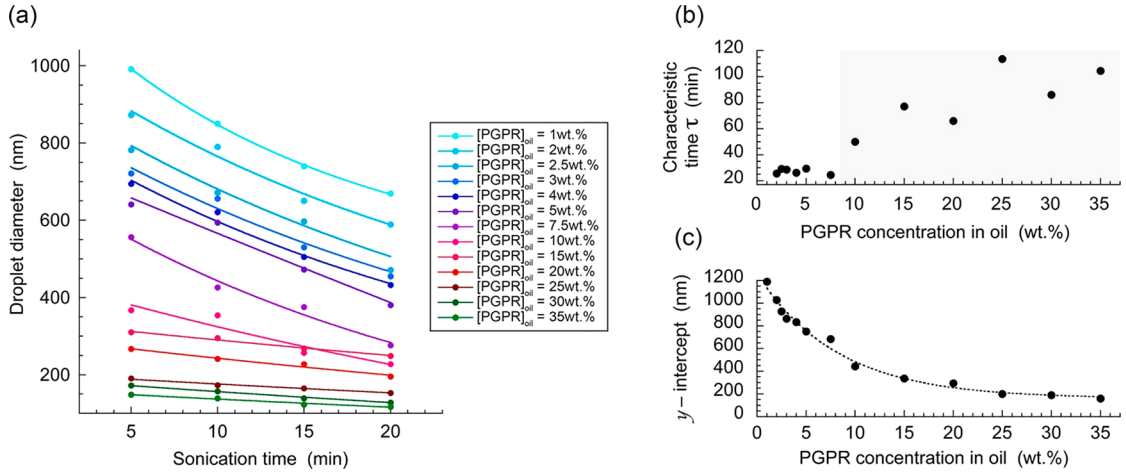

Figure 2. Dependence of the size of w_1/O nanoemulsion as a function of time and concentration of surfactant (PGPR) in oil. (a) The curves of the dependence of the size of the w_1/O nanoemulsion (ϕ_V^{water} = 20%) as a function of the sonication time were fitted by an exponential model (details in the text). (b) Characteristic time and (c) y intercept from the curve fits of (a) vs surfactant concentration.

SR101 induced by an ACQ (aggregation-caused quenching) effect. SR101 is included in the inner water at high concentration (100 μM in w_1) to ensure the dye detectability for the different formulation stages that involve its dilution. On the other hand, to prove that SR101 is not soluble in oil, it was dispersed in Labrafac WL 1349 as follows: 2.3 mg of SR101 was mixed in 500 μL of Labrafac WL 1349, held at 60 °C for 1 h, and then slightly centrifugated to remove nondispersed crystals, collecting the supernatant for fluorescent measurement. Fluorescent spectra were recorded in triplicate on three different formulations, reporting the mean spectra in the figure.

RESULTS AND DISCUSSION

The great interest in double emulsions, even today, remains undeniable, probably due to the lack of appropriate solutions for encapsulating hydrophilic materials or for coencapsulating hydrophilic and lipophilic materials. However, because the double emulsions are of limited stability, the present study proposes a simple modification of the conventional two-step preparation process used to stabilize them by reinforcing the w_1/O interface with a small silica membrane. This innovative methodology makes it possible not only to create stable micrometric double emulsions (of about 10 μm) but also to formulate double nanodroplets of <130 nm in diameter. The formulation process and the structure of the formulated double droplets are described in Figure 1.

For the formulation of the first emulsion, the oil phase, contains a lipophilic surfactant and a silica precursor. The energy supplied by the sonication process has two roles: (i) it allows the creation of the nanodroplets and (ii) it induces the polycondensation of the silica precursor[19−22,35] specifically at the water/oil interface. As a result, this first process produces aqueous nanodroplets in the form of silica nanocapsules.[36,37] Next, this primary emulsion is used as the oil phase for a second emulsification process in order to generate micrometric double droplets by using a mechanical method (rotor/stator, Ultraturrax), or nanometric double droplets by spontaneous emulsification.[32,38] In the following sections, we will investigate in depth the formulation of the primary emulsion and analyze the impact of the formulation parameters on its properties, and then we will characterize the macroscale and nanoscale double emulsions.

Primary w_1/O Nanoemulsions and Silica Nanocapsules. The singularity of the nanoemulsification process based on ultrasonication lies in the amount of energy focused on a small volume. The high acoustic field leads to the gradual growth of cavitation bubbles, up to their implosion. This induces huge shearing forces that break up the aqueous droplets into smaller ones that are stabilized by the surfactants (PGPR). The average droplet size decreases as a function of the quantity of energy supplied.

To prevent the destruction of the double droplets during and after the second emulsification, the original approach proposed in this study resides in the stabilization of the water/oil interface of the primary droplets by a silica membrane synthesized in situ to preserve the aqueous droplets and their encapsulation properties. On the basis of previous work,[19−22] the silica precursors were introduced into the oil phase, and the interfacial polycondensation was initiated through a sonochemistry-mediated reaction. Two different silica precursors, TEOS and APTES, were studied. The growth of the silica chains occurs by the simultaneous presence of water and precursors solubilized in oil, and the silica shell is therefore formed and trapped at the water/oil interface.

Reverse Nanoemulsification. In this section, we will focus on the emulsification itself without silica and investigate the influence of the surfactant concentration and processing time on the size and polydispersity of the primary w_1/O nanoemulsions. By monitoring the impact of the sonication time for different PGPR concentrations (ϕ_V^{water} = 20%), we observed, as expected,[39−42] a decrease in the droplet size (Figure 2a) according to a monoexponential decay $d = Ae^{(-t/\tau)} + d_\infty$ where d is the droplet diameter, A is a constant, d_∞ is the saturation diameter (diameter after stabilization of the monoexponential function), t is the sonication time, and τ is the characteristic time of the exponential. The choice of this monoexponential model was based on the literature, considered to be the more accurate description of the droplet size decrease, as a consequence of the droplet fractionation induced by ultrasonication.[39] The droplet fractionation directly results from the amount of energy supplied and gradually stabilizes up to a saturation size d_∞. The droplet size is clearly dependent on the surfactant concentration, with a decrease by about 800 nm between 1 and 35 wt %. Reporting the values of the characteristic time τ as a function of the sonication time (Figure 2b) revealed that the

DOI: 10.1021/acs.langmuir.8b03919
Langmuir 2019, 35, 2313−2325

time necessary to stabilize the droplet size showed first (up to 7.5 wt %) a plateau giving $\tau \approx 30$ min, indicating that the nanodroplets are rapidly stabilized independently of the PGPR concentration.[38,43,44] Then, a second regime appears (from 10 wt %) in which the τ values are much higher and gradually increase up to 100 min. This regime likely corresponds to a saturation regime in which the droplets are rapidly stabilized after their formation, followed by a further evolution of the size much more slowly. The threshold of 10 wt % PGPR is believed to correspond to the saturation regime that allows very small sizes to be achieved. When extrapolating the curve fits at $t = 0$ (Figure 2c), the sizes also show a stabilization for PGPR concentrations higher than 10−15 wt %. The y intercept reported in Figure 2c is an interesting parameter reflecting the whole behavior of the emulsification process, thus allowing a comparison between the different PGPR concentrations.

To formulate reverse nanoemulsions below 300 nm, our data pointed out that a PGPR concentration in oil of at least 10 wt % is required. However, a sonication time of 20 min is too long for a potential industrial application because it may destroy the encapsulated materials, increase the sample temperature, and release a large number of titanium nanoparticles from the sonication tip. An ideal sonication time should be no more than 5 min. In addition, to obtain double nanoemulsions based on this primary emulsion, the droplet size should be ideally decreased to 100 nm or less.[45,46]

Accordingly, the sonication time was fixed to 5 min, and the PGPR concentration was varied from 10 to 35 wt %. The results reported in Figure 3 confirmed the trend revealed in Figure 2, with a significant size decrease as a function of the surfactant concentration. At $[PGPR]_{oil} > 25$ wt %, sizes below 160 nm were observed. However, the variability of the results was quite high, likely related to the polydispersity of the nanoemulsions because PDI values ranged from 0.3 to 0.5 for all measurements with pure water as reported in Figure 3. In line with previous reports[44,47] showing that the emulsifying properties of PGPR can be improved when calcium chloride is added to the aqueous phase, the emulsification process was clearly more efficient in the presence of this additive (Figure 3, open symbols), providing droplets below 100 nm for [PGPR] ≥ 10 wt % and down to 50 nm for [PGPR] ≥ 30 wt %. Moreover, calcium chloride also improves the homogeneity and reproducibility (standard deviations are between 3 and 10 nm) of the results as well as the monodispersity (PDI values are equal to 0.16 ± 0.10 for [PGPR] = 10 wt % and to (0.06 ± 0.05) for [PGPR] ≥ 25 wt %).

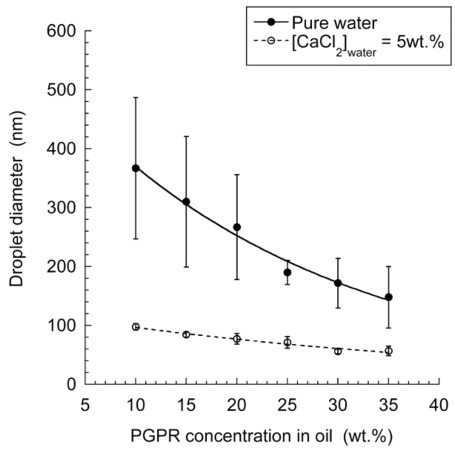

Figure 3. Effect of the PGPR concentration on the size of w_1/O nanoemulsions at a fixed sonication time of 5 min and $\phi_V^{water} = 20\%$. The experiments were done with pure distilled water as the aqueous phase (pure water) and water-containing calcium chloride as an additive ($[CaCl_2]_{water} = 5$ wt %) ($n = 3$). Lines are drawn to guide the eye.

The strong effect of $CaCl_2$ on the emulsification process may be a consequence of the modification of PGPR activity. Indeed, $CaCl_2$ is a chaotropic salt[48] that affects the hydrogen bonding between the water and the PGPR molecules. As a result, the lipophilicity of the emulsifier may be increased and its HLB may be lowered. In addition, $CaCl_2$ can also directly affect the interfacial tension and improve the emulsification properties.[44,47,49] In these articles, the authors have shown that the addition of $CaCl_2$ to water can decrease the droplet size and improve the stability of the primary w_1/O emulsion. This was explained by a specific action on the hydrophilic part of amphiphile-like PGPR through an increase in the surfactants' adsorption density, giving rise to decreasing interfacial tension along increasing interfacial elasticity and involving a reduction in the attractive forces between water droplets after their formation. Finally, all of these effects combined can strongly impact the emulsification process, lowering the rate of droplet recombination during sonication and thus decreasing the size, polydispersity, and variability of the results (i.e., lowering the standard deviation as it is presented in Figure 3). To conclude, in view of these results, the formulation with $[PGPR]_{oil} = 30$ wt % (giving a droplet size of (57 ± 4) nm and a PDI value equal to 0.06) was selected as the primary emulsion for the fabrication of the double emulsions.

Silica Nanocapsules. As described above, the silica shell is built at the water/oil interface of the reverse nanoemulsions through sonochemistry.[19−22,35] Two different silica precursors (TEOS and APTES) were solubilized in the oil phase. The silica precursors hydrolyze first and then undergo the condensation process. The hydrolysis of APTES and TEOS leads to the production of ethanol and trisilanols. The Si−C bond will not be hydrolyzed because this bond is hydrolytically stable, and thus the aminopropyl group will stay in the polymer structure. On the other hand, the transient silanol groups will condense with other silanols to produce the amino-functionalized network. Interestingly, the impact on the double emulsion of the alcohol formed during the chemical reaction cannot be specifically determined but will be included in the global determination of the encapsulation efficiency values, along with the other formulation and processing parameters. The emulsification process was performed under the same conditions as described above: $\phi_V^{water} = 20\%$, sonication time = 5 min, and $[PGPR]_{oil} = 30$ wt %. The sizes of the reverse nanodroplets (Figure 4) were compared for the APTES and TEOS precursors.

In both cases, the introduction of the silica precursor in oil before sonication increases the size of the water droplets, likely due to the formation of a silica shell around the droplets. Moreover, in both cases, the shell thickness is linearly related to the concentration of silica precursor in oil. Nevertheless, the slopes are different because, probably, part of the silica remains in the oil or has been expelled in water. It is important to note that we cannot prove that the water droplets do not increase when the amount of silica precursor is increased. However, we have thus assumed that because the formulation parameters were fixed ($\phi_V^{water} = 20\%$, sonication time = 5 min, $[PGPR]_{oil} =$

DOI: 10.1021/acs.langmuir.8b03919
Langmuir 2019, 35, 2313−2325

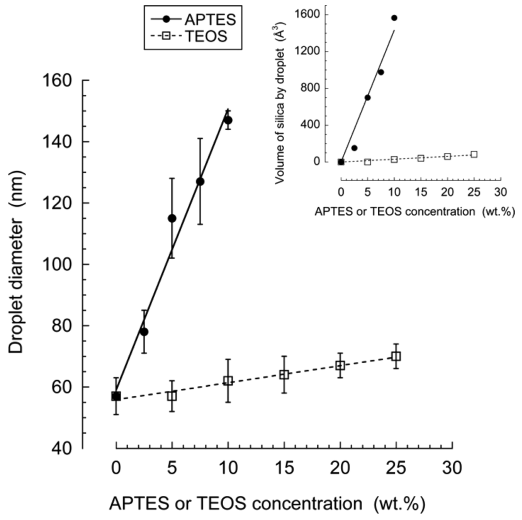

Figure 4. Effect of the concentration of the silica precursor (APTES or TEOS) on the size of the primary w_1/O nanoemulsion (n = 3). (Inset) Dependence as a function of the silica precursor of the volume of the nanodroplets, calculated from their diameter.

30 wt %), the size of the water droplet core is considered to be constant and the silica shell gradually grows around it. In addition, the fact that the relationship between droplet size and silica precursor concentration is linear supports the assumption that the size of the water cavities should be the size of the initial aqueous droplets without silica (around 60 nm in the example shown in Figure 4), and the silica shells grow around it.

However, APTES appears to be much more efficient than TEOS for interfacial polycondensation. For example, at a concentration of 10 wt %, TEOS induced a shell thickness of about 3 nm, while it reached about 45 nm with APTES. On the basis of these data, the global volume of the silica shell can be estimated as a function of the precursor concentration (Figure 4, inset). The comparison of the growth rates (slopes of the linear fits, 3.0 and 143.2 $Å^3$ wt $\%^{-1}$ for TEOS and APTES, respectively) indicates that 50 times more material is synthesized at the interface with APTES than with TEOS. The silica shell thus appears to be important in stabilizing the primary emulsion in order to formulate the double droplets, and these results demonstrated the feasibility of the in situ synthesis of the silica shell in the water/oil interface of the droplets. The linear relationship between the shell thickness and the concentration of the silica precursor indicates that the shell thickness can be adjusted very finely and thus controls the encapsulation and release properties of the double emulsions. The reason that APTES is more efficient than TEOS in the polycondensation process may be related to its chemical structure.[50] Unlike TEOS, the amphiphilic properties of APTES likely play an active role in their concentration at the water/oil interface. Indeed, because the pK_a of APTES, $(CH_3{-}CH_2{-}O)_3{-}Si{-}(CH_2)_3{-}NH_2$, is around 8.5, and the aqueous phase containing $CaCl_2$ has a pH slightly below 7, the protonation of the amino function probably accelerates the migration of APTES (from oil) toward the interface, increasing the efficiency of the ultrasound-mediated interfacial polycondensation. In contrast, TEOS, lacking such a function, $(CH_3{-}CH_2{-}O)_4{-}Si$, may encounter the interface only because of molecular diffusion.

Micrometric Double Emulsions $w_1/O/W_2$. To prove that double droplets are stable when the inner droplet interface is reinforced by a silica membrane, the micrometric double emulsions formulated by a rotor/stator (Ultraturrax) device were characterized for their aspect, morphology, and size by optical microscopy (Figure 5). The microscopy images show the controls without primary emulsions O/W_2 (Figure 5a), the double emulsions $w_1/O/W_2$ without silica precursor (Figure 5b), the double emulsions $w_1/O/W_2$ with 2.5 wt % APTES (Figure 5c), and the double emulsions $w_1/O/W_2$ with 10 wt % APTES (Figure 5d).

The double droplets and the control exhibit a quite homogeneous distribution. While in the control (a), the oil droplet core appears to be clear and transparent, and the primary emulsion is clearly visible as small "corrugations" within the double droplets in b–d. These corrugations are likely due to the light diffraction of the aqueous internal droplets and the limited resolution of the optical microscope around 300 nm. On the basis of these images, the double droplet size distribution was determined by a graphical analysis

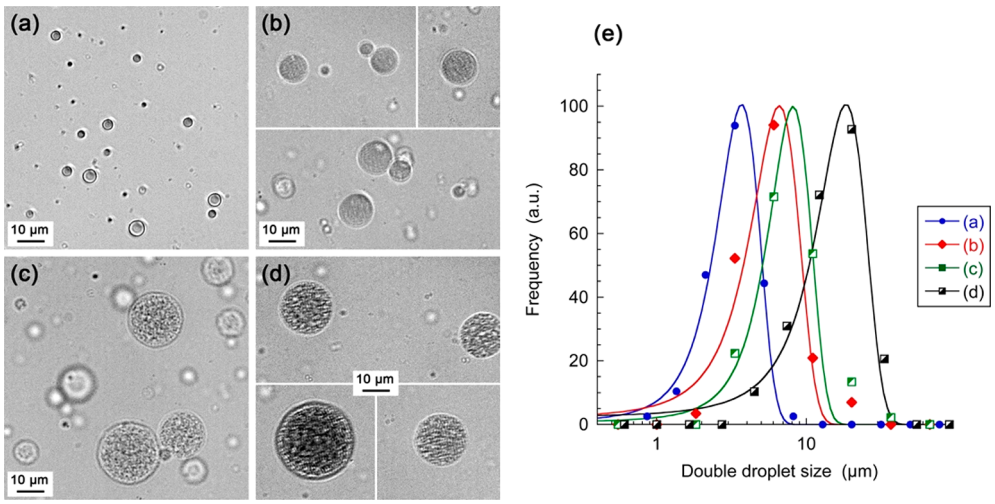

Figure 5. Optical microscopy of controls without primary emulsions O/W_2 (a), double emulsions $w_1/O/W_2$ without the silica precursor (b), and double emulsions $w_1/O/W_2$ with 2.5 wt % APTES (c) and with 10 wt % APTES (d) ($\phi_V^{\text{oil phase}}$ = 20% and [Kolliphor ELP] = 25%). (e) Corresponding size distribution analysis of samples of 100 droplets fitted by a Gaussian function.

DOI: 10.1021/acs.langmuir.8b03919
Langmuir 2019, 35, 2313–2325

(Figure 5, right) for about 100 droplets each time. The experimental data were successfully fitted with a Gaussian equation, giving average sizes of 3.7, 6.6, 8.1, and 18.3 μm, respectively for a−d. As expected, the emulsification process is affected by the presence and size of the primary droplets. Indeed, because the size of these droplets playing the role of the template increases with increasing APTES concentration, the size of the double droplets increases as well.

To investigate the stability of these double emulsions in the formulation process, we monitored the leakage of methylene blue (MB) solubilized in the inner water w_1 toward the external water W_2. It is important to note that the EE values are those immediately after the second emulsification and thus describe the impact of the process itself on the structure of the double droplets, while the leakage of w_1 induced by storage will be studied and discussed in the following sections. Before discussing the EE values of double droplets, it is important to consider the preliminary controls regarding the full release of MB from the primary emulsion. In these control experiments performed on the primary emulsions (described in the Experimental Section) for APTES varying from 0 to 10 wt % and for TEOS varying from 0 to 25 wt %, values of total release are 99.6 ± 0.2 and 99.2 ± 0.4%, respectively. This clearly demonstrates that encapsulated materials can be released irrespective of the thickness of the silica shell.

The EE values for the double emulsions formulated with APTES and TEOS are reported in Figure 6 for different concentrations of the hydrophilic surfactant (Kolliphor ELP). The EE value for the formulation without silica is relatively weak (~25%) but increases rapidly with the silica concentration. In the case of APTES, the EE value increases rapidly to 80% for [APTES] = 0.25 wt % and reaches about 95% for [APTES] = 10 wt %. A similar trend is observed for TEOS, but higher TEOS concentrations are needed and EE values hardly exceed 60%. These results are in line with the respective efficiencies of APTES and TEOS in the fabrication of the silica shell (Figure 4). They indicate that even at very low concentrations APTES can efficiently reinforce the water/oil interface to stabilize the double emulsion against the second emulsification. The strong effect of low concentrations of APTES on the EE is outstanding and discloses the high potential of the technology to produce stable double emulsions compatible with the regulatory aspects imposed by industrial production and applications. The difference in EE between APTES and TEOS is likely related to the thickness and probably the density of the silica shell (Figure 4), which makes the silica shell more impermeable with APTES. In fact, in the Figure 4 inset, the "volume of silica by droplet" is represented as a function of the precursor concentration, revealing an important difference between APTES and TEOS, so a parallel can be drawn with the EE values correlating the results of Figure 6. Because of its high efficiency, we selected APTES for further stability studies and the formulation of double droplets at the nanoscale. It is noteworthy that the stability claimed herein and brought about by the reinforcement of interface by silica refers to the fact that the internal water droplets are much more robust compared to the ones without silica. The globules formed are much more robust toward changes in temperature, changes in osmotic pressure, and also the formulation processes (large differences in EE when we compare with and without silica). As a result, we can say that classical double emulsions are much more fragile compared to these new stabilized formulations. This is all the more confirmed by the accelerated aging experiment detailed below.

To further investigate the stability of the double droplets, we monitored their EE values at high temperature (90 °C) as a function of time and for several APTES concentrations (Figure 7). The idea here was to place the samples under very harsh conditions, such as those for accelerated aging procedures that are generally worked out (to a lesser extent). The results

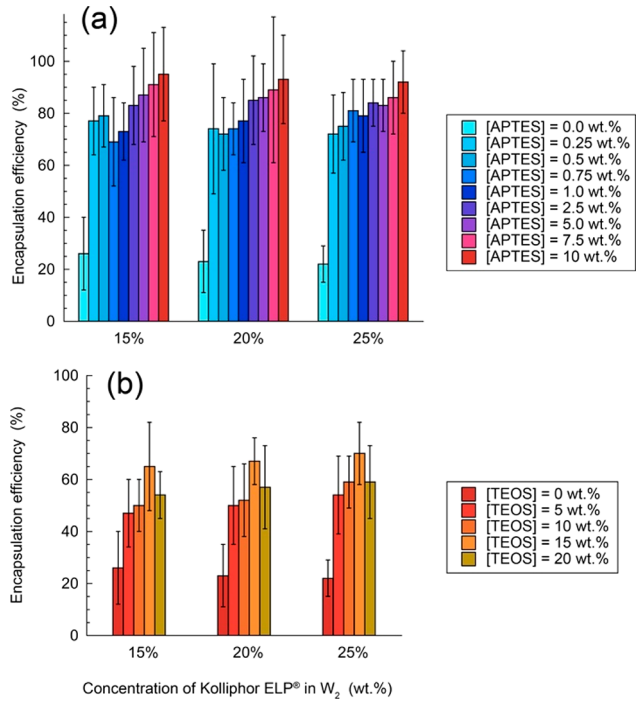

Figure 6. Encapsulation efficiency of MB solubilized in the inner water droplets of macroscopic double emulsions, immediately after the second emulsification. Effect of the concentration of the silica precursor in oil (APTES in a and TEOS in b) and for different concentrations of the hydrophilic surfactant (Kolliphor ELP) in W_2 (n = 3).

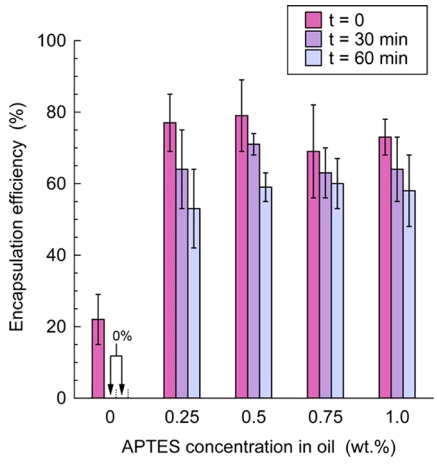

Figure 7. Encapsulation efficiency of MB solubilized in the inner water droplets of macroscopic double emulsions ($\phi_V^{\text{oil phase}}$ = 20% and [Kolliphor ELP] = 25%) immediately after the second emulsification (t = 0) or at high temperature (90 °C) for 30 or 60 min. The $[\text{APTES}]_{\text{oil}}$ = 0 wt % data point corresponds to the control without the silica precursor.

DOI: 10.1021/acs.langmuir.8b03919
Langmuir 2019, 35, 2313−2325

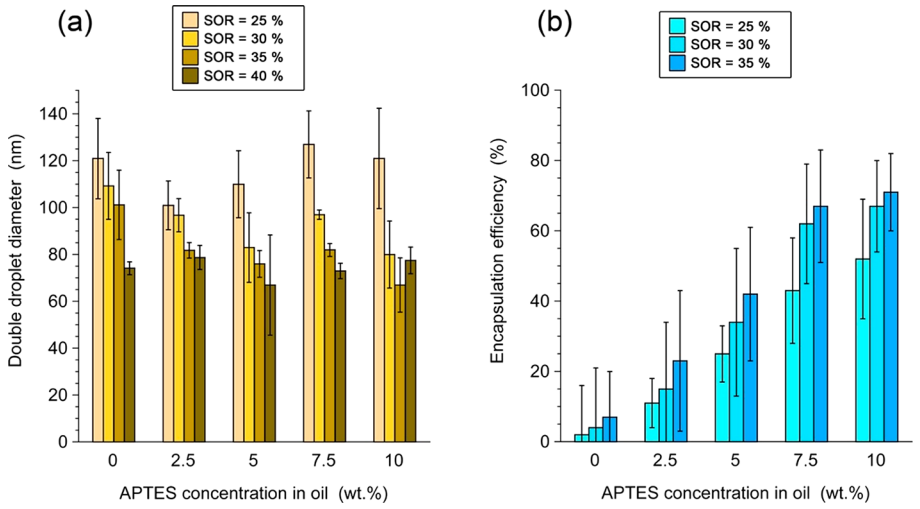

Figure 8. Diameter (a) and encapsulation efficiency (b) of double nanoemulsions for different concentrations of APTES and SOR. The nanoemulsions were obtained by spontaneous emulsification at room temperature. The encapsulation efficiencies were calculated from the concentration of methylene blue measured after the application of fresh samples on size exclusion chromatography columns.

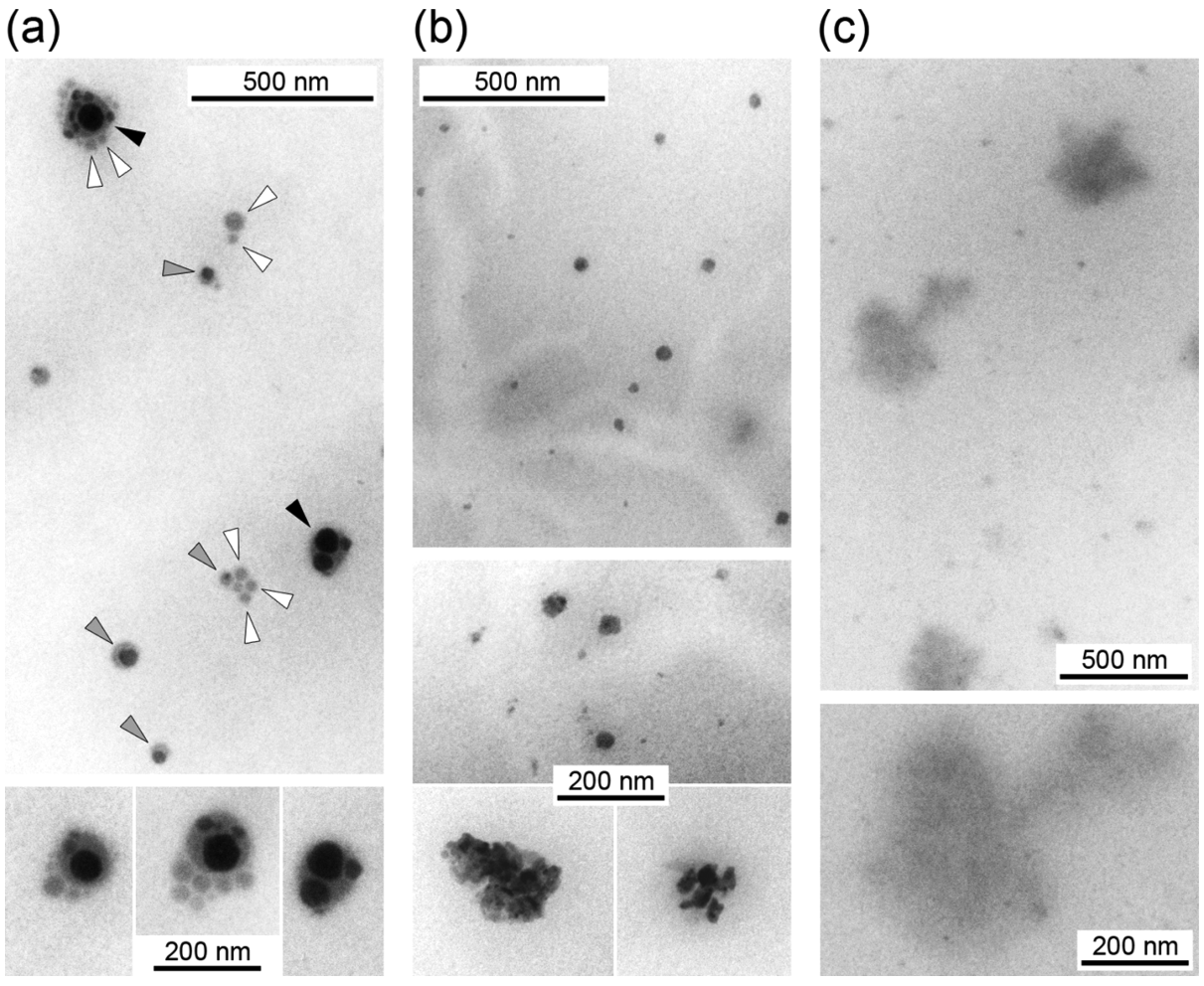

Figure 9. Transmission electron microscopy of double nanoemulsions for APTES concentrations of (a) 10 wt %, (b) 2.5 wt %, and (c) 0 wt %. Oil droplets can contain several (black arrowheads), one (gray arrowheads), or zero (white arrowheads) silica shells containing water droplets.

appear to be in line with our expectation, exhibiting a significant difference between control and silica-protected samples. A temperature of 90 °C was in fact chosen as the higher temperature before boiling to conduct such experiments under harsh temperature conditions. For the control (without APTES), the EE value starts at 23% and decreases to 0% after 30 min, indicating a very rapid release of the encapsulated compounds. In contrast, for [APTES] ≥ 0.25 wt %, the double

DOI: 10.1021/acs.langmuir.8b03919
Langmuir 2019, 35, 2313−2325

droplets appear to be much more resistant. A slow and regular release of dyes was observed, whatever the amount of silica. This observation confirmed the strengthening of the interface by the silica membrane, even at 0.25 wt % APTES, and the still possible release of encapsulated materials with time, as evidenced by the 20−30% decrease in the EE value after 60 min. After 1 h, the encapsulated MB became purple (the color of the crystalline form of this molecule) probably as a result of crystallization, which did not allow this experiment to be continued at 90 °C.

These results indicate that the silica shell formed by APTES is resistant to high temperature, which opens a number of applications. For example, in food applications, the double emulsions can ensure an efficient storage of hydrophilic materials such as flavors and then allow their controlled delivery during cooking.

Nanometric Double Emulsions $w_1/O/W_2$. In this last section, our goal was to transfer the best experimental conditions described for double micrometer emulsions to the formulation of double droplets smaller than 1 μm. For this purpose, the second emulsification has been adapted to be a nanoemulsification process capable of preserving the structure of the primary w_1/O nanoemulsions. Basically, nanoemulsification methods are divided into high-energy processes[51] (high-pressure homogenization or utrasonification) and low-energy processes based on spontaneous emulsification. To preserve the primary emulsion, we selected the gentlest process (i.e., the spontaneous emulsification). In this process, the hydrophilic surfactant in the oil phase (w_1/O nanoemulsion) is mixed at room temperature, and when homogenized, the second aqueous phase W_2 is added, producing spontaneous nanoemulsification.[52,53] Though it is a soft process, the droplets are formed as a result of the turbulent penetration of water in the network made of oil, primary droplets, and Kolliphor ELP. This turbulent droplet formation is less destructive than high-energy methods but is nevertheless aggressive for the small aqueous nanodroplets of the primary emulsion. This is confirmed by the data in Figure 8 correlating the size of the nanometric double emulsion (Figure 8a) with the encapsulation efficiency of MB (Figure 8b) as a function of the surfactant-to-oil weight ratio (SOR) and the APTES concentration (i.e., thickness of the silica shell). The global size of the double nanoemulsions is below 120 nm and, as expected, decreases as the quantity of surfactant increases, reaching 70 nm for SOR = 40%. The general behavior of the size decrease observed is similar whatever the concentration of APTES, indicating that the spontaneous emulsification is robust enough not to be affected by the modification of the oil composition. The EE values (Figure 8b) are strongly impacted by the silica shell. Indeed, without silica ([APTES] = 0 wt %), all of the MB leaks rapidly and the EE value is close to zero. Then, the EE values regularly grow as the APTES concentration in oil increases, reaching 60−70% for [APTES] = 10 wt %. Compared to macroscale double emulsions, the nanoemulsification process has a real destructive effect on the double nanodroplets and thus requires a higher shell thickness to provide efficient encapsulation (i.e., [APTES] = 7.5 wt % versus 0.25 wt % for macroscale double emulsions, see Figure 6a). Interestingly, for a given APTES concentration, the EE value depends on the SOR parameter. As a result, it is observed that the EE value and the size of the double nanodroplets are inversely correlated. This result is very important, even if the order of magnitude of the encapsulation efficiency is slightly below those of microscale double emulsions (discussed above Figure 6), and remains absolutely unprecedented regarding nanoscale double droplets.

To confirm the double structure of the nanoemulsions and further rationalize the data in Figure 8, transmission election microscopy was performed on representative samples (Figure 9).

The sizes of the double droplets correspond well to those in Figure 8a, being centered at about 90 nm for SOR = 30%. The silica shells allow the droplets to conserve their shape upon drying under extensive vacuum on the carbon grid (Figure 9a,b). In contrast, the drying process in the absence of APTES destroys the nanodroplets and results in oil puddles (Figure 9c), as previously reported.[54] For [APTES] = 10 wt % (Figure 9a), the ∼45 nm thickness of the silica shell (given in Figure 4) appears to be strong enough to preserve the nanodroplet structure upon drying. The double nanostructure is clearly visible in this case, with the inner silica substructure in dark gray and the surrounding oil in light gray. Depending on their size, the double nanodroplets can include several (black arrowheads), one (gray arrowheads), or no (white arrowheads) inner water droplets. The TEM pictures also reveal that the double droplets may be deformed by the primary droplets, showing their wettability by the oil (i.e., related to their good affinity for oil because they were not expelled from the oil phase). Once the bulk phase is removed, the capillary phenomenon should give the droplet their final shapes and strongly impacts the preservation of the droplet structure and shape. This is precisely what we observe, by comparing Figure 9a, for which the structure is preserved thanks to the silica shells inside, and Figure 9c, for which the oil spreads into the carbon support. Likewise, when several inner droplets are confined in one oil drop, they also seem deformed, forming a thin planar film in their contact region. These interdroplet interactions in the larger droplets can probably lead to their small degradation compared to smaller ones, explaining the difference in EE observed as a function of their size (Figure 8). The relatively dark aspect of the inner silica-stabilized droplets is likely attributed to the important thickness of the shell, as disclosed in Figure 4. Very comparable visual dark aspects were previously reported according to similar sonochemistry of APTES at the water/oil interface of (this time) direct O/W nanoemulsions.[55] This imagery seems related to the process and to the thickness of the silica shell formed. This large silica shell (in Figure 9a of around 45 nm) can also explain why the encapsulation efficiency is not very high compared to that expected in observing the double droplets by TEM: the water cavities are actually quite small. A remark can be made regarding the oil droplets containing or not containing internal particles. In fact, Figure 9a allows us to show that only larger droplets are able to have a double structure while smaller ones cannot. In fact, the spontaneous nanoemulsification gives rise to a log-normal size distribution, and logically, the inner silica shells can be distributed only in second droplets that are large enough to entrap them.

On the other hand, nanodroplets with [APTES] = 2.5 wt % (Figure 9b) appear to burst when water has escaped (during the sample drying), in line with their low EE values (Figure 8b) of around 15% as compared to 70% for nanodroplets obtained with [APTES] = 10 wt % (Figure 9a). The low EE value suggests that most of the inner water has escaped during the second nanoemulsification process. As a result, one can

DOI: 10.1021/acs.langmuir.8b03919
Langmuir 2019, 35, 2313−2325

observe oil droplets containing the remaining fragments of the shells. Noticeably, a good match is observed between the sizes measured by DLS (Figure 4) and the TEM diameters of 130 nm for [APTES] = 10% and 80 nm for [APTES] = 2.5%. (Even if the droplets are destroyed, the scale appears to be coherent.)

In addition to their encapsulation properties, an important feature of these new multifunctional nanocarriers is their ability to release and deliver an encapsulated material. To investigate this ability, we monitor the release of MB from double nanoemulsions incubated at 37 °C. The curves in Figure 10

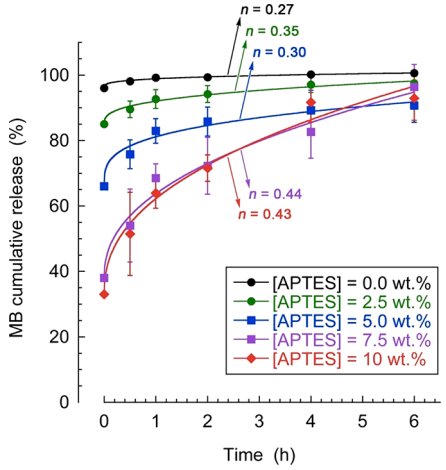

Figure 10. Release of methylene blue encapsulated in double nanoemulsions (SOR = 30%). The *y*-intercept value corresponds to the EE value after the second nanoemulsification. Experimental data are fitted using a Korsmeyer−Peppas equation giving the values of the release exponent *n*, as indicated.

represent the MB leakage into the external water phase (W_2) for up to 6 h after formulation. Because all of the samples have the same initial amount of MB (initially in w_1) but different EE values (Figure 8b), the initial offset corresponds to the MB that has already escaped during the second nanoemulsification. The release profiles are successfully fitted with a classical Korsmeyer−Peppas equation for spherical drug carriers,[56] $M_t/M_0 = K_m t^n$, where M_t/M_0 is the fraction of drug release at time t and K_m is a kinetic constant. The release exponent n allows us to identify the release regime.

For all samples, the encapsulated dye is effectively released (up to 100%), indicating that the double nanoemulsions are effective nanocarriers able to deliver the encapsulated materials. All values of the release exponent n (indicated in Figure 10) remain below the threshold of 0.5, indicating Fickian diffusion. However, a difference should exist between the samples with $n \approx 0.44$ ([APTES] = 7.5 and 10 wt %) indicative of a monodisperse Fickian drug release and the samples with $n \leq 0.35$ ([APTES] = 0, 2.5, and 5 wt %) indicative of a Fickian diffusion of a polydisperse sample.[56−58]

This difference likely arises from the fact that the double emulsions are more fragile for the lower APTES concentrations, as evidenced by the disruption and fusion of their inner droplets observed by TEM images (Figure 9). In contrast, the monodisperse Fickian drug release observed at higher APTES concentrations is in full line with the homogeneous population of internal droplets observed by TEM (Figure 9).

Proving the Presence of Water in the Inner Droplets of Micrometric and Nanometric Double Emulsions $w_1/O/W_2$. To achieve the characterization of the double structure, beyond indirect ways such as EE measurements and TEM observations, and to dispel doubts about the presence of water inside the double micro- or nanodroplets, in this last paragraph we will use a water sensor to prove that inside the double droplets we still have liquid water. The water sensor is a fluorescent dye, sulforhodamine 101 (SR101), which presents a fluorescent signal only when it is solubilized in water. The general idea is to dissolve SR101 in the internal water (w_1, at 100 μM) right from the initial formulation stage and to show that its fluorescent signal is still present within the double micro- or nanodroplets after their separation from the continuous phase. The whole experiment, along with the spectrometric results are summarized in Figure 11, showing the fluorescent spectra at every stage of the experiment. In addition, the control without silica was also reported in parallel to compare the spectra with the double emulsion with APTES 10 wt %. First, the fluorescent signal of reverse nanoemulsions is presented in Figure 11a, showing a very important fluorescent signal with peaks at 606 and 607 nm.

At exactly the same concentration, the two signals with and without APTES show significantly different fluorescence (around 4.6×10^6 and 3.4×10^6 a.u., respectively), likely due to the change in composition that generally affects the environment of the dyes and can modify their fluorescence properties. On the other hand, when dispersed in oil at saturation (Figure 11b), SR101 displays a much lower fluorescence signal of a few orders of magnitude (around 6×10^3) that is not comparable to the former and, important for the discussion, slightly color-shifted around 10 at 596 nm. This huge difference between water and oil signals, compared to the fraction containing double droplets and free dyes, will indicate whether SR101 is still dissolved in water after the separation of the droplets from the bulk.

The formulation of microscale double emulsions is shown in Figure 11c,d before and after droplets separations, respectively. Before separation (Figure 11c), both signals are comparable (around 1.5×10^6 a.u.), in line with the curves of the primary emulsion (Figure 11a) diluted by the formulation process (with the difference between samples with and without silica still visible). Then, the droplet separation shows a much more important signal in the double droplets than in the bulk phase, greater than 1.5×10^6 and smaller than 6×10^3 a.u., respectively. The wavelength of the peak (λ_{max}= 604 and 605 nm) also corresponds to the signal of SR101 solubilized in water and not transferred to oil (see Figure 11a,b). This first result proves that SR101 is still and importantly solubilized in water within the microscale double droplets, thus in the internal water. Interestingly, the signal with and without silica exhibit different fluorescence intensities, higher in both cases corresponding to the samples without silica. This is due to the dye leakage from the double droplets without silica (EE is around 22%) when there is no leakage with silica (EE around 100%) (Figure 6a). This gives rise to the dequenching of SR101 inside the droplets (due to the ACQ effect as it is explained in the Experimental Section), along with an increase in the SR101 concentration in the bulk phase, thus increasing the fluorescence signal in both cases. In addition, a close study of the different fluorescence intensities discloses a decrease in the dye concentration inside the internal droplets, likely due to the dye escape. For example, with "micro-droplets with silica",

DOI: 10.1021/acs.langmuir.8b03919
Langmuir 2019, 35, 2313−2325

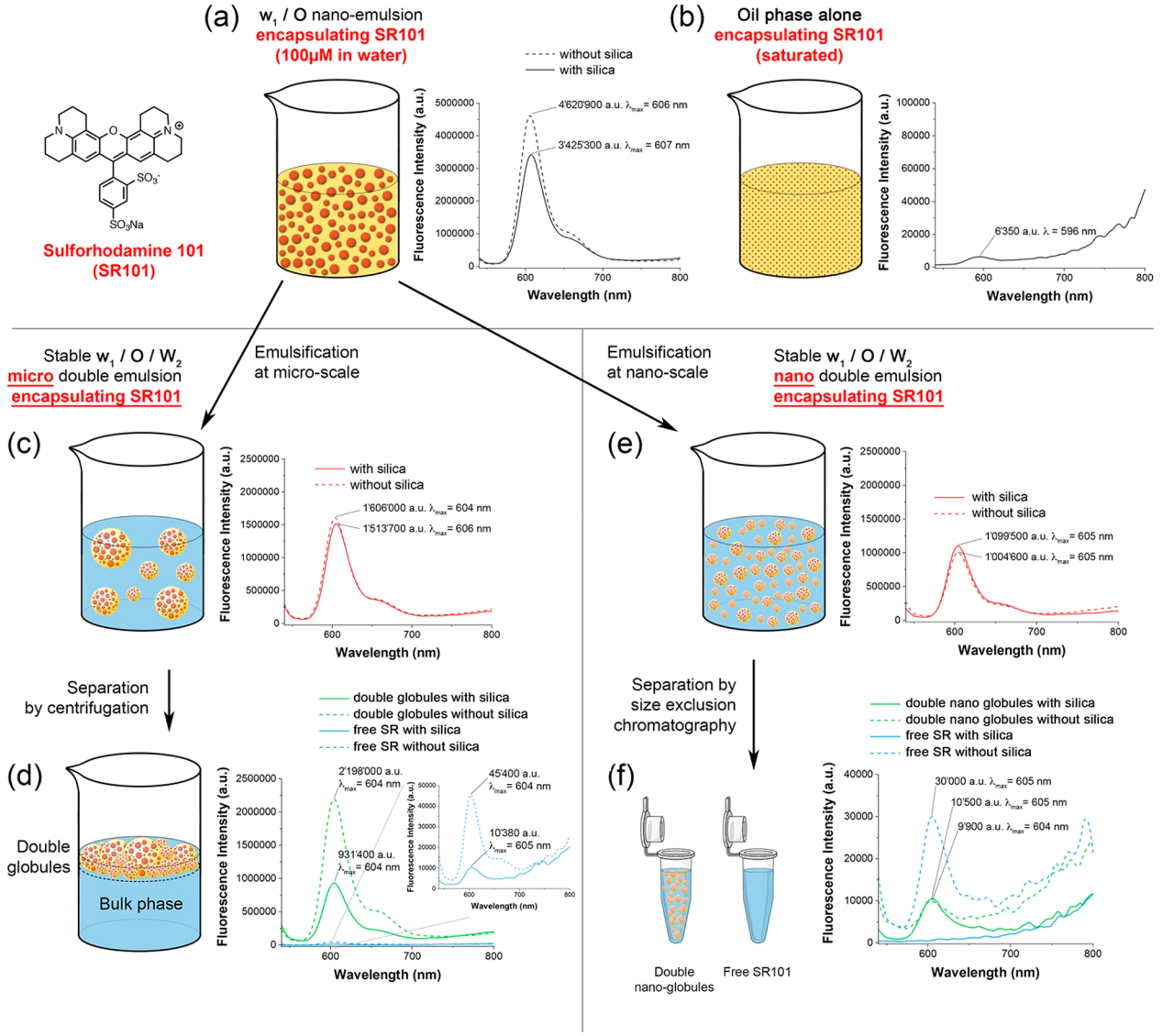

Figure 11. Schematic representation of the protocol followed to prove that liquid water is still present inside the micro and nano double droplets, along with the corresponding fluorescence spectra. Sulforhodamine (SR101) is (a) encapsulated in the w_1/O nanoemulsions with and without silica (APTES 10% in oil), (b) dispersed at saturation in oil as a control, and then encapsulated in micro double droplets (c) before and (d) after separation by centrifugation or encapsulated in nano double droplets (e) before and (f) after separation by size exclusion chromatography.

the dilution factor inherent in the double droplet's formulation is 5 (1.2 mL of primary w_1/O emulsions in 4.8 mL of W_2), while the decrease in the resulting fluorescence signal is only around 2.2 (1.5×10^6 a.u./3.4×10^6 a.u.). This increase follows dye dequenching due to a concentration decrease (i.e., due to the dye release from the inner droplets, as observed with methylene blue).

On the other hand, in the case of nanodouble emulsions, the SR101 signal in double nanoemulsions is slightly more diluted around 1.5×10^6 a.u. (Figure 11e) as a result of the formulation method; however, this dilution is even further increased after the size exclusion chromatography separation (Figure 11f). The fluorescence signal in double nanodroplets with and without silica still appears to be measurable and significant (around 1.0×10^4 a.u.), and importantly, the peak maximums appear at 604 and 605 nm (not at 596 nm when the dye is dispersed in oil in Figure 11b). These two points confirm that SR101 is still solubilized in water, inside the double nanodroplets. Then, the signal of the free dyes appears to be important in the fraction without silica and nonexistent with silica, in line with the former EE results and conclusions established in the previous sections.

■ CONCLUSIONS

In this study, we formulate stable double emulsions from the micrometric to the nanometric scale, with their respective properties. This is achieved by simply reinforcing the water/oil interface of the primary internal water droplet with a silica membrane, resulting in efficient encapsulation of the hydrophilic materials in the internal water. We show that the modulation of the thickness of the silica membrane (by varying the formulation parameters) can modulate the encapsulation efficiency (up to 100% encapsulation), size, and release properties. Such a system paves the way for a large number of applications, from pharmaceuticals with the delivery of hydrophilic active principles to agrifood and cosmetics applications with the long-term storage and protection of fragile, unstable, or volatile compounds. Moreover, the double

DOI: 10.1021/acs.langmuir.8b03919
Langmuir 2019, 35, 2313−2325

emulsion morphology transposed to the nanoscale has never been reported and is a novel solution for the i.v. administration and targeted coadministration of hydrophilic and lipophilic agents.

AUTHOR INFORMATION

Corresponding Author

*Tel: + 33 3 68 85 42 51. Fax: + 33 3 68 85 43 06. E-mail: nanton@unistra.fr.

ORCID

Mayeul Collot: 0000-0002-8673-1730

Yves Mély: 0000-0001-7328-8269

Nicolas Anton: 0000-0002-7047-9657

Notes

The authors declare no competing financial interest.

ACKNOWLEDGMENTS

S.A. would like to acknowledge the Higher Education Commission of Pakistan for providing financial support for PhD scholar. X.W. would like to acknowledge the China Scholarship Council for her Ph.D. fellowship (Grant No. 201706240033 supported this work).

REFERENCES

(1) Lamba, H.; Sathish, K.; Sabikhi, L. Double Emulsions: Emerging Delivery System for Plant Bioactives. *Food Bioprocess Technol.* **2015**, *8* (4), 709−728.

(2) Hearn, T. L.; Olsen, M.; Hunter, R. L. Multiple Emulsions Oral Vaccine Vehicles for Inducing Immunity or Tolerance. *Ann. N. Y. Acad. Sci.* **1996**, *778* (1), 388−389.

(3) Okochi, H.; Nakano, M. Preparation and Evaluation of w/o/w Type Emulsions Containing Vancomycin. *Adv. Drug Delivery Rev.* **2000**, *45* (1), 5−26.

(4) Muschiolik, G.; Dickinson, E. Double Emulsions Relevant to Food Systems: Preparation, Stability, and Applications. *Compr. Rev. Food Sci. Food Saf.* **2017**, *16* (3), 532−555.

(5) Assadpour, E.; Maghsoudlou, Y.; Jafari, S.-M.; Ghorbani, M.; Aalami, M. Evaluation of Folic Acid Nano-Encapsulation by Double Emulsions. *Food Bioprocess Technol.* **2016**, *9* (12), 2024−2032.

(6) Esfanjani, A. F.; Jafari, S. M.; Assadpoor, E.; Mohammadi, A. Nano-Encapsulation of Saffron Extract through Double-Layered Multiple Emulsions of Pectin and Whey Protein Concentrate. *J. Food Eng.* **2015**, *165*, 149−155.

(7) Esfanjani, A. F.; Jafari, S. M.; Assadpour, E. Preparation of a Multiple Emulsion Based on Pectin-Whey Protein Complex for Encapsulation of Saffron Extract Nanodroplets. *Food Chem.* **2017**, *221*, 1962−1969.

(8) Mohammadi, A.; Jafari, S. M.; Assadpour, E.; Esfanjani, A. F. Nano-Encapsulation of Olive Leaf Phenolic Compounds through WPC−Pectin Complexes and Evaluating Their Release Rate. *Int. J. Biol. Macromol.* **2016**, *82*, 816−822.

(9) Matsumoto, S. Development of W/O/W-Type Dispersion during Phase Inversion of Concentrated W/O Emulsions. *J. Colloid Interface Sci.* **1983**, *94* (2), 362−368.

(10) Pradhan, M.; Rousseau, D. A One-Step Process for Oil-in-Water-in-Oil Double Emulsion Formation Using a Single Surfactant. *J. Colloid Interface Sci.* **2012**, *386* (1), 398−404.

(11) O' Dwyer, S. P.; O' Beirne, D.; Ní Eidhin, D.; Hennessy, A. A.; O' Kennedy, B. T. Formation, Rheology and Susceptibility to Lipid Oxidation of Multiple Emulsions (O/W/O) in Table Spreads Containing Omega-3 Rich Oils. *LWT - Food Sci. Technol.* **2013**, *51* (2), 484−491.

(12) Ding, S.; Anton, N.; Akram, S.; Er-Rafik, M.; Anton, H.; Klymchenko, A.; Yu, W.; Vandamme, T. F. T. F.; Serra, C. A. C. A. A New Method for the Formulation of Double Nanoemulsions. *Soft Matter* **2017**, *13* (8), 1660−1669.

(13) Zhang, M.; Corona, P. T.; Ruocco, N.; Alvarez, D.; Malo de Molina, P.; Mitragotri, S.; Helgeson, M. E. Controlling Complex Nanoemulsion Morphology Using Asymmetric Cosurfactants for the Preparation of Polymer Nanocapsules. *Langmuir* **2018**, *34* (3), 978−990.

(14) Malo de Molina, P.; Zhang, M.; Bayles, A. V.; Helgeson, M. E. Oil-in-Water-in-Oil Multinanoemulsions for Templating Complex Nanoparticles. *Nano Lett.* **2016**, *16* (12), 7325−7332.

(15) Zhang, M.; Nowak, M.; Malo de Molina, P.; Abramovitch, M.; Santizo, K.; Mitragotri, S.; Helgeson, M. E. Synthesis of Oil-Laden Poly(Ethylene Glycol) Diacrylate Hydrogel Nanocapsules from Double Nanoemulsions. *Langmuir* **2017**, *33* (24), 6116−6126.

(16) Florence, A. T.; Whitehill, D. The Formulation and Stability of Multiple Emulsions. *Int. J. Pharm.* **1982**, *11* (4), 277−308.

(17) Hanson, J. A.; Chang, C. B.; Graves, S. M.; Li, Z.; Mason, T. G.; Deming, T. J. Nanoscale Double Emulsions Stabilized by Single-Component Block Copolypeptides. *Nature* **2008**, *455* (7209), 85−88.

(18) Mehrnia, M.-A.; Jafari, S.-M.; Makhmal-Zadeh, B. S.; Maghsoudlou, Y. Rheological and Release Properties of Double Nano-Emulsions Containing Crocin Prepared with Angum Gum, Arabic Gum and Whey Protein. *Food Hydrocolloids* **2017**, *66*, 259−267.

(19) Zhao, Y.; Zhang, J.; Li, W.; Zhang, C.; Han, B. Synthesis of Uniform Hollow Silica Spheres with Ordered Mesoporous Shells in a CO2 Induced Nanoemulsion. *Chem. Commun.* **2009**, No. 17, 2365−2367.

(20) Wu, S.-H.; Hung, Y.; Mou, C.-Y. Compartmentalized Hollow Silica Nanospheres Templated from Nanoemulsions. *Chem. Mater.* **2013**, *25* (3), 352−364.

(21) Spernath, L.; Magdassi, S. Formation of Silica Nanocapsules from Nanoemulsions Obtained by the Phase Inversion Temperature Method. *Micro Nano Lett.* **2010**, *5* (1), 28−36.

(22) Attia, M. F.; Anton, N.; Bouchaala, R.; Didier, P.; Arntz, Y.; Messaddeq, N.; Klymchenko, A. S.; Mély, Y.; Vandamme, T. F. Functionalization of Nano-Emulsions with an Amino-Silica Shell at the Oil−Water Interface. *RSC Adv.* **2015**, *5*, 74353−74361.

(23) Hu, Y.; Zou, S.; Chen, W.; Tong, Z.; Wang, C. Mineralization and Drug Release of Hydroxyapatite/Poly(l-Lactic Acid) Nanocomposite Scaffolds Prepared by Pickering Emulsion Templating. *Colloids Surf., B* **2014**, *122*, 559−565.

(24) Nebogina, N. A.; Prozorova, I. V.; Yudina, N. V. Effect of Mineralization of Aqueous Phase and Watering on the Composition of the Interphase Layer of Water-Oil Emulsions. *Chem. Sust. Dev.* **2009**, *17*, 207−212.

(25) Fornasieri, G.; Badaire, S.; Backov, R. V.; Poulin, P.; Zakri, C.; Mondain-Monval, O. Mineralization of Water-in-Oil Emulsions Droplets. *MRS Online Proc. Libr.* **2004**, *847* (1−6). DOI: 10.1557/PROC-847-EE3.5

(26) Kresge, C. T.; Loenowicz, M. E.; Roth, W. J.; Vartulli, J. C.; Beck, J. S. Ordered Mesoporous Molecular Sieves Synthesized by a Liquid-Crystal Template Mechanism. *Nature* **1992**, *359*, 710−712.

(27) Cacace, D. N.; Rowland, A. T.; Stapleton, J. J.; Dewey, D. C.; Keating, C. D. Aqueous Emulsion Droplets Stabilized by Lipid Vesicles as Microcompartments for Biomimetic Mineralization. *Langmuir* **2015**, *31* (41), 11329−11338.

(28) Jutz, G.; Böker, A. Bio-Inorganic Microcapsules from Templating Protein- and Bionanoparticle-Stabilized Pickering Emulsions. *J. Mater. Chem.* **2010**, *20* (21), 4299−4304.

(29) Liberman, A.; Mendez, N.; Trogler, W. C.; Kumme, A. C. Synthesis and Surface Functionalization of Silica Nanoparticles for Nanomedicine. *Surf. Sci. Rep.* **2014**, *69* (2−3), 132−158.

(30) Jaganathan, H.; Godin, B. Biocompatibility Assessment of Si-Based Nano- and Micro-Particles. *Adv. Drug Delivery Rev.* **2012**, *64* (15), 1800−1819.

(31) Foglia, S.; Ledda, M.; Fioretti, D.; Iucci, G.; Papi, M.; Capellini, G.; Lolli, M. G.; Grimaldi, S.; Rinaldi, M.; Lisi, A. In Vitro Biocompatibility Study of Sub-5 Nm Silica-Coated Magnetic Iron Oxide Fluorescent Nanoparticles for Potential Biomedical Application. *Sci. Rep.* **2017**, *7*, 46513.

DOI: 10.1021/acs.langmuir.8b03919
Langmuir 2019, 35, 2313−2325

(32) Anton, N.; Vandamme, T. F. T. F. The Universality of Low-Energy Nano-Emulsification. *Int. J. Pharm.* **2009**, *377* (1), 142−147.
(33) Anton, N.; Benoit, J.-P.; Saulnier, P. Design and Production of Nanoparticles Formulated from Nano-Emulsion Templates-A Review. *J. Controlled Release* **2008**, *128* (3), 185.
(34) Anton, N.; Vandamme, T. F. Nano-Emulsions and Micro-Emulsions: Clarifications of the Critical Differences. *Pharm. Res.* **2011**, *28* (5), 978−985.
(35) Ocotlán-Flores, J.; Saniger, J. M. Catalyst-Free SiO2 Sonogels. *J. Sol-Gel Sci. Technol.* **2006**, *39* (3), 235−240.
(36) Kentish, S.; Wooster, T. J.; Ashokkumar, M.; Balachandran, S.; Mawson, R.; Simons, L. The Use of Ultrasonics for Nanoemulsion Preparation. *Innovative Food Sci. Emerging Technol.* **2008**, *9* (2), 170−175.
(37) Mahdi Jafari, S.; He, Y.; Bhandari, B. Nano-Emulsion Production by Sonication and Microfluidization—A Comparison. *Int. J. Food Prop.* **2006**, *9* (3), 475−485.
(38) Anton, N.; Benoit, J.-P.; Saulnier, P. Design and Production of Nanoparticles Formulated from Nano-Emulsion Templates—A Review. *J. Controlled Release* **2008**, *128* (3), 185−199.
(39) Delmas, T.; Piraux, H.; Couffin, A.-C.; Texier, I.; Vinet, F.; Poulin, P.; Cates, M. E.; Bibette, J. How To Prepare and Stabilize Very Small Nanoemulsions. *Langmuir* **2011**, *27* (5), 1683−1692.
(40) Tang, S. Y.; Shridharan, P.; Sivakumar, M. Impact of Process Parameters in the Generation of Novel Aspirin Nanoemulsions − Comparative Studies between Ultrasound Cavitation and Microfluidizer. *Ultrason. Sonochem.* **2013**, *20* (1), 485−497.
(41) Gaikwad, S. G.; Pandit, A. B. Ultrasound Emulsification: Effect of Ultrasonic and Physicochemical Properties on Dispersed Phase Volume and Droplet Size. *Ultrason. Sonochem.* **2008**, *15* (4), 554−563.
(42) Manchun, S.; Dass, C. R.; Sriamornsak, P. Designing Nanoemulsion Templates for Fabrication of Dextrin Nanoparticles via Emulsion Cross-Linking Technique. *Carbohydr. Polym.* **2014**, *101*, 650−655.
(43) Abismaïl, B.; Canselier, J. P.; Wilhelm, A. M.; Delmas, H.; Gourdon, C. Emulsification by Ultrasound: Drop Size Distribution and Stability. *Ultrason. Sonochem.* **1999**, *6* (1−2), 75−83.
(44) Marquez, A. L.; Wagner, J. R. Rheology of Double (W/O/W) Emulsions Prepared with Soybean Milk and Fortified with Calcium. *J. Texture Stud.* **2010**, *41* (5), 651−671.
(45) Gupta, A.; Eral, H. B.; Hattona, T. A.; Doyle, P. S. Controlling and Predicting Droplet Size of Nanoemulsions: Scaling Relations with Experimental Validation. *Soft Matter* **2016**, *12*, 1452−1458.
(46) Gupta, A.; Eral, H. B.; Hatton, T. A.; Doyle, P. S. Nanoemulsions: Formation, Properties and Applications. *Soft Matter* **2016**, *12* (11), 2826−2841.
(47) Márquez, A. L.; Medrano, A.; Panizzolo, L. A.; Wagner, J. R. Effect of Calcium Salts and Surfactant Concentration on the Stability of Water-in-Oil (w/o) Emulsions Prepared with Polyglycerol Polyricinoleate. *J. Colloid Interface Sci.* **2010**, *341* (1), 101−108.
(48) Luo, H.; Macapagal, N.; Newell, K.; Man, A.; Parupudi, A.; Li, Y.; Li, Y. Effects of Salt-Induced Reversible Self-Association on the Elution Behavior of a Monoclonal Antibody in Cation Exchange Chromatography. *J. Chromatogr A* **2014**, *1362*, 186−193.
(49) Lee, L.; Hancocks, R.; Noble, I.; Norton, I. T. Production of Water-in-Oil Nanoemulsions Using High Pressure Homogenisation: A Study on Droplet Break-Up. *J. Food Eng.* **2014**, *131*, 33−37.
(50) Wibowo, D.; Zhao, C. X.; Middelberg, A. P. Emulsion-Templated Silica Nanocapsules Formed Using Bio-Inspired Silicification. *Chem. Commun.* **2014**, *50* (77), 11325−11328.
(51) Jakhmola, A.; Vecchione, R.; Guarnieri, D.; Belli, V.; Calabria, D.; Netti, P. A. Bioinspired Oil Core/Silica Shell Nanocarriers with Tunable and Multimodal Functionalities. *Adv. Healthcare Mater.* **2015**, *4* (17), 2688−2698.
(52) Saberi, A. H.; Fang, Y.; McClements, D. J. Fabrication of Vitamin E-Enriched Nanoemulsions: Factors Affecting Particle Size Using Spontaneous Emulsification. *J. Colloid Interface Sci.* **2013**, *391*, 95−102.
(53) Guttoff, M.; Saberi, A. H.; McClements, D. J. Formation of Vitamin D Nanoemulsion-Based Delivery Systems by Spontaneous Emulsification: Factors Affecting Particle Size and Stability. *Food Chem.* **2015**, *171*, 117−122.
(54) Attia, M. F.; Anton, N.; Akasov, R.; Chiper, M.; Markvicheva, E.; Vandamme, T. F. Biodistribution and Toxicity of X-Ray Iodinated Contrast Agent in Nano-Emulsions in Function of Their Size. *Pharm. Res.* **2016**, *33* (3), 603−614.
(55) Attia, M. F.; Anton, N.; Bouchaala, R.; Didier, P.; Arntz, Y.; Messaddeq, N.; Klymchenko, A. S.; Mély, Y.; Vandamme, T. F. Functionalization of Nano-Emulsions with an Amino-Silica Shell at the Oil-Water Interface. *RSC Adv.* **2015**, *5* (91), 74353.
(56) Ritger, P. L.; Peppas, N. A. A Simple Equation for Description of Solute Release I. Fickian and Non-Fickian Release from Non-Swellable Devices in the Form of Slabs, Spheres, Cylinders or Discs. *J. Controlled Release* **1987**, *5*, 23−36.
(57) Gupta, A.; Badruddoza, Z.; Doyle, P. S. A General Route for Nanoemulsion Synthesis Using Low Energy Methods at Constant Temperature. *Langmuir* **2017**, *33* (29), 7118−7123.
(58) Badruddoza, A. Z.; Gupta, A.; Myerson, A. S.; Trout, B. L.; Doyle, P. S. Low Energy Nanoemulsions as Templates for the Formulation of Hydrophobic Drugs. *Adv. Ther.* **2018**, *1*, 1700020.

DOI: 10.1021/acs.langmuir.8b03919
Langmuir 2019, 35, 2313−2325

Discussion and Perspectives

Nano-emulsion is well recognized as a promising drug delivery system, especially suitable for Class II and IV drugs in Biopharmaceutical Classification System. However, as most of the nanomedicine systems, there are still many problems waiting to be further investigated. For example, how the nano-emulsion droplets interact with biomolecules in a cell level, and whether nano-emulsion can cross biological membranes as an integrity, to the best of our knowledge, are still in abeyance. Besides, the limited understanding of low-energy emulsification, *e.g.*, the influence of surfactants on the process, to some extent, is slowing down the scale-up of nano-emulsions for industrial applications.

Fluorescence probe and bioimaging is a thriving field in nanoscience as these spectroscopies are sensitive, selective, rich in contrast, and versatile. With the help of fluorescence probe, specific ions, small biomolecules and enzyme activities can be detected, the magnificent images of subcellular organelle or 3D structure of tissues can be visualized, and targeting sites can be identified. In addition, fluorescence-based monitoring can be used for guiding phototherapy and surgery. The combination of fluorophores with nanoparticles may lead to improved brightness, reduced toxicity and selective biodistribution.

In this thesis, we studied nano-emulsions in combination with fluorescence probes, to visualize the nano-scaled droplets in a cell level, to characterize the release from droplets in a simpler way, and to study the spontaneous emulsification from a surfactant point of view.

In Chapter 2, we visualized the single nano-emulsion droplet by optimizing the fluorescence properties of encapsulated model molecules. The study of compatibility between fluorescence properties and nano-emulsion compositions may provide useful information for probe design in nano-emulsions or any other lipid-based delivery systems, and further benefit *in vivo* diagnosis. With such ultra-bright molecules, we may propose an alternative solution to track nanoscale objects, in complementarity to low resolution issues of optical microscopes, making the *in vitro* characterization easier and more intuitive. Besides, in this study, we significantly identified the particles mobility *in cellulo* and proved that the negatively charged particles are more interacted with biological entities, which may be helpful for the study of *in vitro-in vivo* correlation (IVIVC).

With such a high-resolved method for particle tracking, we were also curious about the biodistribution of nano-emulsion droplets on the organelle level. For example, regarding cytoplasmic lipid droplets, the inert fat storage depots (that comply the synthesis of protein in cell plasm) can be hydrophobic enough for interacting with nano-emulsion cargos. However,

our experimental results showed that no specific interactions nor release have been observed with nano-emulsions, which may result from the steric hinderance of the PEG brush that inhibits interactions with foreign species.

Interestingly, during the development of hydrophobic fluorescence probes, we found that some of our probes showed an aggregation-induced emission (AIE) - based photochemical property, that is to say, fluorescence intensity increased with the growing percentage of non-solvent (water in our case, probes shown in Fig. 1). AIE-based probes are gradually developed as environmental response tools for specific and selective sensing; however, to the best of our knowledge, there has been not report in nano-emulsion systems. If achieved, this property would induce a strong signal increase in the case that probe is released and accumulated in the targeted sites (*e.g.,* cancer cells), with alternative properties of these fluorescent nano-emulsions that deserves additional studies.

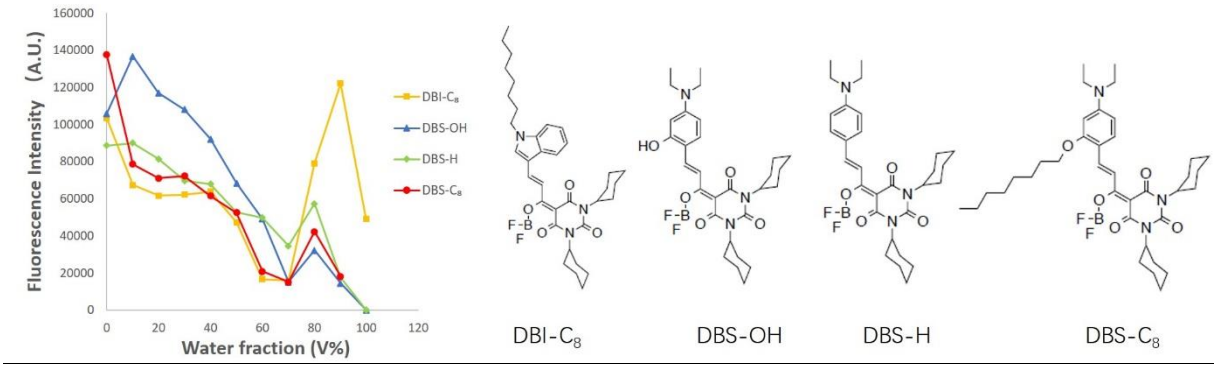

Figure 1 Aggregation-induced emission property of DBS/DBI dyes in THF/water mixture.

In Chapter 3, we investigated the release behavior of a model dye between nano-emulsion droplets based on aggregation-caused quenching (ACQ) phenomenon. Comparing with other methods, our strategy considers the donors and acceptor as a whole system, by detecting the global change of quantum yield, thus allowing us to monitor the mass transfer of dye over time. Besides, selecting quantum yield as the critical parameter of the study (rather than fluorescence intensity), allowed to correct potential fluctuations from the polarity of different media or from the dye precipitation.

Compositional ripening was identified as the driving release mechanism. However, this mechanism is much less known than Ostwald ripening because of the difficulty to quantify and measure. The mass transfer between emulsion droplets, or between droplets and biological molecules is a critical point for studying the formulation stability and clinical application. By

this study, we would like to propose a deep investigation concerning this aspect among different destabilization mechanisms, and to find out the impacts of the formulation parameters on the processes.

It is noteworthy that, all results disclosed are still not clarified, as the case with the release burst between 60°C and 70°C. This gap was attributed to the threshold in the surfactant solubility, below and above the could point that induced a re-emulsification upon a temperature decrease. Even this hypothesis is probable, it would be more reasonable to perform additional studies to verify how the cloud point impact on such a release and whether this result can be observed at different temperatures with other surfactants with different cloud points.

The second discussion point comes with the mechanism of compositional ripening. Although we tried to fit it with the release mechanism used for Ostwald ripening, quantitative models to predict the final equilibrium and the release rate are still missing. Is the equilibrium between water and acceptor entities is effectively the limiting process to the release? Or other phenomena can explain these results, like the collisions between nano-particles, initially declined from hypotheses because of the stability of the nano-emulsions, but it is imaginable they can occur on a reversible way, enough to allow a small dye release. This aspect also deserves further investigations.

In the continuation of this study, further applications would be interesting to investigate, *e.g.*, ACQ effect on the follow-up to droplet integrity *in vitro* or *in vivo*. The global level of fluorescence or quantum yield in a define system would allow following-up the release of encapsulated material in function of the environment properties. As well, the solvatochromism of NR668 could also be an additional parameter to study environmental-sensitive dye releases.

In chapter 4, we proposed three new amphiphilic molecules for spontaneous emulsification, and we would like to discuss the relationship between structure and emulsification property. From the results we can conclude that CMC, HLB values and interfacial charge, are three important parameters which directly impacts on the emulsification efficiency and thus on the size distribution of nano-emulsions. Besides, an appropriate surfactant and water ratio was also optimized and led to increase of the emulsion properties. The study can be considered as a preliminary study and opens further perspectives and new investigations on spontaneous emulsification.

There are also many practical strategies which can be used for optimizing surfactants design. However, plenty of time and labor will be needed for all the experiments, perhaps pharmaceutical high-through put screening can be expected in the field with the development of computational chemistry once we obtain basic information on structure-activity relationship.

Nevertheless, we are optimistically enough to expect more applications of new amphiphilic molecules for nano-emulsions. For example, fluorophores can be grafted on some surfactants, enabling the tracking of the movement of these surfactants on the oil/water interface between two droplets as it was proposed in the droplet core. This could be the subject of further investigations, in parallel to the one presented in Chapter 3, as we could have continued with additional time. In conclusion, as one of the simplest approaches for the formulation of nano-emulsion, spontaneous emulsification still needs to be explored and understood.

The last chapter proposes more examples about how fluorescence probes can be used in lipid-based hybrid, prodrug (in fact *pro-dye*) and in tool for characterization of w/O/W double emulsions. In all the cases, we can notice that, with the development of advanced formulations, characterization methods led by fluorescence labeling are arousing increasing interest, and the tendency of fluorescence probes to be brighter, more efficient and sensitive to more complex environment.

From a macroscopical perspective, with the development of simple nano-emulsification methods, in combination with new possibilities offered by the combination with new lipophilic dyes, fluorescent nano-emulsions will pave the way of the development of brilliant new nano-probes and new tools for tracking drug delivery systems. From an academic point of view, nano-emulsions should be further investigated in the field of 1) more advanced active targeting with a reliable labeling or environmental sensitivity; 2) development of near infrared dyes to investigate sub-skin accumulation effect of nano-emulsions and 3) combination of diagnosis with treatment. From an industrial perspective, the mechanisms study may be beneficial to the scale-up of low-energy emulsification, to the development of more accessible surfactants and nano-emulsion products.

List of Publications

➢ Article

1. Wang, X., Anton, N., Ashokkumar, P., Anton, H., Fam, T. K., Vandamme, T., Klymchenko, A. S. and Collot, M., 2019. Optimizing the Fluorescence Properties of Nano-emulsions for Single Particle Tracking in Live Cells. *ACS applied materials & interfaces*, 11(14), pp.13079-13090.
   DOI: 10.1021/acsami.8b22297

2. Wang, X., Collot, M., Omran, Z., Vandamme, T. F., Klymchenko, A. S. and Anton, N., 2020. Further insights into release mechanisms from nano-emulsions, assessed by a simple fluorescence-based method. *Journal of colloid and interface science*, 578(15), pp.768-778.
   DOI: 10.1016/j.jcis.2020.06.028

3. Akram, S., Wang, X., Vandamme, T. F., Collot, M., Rehman, A. U., Messaddeq, N., Mély, Y. and Anton, N., 2019. Toward the Formulation of Stable Micro and Nano Double Emulsions through a Silica Coating on Internal Water Droplets. *Langmuir*, 35(6), pp.2313-2325.
   DOI: 10.1021/acs.langmuir.8b03919

4. Bou, S., Wang, X., Anton, N., Bouchaala, R., Klymchenko, A. S. and Collot, M., 2020. Lipid-Core/Polymer-Shell Hybrid Nanoparticles: Synthesis and Characterization by Fluorescence Labeling and Electrophoresis. *Soft Matter*, 16(17), pp.4173-4181.
   DOI: 10.1039/D0SM00077A

5. Bou, S., Wang, X., Anton, N., Klymchenko, A. S. and Collot, M., 2020. Near Infrared Fluorogenic Probe as a Prodrug Model for Evaluating Cargo Release by Nano-emulsions. *Journal of Materials Chemistry B*, 8, pp. 5938-5944.
   DOI : 10.1039/d0tb00783h.

➢ Oral presentation

1. Wang, X., Anton, N., Ashokkumar, P., Anton, H., Fam, T. K., Vandamme, T., Klymchenko, A. S. and Collot, M. Encapsulation of super-bright new fluorochrome for single particle tracking in live cells. 26th International Conference on Bioencapsulation. Strasbourg, France. August 27-29, 2019

2. Wang, X., Anton, N., Vandamme, T., Collot, M. and Klymchenko, A. S. Ultra-bright nano-emulsions for single particle tracking in live cells. Journée des Doctorants. Strasbourg, France. December 3, 2019.

3. Wang, X., Anton, N., Vandamme, T., Klymchenko, A. S. and Collot, M. Preparation and Application of Fluorescent Nano-emulsions. Journée de UMR. Strasbourg, France. December 13, 2018

➢ Poster presentation

1. Wang, X., Collot, M., Omran, Z., Vandamme, T. F., Klymchenko, A. S. and Anton, N. Investigation of release mechanism of nano-emulsions by a fluorescence aggregation-caused quenching strategy. Controlled release society annual meeting & exposition. Online. June 29 – July 2, 2020.

2. Wang, X., Anton, N., Ashokkumar, P., Anton, H., Fam, T. K., Vandamme, T., Klymchenko, A. S. and Collot, M. Optimizing the fluorescence properties of nano-emulsions for single particle tracking in live cells. Controlled release society annual meeting & exposition. Valencia, Spain. July 21-24, 2019

3. Wang, X., Anton, N., Vandamme, T., Klymchenko, A. S. and Collot, M. Dioxaborine barbituryl styryl fluorophores for tracking individual ultrabright nano-emulsions. Journée de UMR. Strasbourg, France. December 13, 2018

UNIVERSITÉ DE STRASBOURG

WANG Xinyue

EDSC
École Doctorale des
Sciences Chimiques

Étude de nano-émulsions fluorescentes, formulation, optimisation et étude de l'encapsulation de molécules modèles

Résumé

Les nano-émulsions présentent un potentiel important pour la délivrance de médicaments, notamment dû à l'importante surface spécifique développée par des gouttelettes de phase interne, la faible toxicité, et des procédés d'émulsification simples à mettre en œuvre industriellement. Le but de ce travail de doctorat était d'étudier les nano-émulsions en tant que vecteur de molécules d'intérêts. Une première partie concerne l'étude et l'optimisation des propriétés optiques des nano-émulsions encapsulant des sondes fluorescentes avec pour applications le suivi de particules uniques dans la cellule. Une seconde partie décrit une l'étude de stabilité de l'encapsulation via une méthodologie innovante basée sur la fluorescence. Une troisième partie est focalisée sur le procédé d'émulsification spontanée et l'impact de la composition des surfactants utilisés. Enfin, nous avons conduit d'autres études sur des nano-émulsions qui nous ont permis de développer de nouvelles méthodologies, notamment utilisant l'électrophorèse pour caractériser les morphologies des nanoparticules, les propriétés de nouvelles sondes (pro-sondes) fluorescentes et l'application de la sonde fluorescente sur la caractérisation de la structure d'une w/O/W double émulsion.

Mots clés: Nano-émulsion, surfactant, libération, suivi de particules uniques, intégrité

Abstract

Owing to the relatively high surface area, reduced toxicity, simplified emulsification process, nano-emulsion is showing great potential serving as a good drug delivery system. The aim of this PhD work was to study nano-emulsion as a vector of molecules of interest. The first part concerns the study and optimization of the optical properties of nano-emulsions encapsulating fluorescent probes, with the application on tracking single particles in the cell. The second part studies the stability of the encapsulation using an innovative methodology based on fluorescence. The third part focuses on the spontaneous emulsification process and the impact of surfactants. Finally, we have conducted other studies around nano-emulsions which have enabled us to develop new methodologies, in particular, using electrophoresis to characterize the integrity of nanoparticles, the properties of new fluorescent probes (pro-probes) and the application of fluorescence probe on structure characterization of w/O/W double emulsion.

Key words: Nano-emulsion, surfactant, release, single particle tracking, integrity